



udp UNIVERSIDAD
DIEGO PORTALES

**A MM AND NEAR-IR STUDY OF YSOS:
FROM OUTBURSTING PROTOSTARS TO SATELLITES**

A THESIS SUBMITTED BY

**PEDRO HENRIQUE SOARES DA SILVA DE PINHO
NOGUEIRA**

TO THE

**FACULTAD DE INGENIERÍA Y CIENCIAS
INSTITUTO DE ESTUDIOS ASTROFÍSICOS**

**In partial fulfillment of the requirements for the degree of Doctor of
Philosophy in Astrophysics.**

Supervisor: Alice Zurlo

Co-Supervisor: Lucas Cieza

**UNIVERSIDAD DIEGO PORTALES
Santiago, Chile
2024**

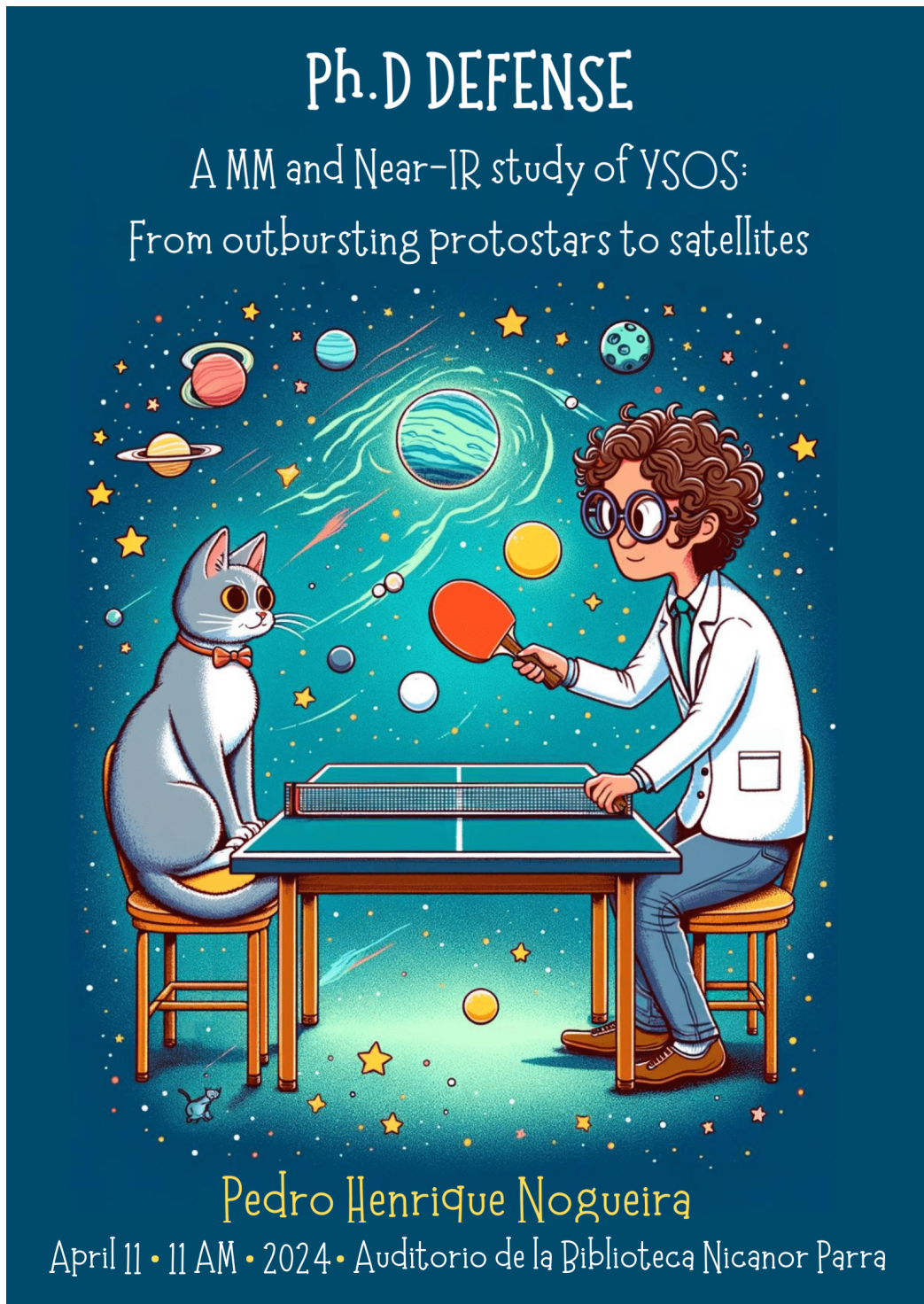


Figura 1: Poster secretly made by UDP friends to advertise others regarding my defense.

APPROVAL REPORT

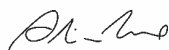
A copy of the approval report signed by the Thesis committee is displayed:



Acta de Deliberación Defensa de Tesis Doctoral

En Santiago, el 11 de abril de 2024 el Tribunal de Defensa de Tesis Doctoral compuesto por la profesora Dra. Alice Zurlo (UDP), Dr. Lucas Cieza (UDP), Dra. Dary Ruiz-Rodríguez (NRAO, EE.UU.), Dr. Anthony Boccaletti (Observatorio de París, Francia) y Dr. Michael Meyer (Universidad de Michigan, EE.UU.) sobre la base del texto del proyecto, la exposición del doctorando y sus respuestas a las intervenciones de los miembros del tribunal, ha resuelto aprobar la tesis doctoral *A MM AND NEAR-IR STUDY OF YSOs: FROM OUTBURSTING PROTOSTARS TO SATELLITES* del doctorando PEDRO HENRIQUE S.S.P. NOGUEIRA.

Los miembros del Tribunal firman para constancia.



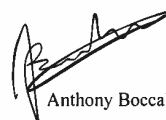
Alice Zurlo
Supervisor, UDP



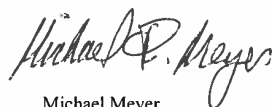
Lucas Cieza, UDP



Dary Ruiz-Rodríguez
NRAO, EE.UU.



Anthony Boccaletti
Observatorio de París, Francia



Michael Meyer
Universidad de Michigan, EE.UU.



Bin Yang
Ministro de fe

Facultad de Ingeniería y Ciencias – Av. Ejército Libertador 441, Santiago



To and for clearer skies ahead

ACKNOWLEDGEMENTS

Acknowledging so many great people who have supported me on this journey is a challenging task, but I will do my best.

First of all, I would like to express my gratitude to my scientific mentors and advisors, Alice Zurlo and Lucas Cieza. Your guidance and support were fundamental in making this achievement possible. I also extend my thanks to the committee members for their help during the development of my thesis and the defense itself. Special thanks go to Camilo, Cecilia, and Trisha. You helped me tremendously behind the scenes, showing immense patience and dedication while teaching and supporting me through the toughest moments.

Thanks especially to Trisha, my extra advisor and super duper friend. You helped me a lot with everything—in work, and in life. Sometimes, just your presence in the office was enough to give me strength and courage to advance more, do more, and be more. You are engraved in my heart, Trishita!

Thanks to the UDP community. I was pleasantly surprised when I first arrived at UDP. The Astronomy Institute is truly an oasis of gentle people. Everyone there is so nice! I really wish all academic environments were like the one in which I had the opportunity to see and live.

Eu queria especialmente agradecer, do fundo do meu coração, meus pais, Vitor e Roseli, e minha irmã, Ana Clara, os quais sempre me apoiaram com esse sonho doido, de entender e alcançar as estrelas, apesar de me levar ao ponto de ficar mais velhinho e ainda viver de forma instável hahaha. É o preço de sonhadores nesse mundo louco em que hoje vivemos, mas posso dizer, ainda hoje, que não me arrependo da trilha que percorri. Agradeço muito todo o apoio que tive para concluir esses suados 12 anos de estudo e dedicação. Para vocês, o meu mais sincero OBRIGADO e AMO VOCÊS!

Agradeço aos amigos que fiz nessa minha longa jornada, alguns que ficaram comigo até hoje e outros que deixaram suas marcas em uma página que já folheei, porém foram fundamentais para mim. A mencionar alguns deles: grupinho do rock de Amparo - a gente se fala e se encontra um dia a cada 1 ou 2 anos mas sempre é muito prazerosa a companhia de vocês. É muito legal acompanhar a nossa trajetória desde o período de crianças/adolescentes até jovens adultos. Desejo o melhor para vocês! Também menciono meu grande amigo Victor. Companheiro desde início/meio da graduação, foi e continua sendo uma ótima pessoa, de grande coração e humor duvidoso (porém similar ao meu). Te agradeço pela companhia e por tudo até hoje. Te desejo o melhor! Agradeço aos amigos da graduação e do mestrado, alguns deles que por consequências da vida ME SEGUIRAM até o Chile (Priscila, Camila, Douglas), e outros que ainda sigo os passos por redes sociais e eventuais mensagens (Eduardo, Yanna, Stephane, Aline, Natasha, Rodrigo, e muitos outros).

Agradeço ao BR chilean gang, grupo esse que reuniu brasileiros únicos porém duvidosos (Priscilla, Camila, Douglas, Carol, Tuila, Danielle, Flor, Johnny, Thallis e Larissa). Vocês fizeram com que minha estadia aqui não fosse tão dolorosa como poderia ter sido. É normal que um estrangeiro sinta um grande impacto ao estar longe de casa, cultura e família. Porém vocês reduziram demais esse possível dano com sua maravilhosa companhia, risadas, diversões, fofocas, memes e muito mais! Amo vocês, lindos!

Agradezco mucho las amistades que hice en Santiago, especialmente a los grupos de tenis de mesa en los que participé. Recordé mi vieja pasión por el deporte y realmente me dediqué mucho a mejorar. Esa experiencia fue increíble gracias a la compañía de gente maravillosa y muy amable. Gracias a los grandes maestros Juan Papić, Francisco Mendoza, Roberto, Luis Peña y Luis “Loco” Fredes por ayudarme a mejorar y desarrollar esa pasión que tenía, y por la paciencia que tuvieron con mi español limitado. Agradezco a mis amigos Milio, Leo, Lucas y Gabriel. Agradezco muchísimo a Milio, que fue un gran amigo, me invitó a su casa para jugar muchas veces, y es una persona increíble, de corazón gigante. Agradezco de corazón a Gabriel, con quien además del tenis de mesa, compartió sus logros, se interesó por los míos, me llevó a cafés y me enseñó acerca de la cultura chilena y de cosas muy raras como películas underground, veás filosóficas/políticas y la participación de Platón en todo eso. Descubrí cuánto me gustaba la comunidad chilena gracias a él. Lamentablemente, dejaré su compañía por ahora, pero dejo aquí constancia de que fue el chileno que más me hizo apreciar su país y su cultura. Un día volveré y te sacaré la chucha en un partido.

I profoundly thank the people from my office. From the veterans who have moved on to other offices across lands and oceans (Aldo, Kacper, Rafi, Emily), to the core members of the Why??? group (Keerthana, Pablo, Trisha, Tatevik, Emilio, Florence, Kevin, and Simon). I don't know if you guys realize how important you were/are to me and how crucial you were for me to keep my sanity during my Ph.D. The never-ending conversations, laughs, and gossips (while of course keeping the working pace) made my stay and my working hours incredibly enjoyable. Every day I was excited to go to the university because of your presence. I love you guys! I will really miss you, and your close family members who I also love (Ranjit and the beautiful Rohini, Karen and the long-awaited Vaneh).

Agora agradeço à minha família mais próxima nesses anos: minha amada esposa, Carol, e meu primogênito felino, Morpheu. Eu amo tanto vocês! São tão parte de mim que não consigo imaginar uma vida sem suas presenças. Estiveram comigo nos momentos difíceis, tristes, felizes, durante derrotas e conquistas! No filme “Dança Comigo”, há um trecho que acho super pertinente a esse parágrafo. A personagem de Susan Sarandon questiona, “Why do people get married?” e logo em seguida diz: “There are billions of people on the planet. What does any one life mean? In a marriage, you are promising to care about everything: the good things, the bad things, the terrible things, the mundane things. All of it. All the time, every day. You are saying, – Your life will not go unnoticed, because I will notice it. Your life will not go unwitnessed, because I will be your witness.” Portanto, deixo aqui palavras mais pertinentes à Carol: Te amo, meu amor! Obrigado por ser minha âncora quando precisei frear, meu motor quando precisei acelerar, mas principalmente minha principal testemunha e cúmplice! Agora, deixo palavras mais pertinentes ao Morpheuzinho: miau, miau, miau, miau, miau, miau, miau, miau, miau. Você sempre foi e sempre será nosso filhinho amado, nosso reizinho, o líder dos gatinhos.

Por fim, agradeço a mim mesmo. Deixo essa nota pessoal para lembrar-me que no final das contas, o carro-chefe de mudanças e progresso é você mesmo. É você quem colhe os frutos que planta, e você é quem deveria ser seu maior motivador e quem mais acredita no seu potencial. Eu consegui! Sou doutor!



“When you feel yourself hitting up against your limit, remember for what cause you clench your fists... remember why you started down this path, and let that memory carry you beyond your limit.”

— All Might, in *My Hero Academia* – Kōhei Horikoshi

ABSTRACT

We are currently in a golden era of observing and characterizing Young Stellar Objects (YSOs), protoplanetary disks, and substellar objects. This period provides essential data that helps unveil the most complex aspects of the formation and evolution of these celestial bodies. In this thesis, we explore two binary systems at different stages of formation.

Firstly, we investigate an eruptive YSO system with ALMA band 6 (1.3 mm) observations, revealing its binarity and dust/gas properties. HBC 494, a FUor object in the Orion Molecular Cloud, displays disk asymmetry at 0.2'' resolution, resolved into two components, HBC 494 N (primary) and HBC 494 S (secondary), at $\sim 0.03''$. The disks, quasi-aligned and with similar inclinations give hints about its formation scenario. The system exhibits a projected separation of $\sim 0.18''$ (75 au). HBC 494 N is ~ 5 times brighter and ~ 2 times larger than HBC 494 S. We notice that the northern component has a similar mass to the FUors, while the southern has to EXors. The HBC 494 disks show individual sizes that are smaller than single eruptive YSOs. The ^{12}CO , ^{13}CO , and C^{18}O molecular line observations reveal bipolar outflows and rotating, infalling envelopes. Cavity features within the continuum disks' area suggest continuum over-subtraction or slow-moving jets and chemical destruction along the line-of-sight.

Secondly, we explored a young binary system with the advent of high-contrast imaging observations performed with the instrument VLT/SPHERE in the H band. We performed astrometric, photometric, and orbital analysis. η Tel, a 18 Myr system, comprises a 2.09 M_{\odot} A-type star and a M7/M8 brown dwarf companion, η Tel B, separated by $\sim 4.2''$ (208 au). New SPHERE/IRDIS coronagraphic observations with a contrast of 1.0×10^{-5} at the location of the companion are presented in this work. Alongside with previous literature astrometric measurements, a η Tel B astrometric follow-up of over a 19-year baseline is provided. The astrometric positions of the companion are calculated with an uncertainty of 4 milliarcseconds (mas) in separation and 0.2 degrees in position angle. The companion's contrast is 6.8 magnitudes in the H band, with a separation of 4.218'' and a position angle of 167.3 degrees. Orbital analysis reveals a low eccentric orbit ($e \sim 0.34$) with an inclination of 81.9 degrees (nearly edge-on) and a semi-major axis of 218 au. The mass of η Tel B is determined to be $48 M_{Jup}$, consistent with previous literature. No significant residual indicative of a satellite or disk surrounding the companion is detected, with limits ruling out massive objects around η Tel B at separations down to 33 au with masses as low as $1.6 M_{Jup}$.

The two studies presented in this thesis establish a couple of different analyses and methodologies, ranging from sub-mm to near-IR wavelength observations. I hope it can help elucidate how diverse, complex, and intriguing the field of (sub)stellar formation/evolution can be.

CONTENTS

Author copyrights	i
Approval Report - Doctoral thesis	ii
1 Introduction	1
1.1 Protoplanetary disks - theory and observations	1
1.1.1 YSOs classification and evolutionary stages	2
1.1.2 Eruptive stars - a “special” case	5
1.1.3 Protoplanetary disks - properties, structure, and principal physical mechanisms	10
1.2 Substellar objects: formation and detection via HCI	23
1.2.1 The main scenarios for substellar objects formation	24
1.2.2 (Sub)stellar multiplicity formation	27
1.2.3 High-Contrast Imaging: instrumentation, observing strategies and data-processing	32
1.2.4 High-Contrast Imaging: observing/characterizing substellar companions	47
1.3 Outline of this thesis	59
2 ALMA resolves the binary HBC 494	60
2.1 Introduction	60
2.2 Observations and data reduction	62
2.2.1 Continuum imaging	62
2.2.2 Line imaging	63
2.3 Results	63
2.3.1 Continuum analysis	63
2.3.2 Line analysis	66
2.4 Discussion	70
2.4.1 Multiplicity and triggering mechanisms	70
2.4.2 Disk sizes and masses	71
2.4.3 Binary formation and alignment	72
2.5 Conclusions	73
2.6 Appendix	74
2.6.1 Effects of continuum over-subtraction	74
2.6.2 ^{12}CO , ^{13}CO and C^{18}O channel maps with contours and the effect of cloud contamination	75
2.6.3 Extra channel maps	75
3 Characterization of the η Tel system	88
3.1 Introduction	88
3.2 Observations and data reduction	90
3.2.1 Observations	90
3.2.2 Data reduction	91

3.3	Methodology and results	91
3.3.1	Astrometry and photometry	91
3.3.2	Orbital fitting analysis	97
3.4	Discussion	101
3.4.1	Orbital fitting constraints	101
3.4.2	Possible formation scenarios	103
3.4.3	The close surroundings of η Tel B	104
3.5	Conclusions	106
3.6	Appendix	110
3.6.1	Cornerplot of the orbital fitting	110
4	Final remarks and conclusions	111
4.1	Specific questions/concepts addressed	112
4.1.1	What is the correlation between stellar multiplicity and accretion processes, and why are binary eruptive systems so infrequently observed?	112
4.1.2	How robust astrometric analysis of a system contribute to its characterization	112
4.1.3	How can one deduct the formation scenario for multiple systems?	113
4.1.4	Is it possible to search for satellites orbiting substellar companions via HCI?	114
	Bibliography	115

LIST OF FIGURES

1	Poster secretly made by UDP friends to advertise others regarding my defense.	i
1.1	Schematic representation of the stages of star/planetary formation	3
1.2	Four main mechanisms proposed to explain transition disks: grain growth, photoevaporation, clearing by a companion and dead zones	5
1.3	Classification of YSOs according to SED classification	6
1.4	Artistic representation of a YSO having an outbursting accretion and rise in luminosity	7
1.5	YSOs variabilities in magnitudes due to bursts and outbursts and their timescales	9
1.6	Schematic representation of regions of an accreting disk	10
1.7	Schematic representation of the structure of protoplanetary disks and how they can be observed depending on the wavelength	11
1.8	Gas surface density profiles for edge-on and large cavity transition disks, with higher CO-based gas-to-dust ratio	14
1.9	Substructures observed in PPDs	15
1.10	Proposed scenario of substructures evolution driven by giant planets formation	16
1.11	Representation of different geometries and structures observed in scattered light and sub-mm continuum	18
1.12	Illustration of the spectral index as a function of radius in a protoplanetary disk	20
1.13	Schematic representation of the outcomes of dust collisions in PPDs	22
1.14	Schematic representation of the grain growth towards planetary formation	26
1.15	Luminosity-time evolutionary tracks computed using the Marley et al. (2007b) methodology	27
1.16	Mechanisms for multiple (sub)stellar formation	28
1.17	Evolution of effective temperature for substellar and low mass stars	33
1.18	Exoplanets population and their respective discovery techniques	34
1.19	Schematic representation of how a contrast curve is interpreted	35
1.20	Diffraction-limited images of two point objects formed by a lens.	36
1.21	Rayleigh's criterion for just-resolvable diffraction patterns.	37
1.22	Simplified AO configuration and its impact in observations	38
1.23	Schematic representation of how a classical Lyot coronagraphic works	39
1.24	Representative examples of possible coronagraphic designs with Lyot stops	40
1.25	Illustration outlining the key stages of ADI observing strategy	41
1.26	Images of the system around GJ 758	42
1.27	Schematic representation of SDI observing strategy coupled with PCA post-processing	42
1.28	Schematic representation of RDI sequence	43
1.29	Typical differential imaging pipeline for speckle/PSF subtraction observing strategies coupled with post-processing techniques	44

1.30	Diagram illustrating the ADI observing strategy with three distinct post-processing techniques for building the speckle model	46
1.31	Representation of the conventional establishment of the position angle (PA), along with the parameter separation (ρ) for companion astrometry	49
1.32	Representation of the six Keplerian orbital elements to uniquely describe the orbit of a companion	50
1.33	Demonstration of key properties inferred from direct imaging observations .	52
1.34	Spectra of ultracool dwarfs from M9 to T7.5	53
1.35	Exoplanets discovered by HCI up to 25-02-2024	55
1.36	Mosaic of remarkable companions and protoplanet candidates detected via HCI	58
2.1	Small-scale moment maps for the analyzed CO isotopologues, ^{12}CO (top), ^{13}CO (middle) and C^{18}O (bottom), without subtraction of the continuum	64
2.2	ALMA observations at 1.3 mm of the HBC 494 system	65
2.3	Radial brightness profile of HBC 494 N and HBC 494 S	66
2.4	^{12}CO channel maps of the HBC 494 system	68
2.5	Large-scale ^{12}CO moment maps split in each one of the bipolar outflow structures	69
2.6	Large-scale moment maps for the analyzed CO isotopologues and spectral fluxes	76
2.7	Small-scale moment maps for the analyzed CO isotopologues, after subtraction of the continuum, and their spectral profiles	77
2.8	Dust disk masses as a function of characteristic radii (FWHM/2)	78
2.9	^{12}CO moment 0 maps before and after continuum removal, along with their spatial profiles	79
2.10	^{12}CO channel maps of HBC 494 system with contours	80
2.11	^{13}CO channel maps of HBC 494 system with contours	81
2.12	C^{18}O channel maps of HBC 494 system with contours	82
2.13	^{13}CO channel maps of HBC 494 system	83
2.14	C^{18}O channel maps of HBC 494 system	84
2.15	^{12}CO channel maps of HBC 494 system, small-scale, after removing the continuum contribution	85
2.16	^{13}CO channel maps of HBC 494 system, small-scale, after removing the continuum contribution	86
2.17	C^{18}O channel maps of HBC 494 system, small-scale, after removing the continuum contribution	87
3.1	ADI-processed from IRDIS coronagraphic sequence (epoch: 2015-05-05; filter: H2) for the η Tel system. The red circle marks the position of η Tel B. The star is masked under the coronagraph at the center of the image. North is up, East is left.	93
3.2	Contrast flux variations for the companion with respect to the star (filter: BB_H).	94

3.3	Contrast curve with respect to η Tel A, using the datacube corresponding to the 2016-06-15 (BB_H) observation. The vertical blue line corresponds to the position of the companion.	95
3.4	Speckle noise estimation for η Tel B in the data set of 2015-05-05. The histograms illustrate the offsets between the true position and flux of a fake companion and its position and flux obtained from the NEGFC technique. The dashed lines correspond to the 1D Gaussian fit from which we determined the speckle noise.	97
3.5	Relative astrometry for η Tel B. The red star marks the position of η Tel A. The blue-filled circles represent astrometric points extracted from the literature. The green-filled diamonds represent the astrometric points from this work. The astrometric point from epoch 2000.378 was not included due to its high uncertainties.	98
3.6	87 randomly selected possible orbits calculated by the Orvara fitting, after excluding orbits based on constraints described in Section 4.1. The black star indicates the position of η Tel A. The best-fit orbit is shown in black.	104
3.7	Analysis of the close surroundings of η Tel B to look for satellites and/or CPDs. In each row, the first panel shows the ADI image zoomed on η Tel B, the second panel shows the model, and the last one the residuals from the subtraction of the two. The three IRDIS epochs are shown. The residuals are expressed in counts. All the panels were normalized to the peak of the central PSF.	105
3.8	Schematic representation of the placement of putative fake satellites around η Tel B to calculate the contrast curves. In this illustration, just one annulus is represented.	107
3.9	Contrast curves with respect to the star η Tel A, centered on the companion as depicted in Fig. 3.8. The three contrast curves, corresponding to different epochs, are showcased. The vertical dashed line indicates the Hill radius of η Tel B under the assumption of an orbit with an eccentricity of $e=0.34$	108
3.10	Corner plot showing the results of the orbital fitting performed by Orvara, after excluding orbits based on constraints described in section 3.4.1. The best-fit values are also reported in Table 3.7.	110

LIST OF TABLES

2.1	List of the Cycle 4 ALMA observations of the target HBC 494, used in this work	62
2.2	ALMA imfit analysis results and physical parameters inferred from the HBC 494 continuum disks.	67
3.1	List of the SPHERE/IRDIS η Telescopii observations used in this work. . .	92
3.2	IRDIS flux contrast in flux and magnitude with respect to the central star for η Tel B.	94
3.3	List of astrometric positions of η Tel B obtained from the IRDIS observations. The error budget is listed in Table 3.4.	98
3.4	Uncertainties used to calculate the error budget for the astrometry of the companion. The values correspond to errors associated with individual frames.	99
3.5	Astrometric positions of η Tel B from the literature and our analysis included in the Orvara analysis.	100
3.6	Priors and initial and distribution of parameters for η Tel system astrometric fitting ^a	101
3.7	Best orbital-fitting parameters for η Tel B calculated from the Orvara orbital characterization.	103

CHAPTER 1

INTRODUCTION

Look up, and then look further. Astronomers are adventurers seeking to discover and unveil the secrets that extend beyond our clouds. Embedded by mighty minds and advanced tools, we are equipped with knowledge meant to be shared.

In this thesis, I am pleased to elaborate on the work conducted during my doctoral stage. My goal is to offer valuable perspectives on stellar and planetary formation by studying a binary eruptive system. I also aim to provide an exhaustive analysis of a young stellar system composed of a giant star and a brown dwarf, on its first Myrs of life. In this chapter, I introduce the scientific background required to provide a comprehensive basis for the subsequent analysis of our research findings.

1.1 Protoplanetary disks - theory and observations

A protoplanetary disk is a rotating circumstellar disk composed of gas and dust. This structure is a direct outcome of angular momentum conservation from a rotating chunk of a molecular cloud, which undergoes flattening as part of its evolutionary process. The protoplanetary disk is formed by the leftover materials that were not accreted into the forming protostar at the center or were evaporated/expelled through other physical mechanisms.

The investigation of protoplanetary disks plays a fundamental role in our comprehension of planetary formation. In an era where observations offer comprehensive insights into the structure and physical mechanisms of disks at various developmental stages, the theoretical aspects of planetary formation are continually refining, yielding physically more accurate models over time. Nevertheless, many questions remain unanswered such as: How do physical and chemical mechanisms vary across different environments and stellar masses? To what extent is chemical complexity necessary for the formation of mature planetary systems? At what frequency rate do protostars accrete and disks expel gas and dust? How and when do planets form, and how do they interact with disks? What processes contribute to the formation of a system like the Solar System, and how common is such an occurrence? These and other questions underscore the complexity of our understanding of this field.

1.1.1 YSOs classification and evolutionary stages

Young stellar objects (YSOs) can be denoted as objects composed of a protostar and its surroundings, mainly the protoplanetary disk and its substructures. A YSO delimits a phase between the formation of a rotating quasi-spherical molecular core around a forming protostar and a main-sequence star and its system.

The connections between stellar/planetary theory and observations allow us to trace how a YSO evolves. According to the most recent compilation/description of protoplanetary disk formation and evolution (Pineda et al., 2023), it can be summarized as follows:

According to observations, bubbles of both neutral and ionized gas are ubiquitously observed in the interstellar medium across the Galaxy. Also, according to models (e.g., Padoan et al., 2017; Kim & Ostriker, 2018; Rathjen et al., 2021), bubbles can be formed by supernova explosions, radiation, and winds from massive stars. Therefore, first, on a scale of 1-100 pc, neutral and ionized hydrogen gas in the shape of quasi-spherical bubbles will expand. The shock between two or more bubbles will generate layers of magnetized molecular gas ($\sim 100 \text{ cm}^{-3}$), which can be described as filaments (scales up to tenths of pc). The filaments will continuously accrete gas and dust and compress it media transverse velocity gradients arising from large-scale inflow, rotation, shearing motions, or a combination of these types of motions. These filaments may further break down into filamentary substructures, called fibers, which can also co-locate with dense cores. These cores will collapse if their local mass per unit length (M_{line}) overcomes the critical $M_{line/crit}$, equals to $2c_s^2/G$, where c_s it is the sound speed at the environment, and G the gravitational constant. If the core starts to collapse, it will trigger gas and dust infalling towards its center. This process will form a hydrostatic core. Consequently, this core, surrounded by a gas and dust thick quasi-spherical shell, will get more dense and hot, thus forming a protostar. Then, due to the conservation of angular momentum, the rotating shell will turn into a disk, becoming flattened and flared. This stage is characterized by episodic accretion and magnetically driven bipolar outflows that are launched from the inner disk. After, the envelope will start to be cleared where the central star, now called pre-main sequence star (PMS). Finally, the primordial disk (protoplanetary disk) will dissipate due to accretion, winds, outbursts, and photoevaporation. However, a debris disk, where second-generation dust will continuously be replenished by the collision of planetesimals, will remain. The evolutionary path here presented usually involves the formation of multiple planets and minor bodies (see figure 1.1). But when and how these planets form still is not well understood.

The presence of circumstellar material was first inferred through infrared excess observations due to the thermal emission of warm dust and through Spectral Energy Distribution analysis (SEDs; Mendoza V., 1966; Cohen & Kuhi, 1979; Kenyon & Hartmann, 1987; Strom et al., 1989). This happened before radio observations assumed a fundamental role. However, even in the current landscape, where interferometry radio data is the primary means for observing disks, allowing for the resolution of substructures, determination of geometries, and identification of multi-components, as well as exploring the involved physical and chemical mechanisms, there remains a common practice of classifying evolutionary stages. This approach is reminiscent of the earlier SED analysis era, measuring

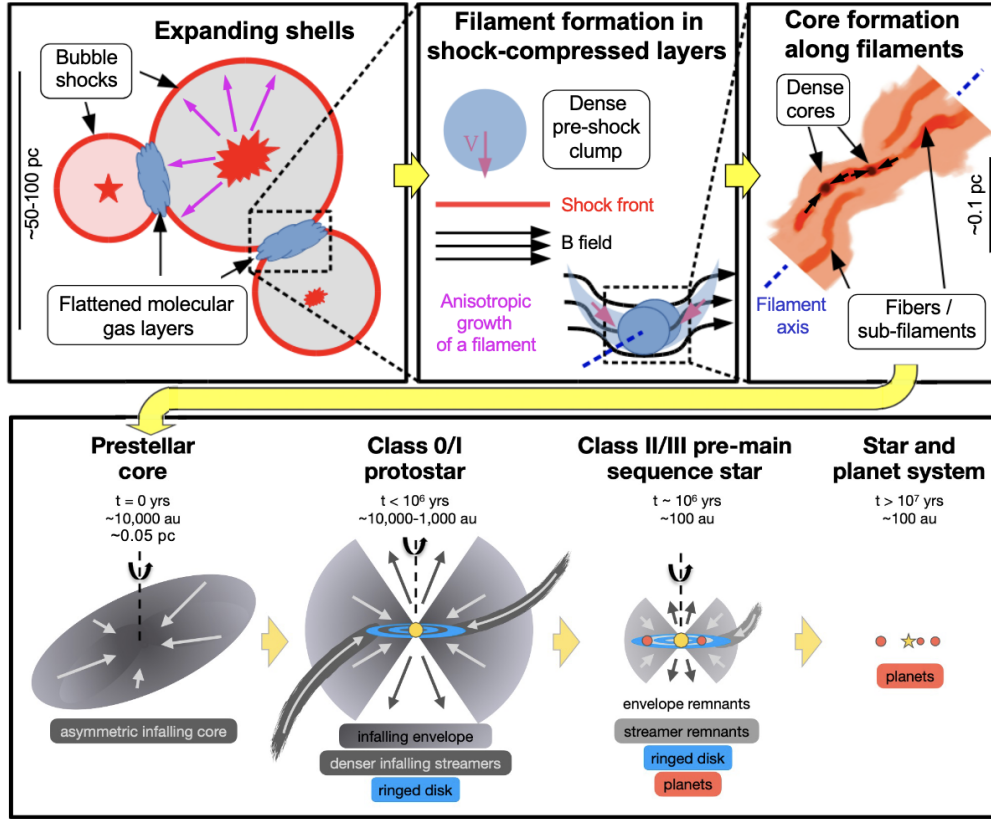


Figure 1.1: Schematic representation of the stages of star/planetary formation, since the formation of filaments through the shock of expanding bubbles mature star/planetary systems. Credits: [Pineda et al. \(2023\)](#).

the slope between about 2 and 25 μm and first formalized by [Lada \(1987\)](#) and [Greene et al. \(1994\)](#):

$$\alpha_{\text{IR}} = \frac{d \log v F_v}{d \log v} = \frac{d \log \lambda F_\lambda}{d \log \lambda} \quad (1.1)$$

These stages include*:

- **Class 0:** These sources are fully embedded by the envelope throughout this short stage ($t < 10^4$ yrs), and they show almost no emission in optical or near-IR wavelengths. Their SEDs are similar to a cold black body and their emission can be detected at longer wavelengths (far-IR to (sub)-mm).
- **Class I:** In this stage, it starts the clearing of the envelope. The SEDs will be constituted by the black body of the protostar, radiation scattered into the line of sight

*It is important to state that this classification can lead to evolutionary misinterpretation depending on the disk's inclination/dust extinction. For example, a class II YSO at high inclination has a similar SED as a class I YSO ([Robitaille et al., 2006](#); [Williams & Cieza, 2011](#))

from dust grains in the disk, emission from the collapsing outer envelope, and thermal emission from a circumstellar disk. The infrared excess slope is positive ($\alpha_{\text{IR}} > 0.3$) in this stage and the SED peaks in the mid to far infrared. The presence of the cold envelope absorbing emission from the dust, gas, and protostar, will produce absorption lines. In this stage, jets and bipolar outflows, playing a fundamental role in clearing the remaining envelope, can be observed. The age of these objects is between 10^4 and 10^5 years.

- **Flat-spectrum:** This stage is an intermediate between Class I and II and has slopes between -0.3 and 0.3 . This stage shows less envelope obscuration and has a greater contribution to the accretion into the SED.
- **Class II:** In this phase, the disks exhibit a slope of $-1.6 < \alpha_{\text{IR}} < 0.3$. The dissipation of the envelope is a defining characteristic, leading to an SED dominated by the stellar photosphere and the circumstellar accretion disk. The initiation of clearing in the accreting circumstellar disk surrounding the now-called pre-main sequence star (PMS) shifts the SED towards the near-IR to the optical range. The SED, wider than a blackbody, reflects the disk's contribution. Concurrently, the YSO's activity begins to diminish, marked by fewer outbursts, jets, and accretion events. These systems typically have an age range of approximately 10^6 to 10^7 years and are commonly referred to as classical T Tauri stars (YSOs leading to a lower mass stellar evolution, up to $2 M_{\odot}$), or Herbig Ae/Be stars (YSOs with spectral type earlier than F0). Moreover, classical T Tauri stars are also known to have strong $H\alpha$ and UV emission, while Herbig Ae/Be stars do not show a so prominent UV excess.
- **Transition disks:** The disks in this stage are known to have large inner gaps due to pressure bumps and/or due to planet formation. They also represent the last stages of inner disk clearing due to accretion onto the PMS. Transition disks are known as having inner cavities between the PMS+inner disk and an outer disk. The process of halting the dust and causing the cavities can be many (see [van der Marel \(2023\)](#) and [Fig. 1.2](#) for further references).
- **Class III:** In this phase, the disk exhibits near-complete passivity with either no or very weak accretion, and the sources demonstrate negative slopes ($\alpha_{\text{IR}} < -1.6$). The spectral energy distribution (SED) closely resembles the blackbody spectrum of the pre-main sequence (PMS) or main-sequence central star. During this stage, the gas content diminishes, leading to the gradual disappearance of the circumstellar accretion disk. These disks host newborn planets, comets, asteroids, and residual pebbles, earning them the designation of debris disks. When the central star remains in the pre-main sequence phase, it is termed a Weak-lined T Tauri, indicating a minimal or absent accretion presence.

A representation of Class 0, I, II, and III YSOs is presented in [Fig. 1.3](#).

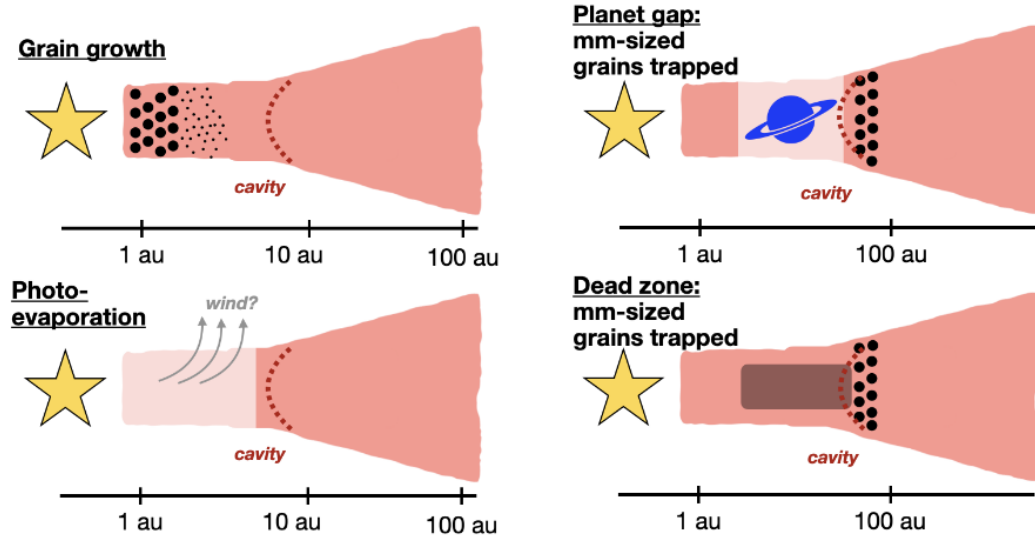


Figure 1.2: Four main mechanisms proposed to explain transition disks: grain growth, photoevaporation, clearing by a companion and dead zones. Credits: [van der Marel \(2023\)](#)

1.1.2 Eruptive stars - a “special” case

Young Stellar Objects (YSOs) have photometric and spectroscopic variability across multiple evolutionary stages. Although understanding the precise mechanisms driving these variations can be challenging in certain cases, it is established that some fluctuations arise from changes in accretion rates.

When a protostar or pre-main sequence (PMS) star experiences a large enhanced phase of accretion, that may last for months to decades, it can be called an eruptive star. During this stage, the accretion disk will transit from a magnetospheric accretion, typical from Class 0-2 YSOs, towards an outbursting accretion. Roughly, the luminosity of the YSO can be expressed as:

$$L_{\text{proto}} = L_{\text{photospheric}} + L_{\text{accretion}} = L_{\text{phot}} + GM_*\dot{M}_{\text{acc}}/R_*, \quad (1.2)$$

where M_* and R_* are the mass and radius of the star, thus stating that an enhancement of accretion will raise the total luminosity (see Fig. 1.4). This process will also trigger more violent outbursts and jets.

Changes in the accretion rate can be measured through different physical components and mechanisms of a YSO. If low-extinct and with a favorable geometry, a direct diagnosis from the heated gas can be done through the UV continuum and several emission lines in UV and optical wavelengths. In the case of more embedded sources, the analysis also can be done up to near-IR. In other cases, a reprocessed emission that occurs at infrared or millimeter wavelengths needs to be used.

For classical T Tauri stars, the accreting gas is conducted by stellar magnetic fields from the disk to the star. The accretion shock heats the photosphere, mostly with X-rays.

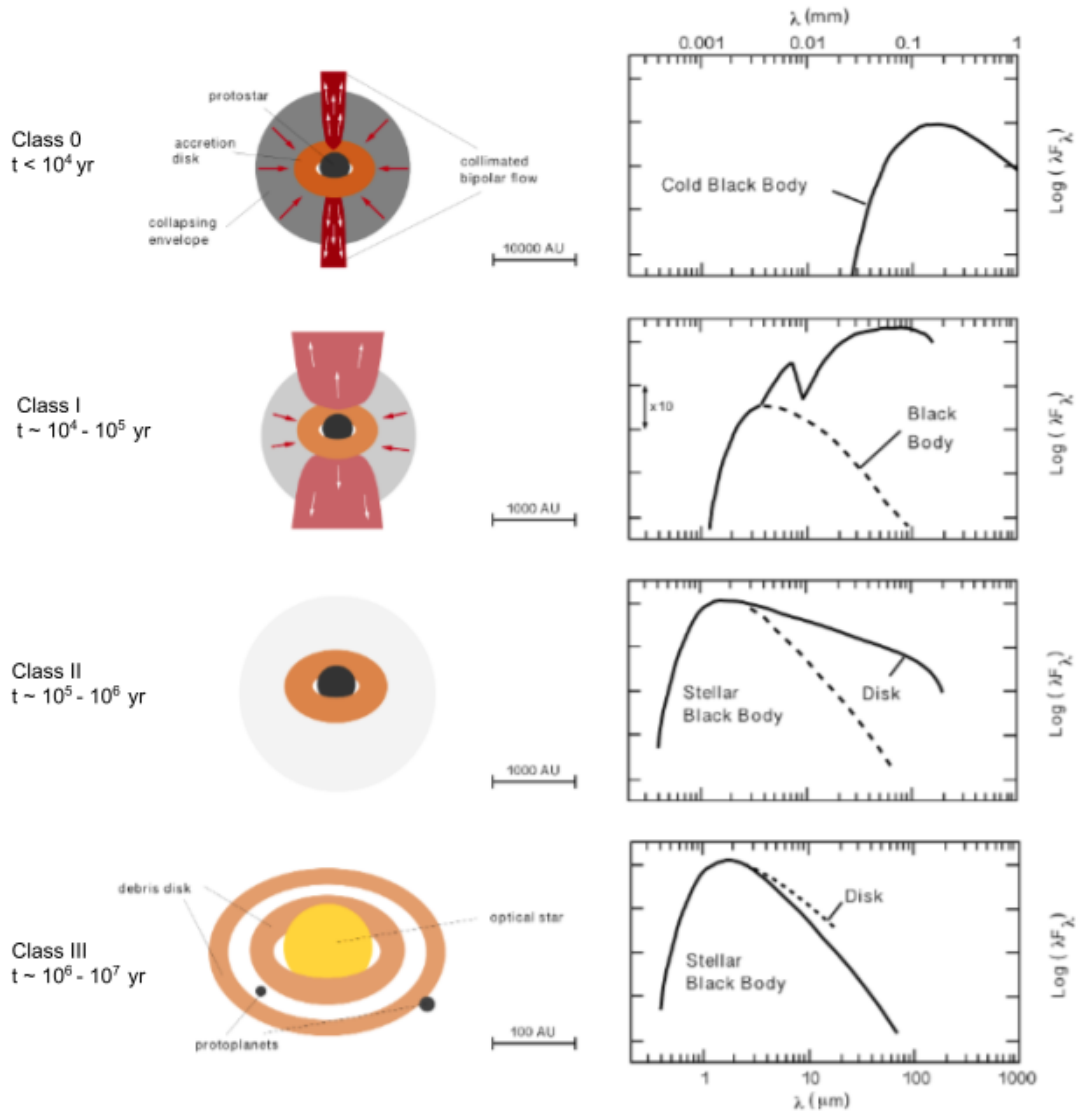


Figure 1.3: Classification of YSOs according to SED classification. The stages represent the standard low-mass star formation. Credits: Adapted from [Macías Quevedo \(2016\)](#).

The heated photosphere and the accretion flow will produce hydrogen recombination, H^- continuum, and line emission, processes observed in optical and UV wavelengths.

For passively heated dust disks (low-accretion, the heating of the dust is essentially from the starlight), the innermost dust emits in the near and mid-infrared. The outer disk, however, dominates long-wavelength emission.

For rapidly accreting disks, viscous processes heat efficiently the disk to higher temperatures, which can surpass the stellar one. Therefore, the luminosity of the YSO is dominated

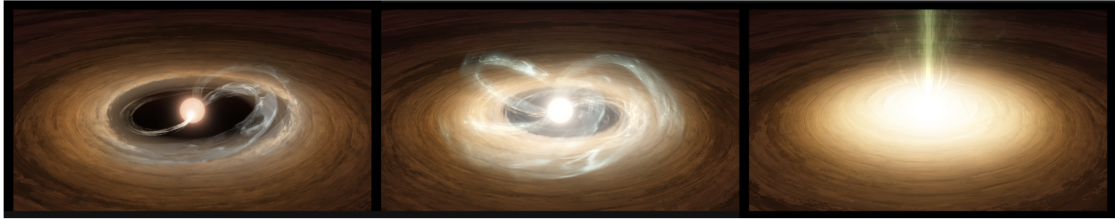


Figure 1.4: Artistic representation of a YSO having an outbursting accretion and rise in luminosity, becoming an eruptive star. Credit: T. Pyle (Caltech/IPAC).

by the accretion, which can be measured at optical and infrared wavelengths. If a typical low-state accretion disk temporarily turns to be a high-state viscously heated disk, as expected for eruptive disks, a large increase in brightness will be detectable at optical and infrared wavelengths.

Historically, since the review from [Audard et al. \(2014\)](#), eruptive stars are mainly classified into two groups, the EX-Lupi-like stars or EXors and the FU-Ori-like stars or FUors. Nowadays, however, due to several eruptive stars having different spectroscopic signatures, or having peak luminosities and different light curves than the regular FUors and EXors, this classification is being challenged (for an updated review, see [Fischer et al. 2023](#)). For the sake of simplicity, I will proceed to explain these two categories.

EXors are YSOs that present 2.5-5 magnitude optical outbursts that last for months to years and may recur after a few years. These objects were inspired by Ex Lupi, a T-Tauri star in the constellation of Lupus. During the periods of quiescence, Ex-Lupi, and other EXors can't be distinguished from a regular T-Tauri in optical and near-IR wavelengths, and spectroscopically in absorption lines of Na, Ca, K, Fe, Ti, Si, and CO. However, in outbursts, most absorption lines turn into emission and many emission lines become stronger. Also, the emission line fluxes concerning accretion, as Paschen β and Brackett γ , show accretion rates on the order of 10^{-7} to $10^{-6} M_{\odot} \text{ yr}^{-1}$.

FUors, from the precursor FU Orionis, are a type of Young Stellar Objects (YSOs) distinguished by more intense and prolonged outbursts compared to EXor variables. During an outburst, the bolometric luminosity of a FUor undergoes a substantial increase, reaching tens to hundreds of solar luminosities. Their accretion rates can vary from 10^{-6} to $10^{-4} M_{\odot} \text{ yr}^{-1}$. Spectroscopically, FUors in outburst exhibit features typical of a viscously heated accretion disk overshadowing the central protostar across all wavelengths. However, their behavior differs at various wavelengths—longer wavelengths reveal colder and slower-rotating regions of the disk. In the optical, they display absorption spectra resembling F or G supergiants, featuring broad lines indicating strong winds, a P-Cygni profile, and notable Li absorption ([Hartmann & Kenyon, 1996](#)). In the infrared, their characteristics are more similar to M or K giants and supergiants, showing strong CO absorption, water, TiO, or VO absorption bands, and prominent He I absorption ([Connelley & Reipurth, 2018](#)).

In an early investigation of protostars within the Taurus-Auriga region, [Kenyon et al. \(1990\)](#) introduced the "luminosity problem." This concept pointed out a statistical anomaly, indicating that protostars displayed lower luminosity than anticipated, considering a steady

accretion scenario and the expected duration for star formation. At the time, two explanations were proposed: protostellar lifetimes last longer than 10^5 yrs proposed by the authors, or episodic bursts of accretion, akin to EXors and/or FUors, accelerating the process. Later, it was inferred from mid-infrared surveys that protostellar lifetimes are ~ 5 times longer than expected (Evans et al., 2009; Dunham et al., 2014a, 2015), reducing the luminosity necessary to be observed in YSOs in case of steady accretion. Although some authors like Offner & McKee (2011), consider the “problem” solved, discrepancies in luminosity persist, ranging from 2 to 10 times lower than expected from a steady accretion scenario. Following, Fischer et al. (2017) have shown that protostellar luminosities have different accretion rates in different evolutionary stages, lowering the rate between Class 0 and I YSOs. This reinforced that a variable scenario, not necessarily episodic or with regular frequency in nature, can match observed protostellar luminosities. Therefore, even though episodic accretion was detected in several sources, it is hard to establish they occur in all YSOs and during all of their evolution. A contemporary understanding of the “luminosity problem” diverges from its initial meaning, now more fittingly used to emphasize the wide range of protostellar luminosities observed in different sources, environments, and stages of evolution. To better represent the variabilities in magnitudes and timescales where a YSO can undergo, see Fig. 1.5.

Up to now, a few tens of eruptive stars have been detected and spectroscopically characterized. Considering that variability in accretion is fundamental to connecting models to observations and inferring important physical parameters such as lifetime and efficiency of mass bulking towards the star, a lot of questions remain unanswered. One of the most crucial ones refers to triggering mechanisms. What drives FUors/EXors accretion variability in a YSO? And how do they stop? In literature, the triggering processes are usually summarized in 3: 1) disk fragmentation (Vorobyov & Basu, 2005, 2015; Zhu et al., 2012); 2) magneto-rotational instability (MRI) (Armitage et al., 2001; Zhu et al., 2009); and 3) tidal interactions between a disk and a companion (Bonnell & Bastien, 1992; Lodato & Clarke, 2004; Borchert et al., 2022b).

The mechanism of disk fragmentation is based on gravitational instabilities usually producing clumps, which will be rapidly inward driven towards the inner disk, and possibly tidally disrupted replenishing material in the viscously heated part. Disk fragmentation can also induce magneto-rotational instabilities (MRI) in the inner disk, another important triggering process.

Magneto Rotational Instability (MRI) is an efficient triggering mechanism. As YSOs undergo radial rotation at different angular velocities, the embedded magnetic fields become twisted and distorted, thereby initiating the MRI. This instability induces turbulence in the disk, enabling the efficient inward transport of gas and dust. Consequently, the MRI redistributes angular momentum, preventing its excessive accumulation in specific regions. However, a certain level of ionization is necessary to couple the material to the magnetic field, making it susceptible to MRI. The dynamically cold regions in a disk, thus, stall the inward transport, accumulating self-gravitating material in the outer disk (see Fig. 1.6). All of the potential solutions to break this flow discontinuity point towards episodic mass accretion events, generated by heat-inducing of the outer disk to the dynamically cold region,

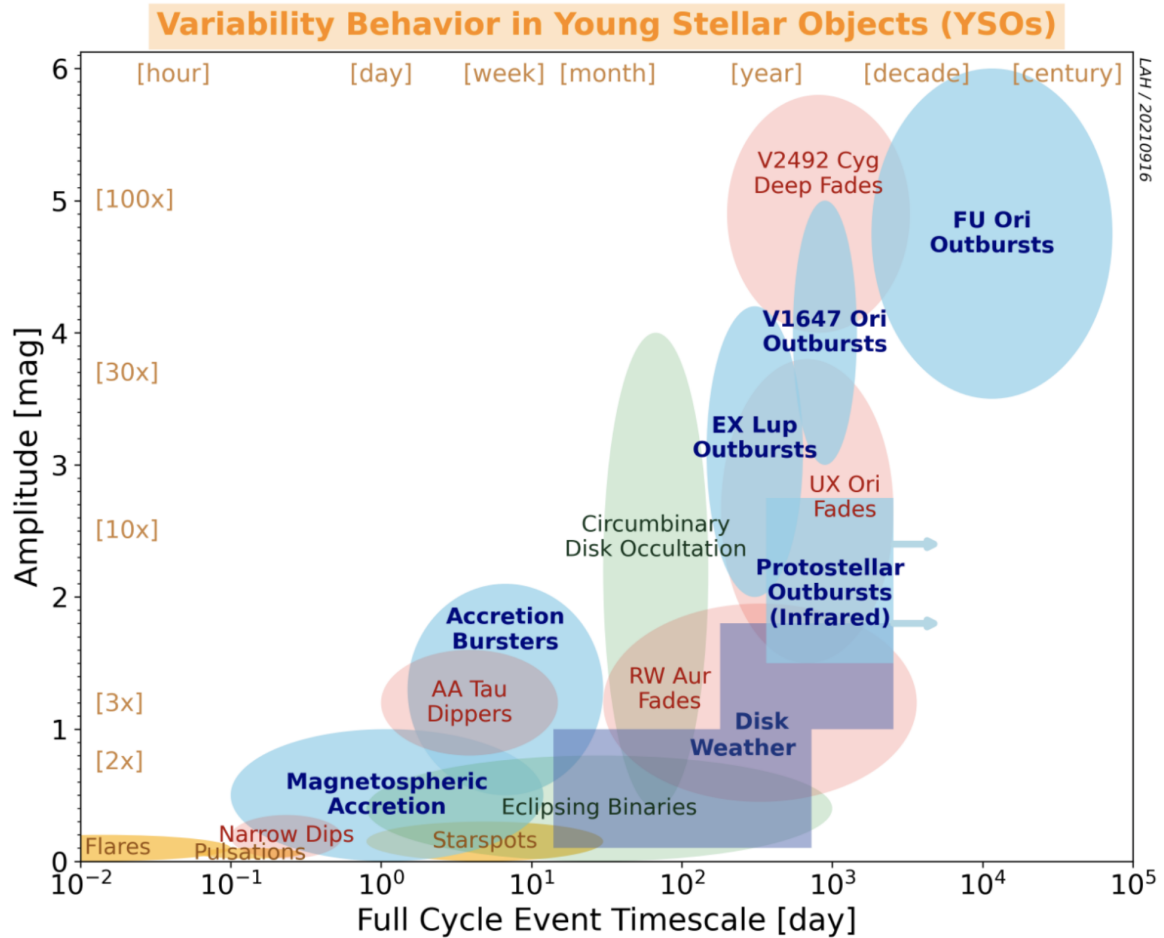


Figure 1.5: YSOs variabilities in magnitudes due to bursts and outbursts and their timescales. I call attention to the already mentioned EX Lup and FU Ori outbursts, being V1647 Ori one intermediate case between both. Credits: Fischer et al. (2023).

re-engaging the transport of material to the inner disk.

The tidal disruption due to a companion is a mechanism, not as efficient as MRI since depends on close encounters with external companions, which may be or not periodic and may be less common to happen. The gravitational disturbance, thus, can form spiral arms, density waves, or other features, redistributing the material in the disk, or even causing disk fragmentation, leading to another mechanism already mentioned and its consequent episodic accretion.

All these mechanisms are not constant and, thus, could explain the return to quiescence stages.

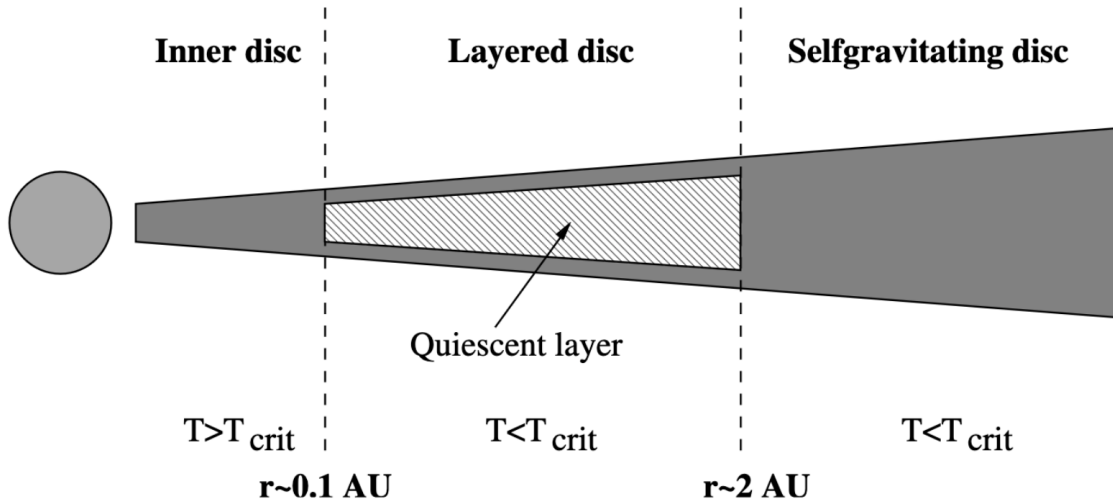


Figure 1.6: Schematic representation of regions of an accreting disk, showing the inner disk coupled to MRI; a quiescent layer, with a temperature lower than the required to couple material to MRI, thus stalling inward transport; and the outer disk which has its material transported by self-gravity. Credits: [Armitage et al. \(2001\)](#).

1.1.3 Protoplanetary disks - properties, structure, and principal physical mechanisms

Here, I characterize the protoplanetary disk (PPD) as the circumstellar disk, excluding consideration of the envelope. A PPD primarily consists of gas and dust inherited from the natal envelope, with molecular hydrogen (H_2) and helium (He) dominating the gas composition, alongside (sub)micron-sized dust particles. The gas constitutes approximately 99% of the PPD's total mass ([Ollivier et al., 2009](#)). Typically, the temperature distribution exhibits higher temperatures in the innermost regions (closer to the star), gradually decreasing radially towards the outermost regions. However, the disk's vertical structure also significantly influences temperature distribution and the distribution of grain sizes. Additionally, different regions within the disk exhibit variations in the movement velocity of both dust and gas, guided by distinct physical mechanisms. Subsequently, I provide a more detailed exploration of the principal parameters and physical mechanisms inherent in a PPD. A schematic representation of the different disk components probed by different wavelength ranges and instruments can be seen in Fig. 1.7, both panels. Specifically, the temperature distribution is depicted at the top panel, while the bottom panel shows different grain evolution processes.

Disk mass

Knowing the total content of dust in a PPD is crucial to determine accretion rates, lifetime, and which substructures and objects can be formed within. Additionally, the grain size distribution is important to determine which grain size can be observed in different wave-

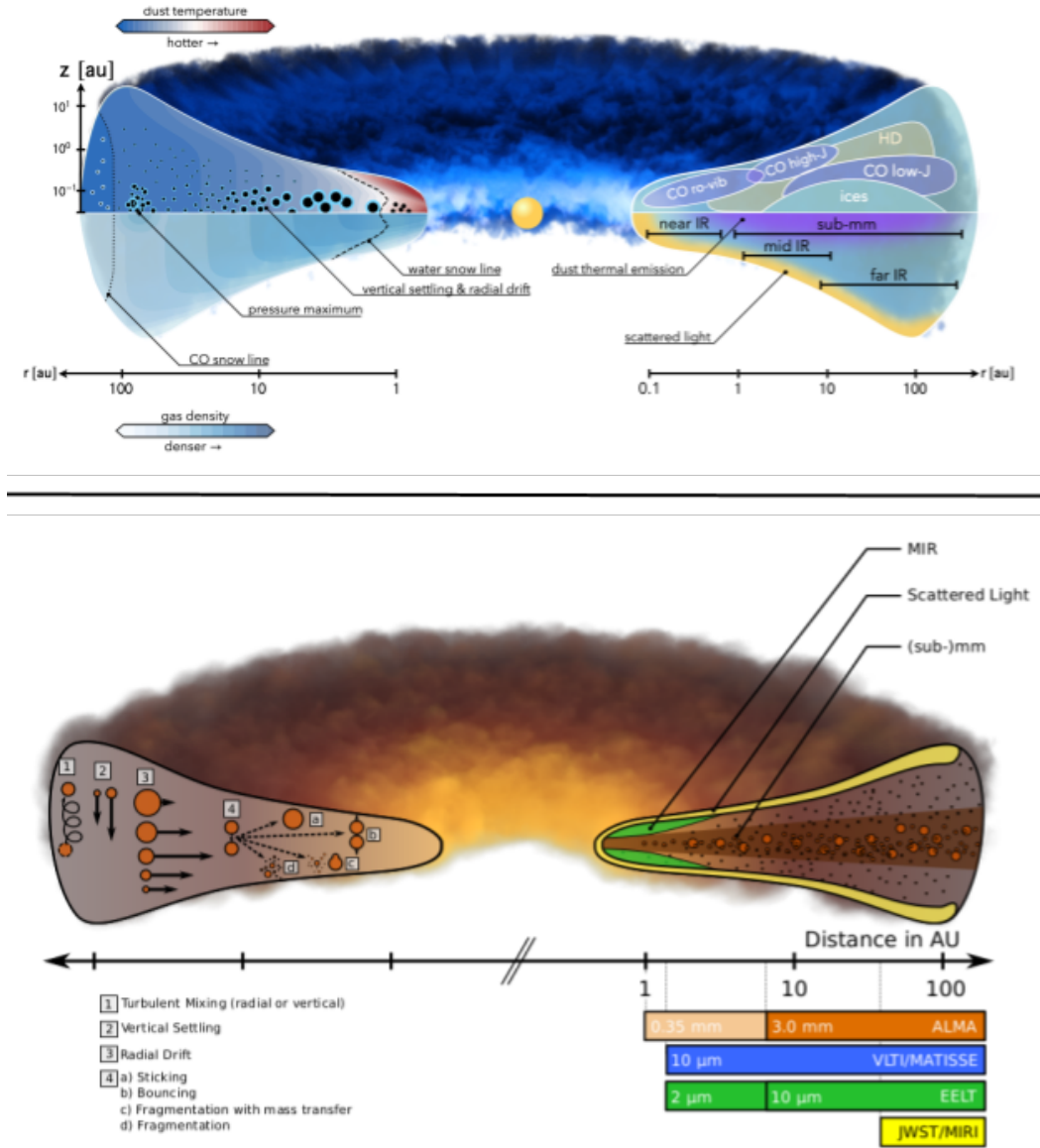


Figure 1.7: Schematic representation of the structure of protoplanetary disks and how they can be observed depending on the wavelength. *Top panel:* dust temperature profile and gas density structure. On the left, the grain sizes are represented according to the size of black-filled circles, when blue contours representing icy water, and white contours CO-coat. On the right, different gas emission regions of the main simple molecules are shown, and dust thermal and scattered emissions are highlighted in purple and yellow, respectively. Credits: [Miotello et al. \(2023\)](#). *Bottom panel:* dust evolution main transport and collision mechanisms are represented on the left. On the right side, areas of the disk that can be observed by different wavelengths and current/future instruments to detect them are shown. Credits: [Testi et al. \(2014\)](#).

lengths and also helps to disentangle problems in planetary formation models regarding

where, when, and how rocky planets/cores of giant planets are formed. Therefore, it is crucial to determine masses and surface densities, which describe how the mass is distributed per unit area on the observed surface (this distribution can vary with depth depending on the wavelength used for observation).

Disk masses are typically derived from observations of thermally heated dust grains. This involves measuring the dust mass and, based on an assumed dust-to-mass ratio, inferring the total mass of the disk. A frequently adopted assumption is a gas-to-dust ratio of 100, assuming a fixed Interstellar Medium (ISM) (Andrews & Williams, 2005, 2007). The continuum emission is optically thin, except for the innermost regions of the disks (approximately less than 10 astronomical units, at 1 mm observations), where the column density becomes too high. The determination of the disk mass from the optically thin reprocessed emission involves employing the following equation:

$$M(\text{gas} + \text{dust}) = \frac{F_\nu d^2}{\kappa_\nu B_\nu(T)}, \quad (1.3)$$

where F_ν is the measured flux at frequency ν , d is the distance to the source, κ_ν is the dust opacity, and $B_\nu(T)$ is the Planck function. At (sub)mm wavelengths, the Planck function approximates to the Rayleigh-Jeans limit, and the following approximation can be done:

$$B_\nu(T) = \frac{2h\nu^3}{c^2} \frac{1}{e^{\frac{h\nu}{k_B T}} - 1} \approx \frac{2h\nu^3}{c^2} \cdot \frac{k_B T}{h\nu} = \frac{2\nu^2 k_B T}{c^2}, \quad (1.4)$$

where h is Planck's constant, c is the speed of light and k_B is the Boltzmann constant. Therefore, observing at these wavelengths provides a dust temperature profile that linearly varies with radius, contrasting with an exponential trend.

Although equation 1.3 is countless times used in literature, it is highly dependent on the determination of average temperature and dust opacity. A good and classical approximation for both is a temperature of 20 K, consistent with IR-millimeter modeled SEDs, CO observations, and theoretical expectations (Andrews & Williams, 2005; Qi et al., 2004; Chiang & Goldreich, 1997 and references therein) and a dust opacity for mm wavelengths from Beckwith et al. (1990), expressed as:

$$\kappa_\nu = 0.1 \left(\frac{\nu}{10^{12} \text{ Hz}} \right)^\beta \text{ cm}^2 \text{ g}^{-1}, \quad (1.5)$$

where the power-law index, β is related to the size distribution and composition of the dust grains (Ossenkopf & Henning, 1994; Pollack et al., 1994). It is commonly assumed a β is equal to 1 for 1.3 mm observations. In addition, the assumptions do not provide good estimations for mass accountability of larger grains, which remains a source of great uncertainty, offering the idea that mass estimations through equation 1.3 may be underestimated. A more complicated scenario is driven by the more recent studies, stating that not only the spectral index β can vary a lot depending on the properties of the grains, such as how porous it is but also estimates big mass content in disks arising from optical thick regions. Additional analyses and methodologies have been explored and suggested for estimating disk masses based on gas content, primarily utilizing CO isotopologues and HD emission. This

approach is taken because H_2 lacks an electric dipole moment as a symmetric molecule, resulting in rare transitions capable of emitting radiation (for a review about mass measurements from gas, see e.g. [Bergin & Williams, 2017](#); [Miotello et al., 2023](#)).

Disks structure and temperature distribution

As aforementioned, how disk material and temperature are distributed in a PPD, is of major importance. During the lifetime of a disk, those distributions can highly vary, as part of the disk will be accreted onto the protostar/PMS, dissipated, and/or radially and vertically. In particular, which process dominates will impact the surface density distribution, $\Sigma(R)$, and the disk outer radius, R_{out} [†]. Therefore, these two parameters are priorities whenever PPDs are been analyzed.

The surface density of a disk can be modelled and analyzed in total or split into gas and dust counterparts, depending on the estimations you are accounting for. A common prescription to describe the radial distribution of the dust and the gas in a viscous disk, and which fits interferometric observations is given by:

$$\Sigma(R) = (2 - \gamma) \frac{M_{disk}}{2\pi R_c^2} \left(\frac{R}{R_c} \right)^{-\gamma} \exp \left[\left(-\frac{R}{R_c} \right)^{2-\gamma} \right], \quad (1.6)$$

where M_{disk} is the disk mass, R_c is the characteristic radius, and γ is the power-law exponent that describes the radial dependence of the disk viscosity ([Lynden-Bell & Pringle, 1974](#); [Hartmann et al., 1998](#)). In this equation, the characteristic radius refers to the region where the surface density starts to deeply steepen from the power law, where it indicates at which part of the disk is viscously dominated. More recently, mainly due to ALMA observations, a recurring observation of continuum substructures, such as gaps and rings, has emerged in most disks observed at sufficient spatial resolution. Additionally, faint optically thin molecular lines could be detected in several cases, tracing disk masses and gas distributions. These findings indicate considerable variability in surface density profiles, deviating from the assumptions of a simple model (see an example in [Fig. 1.8](#)). To improve surface density models, multi-wavelength observations of resolved disks become crucial. Such observations may not only disentangle the degeneracy among temperature, dust surface density, and dust opacity but also provide valuable insights for accurately modeling radial variations in dust particle sizes and scattering opacities ([Miotello et al., 2023](#)). As for gas direct detections to model the surface densities, it is necessary to find optically thin emissions, which are usually faint and rarely show emission from the outer disk in small disks ($R_c < 100$ au; [Williams & McPartland, 2016](#); [Miotello et al., 2018](#)). Detecting them implies observations with high sensitivity and well-known ratios of the tracer to other more abundant tracers. Usually CO gas mass is traced using ^{13}CO or C^{18}O , and adopting a ratio CO-to- H_2 .

Outer gas disk radii, as observed in many ^{12}CO observations, are generally larger than the radii of (sub)mm-sized dust particles. The reason behind this difference is currently

[†]There is no total consensus and a robust physical definition for R_{out} , besides as being the radius that encloses a chosen percentage of the emission. However many authors recently have been using $R_{out} = R_{68\%}$.

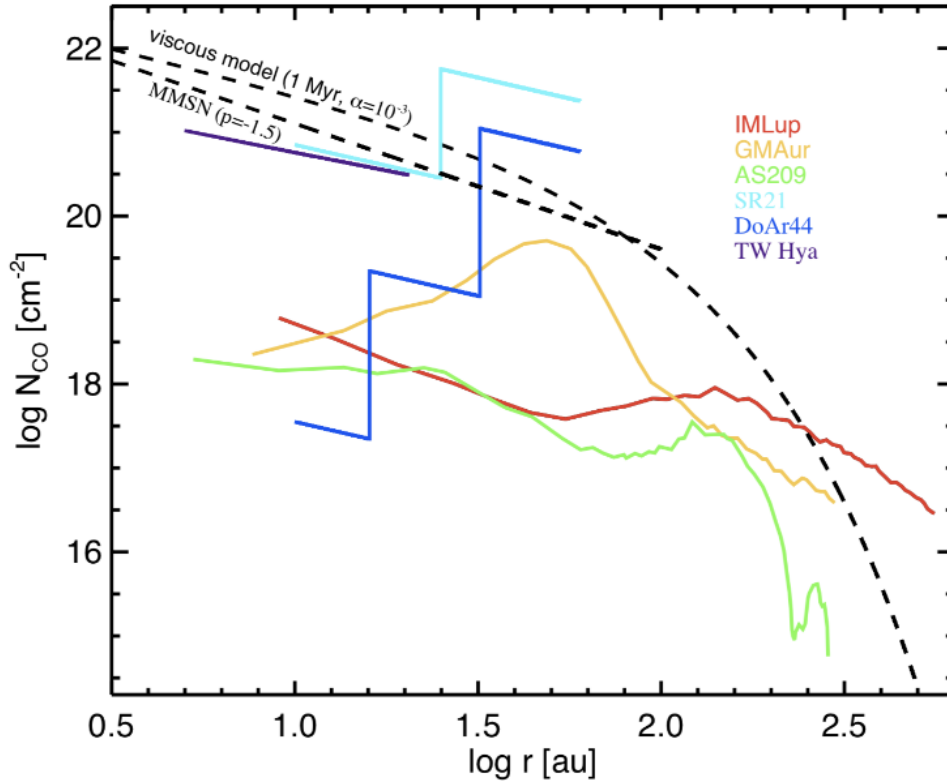


Figure 1.8: Gas surface density profiles for edge-on and large cavity transition disks, with higher CO-based gas-to-dust ratio. The dashed black lines provide the Minimum Mass Solar Nebula (extrapolated to 100 au) and a viscous disk profile for comparison. Credits: [Miotello et al. \(2023\)](#).

under discussion. It could be due to optical depth effects, where CO remains optically thick and bright in the outer disk, while the dust becomes optically thin, and thus faint and challenging to detect. Another possibility is the efficient radial drifting of dust, leading to a reduction in dust radii. The ongoing debate revolves around determining whether optical depth effects, radial drifting, or a combination of both factors contribute to this observed difference. Moreover, according to recent models (e.g., [Toci et al., 2021](#)), if radial drifting is the main process, it is extremely efficient, halting the disk size way more quickly than expected from observations. Thus, it is needed in such cases to invoke substructures that locally slow down or stop radial drifting, as gaps.

Analyzing a sample of 470 YSOs observed at NIR and/or mm wavelengths, [Bae et al. \(2023\)](#) offered a comprehensive statistical and morphological overview of substructures. From this examination and prior analyses, it is accurate to assert that Class II-to-Class III disks can exhibit three primary classes of substructures: rings and gaps, spirals, and crescents (see Fig. 1.9).

Rings are generally defined as circular and azimuthally symmetric. They are the most

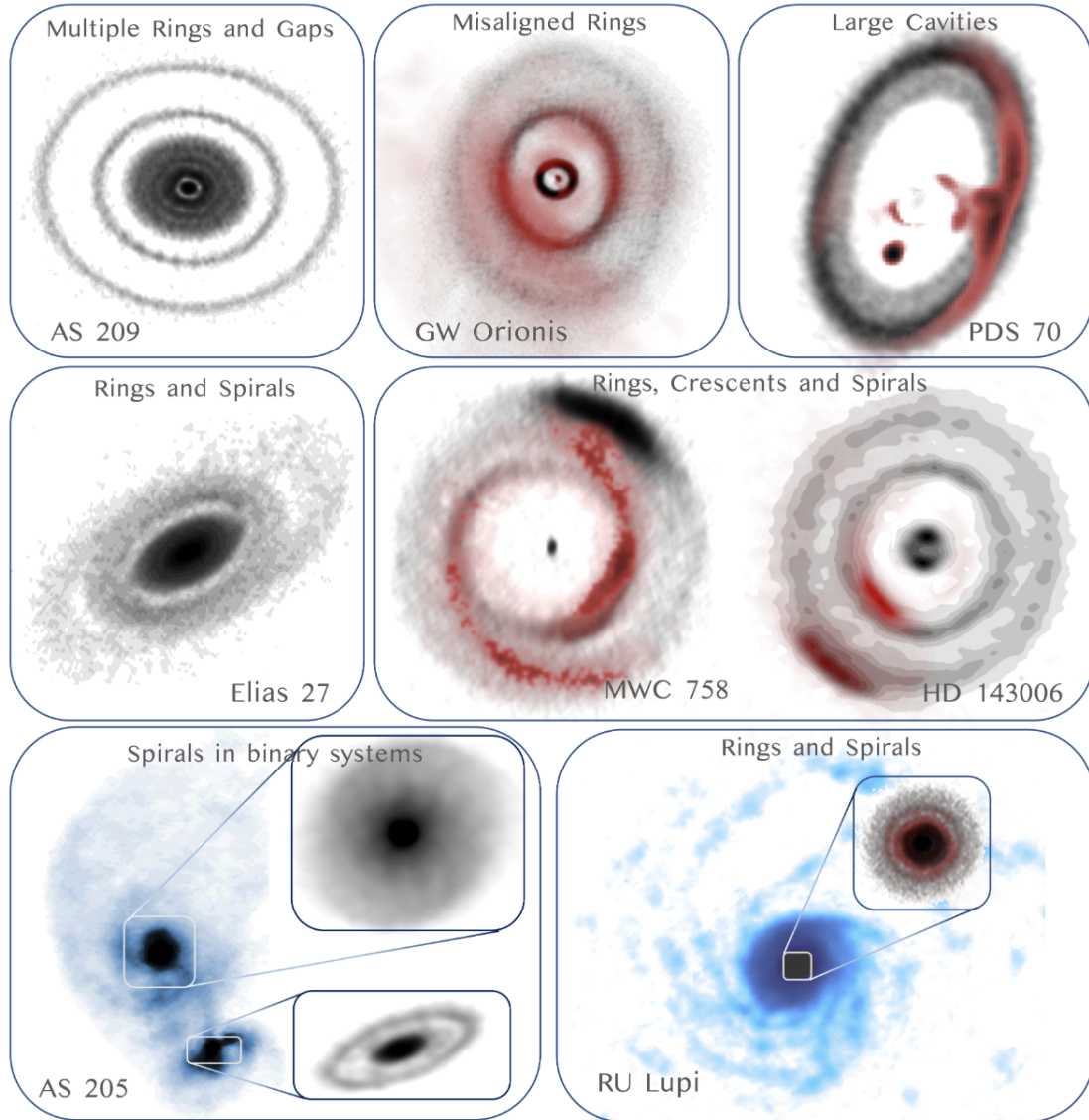


Figure 1.9: Example of substructures observed in PPDs. Black and white contours show millimeter continuum observations, blue contours show millimeter line observations and red contours show near-IR observations. Credits: [Bae et al. \(2023\)](#).

common type of substructure detected until the moment. Gaps are the regions of reduced surface density between denser resolved rings. Rings and gaps are most commonly observed in mm observations rather than near-IR. The apparent discrepancy between both wavelengths can be explained by considering the possibility that the observed rings correspond to pressure maxima within the protoplanetary disk. In such regions, larger particles may be efficiently trapped, leading to their enhanced detection in mm observations. Rings and gaps play a crucial role in the study of planetary formation, as they can be carved by the presence of giant planets forming and opening gaps in the protoplanetary disk. In recent studies, there has been a focus on understanding the evolution of these substructures over

time. Some of the proposed scenarios associate these substructures with the formation of giant planets and their consequent migration (see e.g. [Cieza et al., 2021](#) and Fig. 1.10).

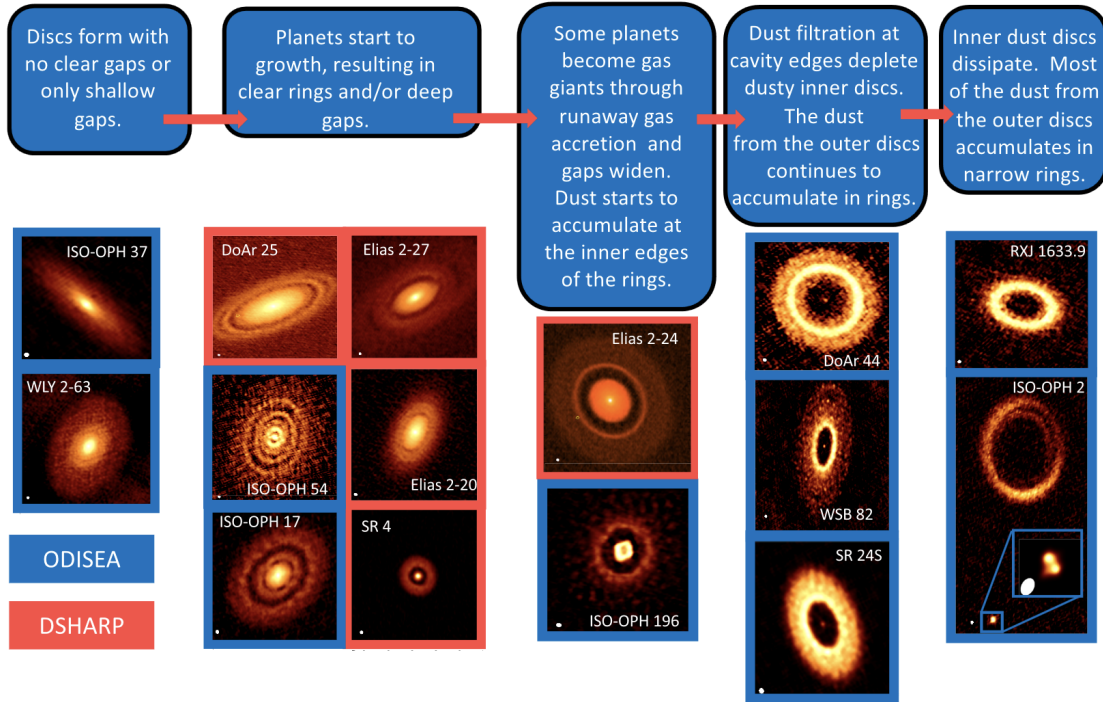


Figure 1.10: Proposed scenario of substructures evolution driven by giant planets formation using massive disks from ODISEA sample. Credits: [Cieza et al. \(2021\)](#).

Spirals are more commonly detected at NIR than in mm observations, mainly because they are linked to smaller grains that are coupled to the gas. While several mechanisms have been suggested to explain the formation of these substructures, the only one that has been conclusive confirmed involves tidal interactions with companions, whether gravitationally bound or not (see discussion and references in [Bae et al., 2023](#)). Detecting stronger spirals is expected to be associated with higher companion masses, making it challenging to observe these substructures in the presence of giant planets using current observational capabilities. Therefore, spiral observations are more commonly associated with brown dwarfs or larger objects. Another popular scenario that arises to explain spirals is gravitational instability (GI), where pitch angles are inversely proportional to disks' mass. When the disk is sufficiently massive ($M_{disk}/M_* \geq 0.25$, based on numerical simulations to explain Elias 2-27 spirals morphology), such that the Toomre parameter $Q = c_s \Omega / (\pi G \Sigma)$ is ≤ 1 , perturbations at intermediate scales are subject to GI ([Toomre, 1964](#); [Kratter & Lodato, 2016](#)). This may lead to the formation of non-axisymmetric spirals which can efficiently transport angular momentum through gravitational torques. Finally, infalling streamers and sound wave propagation can also be invoked as possible causes for spirals.

Crescents, the less commonly observed substructure, are rings that have an azimuthal variation in intensity. Only two leading mechanisms can explain crescents: vortices, created

by hydrodynamic instabilities trapping particles at the region, and lumps created by angular differential velocities in eccentric disks or by trapping material in Lagrangian points. Different from the other two substructures, there is no clear evidence that companions or planet formation are connected to crescents.

Protoplanetary disks have finite thickness and are flared mainly due to pressure support from the gas disk balanced by the gravitational force of the star. In a disk, at a radius r from the star, and at a height of z above the mid-plane, the pressure p of the gas is given as:

$$\frac{dp}{p} = \frac{\Omega_K^2}{v_s^2} z dz \quad (1.7)$$

where v_s is the speed of sound, and Ω_K is the keplerian angular velocity defined by $\Omega_K = \left(\frac{GM_\star}{r^3}\right)^{1/2}$. From equation 1.7, I derive the scale height h_g of the disk (Kenyon & Hartmann, 1987):

$$\frac{h_g}{r} = \left(\frac{v_s^2 r}{GM_\star}\right)^{1/2}, \quad (1.8)$$

or simply, $h_g = v_s/\Omega_K$. If the internal temperature of the disk, which is proportional to v_s^2 decreases more slowly than r^{-1} , the height scale will increase outwards. And the warmer the disk, the higher will be its maximum height - it will be thicker. How the dust vertical structure is deployed, however, depends on the dust coupling to the gas, which also depends on the thermal speed of the gas, grain sizes, and relative velocity between gas and dust and their interaction timescales. The mechanism responsible for this process is aerodynamic drag, which proves to be more effective with smaller dust grains, in less dense regions. Consequently, to capture the emissions and flared surface characteristics of a disk through dust observations, a more effective strategy involves observing at shorter wavelengths, specifically in the infrared range. This approach targets the scattering emissions of smaller grains. On the other hand, sub-mm continuum emission access larger grains decoupled from the gas, which are settled in the mid-plane. Thus, mm-sized grains settle to a thin layer as smaller grains provide a greater vertical distribution (see Fig. 1.11).

Understanding the distribution of temperature is crucial for modeling dust dynamics, gas flow, and chemical mixing within protoplanetary disks. In disks maintaining a steady state (radiative equilibrium), the balance between cooling through radiation emission and heating through absorption of starlight (in passive disks) or a combination of starlight absorption and accretional heating due to viscous dissipation (in active disks) is essential. Theoretical models suggest that 2D temperature profiles for both types of disks should exhibit vertical increases from edges to mid-plane and radial decreases from inner to outer regions (see Fig. 1.7). In the innermost part of the disk, stellar radiation significantly affects the gas and dust at the surface. Smaller grains at the surface scatter, absorb, and re-emit radiation to larger grains in the mid-plane. For dust particles, thermal and scattered continuum emission at a wavelength of λ are dominated by grains with sizes similar to $\lambda/2\pi$. Thus, at a certain distance from the star, temperature profiles are dominated by reprocessed emission throughout the vertical distribution. Radially, from the region where dust is not

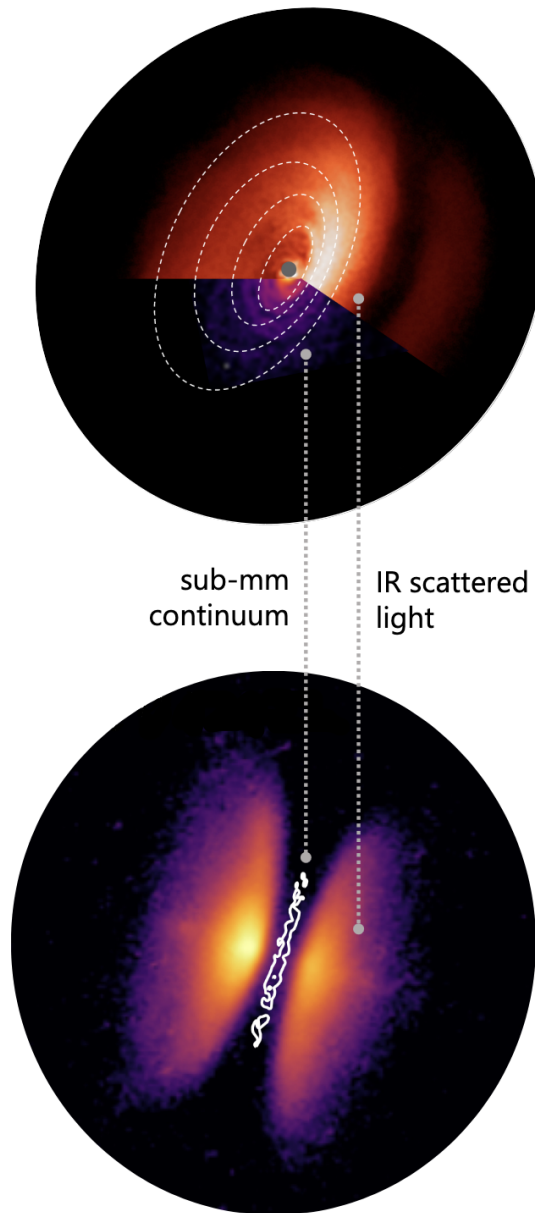


Figure 1.11: Representation of different geometries and structures observed in scattered light and sub-mm continuum. *Top*: Collage of observations of IM Lup, where the white dashed lines represent the disk surface layer. Credits: [Avenhaus et al. \(2018\)](#); [Andrews et al. \(2018\)](#). *Bottom*: Combined observations of the edge-on disk Tau 042021. Credits: [Villenave et al. \(2020\)](#).

sublimated towards the outer regions, the inner disk experiences a mixture of stellar irradiation and viscous accretional heating until it encounters “dead zones” where low ionization levels inhibit MRI, locally halting viscous transport and heating toward the star. Further

from the star, self-scattering and re-emission dominate, implying that a higher scale height at a specific distance results in a colder mid-plane. Vertically, uppermost disk layers with sufficient stellar irradiation exhibit higher temperatures, while intermediate layers, shielded by the upper layers, remain warm ($>30\text{--}40\text{ K}$). The heavily shielded disk mid-plane is cold ($<30\text{ K}$) and harbors the highest gas densities. Despite more complex models considering additional mechanisms and deviating from standard vertically isothermal assumptions, these common simplifications persist due to their practical simplicity.

An essential feature in protoplanetary disks (PPDs), driven by the radial temperature distribution in the mid-plane, is the presence of ice lines – a key element in the context of planetary formation. Icelines mark the radial positions where volatiles undergo sublimation and deposition. These locations are composition-dependent, with different volatile species exhibiting ice lines at distinct radial distances due to their varying sublimation temperatures. For example, N_2 , CO , CO_2 , and H_2O have sublimation temperatures of $\sim 10\text{--}20$, $20\text{--}30$, $60\text{--}70$, and $130\text{--}160\text{ K}$ at typical disk densities, respectively (Zhang et al., 2015). Ice formation within and beyond these regions introduces a new dynamic to dust interactions and the distribution of volatiles. The presence of icy caps can enhance the stickiness of grains, promoting the coagulation and lumpiness essential for the formation of giant gas planet cores in the outer regions of disks (see, e.g., Chambers, 2014; Banzatti et al., 2015). Furthermore, the inward transport of ice or icy caps, upon sublimation, releases vapor that can be transported outward by turbulence. Additionally, larger grains, upon losing their icy mantles, may fragment, causing a sudden increase in optical depth in inner regions—a scenario proposed as one hypothesis to explain gaps. As small fragments drift more slowly than larger ones, they may accumulate near the ice lines (see, e.g., Saito & Sirono, 2011; Ida & Guillot, 2016; Hyodo et al., 2019 and Fig. 1.12). However, current observations do not show a clear correlation between rings and the expected locations of ice lines, challenging the notion of ice lines co-locating with these substructures (Bae et al., 2023).

To determine disk temperature profiles from observations, optically thick tracers as ^{12}CO were used. More recently, with the help of high-resolution observations, better results can be obtained. For example, to study the *molecular layer* of the disk (the region between which molecules are shielded from dissociating radiation but are warm enough to remain in the gas phase), three main techniques can be used:

- Chemistry: Through freeze-out regions for each molecule. For example, observing sharp drops in a sub-mm emission may indicate a freeze-out of specific molecules.
- Line excitation: Through multiple transitions of optically thin lines, the excitation temperatures can be inferred.
- Line optical depth: If the spectral line emission is optically thick, the brightness temperature at a certain region can be interpreted as gas temperature.

For the *mid-plane*, the same techniques can be used. However, as this region contains larger dust grains, additional techniques may come into play:

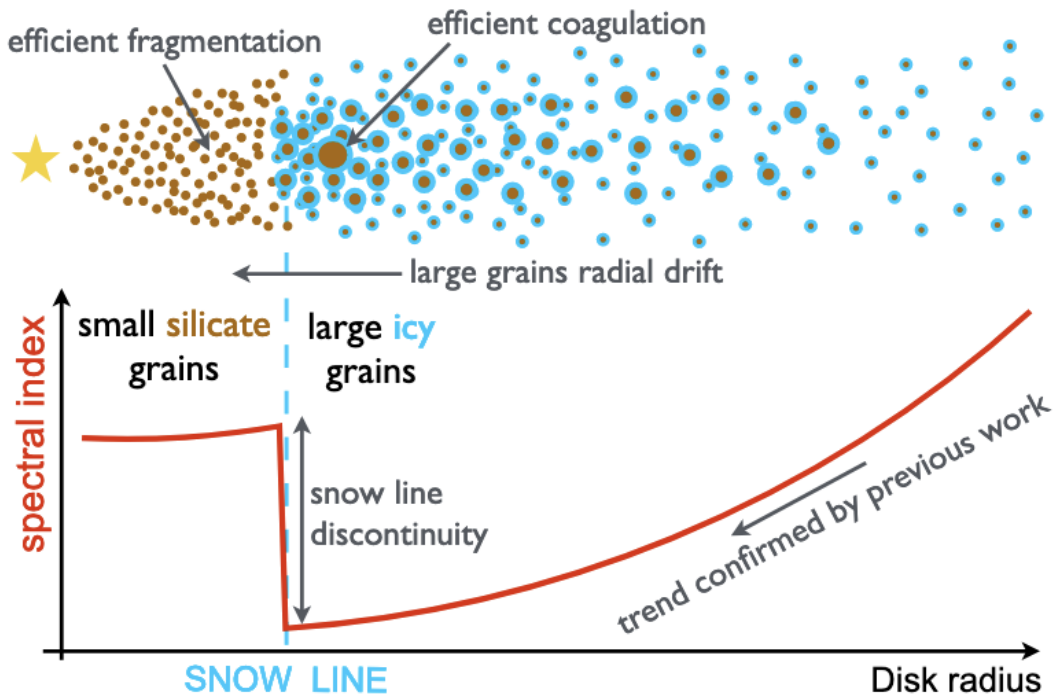


Figure 1.12: Illustration of the spectral index as a function of radius in a protoplanetary disk. Credits: [Banzatti et al. \(2015\)](#).

- Dust optical depth: Millimeter dust grains may have optically thick emission in the inner disk. In such a case, the brightness temperature reveals the dust temperature, which is equal to the gas temperature where collisions counterbalance these two components' temperatures.
- Polarization fractions: Temperature gradients can manifest in the observed polarization fraction due to distinct polarization angles probing varying line-of-sight optical depths. This methodology has been developed by [Lin et al. \(2020\)](#), where conversions from polarized flux patterns to line-of-sight temperature gradients.
- Optically thick gas lines in highly inclined disks: This method utilizes projection effects to derive temperature differentials between the near and far sides of the disk ([Dullemond et al., 2020](#)). It is effective for warmer regions of low-mass star disks or disks around more massive stars with extended CO ice lines.

Grain growth

The grain growth process within a PPD is predominantly influenced by collisions among smaller dust particles. Despite persistent efforts in experiments and modeling, challenges arise in explaining the emergence of dust particles exceeding (sub) μm sizes to mm/cm sizes

or larger (see e.g. [Tu et al., 2022](#)). The collisional processes leading to particles of this scale can be categorized into four main mechanisms, dependent on factors such as the relative size/velocities and composition of the grains involved (see, for example, [Testi et al., 2014](#), Fig. 1.7, bottom panel, and Fig 1.13):

- **Sticking:** It is the dominant mechanism for smaller scales between grain sizes and relative velocities, thus being the dominant outcome from collisions at early stages. Assuming minimal influence from electrostatic charges or magnetic materials during collisions between dust grains, their interaction can lead to sticking through van der Waals forces ([Heim et al., 1999](#); [Gundlach et al., 2011](#)). At lower velocities, grains can grow up to mm sizes.
- **Bouncing:** Even at the same relative velocities as the previous sticking regime, if grains are of similar sizes and are too large (mm-cm sizes), their collisional outcome will be bouncing instead of sticking. This stage/size scale is also known as the "bouncing barrier" ([Zsom et al., 2010](#)).
- **Fragmentation/erosion:** If the grains surpass the bouncing barrier, getting larger, or if the grains have higher relative velocities, they may undergo fragmentation. This process is important to replenish the disk with smaller grains and provide slower grain growth and slower inward migration.
- **Mass transfer:** If grains with different sizes collide at a relative velocity approaching the fragmentation velocity, the collision can lead to substantial mass transfer from the smaller to the larger particle. This mechanism can surpass the bouncing barrier, enabling grains to grow to the size of planetesimals.

Therefore, small dust grains can efficiently grow up to mm sizes through sticking. Subsequently, mass transfer becomes a dominant factor. Throughout this process, fragmentation/erosion continually replenishes the population of small grains in the disk ([Birnstiel et al., 2009](#)). However, this straightforward model may exhibit discrepant size scales and relative velocities depending on the composition, porosity, and the presence of ice or icy shells.

Coupling between gas and dust

Different processes are associated with dust transport and migration, mainly driven by dust-to-gas interaction through aerodynamic drag forces and turbulence (see Fig. 1.7, bottom panel).

Aerodynamic drag forces are caused by the relative motion between gas and dust particles, which produces a friction force. When the grains radii a are smaller than the mean free path between gas particles, they will be subject to Epstein drag ([Epstein, 1924](#)). In the Epstein regime, the drag force F_D is given by:

$$F_D = -\frac{4}{3}\pi a^2 \rho_g \Delta v v_{\text{th}}, \quad (1.9)$$

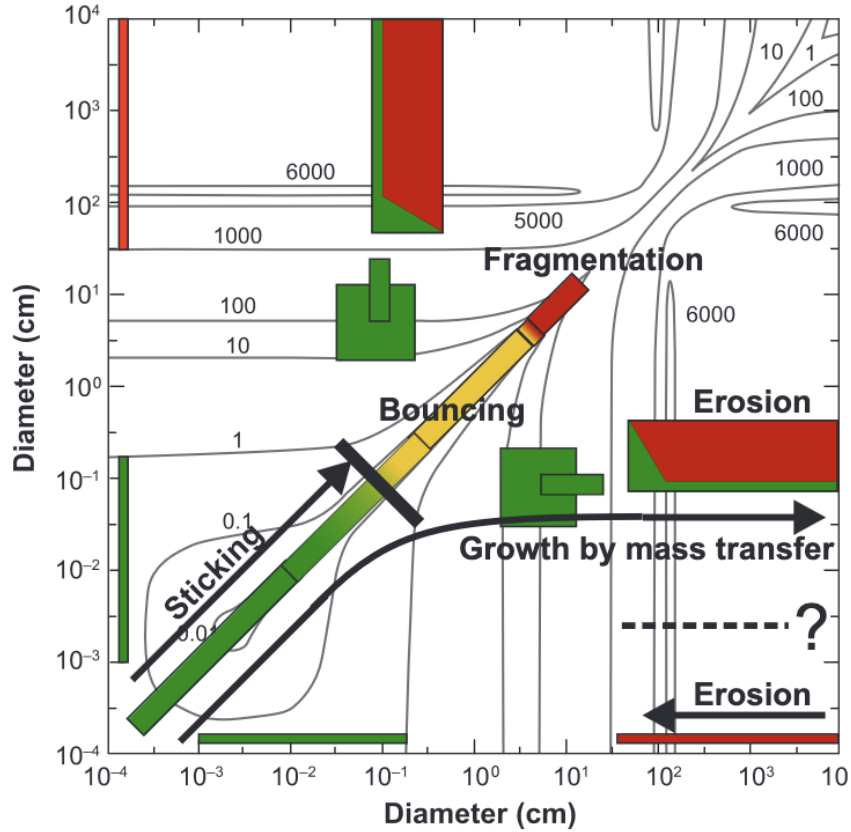


Figure 1.13: Schematic representation of the outcomes of dust collisions in PPDs. It displays collision velocities (denoted by contours, in units of cm/s) between two non-fractal dust agglomerates in a minimum-mass solar nebula model at 1 AU. The green, yellow, and red boxes represent the explored parameter space and results of laboratory experiments, where green signifies sticking or mass transfer, yellow bouncing, and red fragmentation or erosion. The arrow labeled “Sticking” indicates the direct growth of mm-sized dust aggregates, as observed in simulations by Zsom et al. (2010). Further growth is impeded by bouncing. The arrow labeled “Growth by mass transfer” suggests a potential direct path to the formation of planetesimals. Credits: Testi et al. (2014).

where ρ_g is the gas density, Δv is the relative velocity between the particle and the gas, $v_{\text{th}} \equiv \sqrt{8/\pi}c_s$ is the thermal speed of the gas molecules and c_s is the sound speed.

The drag force acts opposite to Δv , so the solid particle loses angular momentum. The timescale over which this happens is called stopping time $t_{\text{stop}} \equiv m\Delta v/|F_D|$, where m is the mass of the solid particle of interest. The stopping time can be converted to a dimensionless number, called Stokes number (St):

$$St = \Omega_K t_{\text{stop}}, \quad (1.10)$$

where Ω_K is the local Keplerian frequency. In the context of dust dynamics in protoplanetary disks, the St plays a crucial role in determining the behavior of dust particles relative

to the gas. Mathematically, when t_{stop} is less than the dynamical time t_{dyn} or when $St \ll 1$, the term Δv vanishes, indicating that the dust particles follow the gas motion (more aerodynamic drag force). When $St \gg 1$, aerodynamic drag becomes negligible, and the particle decouples from the gas. Physically, the Stokes number reflects how well particles are coupled to the gas and how they respond to thermal pressure in less dense environments. In the case of small particles (sub-micron sizes), they are significantly influenced by gas thermal pressure and remain coupled to the gas, with little acceleration produced by drag forces. On the other hand, large particles (mm - cm sizes) experience higher drag force acceleration until they grow to approximately km sizes, beyond which the drag force becomes negligible (Weidenschilling, 1977).

Aerodynamic drag forces are fundamental to explain two dynamical processes, horizontal drift and vertical settling. Due to a balance between centrifugal force, stellar gravity, and a radial gas pressure gradient that increases towards inner regions, the gas in protoplanetary disks (PPDs) rotates at sub-Keplerian velocities. Conversely, large enough particles, not entirely dragged by the gas, would rotate at Keplerian velocities. Consequently, these particles experience a headwind from the gas, leading to the removal of their angular momentum and causing inward drift, commonly referred to as radial drift. In terms of the vertical structure, grains located above the midplane experience the vertical component of stellar gravity pulling them toward the midplane. This gravitational force is counteracted by the pressure gradient force pointing outward from the midplane. Unlike lighter and smaller particles that are primarily influenced by gas pressure and are less affected by gravity, larger particles undergo more efficient vertical settling due to the gravitational forces acting upon them. Thus, there is a larger concentration of larger dust particles in the mid-plane, while smaller particles are more vertically scattered. Moreover, PPDs are marked by significant turbulence. Turbulence is characterized by chaotic changes in pressure and flow velocity of the gas, facilitating the mixing and diffusion of particles in all directions. This turbulent setting proves especially efficient for grains with stronger coupling, characterized by lower Stokes numbers.

The interplay between turbulent mixing, affecting principally smaller dust particles, and drag forces, primarily influencing larger particles, governs the overall size distribution of dust grains within the disk.

1.2 Substellar objects: formation and detection via High-Contrast Imaging

A star is defined as a self-luminous astronomical object, maintained by the balance between gravity and gas pressure (known as hydrostatic equilibrium), and possessing sufficient mass to initiate thermonuclear fusion of hydrogen isotopes, particularly ^1H .

In contrast, a substellar object is a celestial body with less mass, insufficient for triggering ^1H fusion. Its luminosity may vary, and this term is commonly associated with brown dwarfs, possessing enough mass for deuterium (^2H) fusion, and giant planets. Importantly, giant planets do not exhibit self-luminosity; they depend on reflected sunlight for visibility,

or, when young, on the formation heat.

In this Section, I intend to detail how substellar objects can be formed and consequently detected and characterized by high-contrast imaging observations and post-processing techniques.

1.2.1 The main scenarios for substellar objects formation

Among several possible scenarios for planetary formation, the two widely discussed and accepted models are the gravitational instability (henceforth GI) (Boss, 1997 and references therein) and the core-accretion (henceforth CA) (e.g., Pollack et al., 1996 and references therein). Both theories require different initial conditions to explain the formation of planets and minor bodies observed to date. Also, each one presents its pros and cons while explaining observed systems; none can be discarded. Below, I highlight their more important characteristics and their type of planetary outputs.

Core-accretion: the bottom-up process

The core accretion (CA) model serves as a paradigm for the formation of giant gas planets, particularly for objects orbiting within the range of 10-50 astronomical units (au) (Perryman, 2014). Moreover, it extends its applicability to the formation processes of rocky planets and minor celestial bodies. It works under the assumption that smaller grain interactions will eventually form larger bodies and, possibly, planetary cores. The model steps can be summarized as the following.

First, dust and ice particles (sub-micron to micron) will start to agglutinate when they hit each other due to van der Waals forces. With these initial sizes, the dust grains are still well coupled to the gas. Thus, as the solids grow, they eventually will settle to the disk mid-plane (Kusaka et al., 1970).

The higher surface densities in mid-plane promote collisional growth, leading to the formation of larger (m-km sized) rocky/metal structures. However, the growth of meter-sized objects is yet to be fully explained, since they are expected to quickly drift towards the star and also fragment when colliding at high speed (meter-size barrier; Adachi et al., 1976; Weidenschilling, 1977; Blum & Wurm, 2008 and references therein).

Next, km-sized objects, also known as planetesimals, will induce gravitational interactions, quickly attracting more dust and other planetesimals. This particular stage, heavily dependent on the masses of the objects, is called runaway growth (Stewart & Wetherill, 1988; Wetherill & Stewart, 1989) and it precedes the oligarchic growth, the second to last stage of planetary formation in the CA model.

After reaching ~ 100 - 1000 km, the bodies, now called planetary embryos, will move on their planetary feeding zone, thus accreting matter while perturbing their vicinities. They will achieve an isolation mass, thus, causing a lower growth rate at the time.

The previous stages are thought to cease in less than 1-10 Myr. The last stage, called post-oligarchic or chaotic growth, is a slow stage that lasts as much as 100 Myr or more. This stage leads to the formation of planets larger than Mars. Additionally, during this

step, the remaining planetary embryos may cross other orbits, leading to an increase in eccentricities, inclinations, and numbers of catastrophic collisions.

From the continuous interactions and growth of some planetary embryos, a critical core mass (Bodenheimer & Pollack, 1986; Pollack et al., 1996), thought to be between $\sim 3.5 M_{\text{earth}}$ and $\sim 8.5 M_{\text{earth}}$ (Piso & Youdin, 2014), will trigger a gas accretion rate that exceeds the ones that planetary embryos induce. Consequently, this process may lead to gas giant planets' formation (for further details, see figure 1.14 and Perryman 2014).

Finally, it is possible to cite some characteristics of CA: it can efficiently produce metal-enriched objects, rocky planets, and minor bodies. However, the classical CA process, fed principally by km-sized objects (planetesimals), faces two major problems. Firstly, the model requires extremely high column densities of planetesimals to construct the observed core masses of gas giants within their respective feeding zones. This raises concerns about the fate of the majority of planetesimals that are not utilized in core formation. Additionally, the accretion rates of planetesimals decrease significantly with distance from the star, since they migrate fast, making the formation of cold giant cores and subsequent atmosphere formation particularly challenging within the protoplanetary disk's lifetime. Secondly, the assumption that cores grow in isolation and can accrete planetesimals with negligible velocity dispersion has been challenged by dynamic simulations. Consequently, these challenges have been the inspiration to alternative perspectives.

To address the challenges encountered in the classical Core Accretion (CA) through planetesimal accretion, a more efficient model has been developed – pebble accretion coupled with streaming instabilities (see reviews by Chiang & Youdin, 2010; Johansen et al., 2014; Johansen & Lambrechts, 2017). Pebbles, typically ranging from millimeter to meter sizes, are scattered radially throughout the entire disk, vertically confined on its majority in the mid-plane, and exhibit partial decoupling from the gas (see subsection 1.1.3). The aerodynamic drag can reduce the speed difference between pebbles and larger bodies as they reach closer. This slowdown prevents some pebbles from escaping the gravitational pull of the larger bodies or from having collisional speeds leading to fragmentation (see Fig. 1.13). As a result, these pebbles spiral or settle toward the surface of the larger body and become accreted. This entire process enhances the effective cross-sectional area for the accumulation of material by larger bodies, accelerating their growth. Conversely, streaming instability is a process where pebbles within the disk undergo collective gravitational collapse due to aerodynamic drag. This leads to the formation of dense filaments, providing favorable sites for rapid particle growth and subsequent planetesimal formation, up to objects of ~ 100 km. According to pebble accretion models, they thus become the dominant growth mechanism over planetesimals accretion, at a starting point from the mass of Ceres/mass of the Moon. Consequently, the process is halted at the pebble isolation masses of approximately $10 M_{\oplus}$, where contraction of the gas envelope to form giant planets starts. Therefore, streaming instability, working in conjunction with pebble accretion, contributes to the quicker and more efficient formation of planetary building blocks, even at larger distances from the star.

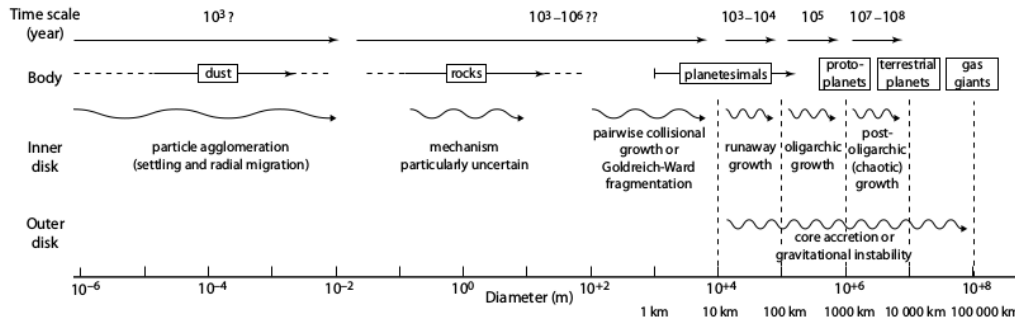


Figure 1.14: Schematic representation of the grain growth towards planetary formation, starting with sub-micron dust, and extending up to the terrestrial planets in the inner disk, and the gas giants in the outer disk. Some indicative time scales are given, although some intervals, especially around the meter-size barrier, remain highly uncertain. Credits: [Perryman \(2011\)](#)

Gravitational instability: the top-down process

The planetary formation by GI, derived from the Nebula Hypothesis ([Kant, 1755](#); [Laplace, 1796](#)), works under the assumption of large clumps of gas and dust collapsing and forming giant planets. This process, which starts similarly to the formation of chunks by instabilities in molecular clouds, can be summarized as follows.

During the protoplanetary disk evolution, instabilities can cause over-densities and clumps. However, interactions with another over-density or tidal shredding due to slow cooling/rapid migration can easily disrupt these clumps and stop the process. Therefore, if a massive clump subject to self-gravity survives to dispersal, a giant body (planet, brown dwarf, or low-mass star) will begin to form.

In the context of planetary formation, GI modeling may be challenging to explain observations. GI planets' cores don't need to be dense nor reach a minimum value to explain the extended atmospheres that gas/ice giants show. Nevertheless, disks and clumps susceptible to GI show that the initial disk must be very massive ($M_{disk}/M_{star} \geq 0.1$; [Kratter & Lodato, 2016](#)), which is not so observed[‡]. Also, it is known that the amount of gas on a clump that lasts attached until the formation of a denser structure usually leads to brown dwarfs or low-mass star objects (e.g., [Kratter & Matzner, 2006](#); [Stamatellos & Whitworth, 2009](#); [Kratter et al., 2010b](#); [Zhu et al., 2012](#); [Forgan & Rice, 2013](#)).

Finally, when comparing GI and CA processes, it is possible to affirm that the first is rather faster ($\sim 10^3-10^4$ years) than the latter ($\sim 10^7-10^8$ years), and young GI planets are hotter and irradiate more than recently formed CA planets with similar conditions. It is common to say that GI planets have a “hot start” and CA planets have a “cold start” (see figure 1.15).

[‡]For a list of references measuring the percentage of observations that have disk masses prone to GI, check section 2.2.1, [Kratter & Lodato \(2016\)](#).

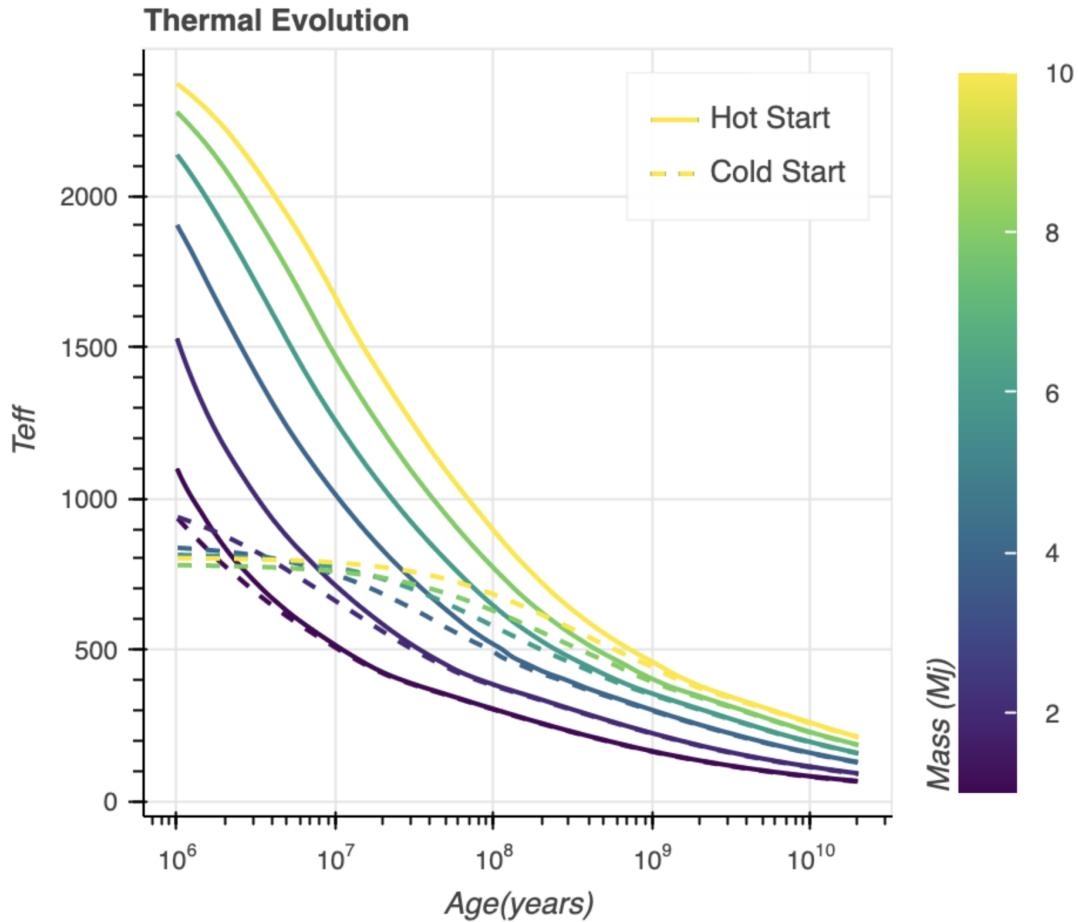


Figure 1.15: Luminosity-time evolutionary tracks computed using the [Marley et al. \(2007b\)](#) methodology. The hot start, credited to gravitational instability planets (solid), and the cold start, representing the core-accretion planets (dashed) are shown, according to the initial planetary masses (1-10 M_{jup}). Credits: Natasha Batalha; https://natashabatalha.github.io/picaso/notebooks/workshops/SaganSchool2021/1_Spectroscopy.html

1.2.2 (Sub)stellar multiplicity formation

Multiple (sub)stellar systems can be defined as systems with two or more gravitationally bound stars/brown dwarfs with separations $\lesssim 0.1$ pc. Multiple formation requires two or more events of gravitational collapse that will thus form a bound system. The process by which self-gravitating objects develop substructures that independently collapse is called fragmentation. If formed at a certain distance, within time, they can gradually approach each other and become gravitationally bound. Following, the main models for multiple star formation are better detailed.

The multiple formation models can be categorized in three: 1) fragmentation of a core or filament; 2) fragmentation of a massive accretion disk; or 3) through dynamic interactions (see Fig. 1.16). Following, these processes are better detailed:

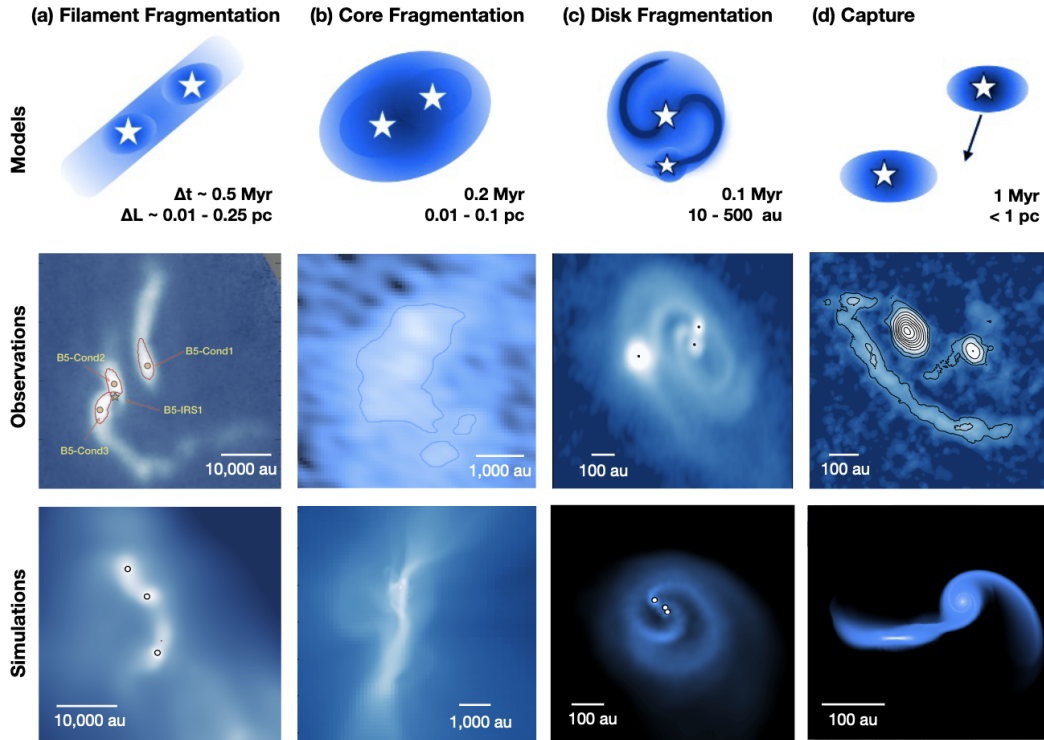


Figure 1.16: Mechanisms for multiple (sub)stellar formation. The model (top row) presents an approximate range of time and length scales for each process. The middle row shows proposed observational examples for each case. The bottom row shows examples of each formation model from numerical simulations. Credits: [Offner et al. \(2022\)](#). The observations/simulations references are listed in Figure 5 caption of that work.

- Core and filament fragmentation:** The processes of core and filament fragmentation occur in dense embedded structures, with each object developing and collapsing within the same parent structure. Filaments are the second largest structures in the stellar formation sequence, formed by the encounter of expanding shells (see subsection 1.1.1). However, hereafter I define cores and filaments as morphological structures, rather than physical ones, which explains the similar scales between the two modes of fragmentation in Fig. 1.16. Therefore, the two presented fragmentation modes are defined by an over-density in a structure formed, before the formation of a disk. Two main mechanisms trigger core/filamentary fragmentation, rotation, and turbulence:

- **Rotation-driven fragmentation:**

When collapsing cores rotate rapidly, they become susceptible to fragmentation if specific criteria, ensuring a balance among thermal, gravitational, and rotational energies, are satisfied. Excluding fragmentation as the initial trigger, the simplified expression by [Inutsuka & Miyama \(1992\)](#) establishes the relationship between the initial ratio of thermal to gravitational energy, α_{vir} , and the ratio of

rotational to gravitational energy, β_{rot} :

$$\alpha_{\text{vir}}\beta_{\text{rot}} = 0.02 \left(\frac{T}{10 \text{ K}} \right) \left(\frac{M}{1M_{\odot}} \right)^{-2} \left(\frac{R}{0.1 \text{ pc}} \right)^4 \left(\frac{\Omega}{10^{-14} \text{ s}^{-1}} \right)^2. \quad (1.11)$$

Here, T , M , R , and Ω represent the local temperature, mass, radius, and Keplerian frequency of the collapsing structure, respectively. The conditions for fragmentation in this expression are $\alpha_{\text{vir}}\beta_{\text{rot}} > 0.12$ and $\alpha_{\text{vir}} < 0.5$. Rotational fragmentation often results in the formation of multiple systems within the same plane, tending towards spin alignment and coplanarity (Offner et al., 2016; Bate, 2018). These characteristics serve as signatures of the formation scenario, which can be used as an educated guess in the case of evolved multiple systems (see chapters 2 and 3).

- **Turbulent fragmentation:** Turbulence is an effective trigger for structure formation, encompassing both stars and brown dwarfs within the same system. Regions within a molecular cloud can fragment when the turbulence seeds collapse and provide pressure support – when the local gravitational energy exceeds the contribution of both turbulent and thermal energy. To initiate fragmentation via turbulence, a critical density ρ_{crit} must be achieved or exceeded. For an isothermal cloud, a relatively straightforward expression is provided by:

$$\rho_{\text{crit}} = \frac{\rho_0}{1 + \mathcal{M}^2} \left(\frac{R}{R_0} \right)^{-2} \left[1 + \mathcal{M}^2 \left(\frac{R}{R_0} \right)^{p-1} \right], \quad (1.12)$$

where ρ_0 , R_0 and \mathcal{M} are the initial density, radius, and Mach number of the parent cloud (ratio of local flow velocity to the sound speed of the medium), respectively (Guszejnov & Hopkins, 2015; Guszejnov et al., 2017). In this expression, p denotes a term equal to 2 for supersonic turbulence and 5/3 for subsonic scales. Additional contributions can also increase the complexity. For example, an isothermal filament collapses if its mass per unit length, M_l , exceeds a critical value. A filament threaded laterally by a magnetic field, B_{\parallel} , will become unstable when M_l exceeds (Inutsuka & Miyama, 1997; Tomisaka, 2014):

$$\begin{aligned} M_{l,\text{crit}} &\simeq \frac{2c_s^2}{G} (1 + \beta_{\text{mag}}^{-1}) \\ &\simeq 16.4 \left(\frac{T}{10 \text{ K}} \right) + 7.8 \left(\frac{n_{\text{H}}}{10^4 \text{ cm}^{-3}} \right)^{-1} \left(\frac{B}{10 \mu\text{G}} \right)^2 M_{\odot} \text{pc}^{-1}, \end{aligned} \quad (1.13)$$

where $\beta_{\text{mag}} = 8\pi c_s^2 \rho / B_{\parallel}^2$ is the ratio of thermal to magnetic pressure. Furthermore, within filaments, if turbulent support after triggering the collapse is negligible, the critical mass can be stated as:

$$\begin{aligned} M_{\text{crit}} &\simeq 1.3 \frac{c_s^4}{G^2 \Sigma_{\text{fil}}} \\ &\simeq 1.1 \left(\frac{T}{10 \text{ K}} \right)^2 \left(\frac{M_{l,\text{crit}}}{40 M_{\odot} \text{pc}} \right)^{-1} \left(\frac{W_{\text{fwhm}}}{10^4 \text{ au}} \right) M_{\odot}, \end{aligned} \quad (1.14)$$

where the filament surface density, Σ_{fil} , is the ratio of the filament mass-per-length to the width of the filament $\Sigma_{\text{fil}} = M_{\text{line}}/W_{\text{fwhm}}$ (André et al., 2019). Multiple systems originating from the same parent structure through turbulent fragmentation are expected to share similar ages and typically exhibit a modest number of members, typically two to three within a core. They are usually formed at wider separations (set to a scale of 102 au to 0.1 pc; Offner et al., 2022) compared to objects formed through rotational-driven fragmentation. As a result, they accrete gas at varying rates and have distinct spin alignments and rotational speeds. Consequently, (sub)stars resulting from turbulence-driven fragmentation tend to have misaligned stellar spins, accretion disks, and protostellar outflows (Bate, 2000; Offner et al., 2016; Bate, 2018; Lee et al., 2019).

- **Disk fragmentation:** Circumstellar disks can undergo fragmentation at later stages compared to the previously mentioned fragmentation modes. This particular type of fragmentation is expected to occur in massive forming disks through gravitational instability (GI), as discussed in subsection 1.2.1. Referenced in 1.1.3 as a mechanism for triggering spirals in circumstellar disks, GI can also cause instabilities that may lead to fragmentations when the Toomre parameter Q is ≤ 1 (Toomre, 1964; Kratter & Lodato, 2016) in razor-thin disk. The Toomre parameter criteria can also be described in terms of the mass of the protostar/PMS and the disk, aspect ratio and radial distance:

$$Q = \frac{c_s \Omega}{\pi G \Sigma} = f \frac{M_* H}{M_d r} \leq 1 \quad (1.15)$$

where c_s is the disk sound speed, Ω the disk orbital frequency, Σ the surface density, M_*/M_d the star-disk mass ratio, H the disk scale height, r the radial distance, and f the order unity scale factor which depends on the assumed surface density power law (Offner et al., 2022). However, gravitational instability (GI) does not inevitably lead to fragmentations; it serves as the mechanism causing local instabilities. For fragmentation to occur after GI is triggered, effective cooling must counteract the inflation caused by higher temperatures. In the case of thick disks, the critical Q significantly drops below unity due to the extended vertical distribution of matter (Lau & Bertin, 1978). This implies that gravitational instability (GI) in such disks can be triggered in outer regions, specifically when the disk is not excessively flared and is located at a distance with sufficient gas density – in these outer regions, lower temperatures are associated with higher radial distances. However, the probability of gravitational instability fragmentation increases during the early stages of disk formation, particularly when the infall rate dominates over viscous accretion (typically in the Class 0 phase) since during this phase, an increase in surface density does not necessarily correspond to higher temperatures that could inhibit gravitational instability (Kratter et al., 2010a; Harsono et al., 2011; Zhu et al., 2012). This scenario is likely linked to the rapid formation of binaries sharing approximately the same mass (Bate & Bonnell, 1997; Ochi et al., 2005; Young & Clarke, 2015). An alternative pathway

to GI fragmentation arises when the disk temperature decreases more rapidly than accretion can modify the surface density. A plausible explanation for this scenario is variations in stellar luminosity resulting from accretion changes (see section 1.1.2). Fragmentation may occur suddenly if there is a significant decrease in central luminosity, provided that the temperature drop does not coincide with an increase in the cooling timescale (Dunham et al., 2014b; Kuffmeier et al., 2018). Regardless of the process that triggers gravitational instability (GI) fragmentation, the binary companion must overcome interactions with the disk and subsequent tidal forces induced by inward migration.

- **Dynamic interactions:** A more effective mechanism to elucidate the formation of close binaries is through capture and subsequent orbital evolution.

The effectiveness of the capture mechanism depends on the environment, whether it is gas-dense or has less gas. In gas-dense environments, objects within a stellar cluster may transition between unbound and bound states due to energy and angular momentum exchange with the surrounding gas cloud or individual circumstellar disks. This process, known as gas-mediated capture, is observed in various scales in numerical simulations and can lead to the formation of bound systems. However, the net frequency of capture through this mechanism is likely low, making these systems observationally indistinguishable from those formed via fragmentation, except in cases where two disks seem to be on a collision course. On the contrary, in regions of high stellar density without much gas, interactions between truly unbound stars can lead to the formation of new binaries and partner exchange. Recent work emphasizes the contributions of higher order multiples to overall interaction rates in moderately dense clusters, producing a more diverse set of outcomes, including the formation of very compact binaries (Geller & Leigh, 2015; Dorval et al., 2017; Hamers & Samsing, 2020). These processes are more relevant for dense open clusters and globular clusters but are sub-dominant in gas-rich environments. In addition, widely separated bound binaries can reduce their separations through the dynamical friction force, caused by the torque provoked by accreting systems trailing their material during close encounters (Bate & Bonnell, 1997; Stahler, 2010; Lee & Stahler, 2011), by numerical viscosity and mergers (Vorobyov & Basu, 2005; Zhu et al., 2012) or by Kozai-Lidov cycles coupled with tidal friction (Kozai, 1962; Lidov, 1962; Fabrycky & Tremaine, 2007). The latter scenario occurs when binaries exchange angular momentum with an inclined tertiary object, which thus leads to a periodic exchange between eccentricity and inclination of the binary, therefore leading to circularization and a hardening of their orbits.

1.2.3 High-Contrast Imaging: instrumentation, observing strategies and data-processing

In the Galaxy, more than 5500 exoplanets have been identified to date[§], alongside a few thousand brown dwarfs[¶] (hereafter called BDs). While various techniques can unveil the existence and characteristics of these objects by observing their interactions with the brighter stars they orbit, high-contrast imaging (HCI), also known as direct imaging (DI), stands out as the sole method capable of directly revealing their presence. Thus, the HCI offers the advantages of extracting the flux and astrometry of the detected source. With a few observations of the latter, orbital characterization can also be performed. Lastly, HCI provides a recovery of the photometric spectra, which can provide key parameters such as effective temperature, surface gravity, mass of the object, and presence of clouds and certain molecules.

Planck's law defines that a black body, an object that is a perfectly efficient energy absorber and emitter, will have its radiation characterized by its temperature. Assuming that stars and substellar objects can emit approximately black bodies, an observational instrument will be more susceptible to detect them using broadband filters covering wavelengths close to the peak emission. The detectability of such objects will also depend on the instrument's sensibility, resolution power, and possible interference from background sources. Black-body objects with a radiation peak in the optical/IR can emit in two different ways. They can produce their radiation through nuclear reactions (as in the case of low-mass stars and deuterium-burning objects) or they can emit thermal radiation due to atomic and molecular agitation. The latter applies to newly formed planets and moons, which have enough primordial heat derived from their origin. Brown dwarfs are a special case, where their deuterium-burning phase does not last a long time and therefore, similarly to giant planets, they will cool down gradually with time (see Fig. 1.17).

The HCI technique relies on enhancing the contrast of substellar objects, by suppressing the starlight from the host star. This technique focuses on detecting objects that still retain heat from their formation, which are faint in comparison with the host star. In summary, the technique is optimized for detecting massive substellar objects on their first millions of years (Myrs) and at wider separations from their host star using Optical/near-IR wavelengths (see Fig. 1.18, where discovered by imaging planets (HCI/DI planets) are compared to planets detected by other techniques).

Despite its potential, HCI effectivity has significant challenges as it requires a certain level of contrast between star-companion, and also a certain angular resolution between both. The contrast is quantified by the flux ratio F_{object}/F_{host_star} , a value influenced by both the angular separation of the sources and their intrinsic brightness corresponding to the observed wavelength. In the most favorable cases, with the best instruments and post-processing algorithms at the moment, contrasts can be reached in the order of 10^{-6} to 10^{-5} .

[§]For more information, refer to sources such as <https://exoplanetarchive.ipac.caltech.edu/> and <http://www.exoplanet.eu/catalog/>

[¶]For details, see resources like <http://www.johnstonsarchive.net/astro/browndwarflist.html> and <https://simple-bd-archive.org>

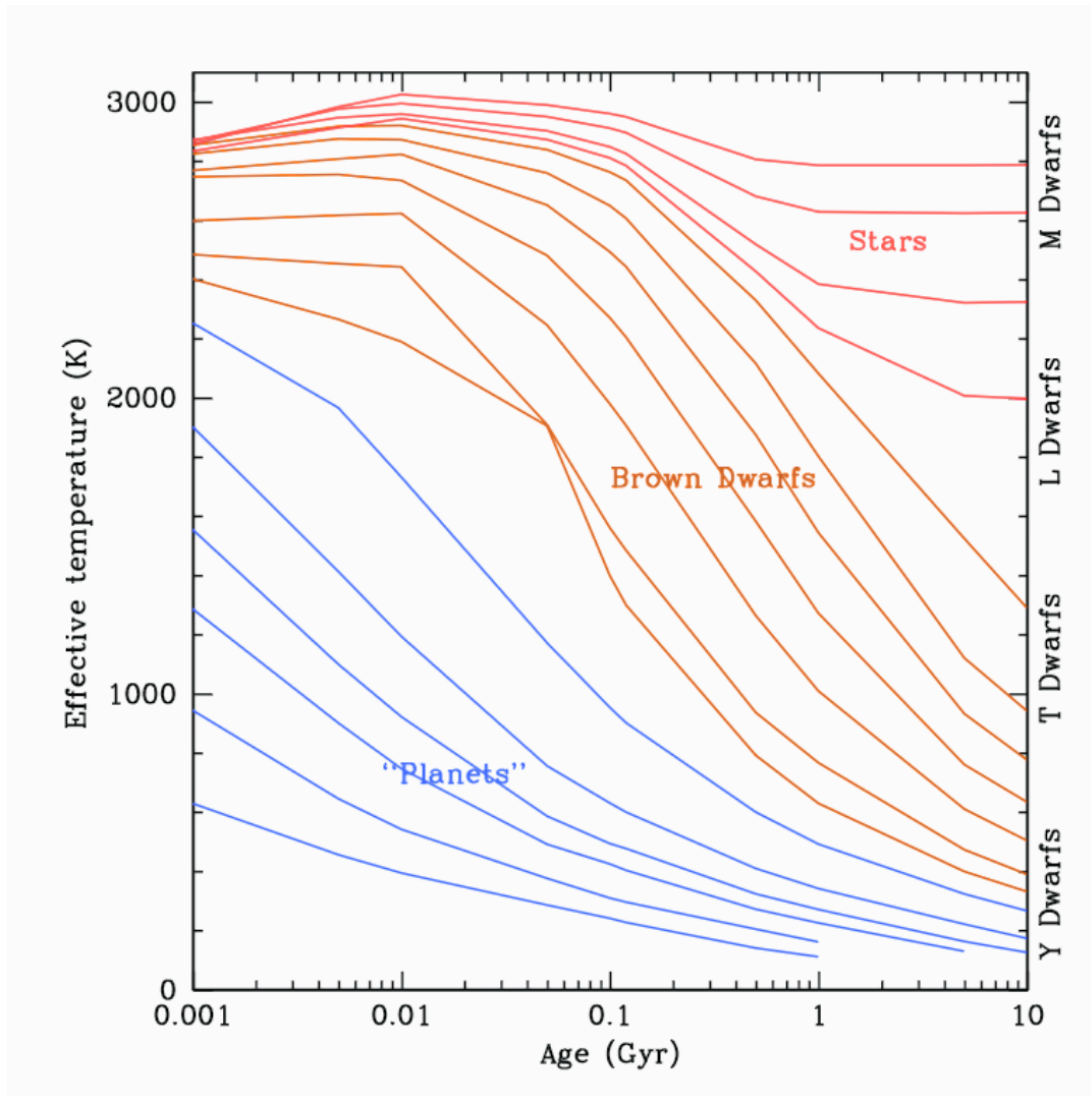


Figure 1.17: Evolution of effective temperature for substellar and low mass stars. The red lines trace stars (masses above the hydrogen-burning limit), the orange track brown dwarfs, and the blue trace objects below the deuterium-burning limit. Credits: Adaptation of [Bailey \(2014\)](#).

Greater contrast values result in brighter companions compared to the host star, hence aiming for lower values (fainter objects – less massive or older companions) is the objective for the new generation of telescopes and post-processing methodologies dedicated to HCI (see Fig. 1.19). The angular resolution is determined by a combination of the orbital separation between the objects, linked to the distance observer system.

Instrumentation

In order to perform HCI/DI, it is required a proper instrumentation, characterized by adaptive optics (AO) in the case of terrestrial telescopes, and coronagraphs for all cases.

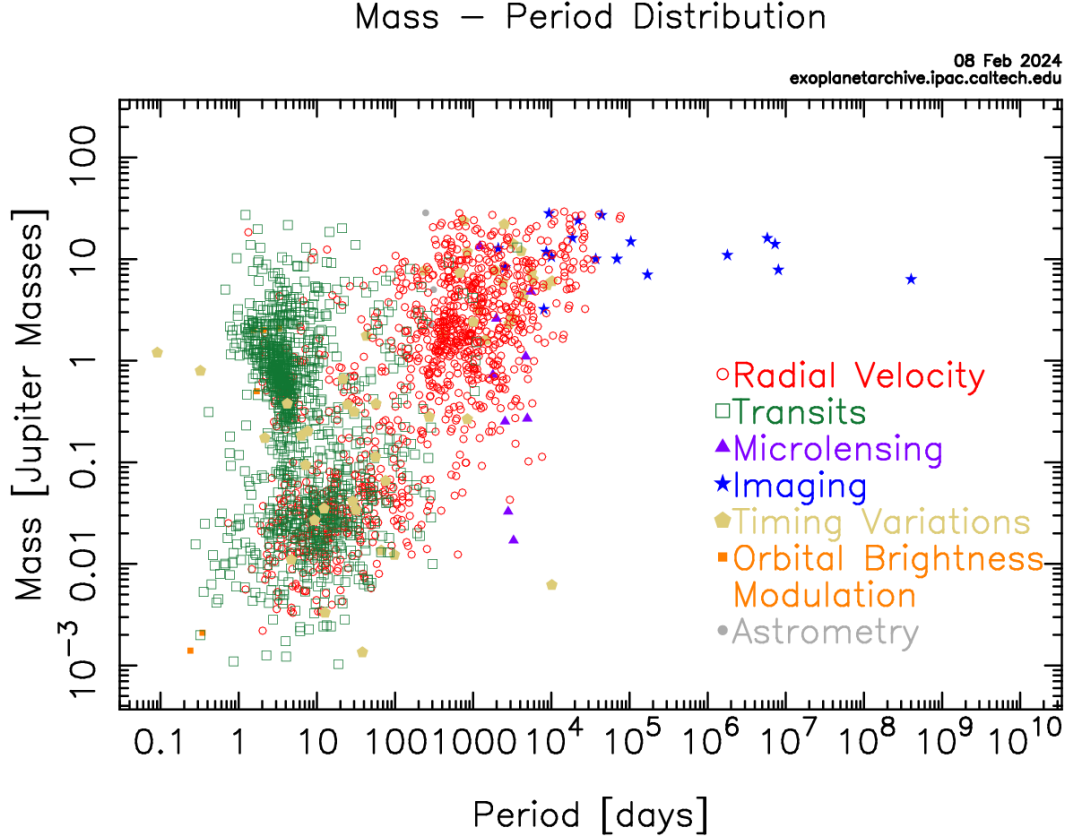


Figure 1.18: The diagram depicts the population of exoplanets and the corresponding discovery techniques. It illustrates masses in Jupiter masses versus orbital periods in days. The high-contrast imaging/direct imaging planets are specifically highlighted by blue-filled stars. Credits: https://exoplanetarchive.ipac.caltech.edu/exoplanetplots/exo_massperiod.png.

The light coming from celestial objects, which travels approximately a quasi-infinite distance, should be a perfect plane wave when entering the pupil of the telescope. In such case, without interference from the atmosphere, these spherical waves should ideally form an “Airy Disk” diffraction pattern at the telescope focal plane (see Fig. 1.20). This diffraction pattern will thus form the ideal Point Spread Function (PSF), with an angular resolution θ_{diff} (angular radius of the central airy disk maximum) given by:

$$\theta_{diff} = 1.22 \frac{\lambda}{D} \quad (1.16)$$

where D is the diameter of the telescope’s aperture and λ is the wavelength of the observation (see e.g., Pedrotti et al., 2017 and also Fig. 1.21). θ_{diff} is of the order of 30 mas for $\lambda = 1\mu\text{m}$ and $D \sim 8$ m.

AO is the technology used in the instrument to compensate for the effects of atmospheric turbulence. The wavefronts coming from the sources are susceptible to unpredictable Earth’s atmospheric variations. The atmosphere is formed by layers of turbulent “bub-

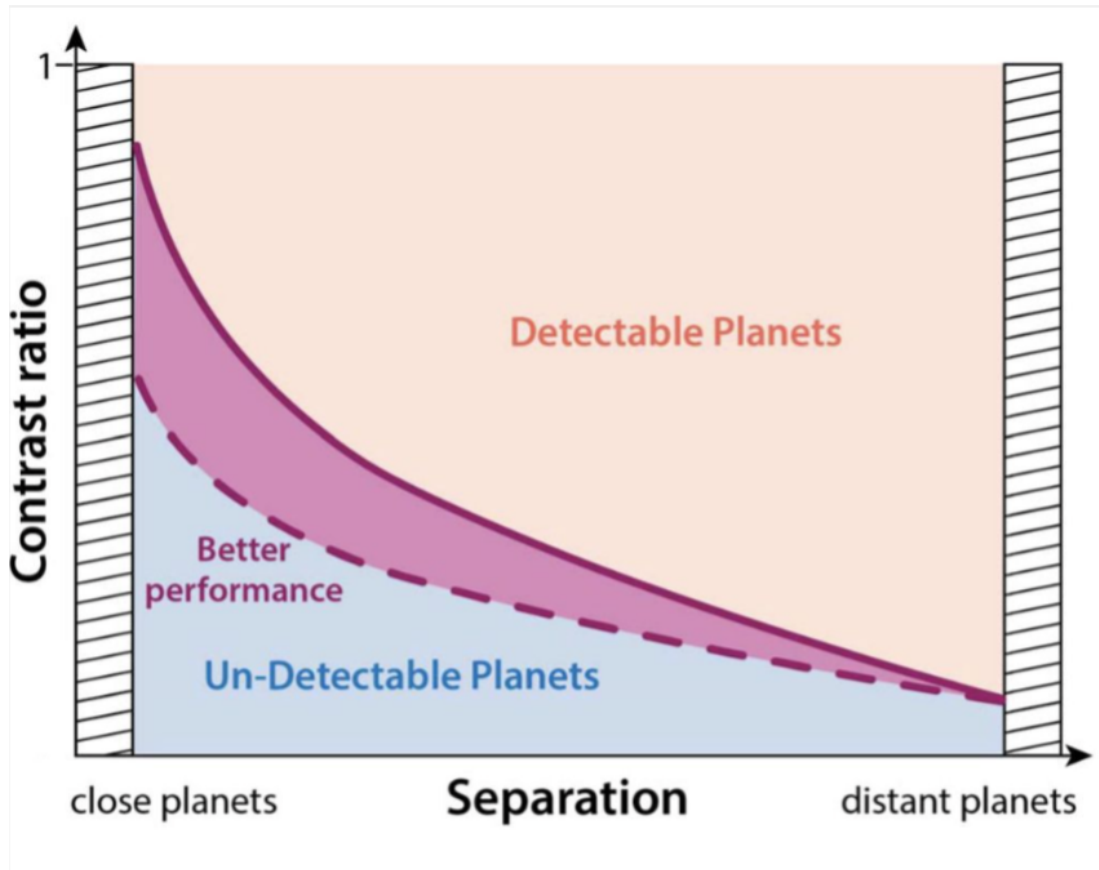


Figure 1.19: The chart illustrates how to interpret a contrast curve, where a companion becomes detectable when positioned above the solid curve at a particular contrast and separation. Notably, the achieved contrast strongly depends on the separation from the central star, making only the brightest planets detectable at close separations. The dashed line represents a deeper contrast curve compared with the solid line. A deeper contrast curve improves the effectiveness of high-contrast imaging, making it more probable to detect faint objects at closer separations. Credits: Adapted from [Follette \(2023\)](#).

bles”. Before reaching the telescope’s pupil, the incoming light is often divided into sub-apertures determined by the radius of these bubbles. The interference of these sub-apertures creates fringes-patterns of constructive and destructive interference. In regions where the sub-apertures interfere constructively, bright regions (speckles) are formed. On the contrary, in regions of destructive interference, dark regions appear. The resulting pattern is the speckle pattern. The speckles exhibit dimensions of approximately λ/d , determined by the separation d between the two sources of interference. When $d \sim D$, these speckles will share identical dimensions with the PSF of the star, making it challenging to differentiate them from an astrophysical source with equivalent brightness. To mitigate these wavefront variations, a control system must continuously measure the impact of the fluctuations at a high frequency during observations, and subsequently provide corrections as/when needed. To simulate atmospheric behavior, a reference point source, usually a star, is employed.

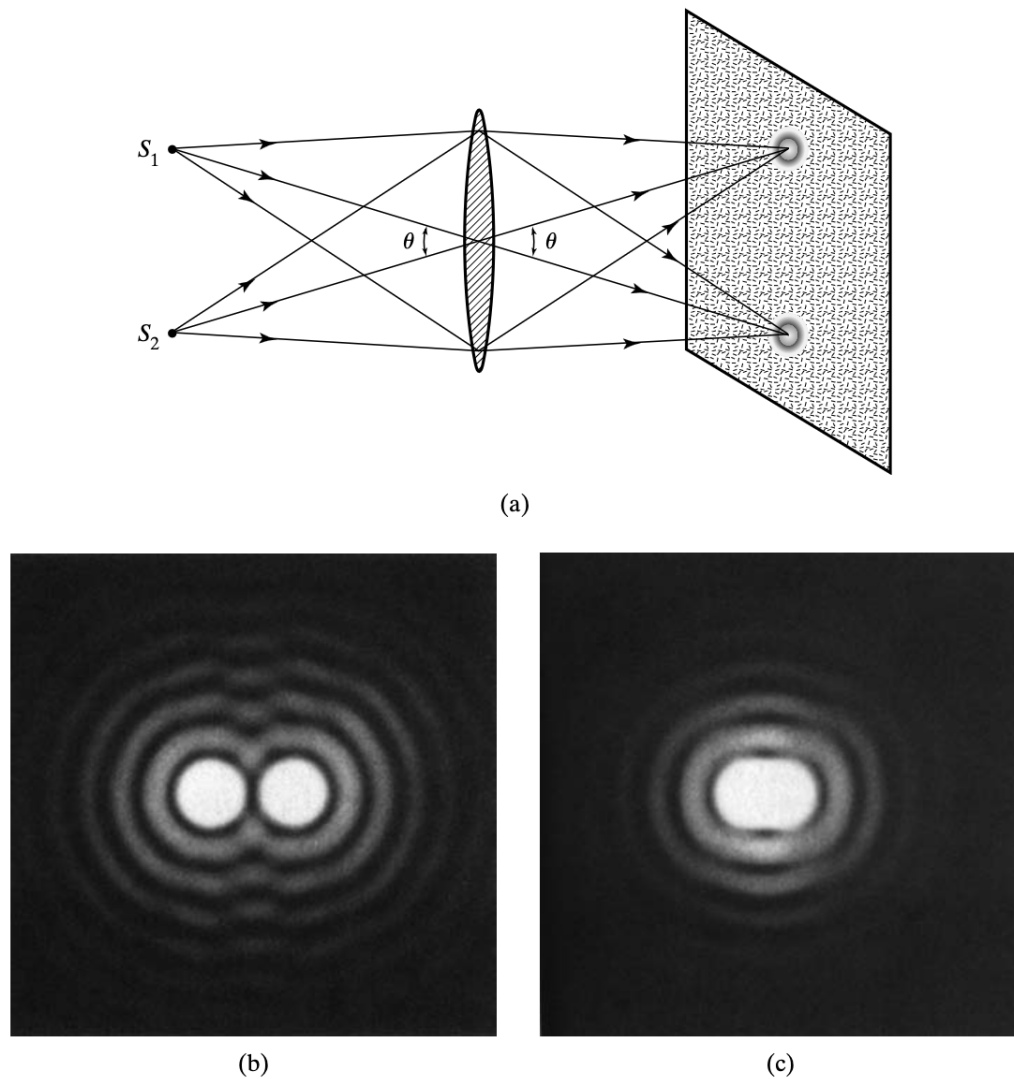


Figure 1.20: Diffraction-limited images of two point objects produced by a lens are illustrated. In the schematic depiction shown in Figure (a), two airy disks are formed upon crossing a lens, originating from two distinct points S_1 and S_2 . Figures (b) and (c) respectively depict scenarios where the sources are resolved and unresolved. Credits: [Pedrotti et al. \(2017\)](#).

This source should be sufficiently bright to ensure a high signal-to-noise ratio (SNR) in the wavefront sensor. Certain instruments offer the option of employing an artificial reference, specifically the laser guide star (LGS) or natural point sources when a bright star is unavailable, or even the host star. The instrument responsible for quantifying these fluctuations is known as a wavefront sensor, providing valuable information about phase variations. A real-time calculator then analyzes this data and determines the precise adjustments required to compensate for wavefront errors, transmitting instructions to deformable mirrors

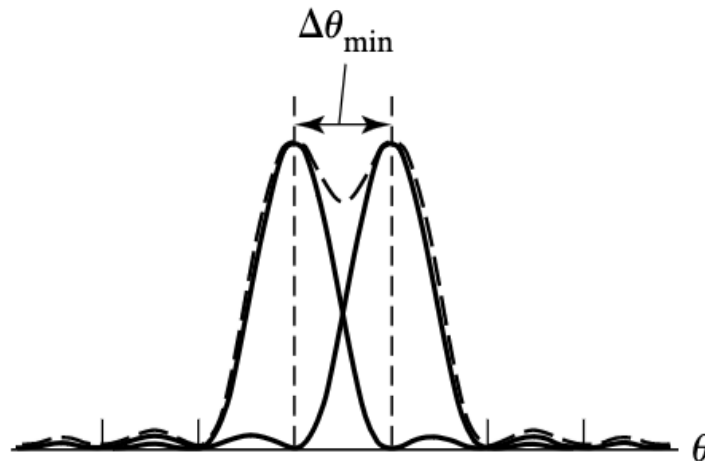


Figure 1.21: Rayleigh's criterion for just-resolvable diffraction patterns. The dashed curve is the observed sum of independent diffraction peaks. Credits: [Pedrotti et al. \(2017\)](#).

in a closed-loop system (see [Madec, 2012](#) and Fig. 1.22). More recently, Extreme Adaptive Optics (ExAO or XAO) systems were developed in high-performance high-contrast imagers as Spectro-Polarimetric High-contrast Exoplanet Research (VLT/SPHERE, [Beuzit et al., 2019](#)) and Gemini Planet Imager (GPI, [Macintosh et al., 2008](#)). They are able to provide Strehl ratios (ratio of maximum diffraction intensities of an aberrated wavefront to a perfect wavefront) up to 95%.

Coronagraphs are optical devices designed to suppress the brightness of stars, thereby improving the contrast for observing faint substellar objects and structures in the context of HCI. According to [Guyon et al. \(2006\)](#), the classical coronagraphic designs can be classified into four, 1) the interferometric coronagraphs, 2) the pupil apodized coronagraphs, 3) the Lyot coronagraphs, and 4) hybrid designs combining elements from the aforementioned categories. Modern coronagraphic designs often integrate elements from these categories, with variations centered around the apodizer concept, mask properties, and the complexity of the coupled Adaptive Optics (AO) system and mirrors' disposition.

The most simple description of such a system, following the incoming light towards the detector focal plane unfolds as follows: to attenuate incoming light, an apodizer may be introduced into the telescope pupil, modifying the amplitude or intensity profile – typically gradually attenuating the intensity towards the apodizer's edges. Following the pupil, and potentially the apodizer, the light advances through a lens, converging at the initial focal plane. At this stage, a mask is implemented, serving either as a physical occulting mask or a phase mask. The latter works through destructive interference, thus also blocking the starlight as the former. Following another passage through a lens and the alignment of the wavefront, a component known as the Lyot stop is strategically positioned. This device partially obstructs the light and serves to attenuate the diffraction caused by the mask. The

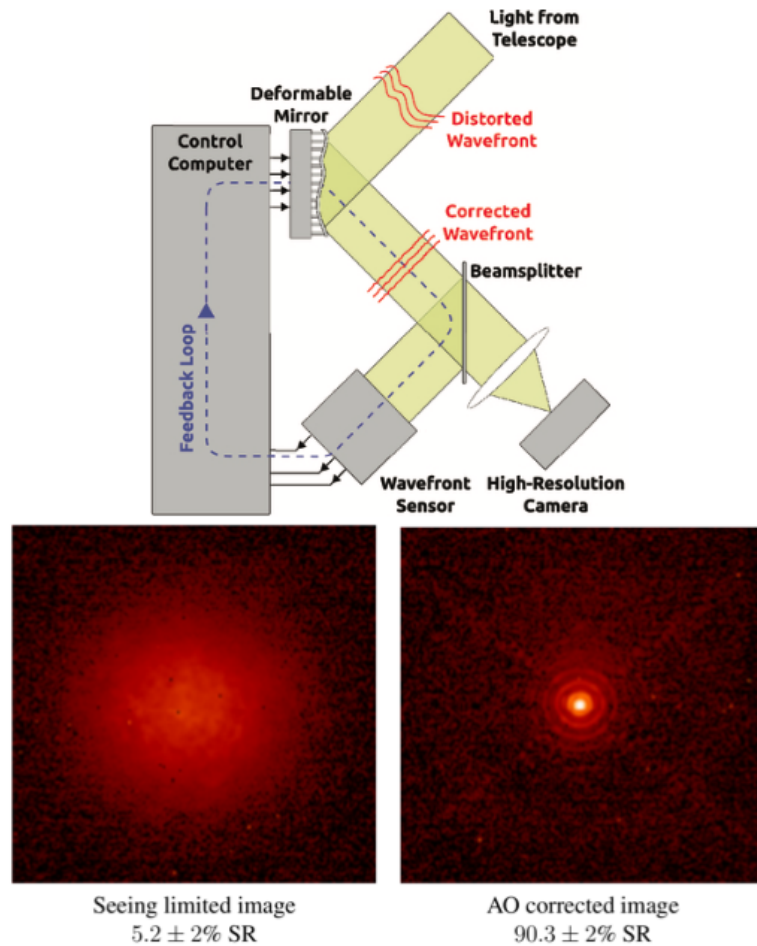


Figure 1.22: Simplified AO configuration and its impact in observations. Upper panel: a diagrammatic representation of an Adaptive Optics (AO) system according to [Rigaut \(2015\)](#). Real-time correction of the distorted wavefront involves a wavefront sensor, a feedback loop, and a deformable mirror. Lower panel: illustration of an image with a distorted wavefront before AO correction (left) and the same image after AO correction (right), revealing the Airy pattern ([Sauvage et al., 2016](#)). Credits: [Bhowmik \(2020\)](#).

Lyot stop will thus permit the incoming of a predominant portion of light from surrounding sources close to the limits of the mask, therefore contributing to the final image as it converges on the detector plane. A schematic representation of how a Lyot stop works is presented in Fig. 1.23. Three representative examples of possible coronagraphic designs with Lyot stops are presented in Fig. 1.24. The instrument used in the work presented in chapter 3, VLT/SPHERE, provides a possibility of using three coronagraphic designs, a classical Lyot coronagraph (CLC, without an apodizer), an apodized pupil Lyot coronagraph (ALC or APLC), and a four-quadrant phase-mask (4QPM, with a phase mask instead of an amplitude mask as the previous mentioned configurations).

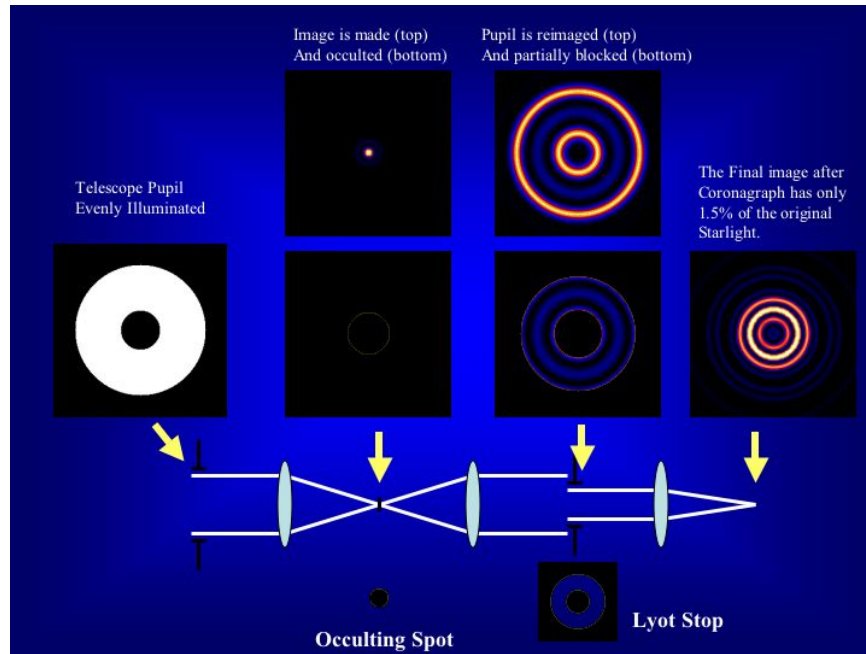


Figure 1.23: Schematic representation of how a classical Lyot coronagraphic works. The figure also shows how a Lyot stop can enhance the signal from regions closer to the borders of a physical mask. Credits: Ben R. Oppenheimer – <https://lyot.org/background/coronagraphy.html>.

Observing strategies

In addition to the speckle patterns produced by the atmospheric variations, a second type of speckle pattern that changes relatively slowly over time and arises from residual aberrations and imperfections in the optical system is called quasi-static speckle. They are mostly permanent during an exposure of tens of minutes (see e.g. Soummer et al., 2007). These speckles can be partially suppressed using post-processing techniques after the observation sequence is completed. To do so, an observing strategy, determining how data is acquired at the instrument level, provides the raw data, which is subsequently processed through a post-processing technique. The main observing strategies to detect substellar companions can be categorized into three: 1) angular differential imaging (ADI; Marois et al., 2006), 2) spectral differential imaging (SDI; Racine et al., 1999; Sparks & Ford, 2002), and 3) reference differential imaging (RDI; e.g. Lafrenière et al., 2009; Soummer et al., 2011; Ruane et al., 2019). They are briefly described as follows:

- **ADI:** Angular differential imaging (ADI) is one of the most commonly used observing strategies to mitigate quasi-static speckles in HCI. The ADI process requires the science target to pass near the meridian passage. The procedure follows as the pupil of the telescope is fixed in the host star, and its derotator is switched off. Consequently, the coronagraphic frames will maintain the center of the mask fixed with the host star position, while the Field-of-View (FoV) will be noticed rotating. This will result in the acquisition of frames with different parallactic angles throughout

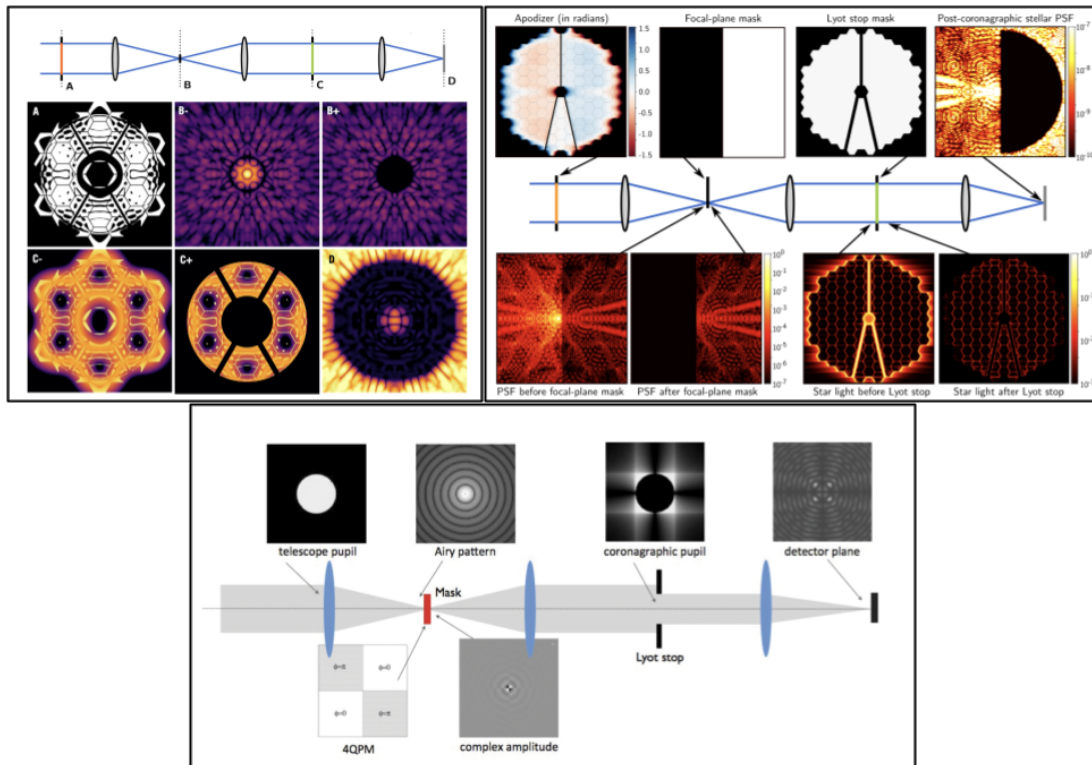


Figure 1.24: Representative examples of possible coronagraphic designs with Lyot stops. Top-left panel: Schematic layout of an apodized pupil Lyot coronagraph (APLC). The incoming light follows the sequence from A to D. The labels “-” and “+” represent before and after the stage/instrument utilization, represented by the letters. Credits: [Por et al. \(2020\)](#). Top-right panel: Schematic layout of a phase-apodized pupil Lyot coronagraph (PAPLC). In that case, the apodizer has a phase shift in different regions, and the mask only covers the brighter half-side of incoming light. Credits: [Por \(2020\)](#). Bottom panel: a schematic representation of a four Quadrant Phase-Mask (4QPM). In this case, no apodizer is presented, and a phase mask is utilized. Credits: [Boccaletti et al. \(2015\)](#).

the observation sequence. Moreover, the stabilization of the pupil ensures that the aberrations it induces remain relatively constant across all parallactic angles. This is crucial, as a significant portion of quasi-static speckles originates from the pupil and its supporting structures (spiders). By having the frame sequence, a model of the speckle halo will be created and then subtracted from all frames, thus removing substantially the quasi-static speckles. The frames will thus be derotate, aligning whichever possible companion/structure at the same position, thus enhancing its signal (see a general schematic representation of ADI sequence, independently of the post-processing model used in, Fig. 1.25). The post-processing technique used will define how the speckle field models will be created and how the signal of the companion will be reconstructed (see subsection 1.2.3 and Fig. 1.30).

- **SDI:** The spectral differential imaging (SDI) consists of decoupling the companion/structure from the speckles using different wavelengths (rather than azimuthal

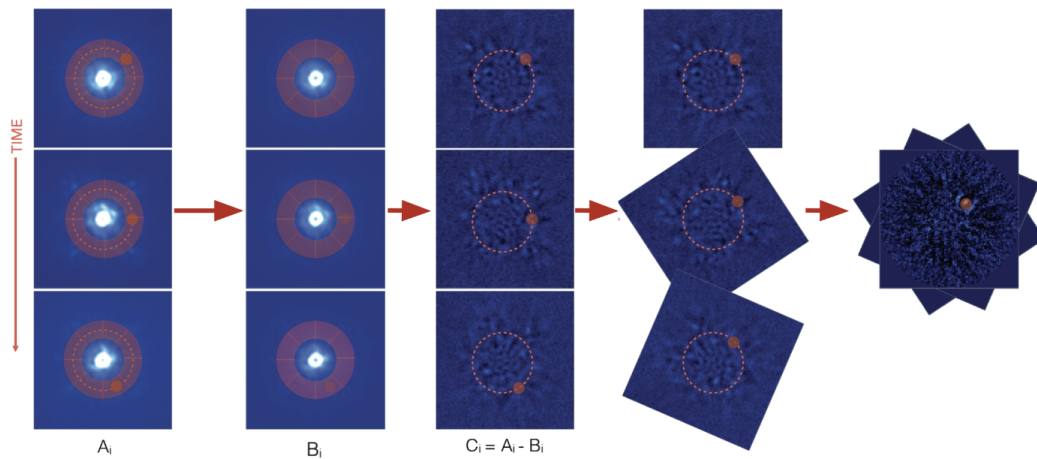


Figure 1.25: Illustration outlining the key stages of ADI observing strategy. From left to right, the sequence includes the calibrated science images (A), the frame-wise reference PSF (B), the residual images (C), the derotated residual images, and the final residual map. Credits: [Dahlqvist \(2022\)](#).

rotation as ADI). This observing strategy was first proposed by [Racine et al. \(1999\)](#). The researchers relied on two images taken in adjacent bands, aiming to exploit the presence/absence of an exoplanet's signal in two or more adjacent bands. Their idea was to carefully select two wavelengths to ensure the exoplanet's presence in one image while limiting its brightness in the other, often utilizing the methane absorption line. This approach effectively reduced speckle noise without causing self-cancellation of the planetary signal during subtraction. One example, where the methane absorption is more pronounced in one band than in the other is presented in [Fig. 1.26](#). A more advanced SDI approach, also known as the spectral deconvolution technique (SD), was introduced by [Sparks & Ford \(2002\)](#). Their concept exploits the fact that quasi-static speckles exhibit radial scaling proportional to λ (appearing to move radially from the image center), while real objects remain stationary. This difference becomes noticeable when frames observed with different bands are appropriately rescaled (see [Fig. 1.27](#)). To ensure a more robust analysis, it is essential to observe multiple bands simultaneously, invoking the utilization of Integral Field Spectrograph (IFS) datacubes, as suggested later by [Thatte et al. \(2007\)](#).

- **RDI:** Reference-star differential imaging (RDI) is an observing strategy that consists of observing different stars to build a model of the speckle field. This procedure uses the same setup as the one used for the target of interest. After scaling the flux/brightness, the PSF model can be used to subtract the quasi-static speckles of the science data frames, which are mainly created by the instrumentation (see [Fig. 1.28](#)). RDI has the detectability advantage under a small rotation of FoV in comparison to ADI or SDI. However, this technique requires high stability of the instrument,

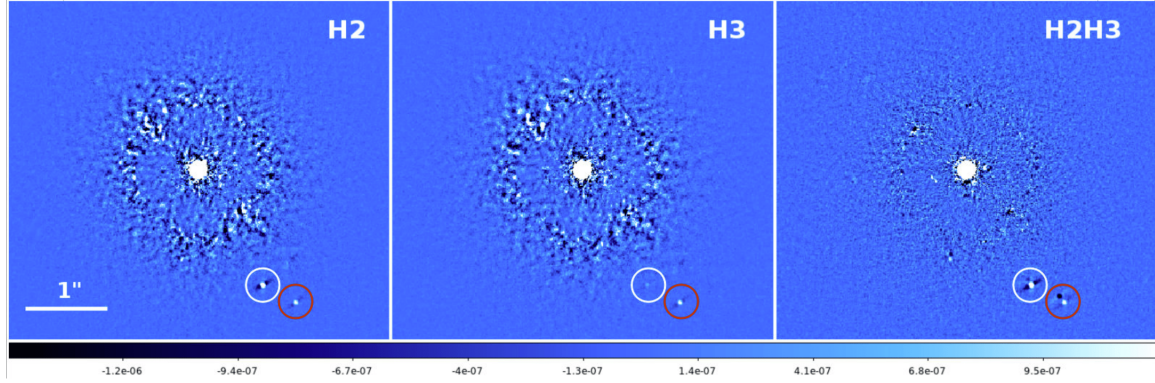


Figure 1.26: Images of the GJ 758 system, highlighting the late T-dwarf GJ 758 B within the white circle. A background star is indicated in the red circle. The methane absorption in the H3 filter is evident, showcasing lower flux in the object. In the SDI combination of the two filters, the T-dwarf displays two distinct peaks, while the neighboring star exhibits equal peaks. Credits: Adapted from [Vigan et al. \(2016\)](#).

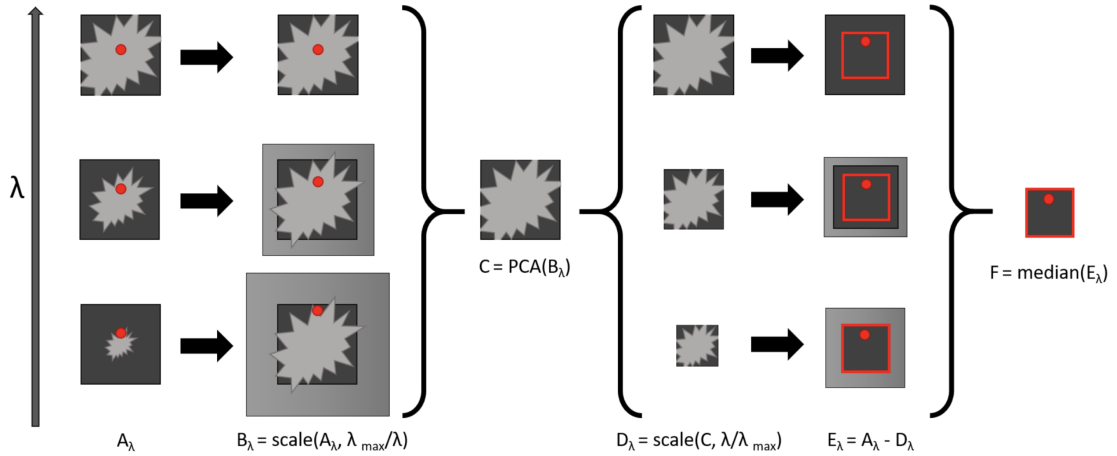


Figure 1.27: Schematic illustration of the Spectral Differential Imaging (SDI) observing strategy in combination with Principal Component Analysis (PCA) post-processing. The process involves scaling the images (A_λ) inversely proportional to their wavelength (B_λ), followed by the creation of a stellar PSF model (C) using PCA analysis. The stellar PSF model (C) is then rescaled for each wavelength channel proportional to its wavelength (D_λ) to match the original images' scaling (A_λ). This results in a reduced Field of View (FoV) marked by a red border, with the outer region of small wavelength images not covered by the scaled stellar PSF models (D_λ). The companion is denoted by a red dot. Credits: [Kiefer et al. \(2021\)](#).

short duty cycles, and relatively similar magnitudes between the target and the reference star. Some contemporary ground-based HCI systems have an observing mode called “star-hopping” (see e.g. [Wahhaj et al., 2021](#)). This functionality enables the AO loop to pause temporarily on a target, like the science target, and resume when the telescope points to another nearby target, such as the PSF reference star. This

ensures a close match in their PSFs. Additionally, RDI can be carried out to improve performance, especially using space telescopes like Hubble space telescope (see e.g., Golimowski et al., 2006; Schneider et al., 2009).

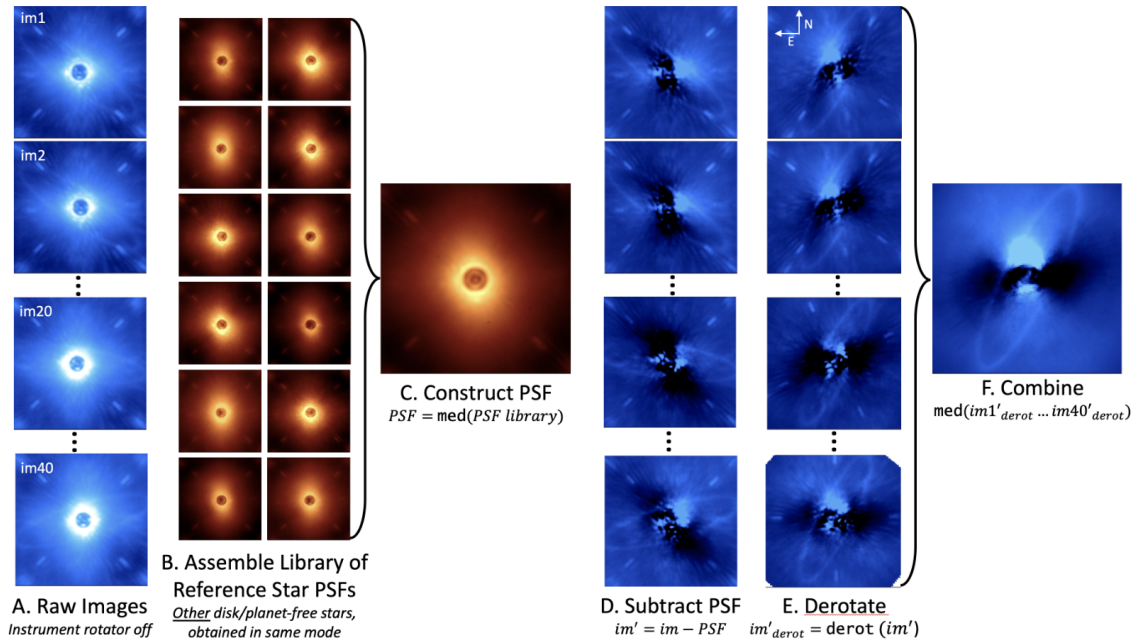


Figure 1.28: The figure depicts the Reference Differential Imaging (RDI) process using Gemini Planet Imager H-band images of HR 4796A. RDI involves a library of images of stars without known disk or planet signals, serving as references. These reference images can be straightforwardly combined or employed to create a customized PSF for each target image in the sequence. In cases where the instrument derotator is turned off, subtracted images are rotated to a common on-sky orientation and combined, as in the ADI procedure. Credits: Follette (2023)

Post-processing techniques

Following the acquisition of data through an observing strategy executed in the instrument/coronagraphic observation, a post-processing procedure designed to enhance the contrast of faint companions/substructures will be employed. Post-processing techniques can be categorized into three primary groups: (1) speckle subtraction techniques, (2) maximum likelihood techniques, and (3) supervised machine learning techniques (Dahlqvist, 2022).

Speckle subtraction techniques, often referred to as PSF-subtraction techniques, are widely utilized within the High-Contrast Imaging (HCI) community. The process typically involves the following steps outlined in Fig. 1.29. Initially, the process involves estimating a model of the speckle field (also referred to as the reference PSF), subtracting this model from each science image, and performing de-rotation (ADI) and/or rescaling (SDI) of the PSF-subtracted images. Subsequently, these processed images are combined to produce a residual image.

The maximum likelihood post-processing techniques involve addressing the potential distortion of the planetary signal due to the subtraction of the speckle field model. Instead of subtracting the reference PSF or decomposing it into multiple components, these techniques replace or complement reference PSF subtraction with forward modeling of the planetary companion. This approach includes a maximum likelihood-based estimation of the planetary flux. By modeling and tracking the planetary signal based on knowledge of speckle noise statistics, the expected planetary movement (depending on the observing strategy), and the impact of speckle field modeling, these techniques employ a maximum likelihood approach to provide estimated contrast values for each position within the field of view. Additionally, they may provide a detection map based on SNR.

The post-processing techniques employing supervised machine learning can be categorized into two main methods: decision trees and deep neural networks. These approaches, exemplified by the SODINN (Supervised exOplanet detection via Direct Imaging with deep Neural Networks) algorithm proposed by [Gomez Gonzalez et al. \(2018\)](#), redefine the task of exoplanet detection as a binary classification problem (is it an astrophysical source or a speckle?). The primary challenge lies in obtaining a substantial number of labeled samples for effective training since few planets were detected with HCI. The negative classes (speckle noise) can be generated by standard machine learning data-augmentation techniques ([Gomez Gonzalez et al., 2018](#)) or through the use of Generative Adversarial Networks (GANs; ([Hou Yip et al., 2019](#))). On the contrary, the positive classes can be generated by injecting synthetic substellar companions at various SNR levels, using an off-axis PSF of the host star as model.

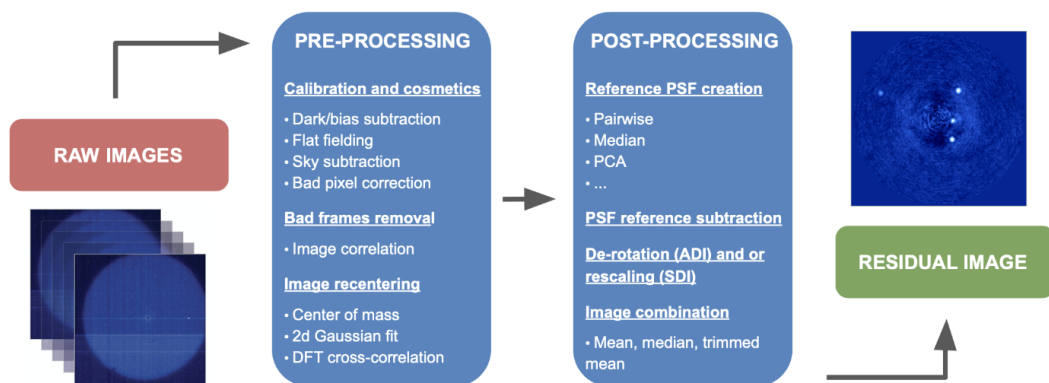


Figure 1.29: Typical differential imaging pipeline for speckle/PSF subtraction observing strategies coupled with post-processing techniques. Credits: [Dahlqvist \(2022\)](#).

Although an exhaustive list of post-processing techniques and their variations, associated with various observing strategies could be provided and described, I will narrow the focus to speckle subtraction techniques which can be coupled with ADI. Specifically, I will briefly mention the median subtraction, Principal Component Analysis (PCA), and Locally Optimized Combination of Images (LOCI) techniques. These three were employed throughout the course of the work outlined in Chapter 3:

- **Median subtraction:** The most simple approach to create a speckle model is to perform a median frame with the pre-processed frames from an observing sequence. This technique, originally developed alongside ADI (Marois et al., 2006), relies on the fact that a moving planet is not visible in the median image of the sequence, which can be used as an initial estimation of the speckle model. Subsequently, after subtracting the median, the residual noise averages incoherently when the images are aligned to a common north. This initial approximation, however, is less effective in the immediate vicinity of the host star. In this region, residual speckle noise is more concentrated and intense, and the companion’s differential angular displacement is lower, leading to more pronounced self-subtraction. Median subtraction, thus, performs better for brighter and more angular separated sources.
- **Locally Optimised Combination of Images (LOCI):** The LOCI technique, similar to median subtraction, generates speckle model frames through a combination of pre-processed frames. However, LOCI’s models are more robust as they are constructed using a linear combination of selected images. In LOCI, reference frames are segmented into subsections, both radially and azimuthally. Coefficients, derived from a reference frame and through residual minimization, are calculated to weight each section across all frames. Consequently, the model frames utilize these weighted linear combinations of images, resulting in an enhanced speckle model. Since its original development by (Lafrenière et al., 2007), various adaptations of LOCI have been introduced (see e.g., Pueyo et al., 2012a; Marois et al., 2014; Currie et al., 2012).
- **Principal Component Analysis (PCA):** PCA-based techniques (Soummer et al., 2012a; Amara & Quanz, 2012a) are widely utilized as a statistical tool in post-processing for HCI images. In HCI, PCA serves as the builder of speckle models for each pre-processed frame. Mathematically, PCA techniques involve the projection of images onto a lower-dimensional orthogonal basis. By vectorizing pre-processed images along their uncorrelated dimensions, such as position, rotation, wavelength, brightness, and other n-parameters, a covariance matrix can be built. If there is more variation in specific aspects of information across different images, more vectors for a complete representation are needed. These vectors, within the orthogonal basis, are termed principal components – the number of principal components needed to express the required information is selected by the PCA user. The initial components of a PCA encapsulate more information than higher-order components. Therefore, the principal components can be defined as a truncation of the orthogonal basis, where the higher the number of principal components, the closer the information expressed to the original data. In the context of PCA for HCI applications, the conceptual idea involves identifying patterns across multiple pixels present in both the target image and a certain number of reference images. The initial principal components typically capture large-scale PSF structures, while the higher-order principal components resemble various manifestations of the speckle pattern. For the aforementioned observing strategies, it can be used as a tool to select just a part of the more correlated information, taking advantage of the fact that the companion rotates in the FoV but

not the quasi-static speckles. The addition of components to the model enhances its “aggressiveness”, increasing the probability of a well-matched PSF model. However, this also raises the likelihood of over-subtracting or self-subtracting the companion’s signal.

A diagram illustrating the ADI observing strategy and the functionality of the three described post-processing techniques is presented in Fig. 1.30.

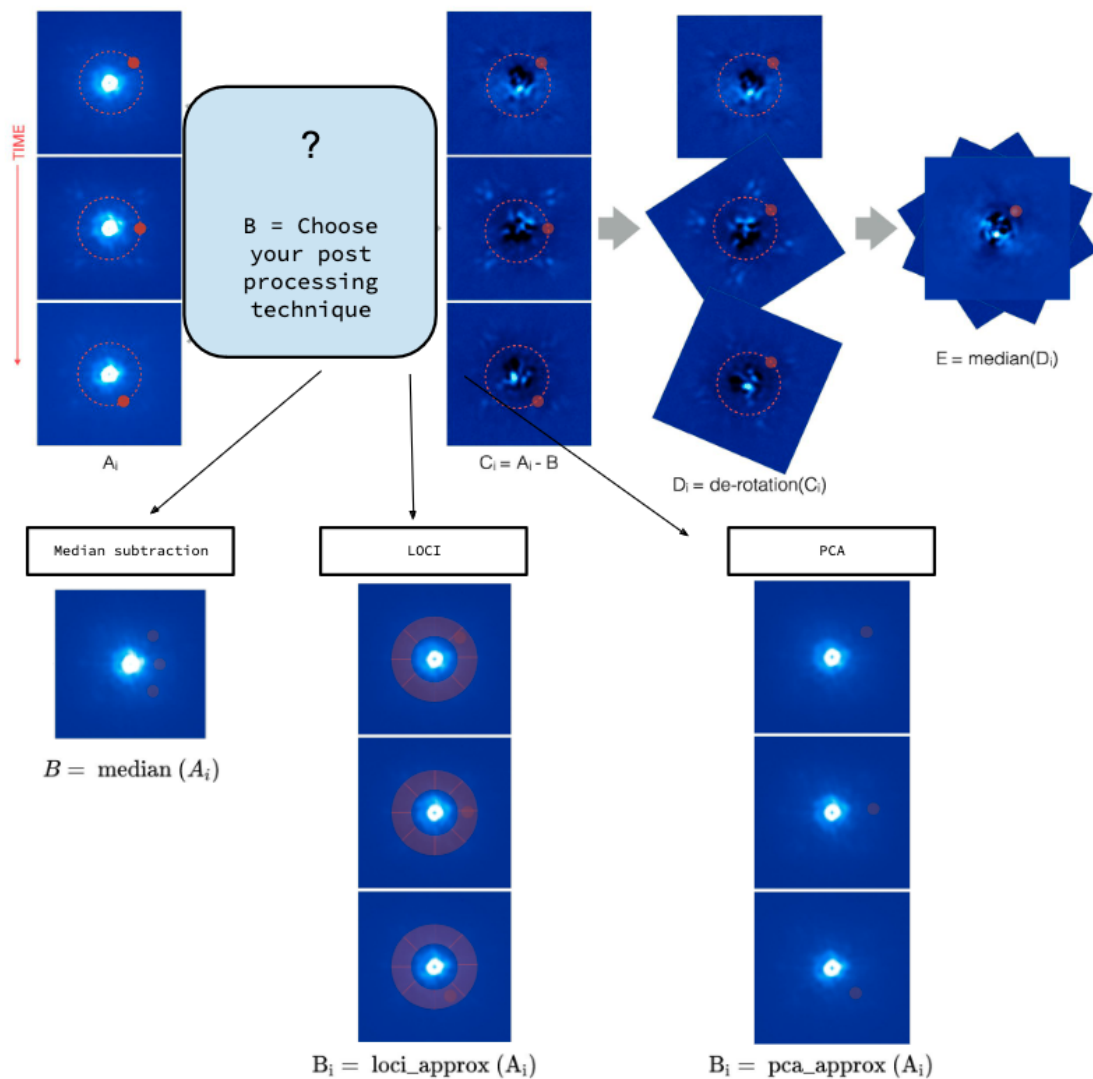


Figure 1.30: Diagram illustrating the ADI observing strategy with three distinct post-processing techniques for building the speckle model: 1) median subtraction (bottom-left), 2) LOCI (bottom-center), and 3) PCA (bottom-right). The subsequent steps follow the procedure outlined in subsection 1.2.3 and Fig. 1.25. Credits: Adapted from Gómez González (2017).

1.2.4 High-Contrast Imaging: observing/characterizing substellar companions

The HCI technique, as previously mentioned, is an adequate tool to detect and study substellar companions. Usually, companions detected by HCI play a fundamental role in connecting the formation of these objects in disks (see section 1.1) and their later evolution into mature stellar/planetary systems. This section provides a brief description of substellar companions observations, encapsulating the most recent and remarking exoplanetary observations, and highlighting how they were/can be characterized.

Taxonomy of substellar objects

Earlier in this chapter, substellar objects were classified as those lacking sufficient mass to trigger ${}^1\text{H}$ mass fusion. However, within this category, further subdivisions can be made. Based on their nature and properties, substellar objects can be categorized into planetary objects, and brown dwarfs, which can exist either as free-floating objects or companions.

According to the “classical” definition, a BD can be defined as a deuterium-burning object, whereas a threshold between planets and BDs should occur at $\sim 13 M_{Jup}$, and between a BD and star $\sim 80 M_{Jup}$, with metallicities involved on the uncertainties (see e.g., [Chabrier & Baraffe, 1997](#); [Spiegel et al., 2011](#) and further references). When defining BDs and planets, is still commonly used the definition proposed by the IAU Working Group Definition ([Boss et al., 2007](#)), which states:

1) *Objects with true masses below the limiting mass for thermonuclear fusion of deuterium (currently calculated to be 13 Jupiter masses for objects of solar metallicity) that orbit stars or stellar remnants are “planets” (no matter how they formed). The minimum mass/size required for an extrasolar object to be considered a planet should be the same as that used in our Solar System.*

2) *Substellar objects with true masses above the limiting mass for thermonuclear fusion of deuterium are “brown dwarfs”, no matter how they formed nor where they are located.*

3) *Free-floating objects in young star clusters with masses below the limiting mass for thermonuclear fusion of deuterium are not “planets”, but are “sub-brown dwarfs” (or whatever name is most appropriate).*

However, the classical mass classification has been challenged regarding the deuterium burning criteria and formation scenario of these objects. For example, some below the deuterium burning mass limit show indicative of cloud fragmentation formation, including members of quadruple systems with inferred masses as low as 5 Jupiter masses and free-floating objects with sub-deuterium-burning masses ([Todorov et al., 2010](#); [Liu et al., 2013](#)). Also, some observations revealed systems with companions above the deuterium limit but orbiting at low separations and exhibiting characteristics indicating formation is a disk (see e.g. [Quirrenbach et al., 2019](#)). Therefore, more recent criteria have been proposed.

It is possible to categorize substellar objects based on the presence and distance from a host star, and the mass ratio $q = M_*/M_{sub.obj}$. By definition, protoplanets and planetary objects form within a protoplanetary disk. In contrast, a BD can either form within a circumstellar disk (without being the object formed at the center) or exist as an isolated

object, forming separately from the clump that eventually becomes the closest star (refer to subsections 1.2.1 and 1.2.2).

Given that the distributions of PPDs decline to low frequencies at approximately 300 au (Andrews & Williams, 2007), a tentative characterization limit for the separation between substellar objects detected after the dissipation of the disk can be established. Specifically, if an object presents a semi-major axis $a_{sub_obj} > 300$ au from a star, is probably a brown dwarf, while lower separations can denote any of the mentioned objects, including BDs.

Furthermore, a substellar object can be ejected from the formation system, or in the case of BDs, they can form in isolation. In a detection, if no stellar host is present or if the substellar object is not gravitationally bound to any discernible star, it can be referred to as a free-floating or field object. Conversely, if it is gravitationally bound to a star, it will be classified as a companion. In the context of HCI, providing evidence of companionship, especially for wide-separation objects, remains challenging as it requires multi-year observations to disentangle it from a background source.

Demographic analyses of substellar objects also offer criteria for distinguishing planets from brown dwarfs. The substellar mass function, as observed in both previous and recent radial velocity surveys (see e.g. Sahlmann et al., 2011; Kiefer et al., 2019), reveals a local minimum around $m \sin(i) \sim 16\text{-}30 M_{Jup}$. This minimum in the companion mass function may be linked to the primary mass, suggesting that the companion mass ratio q could be a crucial discriminator – binary companions to more massive stars with $q \geq 0.025$ are exceptionally rare (Kraus et al., 2008; Reggiani et al., 2016).

Following all these constrainings, Currie et al. (2023) proposed a modern classification of BDs and planets: planetary companions should have mass $< 25 M_{Jup}$, $q < 0.025$, and $a \lesssim 300$ au. However, I highlight that a unified and accepted classification is lacking at the moment.

Characterization of HCI companions

Ultimately, an HCI object offers three main observable features that can be used to infer other complex properties: astrometric position, photometry, and spectra.

Firstly, astrometry is established by the position of the HCI companion, normally associated with the host star. Knowing the astrometric position of the stellar host and thus measuring the position in right ascension (RA) and declination (DEC) of the companion at the sub-pixel level, the relative position between the objects can be established. Alternatively, two variables can be measured, the separation ρ and the position angle (PA). The separation can be directly measured in arcseconds (") during observations, and it is then converted to physical separation, typically expressed in astronomical units (au). The position angle, also known as the parallactic angle, is the conventional angle measured from the north celestial pole through the east, firstly increasing into the direction of the right ascension. The angle ranges between 0° and 180° when measured east of true north, and 180° to 360° when measured west (see Fig. 1.31). In coronagraphic images, a notable challenge lies in precisely determining the image center, corresponding to the position of the central host star behind the mask. Advanced high-contrast imagers such as VLT/SPHERE

and GPI provide an effective solution for accurately establishing the center using “waffle spots”. These spots are replicas of the central PSF strategically positioned in symmetrical locations around the stellar center, facilitating the determination of the center during the pre-processing stages.

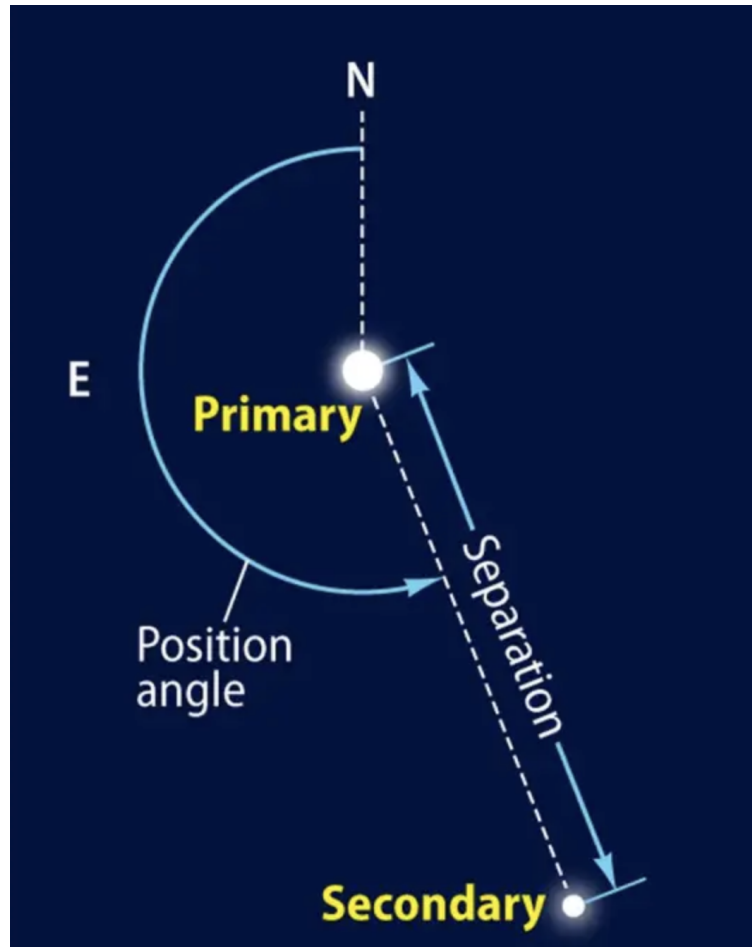


Figure 1.31: Representation of the conventional establishment of the position angle (PA), along with the parameter separation (ρ) for companion astrometry. Credits: <https://www.astronomy.com/science/double-star-fever/>.

As mentioned earlier, achieving comprehensive orbital coverage for HCI companions requires observation periods on the order of years, given their substantial separations from the host star. By having astrometric points, an orbital analysis can be performed, increasing its accuracy as more percentage of the orbital is covered. To precisely characterize the orbit of a companion in relation to its stellar host, it is essential to determine the companion’s velocity vectors and positions over time. The conventional mathematical representation of the orbit, typically an ellipse in relation to a reference plane, employs six Keplerian elements (refer to Fig. 1.32):

- Eccentricity (e): Describes the shape of the ellipse, indicating how much it is elongated compared to a circle.

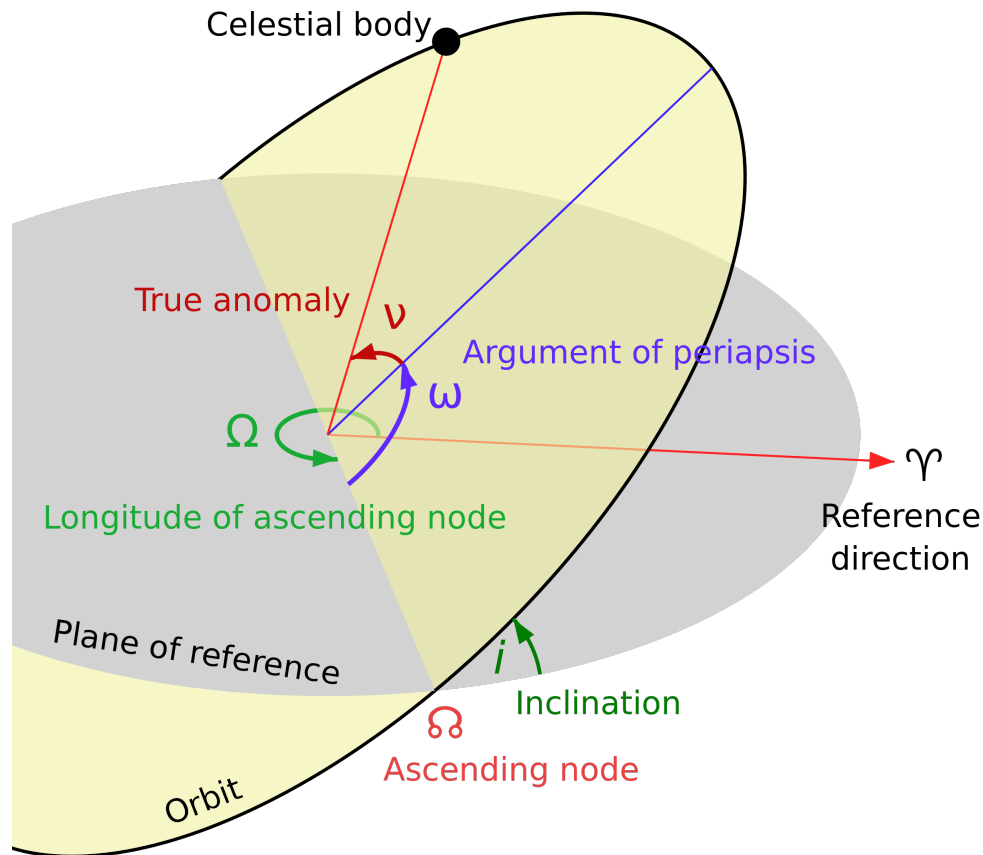


Figure 1.32: Representation of the six Keplerian orbital elements to uniquely describe the orbit of a companion. Credits: By Lasunncty at the English Wikipedia, CC BY-SA 3.0, <https://commons.wikimedia.org/w/index.php?curid=8971052>

- Semi-major axis (a): Represents half the sum of the periaapsis and apoapsis distances. For classic two-body orbits, it is the distance between the centers of the bodies, not the distance of the bodies from the center of mass.
- Inclination (i): Denotes the vertical tilt of the ellipse concerning the reference plane, measured at the ascending node. The tilt angle is measured perpendicular to the line of intersection between the orbital plane and the reference plane.
- Longitude of the ascending node (Ω): Horizontally orients the ascending node of the ellipse (where the orbit passes from south to north through the reference plane) concerning the reference frame's vernal point.
- Argument of the periaapsis (ω): Defines the orientation of the ellipse in the orbital plane, representing the angle measured from the ascending node to the periaapsis (the closest point the satellite object comes to the primary object around which it orbits).
- True anomaly (ν) at a specific time t_0 : Specifies the position of the orbiting body

along the ellipse at a specific time.

Using the orbital elements, it is also possible to determine key aspects of the orbit, such as the period, periapsis, and apoapsis. Typically, for companion objects, orbital characterization (orbit fitting) can be accomplished through various algorithms. Some of these algorithms utilize astrometric data of the companion, astrometric tracking of the star through surveys like Hipparcos and Gaia, and additional information such as radial velocity data points.

Other key information extracted from HCI observations is the photometry. Photometry is determined by measuring the contrast between the PSF of the host star and that of the companion. To achieve this, off-axis observations of the star (without the mask) are valuable throughout the observing sequence. Utilizing the flux ratio, the magnitude difference Δm_x in a specific band x can be computed as $\Delta m_x = -2.5 \log_{10}(F_{x_{comp}}/F_{x_*})$. Thus, knowing the absolute magnitude of the host star, which represents its intrinsic brightness at a standard distance of 10 parsecs, allows for the direct determination of the absolute magnitude of the companion.

The fluxes can also be converted to luminosities using the relationship $F_{comp} = L/4\pi r^2$, where L is the luminosity, and r is the distance of the object from the observer. Assuming the companion behaves like a black body, the Stefan-Boltzmann law, $F_* = \sigma T^4$, where T is the temperature in Kelvin and σ is the Stefan-Boltzmann constant ($\sigma = 5.67 \times 10^{-8} \text{ W m}^{-2} \text{ K}^{-4}$), can be applied to determine the flux at the surface of the object. Consequently, a direct relation between luminosity and temperature can be established. As illustrated in Fig. 1.15, models can utilize the temperature, indirectly inferred through photometric measurements, along with the age of the companion (assumed to be the same as the system/stellar host's age) to estimate an approximate mass. However, precise measurements of photometry and the stellar age are essential for accurate estimations. Furthermore, the accuracy of the estimation heavily relies on the model used and the assumed formation origin, whether it is a *hot start* (associated with objects formed from gravitational instability) or a *cold start* (objects formed from core accretion).

Similar to astrometry, observing variations in photometric measurements of substellar objects over several years provides significant insights. Variability in these objects is often associated with factors such as rotation and the presence of clouds. Objects with rapid rotation and uneven atmospheric structures, featuring patchy thin, and thick clouds, tend to exhibit noticeable changes in brightness during different rotational phases. Large-scale surveys of brown dwarfs have consistently identified common variability patterns, with amplitudes reaching up to approximately 20% in the near-infrared (Radigan et al., 2014; Radigan, 2014; Wilson et al., 2014; Metchev et al., 2015). Young, directly imaged giant planets are expected to display even more pronounced variability. The extent and nature of variability of substellar objects, however, is linked to their spectral types. For a list of references concerning variability in giant planets and BDs, encompassing both field objects and companions with various spectral types, please refer to Currie et al. (2023).

Multi-band photometric bands HCI observations can provide hints on the spectral type of substellar objects. While most spectra to date for HCI planets were obtained from low-resolution NIR observations ($R < 100$), higher resolution powers ($R = 2000\text{-}6000$) are

offered in some modern IFS instruments in 8-meter class telescopes (e.g, Gemini/NIFS, VLT/MUSE, VLT/SINFONI, and Keck/OSIRIS). The resolution of the obtained spectra gives how well-resolved, less-spaced, are the points in the spectra. Thus, more resolvable power offers better feature analysis in the HCI object, such as molecular bands/chemical abundances, rotational velocity, presence of clouds, and surface gravity (see Fig. 1.33).

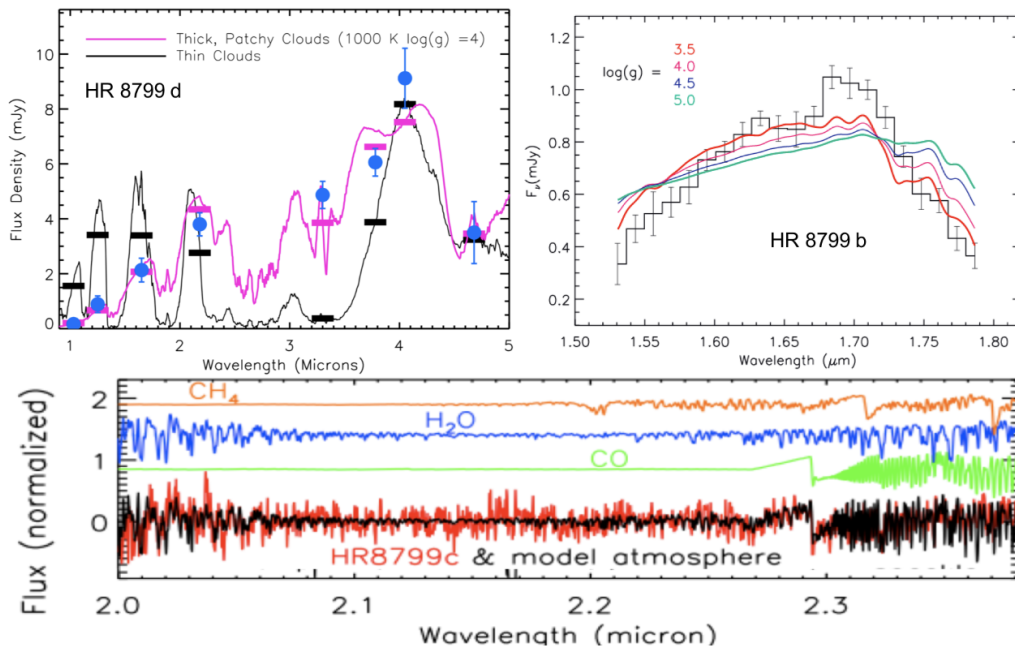


Figure 1.33: Demonstration of key properties inferred from direct imaging observations. Top-left: Fit to HR8799d 1–5 μm photometry showing that models with thick clouds better reproduce the planet data (adapted from Currie et al., 2011). Top-right: Keck/OSIRIS low-resolution H-band spectrum for HR8799b: a sharply-peaked H-band spectrum is a signpost of low surface gravity (Barman et al., 2011). Bottom: Keck/OSIRIS medium-resolution HR8799 c spectrum, revealing lines of CO and H₂O (Konopacky et al., 2013). Credits: Currie et al. (2023).

The category of substellar objects encompasses spectral types from late (redder) M to Y (Kirkpatrick et al., 1999; Cushing et al., 2011). The Fig. 1.34 illustrates some of the main features of substellar objects along the spectral sequence from M to T. Key properties of each spectral class are as follows:

- **M-dwarfs:** Serving as a transitional link between stellar objects and brown dwarfs, the latest types in the M sequence include young objects classified as brown dwarfs. The spectrum is characterized by the presence of TiO and VO. TiO bands increase in strength up to spectral type M6, and VO becomes prominent in the latest types (Bailey, 2014). Broad absorptions due to H₂O are found around 1.4 and 1.9 μm , particularly in later spectral types. Other molecules with strong absorption include FeH, CrH, and MgH.

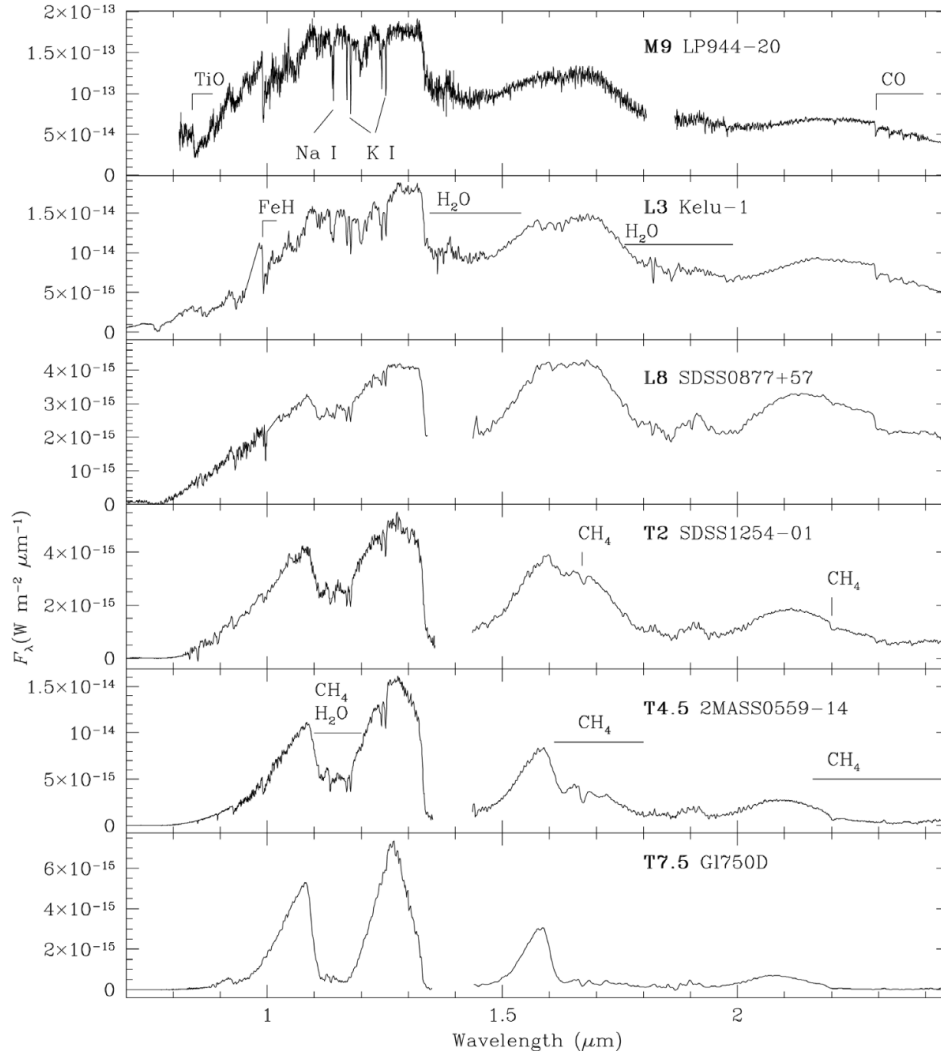


Figure 1.34: Spectra of ultracool dwarfs from M9 to T7.5. Credits: [Bailey \(2014\)](#).

- **L-dwarfs:** TiO and vanadium monoxide diminish in L-dwarfs, replaced by bands of CrH, FeH, and alkaline metals in the optical. In the near-infrared, bands of CO, CrH, and FeH are strong until the mid-L range, after which they become weaker. The L-dwarfs present dusty clouds of species such as enstatite, forsterite, spinel, and solid iron condensing in the upper layers of the atmosphere (see e.g. [Allard et al., 2001](#)).
- **T-dwarfs:** Characterized by methane (CH_4) absorption features in the near-IR region (1-2.5 μm) and water absorption bands, T-dwarfs exhibit blue shifts in the mag/color diagram due to methane absorptions at 1.6 and 2.2 μm (H and K bands). They bear a closer resemblance to the giant planets in the solar system.
- **Y-dwarfs:** Y dwarfs are the coldest class of brown dwarfs ($T \lesssim 450\text{K}$), which can present a rich collection of molecular bands in their atmospheres such as CH_4 , CO_2 ,

H₂O, and NH₄. In the specific case of water, a cutoff of molecular absorption is expected to occur at temperatures lower than $\sim 500\text{K}$, where no water clouds will be formed (see e.g. [Ackerman & Marley, 2001](#); [Burrows et al., 2003](#)).

Therefore, robust characterization of HCI substellar objects can be achieved through astrometric, photometric, and spectroscopic observations. Continuous monitoring and the utilization of multi-wavelength observations, facilitated by IFS instruments, contribute to a more comprehensive analysis and yield detailed results.

HCI exoplanetary detections

Since the first detection of a planetary-mass companion via HCI ([Chauvin et al., 2005](#)), fewer than 40 additional detections have been confirmed (see Fig. 1.35, top-panel). These detections highlight the challenges associated with the technique, as discussed in section 1.2.3. Furthermore, confirming their association with the stellar host and ruling out the possibility of background sources necessitates extensive observation periods, often spanning several years due to their considerable separation. However, the new generations of high contrast imagers, improving contrast power, may provide a notable increase in the number of objects in the upcoming years. Following, a non-exhaustive list of emblematic systems analyzed through HCI is presented:

- **2M1207:** 2M1207 b was the first exoplanet detected via HCI ([Chauvin et al., 2005](#)). It was detected using the instrument NACO/VLT. The host is an M8 type star part of the TW Hydra association (age of ~ 10 Myr; [Barrado Y Navascués 2006](#); [Bell et al. 2015](#)), at a distance of 64.5 ± 0.4 pc ([Bailer-Jones et al., 2021](#)). The companion has a separation of $0.70''$ (55 au). According to HCI observations and evolutionary models, the estimated mass of the companion is approximately $5\text{-}6 M_{Jup}$, and it exhibits an effective temperature of $1200\text{-}1300$ K ([Luhman et al., 2023](#)). The characteristics of this object are unique, as the formation of the planet within the protoplanetary disk is highly improbable due to its considerable distance from the host star. It is often regarded more as a binary system of low-mass objects rather than a conventional planetary system ([Mohanty et al., 2007](#)).
- **HR8799:** HR8799 is the first multiplanetary system discovered by HCI ([Marois et al., 2008, 2010](#)). HR8799 has 4 planets, which were discovered through Keck and Gemini telescopes. HR8799 is a young system (~ 42 Myr; [Hinz et al. 2010](#); [Zuckerman et al. 2011](#); [Bell et al. 2015](#)) at a distance of 40.88 ± 0.08 pc ([Gaia Collaboration, 2020](#)). The host star has a mass of $1.47^{+0.12}_{-0.17} M_{\odot}$ ([Sepulveda & Bowler, 2022](#)). This particular system stands out as one of the most frequently studied subject using HCI, serving as a standard reference for analysis of planetary atmospheres, the dynamics inherent in multi-planetary systems, and the mechanisms guiding their formation. The system also offers an outstanding scenario to study the formation and dynamics of these planets since they orbit at wide separations (the closest planet has a separation of ~ 390 mas = 15.94 au). The masses of the companions, inferred through

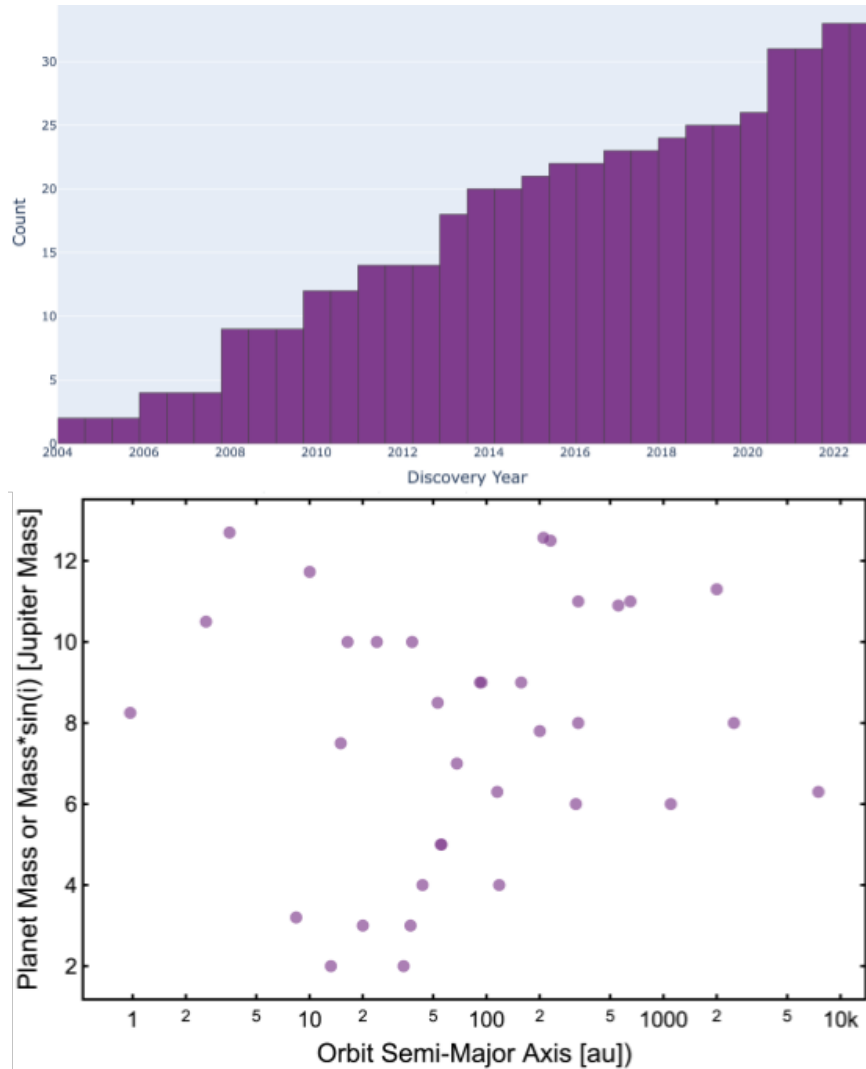


Figure 1.35: Exoplanets discovered by HCI up to 25-02-2024. They were selected through the “classical” mass threshold – objects with less than $13 M_{Jup}$. Top panel: cumulative distribution of discoveries throughout years. Bottom-panel: Mass of the companions in Jupiter masses vs log of semi-major axis in au. Credits: NASA Exoplanet Archive: exoplanetarchive.ipac.caltech.edu.

evolutionary models and dynamical studies, range between 5-10 M_{Jup} (Marois et al., 2010; Currie et al., 2011; Sudol & Haghighipour, 2012; Wang et al., 2018; Brandt et al., 2021b).

- **Fomalhaut:** Fomalhaut is a young system (approximately 500 Myr) at a distance of 7.7 pc, composed of a bright A3V star surrounded by a quasi-face-on debris disk (Gray et al., 2006; Mamajek, 2012; Nielsen et al., 2019). Kalas et al. (2008), using Hubble Space Telescope (HST) observations, revealed a co-moving source in visible light, quasi-nested within the dust belt and at a separation of approximately 119 au from the star. The source was then classified as a planetary object. Fomalhaut b is the

lowest mass planet ever imaged ($3 M_{Jup}$ or lower; [Chiang et al., 2009](#); [Marengo et al., 2009](#)). However, subsequent studies have cast doubt on its classification as a planet. Several factors contribute to this skepticism, including the absence of infrared emission proportional to its visible brightness, thus casting the lack of thermal emission and just presenting reflected light ([Currie et al., 2013](#)), its high eccentric orbit crossing the ring inconsistent with the stability expected of a planetary object ([Beust et al., 2014](#)), and the failure to detect Fomalhaut b in multiple epochs of Spitzer imaging ([Marengo et al., 2009](#); [Janson et al., 2015](#)). Moreover, later observations with HST revealed the object expanding in size while decreasing in brightness ([Gaspar & Rieke, 2020](#)). The prevailing explanation for the nature of Fomalhaut b leans toward it being a slowly dissipating, expanding remnant resulting from the collision of two planetesimals ([Lawler et al., 2015](#); [Gaspar & Rieke, 2020](#)). Despite the controversy about the planetary nature of Fomalhaut b, the system is still investigated concerning planets using HCI, where indicative of other objects has been spotted ([Ygouf et al., 2024](#)).

- **β Pictoris:** β Pic is an intriguing system composed of a young A6V-type star, an edge-on debris disk, and two planets. The system has an age of $\sim 18.5 \pm 2$ Myr ([Miret-Roig et al., 2020](#)) and is situated at a distance of 19.45 ± 0.05 pc ([van Leeuwen, 2007](#)). β Pic b was first imaged by [Lagrange et al. \(2009b, 2010a\)](#), using VLT/NaCo observations. The planet has a mass of ~ 9 - $10 M_{Jup}$ and a semi-major axis orbit of approximately 10 au ([Nowak et al., 2020](#); [Brandt et al., 2021a](#)). More recently, a closer planet was discovered with European Southern Observatory/High Accuracy Radial Velocity Planet Searcher (HARPS) observations, using the radial velocity technique ([Lagrange et al., 2019](#)). It was later confirmed with VLTI/GRAVITY observations ([Nowak et al., 2020](#)). β Pic c has a dynamical mass of $\sim 8 M_{Jup}$ with a semi-major axis of ~ 3 au ([Nowak et al., 2020](#); [Brandt et al., 2021a](#)). Both planets are on eccentric orbits (~ 0.3 and ~ 0.121 for β Pic b and β Pic c, respectively; [Brandt et al., 2021a](#)). Overall, the β Pic system has proven to be an interesting subject for investigating its dynamics and planetary formation scenarios.
- **AF Leporis:** AF Lep constitutes a system featuring an F8V star ([Gray et al., 2006](#)) located at a distance of 26.8 pc ([Gaia Collaboration et al., 2023](#)), accompanied by a debris disk located at $\sim 54 \pm 6$ au from the star ([Pawellek et al., 2021](#)), and a Jupiter-like planet. The system has an age of 24 ± 3 Myr ([Bell et al., 2015](#)). AF Lep b drew attention through its remarkable discovery in three independent and simultaneous studies. Anomalies in the astrometric accelerations observed in the HIPPARCOS-Gaia data (HGCA; [Brandt, 2021](#)) hinted at the potential presence of an undetected orbiting substellar object. Detected through HCI with VLT/SPHERE IRDIS/IFS in Y, J, H, and K bands ([Mesa et al., 2023](#); [De Rosa et al., 2023](#)), and Keck/NIRC2 in the L' band ([Franson et al., 2023](#)), AF Lep b showcased a mass range of 3-7 M_{Jup} , deduced from photometric measurements and astrometric fitting. The planet is situated at a separation of ~ 340 mas = 9 au, possesses an eccentricity ranging from 0.2 to 0.5, and its orbit aligns with the stellar inclination. Its distance from the innermost region of the debris belt suggests the potential existence of other undetected planets within

the system. AF Lep b is one of the least massive planets imaged thus far, exhibiting intriguing and promising features for further imaging and spectral characterization.

- **51 Eri:** 51 Eri is a young system (10-20 Myr; (Macintosh et al., 2015; Lee et al., 2022)) positioned at a distance of 29.90 ± 0.06 pc (Gaia Collaboration et al., 2021). This system revolves around a FOIV star, a member of the β Pictoris moving group (Zuckerman et al., 2001; Bell et al., 2015), and is known for hosting the planet 51 Eridani b. The star is part of a hierarchical triple system, accompanied by the M-dwarf binary GJ 3305AB, situated approximately 2000 au away from 51 Eri (Feigelson et al., 2006; Kasper et al., 2007). Additionally, the system possesses two debris belts, located at 5.5 au and 82 au (Patel et al., 2014; Riviere-Marichalar et al., 2014). The discovery of 51 Eri was initially made by Macintosh et al. (2015) through GPI and Keck/NIRC2 J, H, and Lp observations, and its companionship was later confirmed by De Rosa et al. (2015). The planet orbits at a separation of 449 mas = 13 au. Various studies have attempted to constrain its mass, indicating a range between 2-12 M_{Jup} , with the actual value highly dependent on the assumed formation scenario (Samland et al., 2017; De Rosa et al., 2020; Müller & Helled, 2021; Dupuy et al., 2022). Interestingly, the planet appears to not be coplanar with the distant binary (Montet et al., 2015). Spectral studies reveal an effective temperature of up to ~ 800 K (see e.g. Brown-Sevilla et al., 2023). The planet also shows strong methane spectral signatures, an unusual feature in most directly imaged exoplanets.
- **PDS 70:** PDS 70 is a young system (~ 5.4 Myr), with a K7-type pre-main sequence member of the Upper Centaurus-Lupus group (Riaud et al., 2006; Pecaute & Mamajek, 2016) at a distance of 113.43 ± 0.52 pc (Gaia Collaboration et al., 2016, 2018). The system has two protoplanets located within the cavity, PDS 70 b and c. PDS 70 b was first discovered with SPHERE, NaCo, and Gemini/NICI, H to L' bands' observations (Keppler et al., 2018a). Later, it was imaged with SPHERE K band and Y-H spectroscopic data, imposing an improved characterization (Müller et al., 2018). Its $H\alpha$ accreting nature was later revealed (Wagner et al., 2018). PDS 70 c was later discovered with VLT/MUSE observations in the $H\alpha$ line (Haffert et al., 2019), also showing to be an actively accreting protoplanet. PDS 70 b and c have separations of ~ 180 mas = 20 au and ~ 240 mas = 34 au, respectively (Wang et al., 2020). Subsequently, ALMA sub-mm observations have revealed the first circumplanetary disk detected co-locating with a protoplanet – in this case, PDS 70 c (Isella et al., 2019; Benisty et al., 2021). The masses of the two planets are still uncertain, although both planets are likely lighter than $10 M_{Jup}$ to ensure dynamical stability (Wang et al., 2021) and a non-eccentric outer disk (Bae et al., 2019). Masses inferred from SED modeling remain inconclusive but suggest planet masses between 1 and a few M_{Jup} (Stolker et al., 2020). Consequently, PDS 70 remains one of the most intriguing and extensively studied systems, holding the promise of unveiling crucial properties of its protoplanets and disk.

The systems described above are depicted in Fig. 1.36.

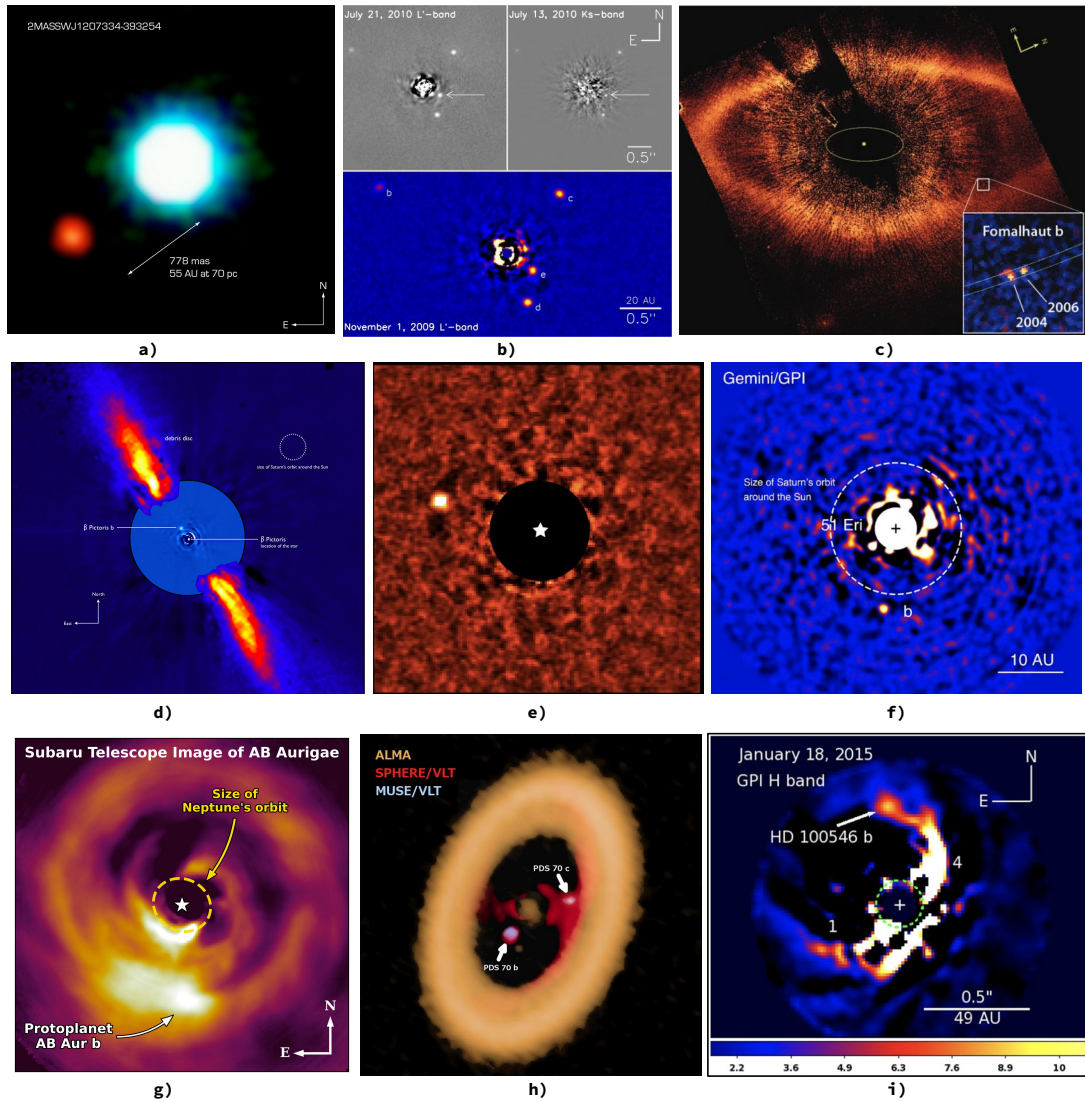


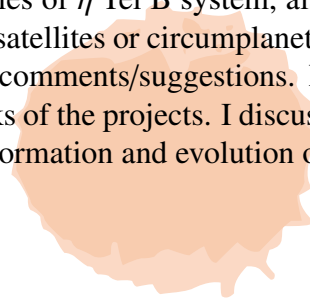
Figure 1.36: Mosaic of remarkable companions and protoplanet candidates detected via HCI. *Panel a*: 2M1207. Credits: [Chauvin et al. \(2004\)](#). *Panel b*: HR8799. Credits: [Marois et al. \(2010\)](#). *Panel c*: Fomalhaut. Credits: [Kalas et al. \(2008\)](#). *Panel d*: β Pic. Credits: ESO/A.-M. Lagrange et al. *Panel e*: AF Lep. Credits: ESO/Mesa, De Rosa et al. *Panel f*: 51 Eri. Credits: J. Rameau, University of Montreal / C. Marois, Herzberg Institute of Astrophysics. *Panel g*: AB Aur. Credits: [Currie et al. \(2022\)](#). *Panel h*: PDS 70. Credits: ALMA (ESO/NAOJ/NRAO)/A. Isella/ESO. *Panel i*: HD 100546. Credits: [Currie et al. \(2015\)](#).

1.3 Outline of this thesis

This dissertation describes the results obtained during my PhD research program. In this thesis, I aim to contribute with new perspectives on how (multi)stellar systems form in eruptive environments, along with the detection and characterization of multiple (sub)stellar objects in later stages. To achieve this, I conduct a detailed analysis using multiple wavelengths and exploring various stages of (sub)stellar formation.

The scientific targets under investigation include the eruptive binary HBC 494, analyzed through ALMA band 6 (1.6 mm) observations, and the η Tel system, consisting of a giant star and a brown dwarf companion, examined through near-infrared high-contrast imaging observations, more specifically with VLT/SPHERE IRDIS in H band.

The following chapters are organized as follows: In Chapter 2, I explore the properties of HBC 494, regarding its dust, gas, and dynamics. This work was published and can be found in [Nogueira et al. \(2023\)](#). In Chapter 3, I provide an intricate study regarding the astrometry, photometry, and orbital properties of η Tel B system, also providing a detailed analysis of its surroundings for looking for satellites or circumplanetary disks. This work is under corrections following the reviewer's comments/suggestions. Finally, in Chapter 4, I summarize the conclusions and final remarks of the projects. I discuss the immediate future steps to keep investigating the (sub)stellar formation and evolution of these sources.



CHAPTER 2

RESOLVING THE BINARY COMPONENTS OF THE OUTBURSTING PROTOSTAR HBC 494 WITH ALMA

The content of this chapter is published in the journal Monthly Notices of the Royal Astronomical Society (MNRAS), see [Nogueira et al. \(2023\)](https://ui.adsabs.harvard.edu/abs/2023MNRAS.523.4970N/abstract) - <https://ui.adsabs.harvard.edu/abs/2023MNRAS.523.4970N/abstract>.

2.1 Introduction

During their evolution, young stellar objects (YSOs) dissipate their envelopes while feeding their developing protostars through accretion via a disk. However, YSOs are underluminous compared to the luminosity and accretion rates expected from steady disk accretion. This discrepancy has been established as the “luminosity problem” (Kenyon et al., 1990; Evans et al., 2009). One potential solution to the luminosity problem is that young stars undergo episodes of high accretion interspersed by quiescent phases. During the episodes of enhanced accretion, large amounts of material are accreted very quickly (e.g., Dunham & Vorobyov, 2012). Such phenomena have been observed in low-mass pre-main sequence stars like FU Orionis and EX Lupi, the prototypes of the two subclasses that display the episodic accretion phenomenon.

FU Orionis type stars, a.k.a. FUors, are pre-main sequence low-mass stars that show variability in both luminosity and spectral type due to variation in the accretion mass rate, on a short timescale (Herbig, 1966). Their optical brightness can dramatically increase due to enhanced mass accretion by more than five magnitudes over a few months. After this “outburst”, FUors can remain in this active state for decades. This occurrence is considered episodic and suspected to be common at the early stages of star formation. Throughout an outburst, the star can accrete $\sim 0.01 M_{\odot}$ of material, roughly the mass of a typical T-Tauri disk (Andrews & Williams, 2005). The bolometric luminosity of the FUors during the outburst is $100\text{--}300 L_{\odot}$ and the accretion rate is between 10^{-6} and $10^{-4} M_{\odot} \text{ yr}^{-1}$ (Audard et al., 2014). EX Lupi type stars, a.k.a. EXors, are a scaled-down version of the FUors, with shorter and less intense outbursts (Herbig, 2007). The EXors enhanced accretion stage can last months to years, with accretion rates ranging from 10^{-7} to $10^{-6} M_{\odot} \text{ yr}^{-1}$, which are the order up to 5 magnitudes brighter than quiescent periods. The episodic recurrence is also on the order of years (e.g., Jurdana-Šepić et al., 2018; Giannini et al., 2022).

The mechanisms producing the eruptions in systems like FUors and EXors have yet to

be understood (Cieza et al., 2018). Several different triggers have been proposed to explain this phenomenon, such as disk fragmentation (Vorobyov & Basu, 2005, 2015; Zhu et al., 2012), coupling of gravitational and magneto-rotational instability (MRI) (Armitage et al., 2001; Zhu et al., 2009), and tidal interaction between the disk and a companion (Bonnell & Bastien, 1992; Lodato & Clarke, 2004; Borchert et al., 2022b). In terms of evolution, a scenario where FUors are understood as an earlier phase followed by an EXor phase could explain some of the observed properties of these systems (Cieza et al., 2018). EXors have less prominent (or lack of) outflows, and smaller masses/luminosities than FUors since the mass loss, accretion, and outbursts will significantly remove the gas and dust material during their evolutionary stages.

If most stars undergo FUor/EXor-like episodic accretions during their evolution, imaging the circumstellar disks of FUors at sub-mm/mm wavelengths can inform or constrain the underlying outburst mechanisms. For class 0/I objects (e.g., those still accreting from their circumstellar disks and envelopes), the massive disk could be expected to be prone to be gravitationally unstable, which can, consequently, trigger the MRI and/or disk fragmentation. Additionally, close encounters of stars can shape both gas and dust disk morphology (Cuello et al., 2019). Inferring which scenario plays in each disk requests an analysis that strongly depends on how well-resolved and which features one can extract from the observations. Consequently, when eruptive disks give a hint of irregular morphology or kinematics, follow-up observations at higher resolution are needed to resolve the substructures and infer the nature of the system.

HBC 494 is a Class I protostar, located in the Orion molecular cloud at a distance of 414 ± 7 pc (Menten et al., 2007), and has been classified as a FUor*. This young eruptive object (also called Reipurth 50) was discovered during an optical survey and described as a bright, conical, and large nebula reflecting light from a 1.5 arcmin away from a $250 L_{\odot}$ infrared source. Both were located at the southern part of the L1641 cloud in Orion (Reipurth, 1985; Reipurth & Bally, 1986). This nebula was claimed to appear after 1955, and its first detailed study showed high variability between 1982 and 1985, a consequence of a primordial IR source variability. Posterior studies have also confirmed its variability. For example, Chiang et al. (2015) reported a dramatic brightening (thus clearing of part of the nebula) that occurred between 2006 and 2014. These events can be explained by an episode of outflow coming from HBC 494. More recently, Postel et al. (2019), using archival photometry data along with Herschel and Spitzer spectra presented the detection of several molecular lines and the spectral energy distribution (SED) of HBC 494. The SED presented strong continuum emission in the mid and far-infrared, which is indicative of envelope emission. Such violent outflows were observed and described in Ruíz-Rodríguez et al. (2017).

ALMA Cycle-2 observations in the millimeter continuum ($\sim 0.25''$ angular resolution) show that the disk is elongated with an apparent asymmetry (Cieza et al., 2018), indicating the presence of an unresolved structure or a secondary disk. In this work, we present ALMA Cycle 4 observations at $\sim 0.03''$ angular resolution that reveal the binary nature of the HBC 494 system. Only Cycle 4 data were used in this work. The paper is structured as follows.

*The FU Ori classification is still controversial and has been contested by Connelley & Reipurth (2018).

Table 2.1: List of the Cycle 4 ALMA observations of the target HBC 494, used in this work

PI	Proj. ID	Ang. Res. (beam minor axis)	Date of obs.	Integration
Zurlo	2016.1.00630.S	0.142''	09/10/2016	8.39 min
Zurlo	2016.1.00630.S	0.027''	26/09/2017	25.55 min

The ALMA observations and data reduction are described in section 3.2. The results from the continuum and line analysis are described in section 2.3. The discussion is presented in section 2.4, while we conclude with a summary of our results in section 3.5.

2.2 Observations and data reduction

HBC 494 has been observed during the ALMA Cycle-4 in band 6 (program 2016.1.00630.S: PI Zurlo) for two nights, one on the 9th October 2016 and the other on the 26th September 2017 (see table 2.1). On the first night, the short baseline configuration was acquired, with a precipitable water vapor of 0.42 mm. The ALMA configuration of antennas was composed of 40 12-m antennas with a baseline from 19 to 3144 m. The flux calibrator and bandpass calibrator were both J0522-3627, and the phase calibrator was J0607-0834. The total integration on the target was 8.39 min. The second night, the long baseline dataset, had precipitable water vapor of 1.08 mm. The ALMA configuration consisted of 40 12-m antennas with a baseline from 42 m to 14851 m. The flux calibrator was J0423-0120, the bandpass calibrator was J0510+1800, and the phase calibrator was J0541-0541. The total integration on the target was 25.55 min.

The central frequencies of each spectral window were: 230.543 (to cover the transition $^{12}\text{CO J}=2-1$), 233.010 (continuum), 220.403 ($^{13}\text{CO J}=2-1$), 219.565 ($\text{C}^{18}\text{O J}=2-1$), and 218.010 (continuum) GHz. The minimum spectral resolution achieved (second night) for ^{12}CO was 15.259 kHz (~ 0.02 km/s), while for ^{13}CO and C^{18}CO , it was 30.518 kHz (~ 0.04 km/s). Both continuum bands presented 2 GHz bandwidths. The data were calibrated with the Common Astronomy Software Applications package (CASA v.5.5, McMullin et al., 2007), and the python modules from CASA API, *casatasks* and *casatools* (CASA Team et al., 2022). The standard calibrations include water vapor calibration, temperature correction, and phase, amplitude, and bandpass calibrations.

2.2.1 Continuum imaging

We started our analysis by fixing the visibilities' phase center on J2000 05h40m27.448s -07d27m29.65s. The image synthesis of the 1.3 mm continuum emission was performed with the *tclean* task of CASA. For the high-resolution data, we used the Briggs weighting scheme with a robust parameter of 0.5, resulting in a synthesized beam size of 41.2×29.8 mas, and a position angle of 40.6. The pixel scale of the image was set to 1.5 mas. One iteration step of self-calibration was applied to both observations. For the first night (low-

resolution image: 142 mas), it resulted in an improvement of ~ 6 SNR. For the second night (high-resolution image: 27 mas), it resulted in an SNR improvement of ~ 1.6 .

Our final continuum image was produced from a concatenated measurement set combining both, the short and the long baseline visibilities, using the *concat* task of CASA. We used the same image synthesis parameters used for the second night of observation.

2.2.2 Line imaging

The visibilities were fixed at the same phase center as was done for the continuum coordinates (see subsection 2.2.1). After producing a dirty image from the visibilities, we noticed that the emission mimicked the presence of gaseous envelopes around the disks (moment 0 maps, see Figure 2.1, left column) but no gas dynamic signatures were revealed (moment 1 map, see Figure 2.1, right column). Therefore, we proceeded to remove the visibility's continuum contributions by using the CASA task *uvcontsub*.

Next, we performed the *tclean* process using Briggs weighting with a robust parameter of 0.5, Hogbom deconvolver, and pixel scale of 6 mas. The total velocity ranged between -6 km/s to 18 km/s, although a smaller range (0 km/s to 11 km/s) was used to create the ^{13}CO and C^{18}O moment maps. We used spectral resolution widths of 1 km/s for ^{12}CO and of 0.3 km/s for ^{13}CO and C^{18}O . The rms values, obtained for the channel without a clear signal on the channel maps (4 km/s), were 1.9, 3.6, and 2.6 mJy/beam for ^{12}CO , ^{13}CO and C^{18}O , respectively.

2.3 Results

2.3.1 Continuum analysis

With the high-resolution data shown in Figure 2.2, we could reveal the binary nature of the HBC 494 system. Each of the components in HBC 494 is surrounded by continuum emission, most likely associated with circumstellar disks.

We performed a 2D Gaussian fitting with the *imfit* tool of CASA in order to characterize the newly resolved components. The projected separation between the two sources is $0.18''$ (75 au). We name each component with the usual convention, i.e. “N” and “S” components, referring to the northern and the southern source, respectively. We assume the northern component to be the primary as it is five times brighter than the southern (secondary) disk. Both individual disks are resolved according to our Gaussian fit. For the primary component, we find a major axis FWHM of 84.00 ± 1.82 mas and a minor axis of 66.94 ± 1.50 mas ($34.8 \pm 0.7 \times 27.8 \pm 0.6$ au), with a position angle of 70.01 ± 4.46 deg (values deconvolved from the beam). For the secondary, the major axis FWHM is 64.60 ± 2.49 mas and the minor axis FWHM is 45.96 ± 1.89 mas ($26.7 \pm 1.0 \times 19.9 \pm 0.8$ au), and the position angle is 65.38 ± 5.32 deg. The integrated fluxes for “N” and “S” are 105.17 ± 1.89 mJy and 21.06 ± 0.63 mJy, respectively. The peak fluxes are 22.96 ± 0.35 mJy/beam and 8.71 ± 0.21 mJy/beam for the primary and secondary sources, respectively. The rms is

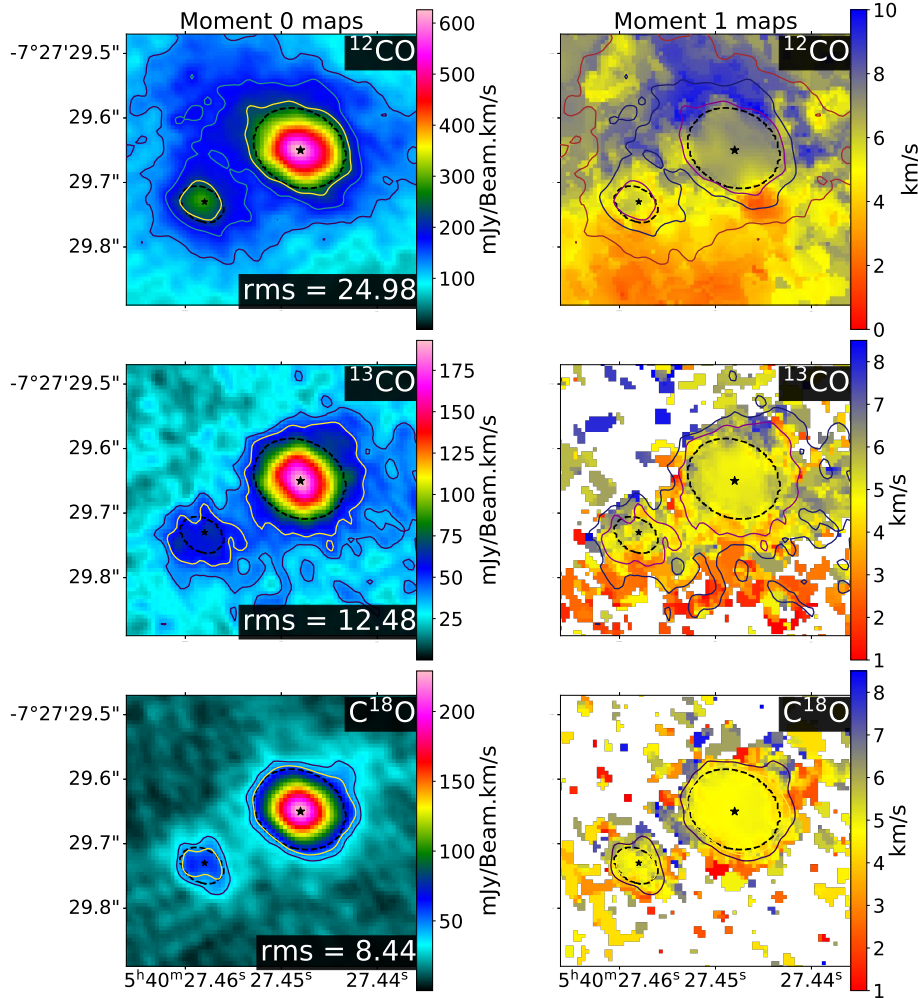


Figure 2.1: Small-scale moment maps for the analyzed CO isotopologues, ^{12}CO (top), ^{13}CO (middle) and C^{18}O (bottom), without subtraction of the continuum. The black stars mark the peak flux positions of the continuum disks. The dashed black contours correspond to $100\times\text{rms}$ from the continuum emission ($100\times 34\mu\text{Jy/beam}$). Left: Moment 0 maps for each mentioned molecular line. The rms values at the bottom of each panel are in units (mJy/beam)(km/s). The ^{12}CO moment 0 map (top-left) has contour levels of 5, 7, and $9\times\text{rms}$ showed at the bottom of the panel. ^{13}CO and C^{18}O moment 0 maps (middle and bottom - left) have contour levels of 3 and $4\times\text{rms}$ showed at the bottom of each panel. Right: Moment 1 maps for each mentioned molecular lines. The contours are the same as each left panel respectively. The maps include only pixels above 3 times the rms measured from the set of channels used for each molecular line (-6 km/s to 18 km/s for ^{12}CO and 0 km/s to 11 km/s for ^{13}CO and C^{18}O).

$\sim 0.034\text{ mJy/beam}$, as observed in a circular region with a radius of 225 mas without emission. The inclinations are calculated using the aspect ratios of the disks. These are assumed as projected circular disks when face-on, thus elliptical when inclined:

$$i = \arccos\left(\frac{b}{a}\right),$$

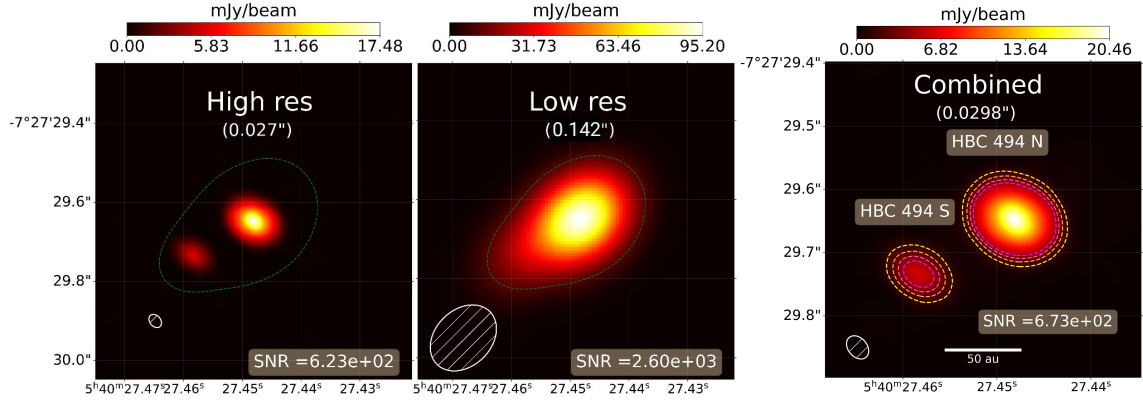


Figure 2.2: ALMA observations at 1.3 mm of the HBC 494 system. The images reveal the binary nature of HBC 494 with two components surrounded by continuum emission associated with circumstellar dust. The respective signal-to-noise ratios of each image are shown in each panel. We show the resulting images from the long baseline observation with a resolution of $0.027''$ (*left*), the short baseline data at $0.142''$ resolution (*middle*), and the combination of the two observations with $0.0298''$ (*right*). Dashed green lines in the left and middle images represent a 3-sigma contour associated with the lower-resolution continuum image. The combined image has a beam size of $\sim 41 \times 30$ mas, shown in the lower-left corner of the image. Its contours correspond, from the yellow (more external) to the pink dashed lines, to 10, 40, 70, and 100 times the rms value, respectively. The rms is ~ 0.034 mJy/beam.

where “b” and “a” are the semi-minor and semi-major axes, respectively. It resulted in 37.16 ± 2.36 degrees inclination for HBC 494 N and 44.65 ± 3.27 for HBC 494 S. At 30 mas resolution, no substructures were detected (see the radial profiles in Figure 2.3).

A large fraction of the mm-sized grains in protoplanetary disks resides in the midplane. They are usually optically thin to their own radiation. Thus, assuming standard disks, we can use the observed fluxes to estimate the dust masses of HBC 494 N and S. For that, we use the following formula (as in Beckwith et al., 1990; Andrews & Williams, 2005; Cieza et al., 2018):

$$M_{\text{dust}} = \frac{F_{\nu} d^2}{k_{\nu} B_{\nu}(T_{\text{dust}})}, \quad (2.1)$$

where F_{ν} is the observed flux, d is the distance to the source, B_{ν} is the Planck function and κ_{ν} is the dust opacity. Adopting the distance of 414 pc, isothermal dust temperature ($T_{\text{dust}} = 20$ K) and dust opacity assuming a $M_{\text{gas}}/M_{\text{dust}}$ fraction of 100, ($\kappa_{\nu} = 10 (\nu/10^{12}\text{Hz}) \text{ cm}^2 \text{ g}^{-1}$; Beckwith et al. 1990) we get dust masses of $1.43 M_{\text{Jup}}$ (HBC 494 N) and $0.29 M_{\text{Jup}}$ (HBC 494 S). Following the standard gas-to-dust mass ratio of 100, we report disk gas masses estimations of $143.46 M_{\text{Jup}}$ for HBC 494 N, and $28.68 M_{\text{Jup}}$ for HBC 494 S. The physical parameters based on the CASA analysis are listed in Table 2.2.

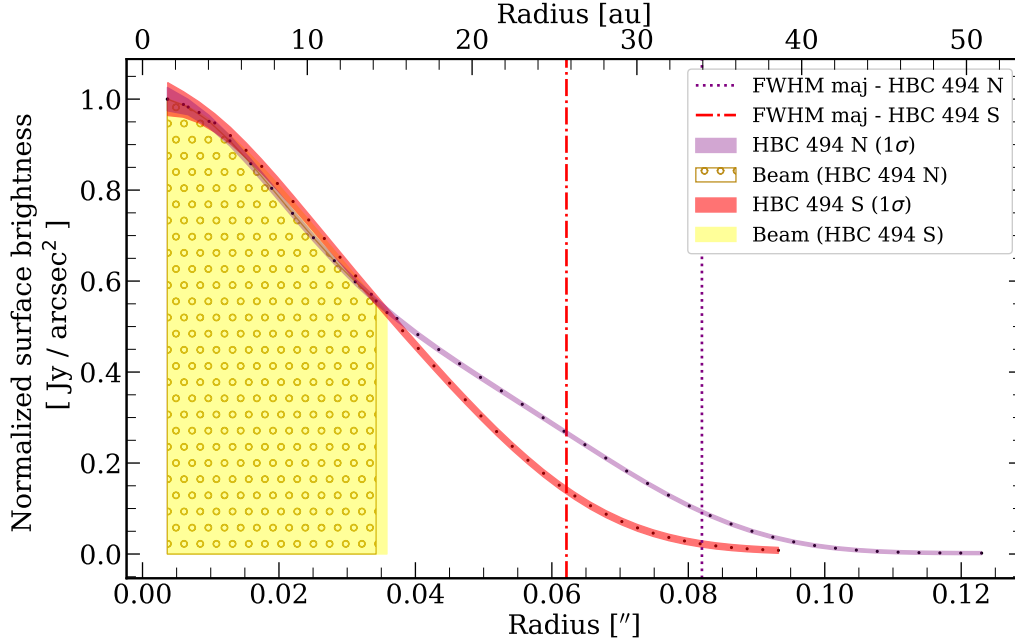


Figure 2.3: Radial brightness profile of HBC 494 N and HBC 494 S. The surface brightness (dots), measured in apertures ranging from the beam’s major axis to 3 times the semi-major axis FWHM of each continuum disk, were normalized to the peak fluxes. The shaded regions indicate 1σ error measured in each aperture. The dashed lines correspond to the ALMA imfit FWHM of each disk.

2.3.2 Line analysis

The next two subsections describe the large and small-scale structure analyses. The large scale, using the extent of 8000 au, shows the results of outflows and envelopes. At such a scale, there is not enough resolution to display both disks’ dynamics and their possible interactions. The small scale (150 au) fulfills this role, and thus, both gas scenarios must be taken into account.

Large-scale structures (8000 au)

The channel maps (Figures 2.4, 2.13 and 2.14) show southern and northern ^{12}CO wide-angle arcs ($\sim 150^\circ$) and no clear signal of large structures from the other molecular lines. This bipolar outflow was previously described in Ruíz-Rodríguez et al. (2017). The wide angular structure shows an outflow morphology expected for Class I disks (Arce & Sargent, 2006). In our observations, the southern and northern arcs are defined by the velocity ranges of $[-6 \text{ km/s to } 1 \text{ km/s}]$ and $[5 \text{ km/s to } 18 \text{ km/s}]$, respectively. The moment 0 and 1 ^{12}CO arcs are shown in Figure 2.5. However, it is noticeable that the northern arc (redshifted emission) dominates the displayed velocities. The lack of signal in the southern arc can be explained by lower molecular density, or due to intracloud absorption. Figure 2.6 shows

Table 2.2: ALMA imfit analysis results and physical parameters inferred from the HBC 494 continuum disks.

	HBC 494 N	HBC 494 S
Flux density (mJy)	105.2 ± 1.9	21.1 ± 0.6
Peak flux (mJy / beam)	23.0 ± 0.4	8.7 ± 0.2
Major axis (mas)	84.0 ± 1.8	64.6 ± 2.5
Minor axis (mas)	66.9 ± 1.5	46.0 ± 1.9
Major axis (au)	34.8 ± 0.7	26.7 ± 1.0
Minor axis (au)	27.8 ± 0.6	19.9 ± 0.8
Position angle (deg)	70.0 ± 4.5	65.4 ± 5.3
Beam major axis (mas)	41.2	41.2
Beam minor axis (mas)	29.8	29.8
Beam Position angle (deg)	40.6	40.6
Beam area (sr)	$3.3\text{e-}14$	$3.3\text{e-}14$
rms (μJy / beam)	34.0	34.0
Dust mass (M_{Jup})	1.4	0.3
Gas mass (M_{Jup})	143.5	28.7
Inclination (deg)	37.2 ± 2.4	44.7 ± 3.3
FWHM Radius (au)	34.8 ± 0.7	26.7 ± 1.0

the three molecular lines' concentration and dynamics (moment 0 and 1 maps), as well as the spectral profile measured within the dashed regions.

The ^{13}CO emission traces the rotating, infalling, and expanding envelope surrounding the system, showing a small deviation from the ^{12}CO outflowing arcs' rotation axis. The blue-shifted emission concentrates around 3 km/s, while the red-shifted emission is around 5 km/s. It is noticeable that the ^{13}CO emission has a rotation axis almost perpendicular to the ^{12}CO outflows axis, ensuring that the physical processes behind the two are different. The spectral ^{13}CO also shows a dip around 4 km/s, but this may not trace an absorption but a lack of signal due to the analyzed uv-coverage or cloud contamination.

The C^{18}O emission, however, is faint and hardly distinguishable from the surrounding gas in moment 0 maps. It has also the lowest abundance of the three analyzed isotopologues, being a good tracer of the higher gas densities in the innermost regions of the cloud. Its velocity maps show that a faint blueshifted motion was detected around 3 km/s, very weak when compared to the redshifted emission detected principally around 5 km/s. Due to the higher concentration of gas in the northern part, it is reasonable that we observed a weak gas counterpart in the southern region. At large-scale, our results are comparable with the ones presented in (Ruíz-Rodríguez et al., 2017). Furthermore, a lower limit of the envelope material of $\sim 600 \text{ Jy.km/s}$ towards HBC 494 could be traced using Total Power (TP), ALMA compact array (ACA), and the main array ALMA observations with C^{18}O data in the range of $4.3 \pm 0.5 \text{ km s}^{-1}$ (Ruíz-Rodríguez private communication).

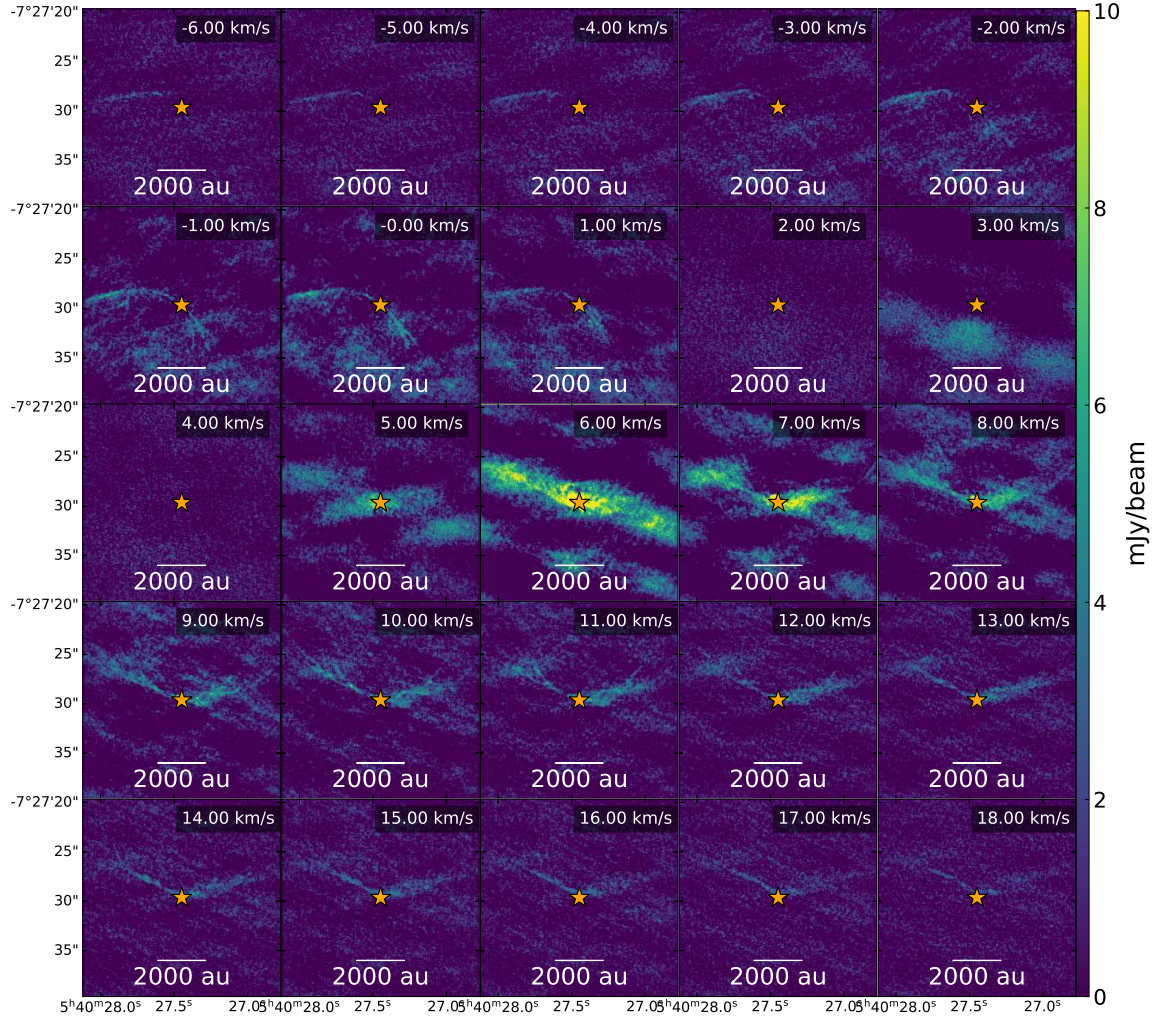


Figure 2.4: ^{12}CO channel maps of the HBC 494 system. The star in the center marks the position of the continuum disks. The southern arc is more evident between the velocities -6 km/s to 1 km/s, while the northern is more easily seen between 7 km/s and 18 km/s.

Small scale structures (150 au resolution)

We started by removing the continuum contribution from all molecular lines observed (^{12}CO , ^{13}CO , C^{18}O). We already expected that ^{12}CO would trace the gas in larger scales due to its optical depth and, thus, could blend with smaller gas signatures. To avoid cloud contamination during the creation of ^{12}CO small-scale moment maps, we removed the channels that were more affected. We considered velocities in the range of -6 km/s to 1 km/s, and from 5 km/s to 18 km/s, as similarly done for the different large-scale arcs described in the previous subsection.

Following, CO channel maps and moment 0 and 1 maps were produced to explore potential hints of interaction between the stars and the two circumstellar disks. In particular,

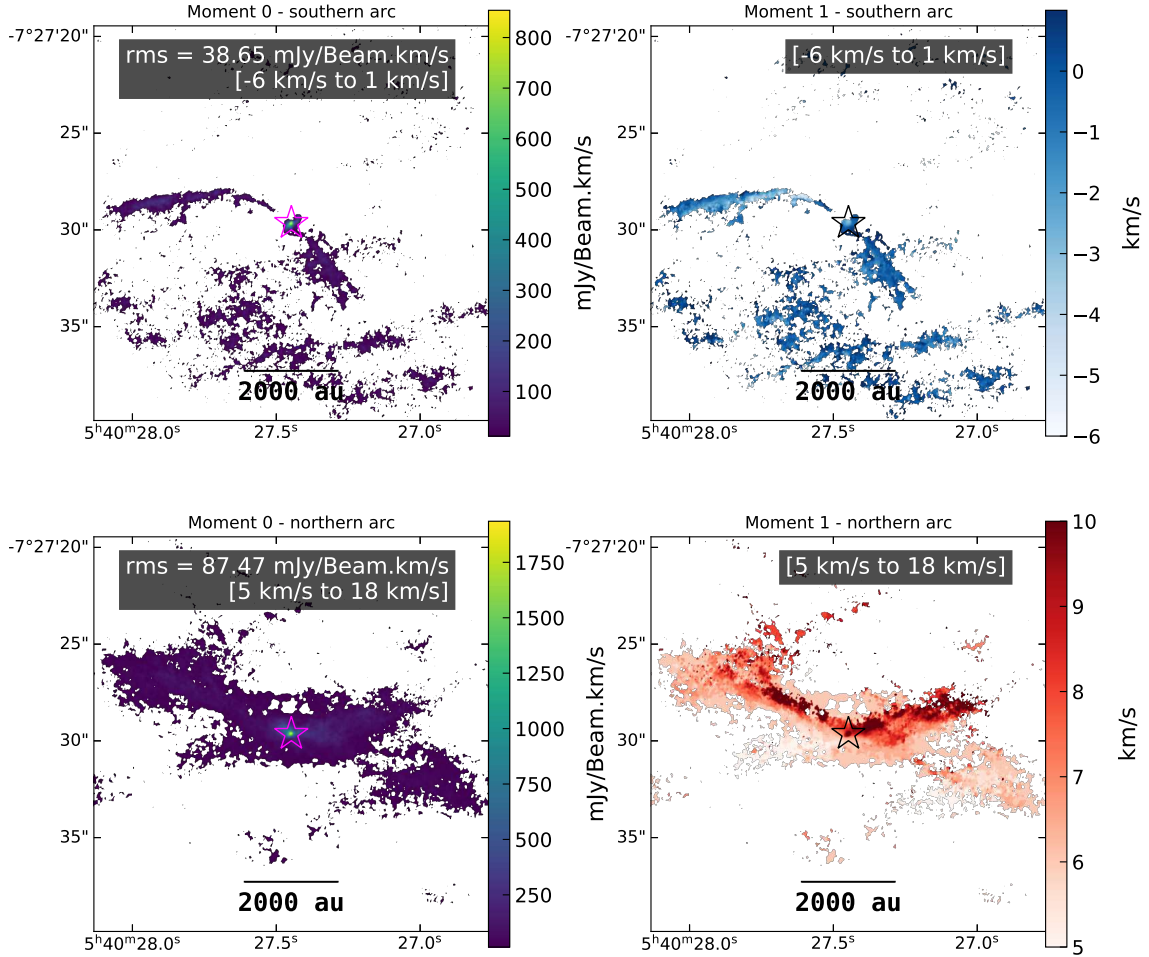


Figure 2.5: Large-scale ^{12}CO moment maps split in each one of the bipolar outflow structures. The left column corresponds to moment 0 maps, and the right column to moment 1 maps. The plots in the same row refer to the same structure, which is the southern arc (*upper row*), and the northern arc (*bottom row*). The position of the HBC 494 N is marked with a star. The maps include only pixels above 2 times the rms measured from the set of channels shown at the top of each panel.

we looked for disk substructures and perturbed rotation patterns. The moment maps can indeed provide valuable information about the binary orbit and the disks' geometry. However, by looking at the molecular lines in this scale (see the moment maps in Figure 2.7, left and middle columns), we could not clearly detect the presence of the disks or their rotational signatures. We can only notice that the ^{12}CO and ^{13}CO moment 0 maps show an interesting pattern, where less gas emission is found where the continuum disks are. Additionally, the area within the continuum disks highlights regions similar to cavities or “holes” (Figure 2.7, left column, upper and middle row). Interestingly, [Ruíz-Rodríguez et al. \(2022\)](#) observed similar features from the same molecular lines, in addition to HCO^+ , for another FUor system, V883 Ori. The work also showed that the origin of cavities and

ring emission around disks can be interpreted in two ways, one based on gas removal and the other on optical depth effects.

If the signal traces the lack of gas surrounding the disks, the leading mechanism may be slow-moving outflows. The central regions of young continuum disks are expected to be constantly carved by the influence of magneto-hydrodynamical jets (Frank et al., 2014). In addition, it is also expected that the lower emission observed comes from the chemical destruction by high-energy radiation (more active disks will create bigger cavities). By looking at the size of the gaps, we can observe that HBC 494 S exerts a smaller influence on the gas than HBC 494 N and, thus, HBC 494 N is the more active disk in the system if this hypothesis is correct.

Another interpretation of the negatives in our gas maps is that this is a spurious result of continuum subtraction. Usually, the continuum emission is inferred from channels devoid of gas line emission. The usual procedure does not consider the line emission where these channels overlap. Suppose the emission lines are optically thick above the continuum. In that case, the foreground gas can significantly absorb the photons coming from the underlying continuum, which may lead to a continuum overestimation. Consequently, in such cases, the continuum may be over-subtracted, causing the “hole” feature that is stronger where the line peaks (see e.g., Boehler et al., 2017; Weaver et al., 2018).

2.4 Discussion

2.4.1 Multiplicity and triggering mechanisms

Besides HBC 494, there are ~ 25 known FUor objects within 1 kpc (Audard et al., 2014). As previously commented, many triggering mechanisms can cause episodic accretion events. From this sample, only HBC 494 and a few other FUor systems are known binaries (e.g., FU Orionis, L1551 IRS, RNO 1B/C, AR 6A/B; Pueyo et al., 2012b and references therein).

Given the high occurrence rate of stellar binaries harboring disks, the lack of detection of multiple YSO systems remains a case of investigation. Additionally, young disks evolve in crowded star-forming regions, enhancing the hypothesis that the outbursts of Class 0/I disks may affect other disks, driving episodic accretion events. Also, surveys and studies using ALMA and NIR data for Class I-III disks, show that there is a lack of detection when only visual multiple systems (separations of 20-4800 au) are considered (e.g., Zurlo et al., 2020a, 2021). When all the possible separations are taken into account, the multiplicity frequencies considerably increase. For Taurus, for example, it goes up to 70% when spectroscopic binaries are included (Kraus et al., 2011). In the case of Orion, 30% of the systems are multiple with separations between 20 and, 10000 au (Tobin et al., 2022). The latter study also noticed that the separations decrease with time (when comparing Class 0, I, and flat-spectrum disks) and that the multiplicity frequency in Class 0 is higher than in the later evolutionary stages. Therefore, multiple eruptive young systems must be common, and more detectable within evolutionary time. They probably are not frequently detected due to the short time duration of enhanced accretion events in comparison with the lifetime of disks in class 0/I stages (see Audard et al. 2014 for a FUors review). Still, it is not clear

if disks belonging to close-separation systems are more susceptible to eruptive events than isolated ones.

For each HBC 494 disk, no clue of trigger mechanisms was found, since the gas and continuum data did not reveal clear spiral or clumpy features indicating a case of infall or GI (see e.g., [Zhu et al., 2012](#); [Kratter & Lodato, 2016](#)). Looking at the dust continuum (Figure 2.2), CO isotopologues moment maps (Figure 2.7), and the scattered ^{12}CO emission (Figure 12 of [Ruíz-Rodríguez et al. 2017](#)), the hypothesis of stellar flybys is also not encouraged since no trace of perturbation was detected ([Cuello et al. 2020, 2023](#)). Moreover, dynamical data (small-scale moment 1 maps) also can provide clues for the triggering mechanism ([Vorobyov et al., 2021](#)). However, it requires clear detection of quasi-keplerian rotation, which was not observed.

In the case of binaries, the first component to ignite the FUor outbursts can quickly trigger the secondary one by inducing perturbations and mutual gravitational interactions ([Bonnell & Bastien, 1992](#); [Reipurth & Aspin, 2004](#); [Vorobyov et al., 2021](#); [Borchert et al., 2022a,c](#)). Therefore, we can assume that all the disks in FUor multiple systems like HBC 494 might have undergone successive enhanced eruptive stages, despite the differences in mass and radius between each component. However, it is not clear how the outbursts in HBC 494 N and HBC 494 S affect each other since the moment maps do not show the connection between disks. Although, on larger scales, we detected the difference in the amount of gas mass detected in the northern regions compared to the southern. This scenario may be described if the more massive disk (i.e. HBC 494 N) has a higher contribution to the outbursts and winds.

With astrometric data, the eccentricity of orbits can be determined. If both disks are still accreting gas from the environment, it is expected that quasi-circular orbits trigger enhanced accretion every few binary periods. Eccentric orbits, on the other hand, can induce eruptive events in every orbit, preferentially when the binaries reach the pericentre (see e.g. [Dunhill et al., 2015](#); [Lai & Muñoz, 2022](#)). Observational evidence of circumbinary disks in different YSO stages was found (see e.g. [Dutrey et al., 1994](#); [Mathieu et al., 1997](#); [Tobin et al., 2016a](#); [Maureira et al., 2020](#)) and are seen as a common counterpart of young binaries in formation. However, no HBC 494 circumbinary gas disk was observed due to cloud contamination and optical depth effects.

2.4.2 Disk sizes and masses

FU Orionis, the precursor of the classification FUor, is also a binary system. HBC 494 system, however, has smaller disks separation compared to the 210 au between FU Orionis north and south components ([Pérez et al., 2020](#)). FU Orionis components have similar sizes and masses between their disks, contrary to the HBC 494 components. We can argue that, due to HBC 494 being a close-packed system with substantially different masses between their components, a scenario of radius truncation can be tested. However, the FU Orionis disks are exceptional compared to other FUors, which are generally more massive and larger. Nevertheless, it is important to check if HBC 494 follows the trend which shows that FUor objects are more massive than class 0/I disks and that disks from multiple systems

are smaller compared to those from non-multiple systems (Cieza et al., 2018; Hales et al., 2020; Tobin et al., 2020; Zurlo et al., 2020b). First, we will describe our results regarding masses and radius. Then, we will compare HBC 494 disks to FUors and Orion YSOs in the literature.

We assumed dust masses (assuming the gas-to-dust ratio of 100) inferred by optically thin approximation (described in section 2.3.1). However, it is worth mentioning that the optically thin analysis can not take into account the innermost regions of the disk (optically thick). This may lead to an underestimation of the dust masses. Also, an underlying miscalculated dust grain temperature can alter the results, overestimating the masses if the dust is warmer than expected. The chosen assumptions of temperatures (fixed 20 K for dust grains) and opacities for both disks lead to $1.43 M_{\text{Jup}}$ and $0.29 M_{\text{Jup}}$ for HBC 494 N and HBC 494 S, respectively. Based on these results, we can say that the HBC 494 N is comparable to other FUor sources, but HBC 494 S has its dust mass comparable to EXor disks (Cieza et al., 2018). The disk sizes were calculated using the deconvolved Gaussian FWHM/2 radius obtained from 2D Gaussian fits. This methodology was also used for other ALMA datasets (e.g., Hales et al., 2020; Tobin et al., 2020). Therefore, it allows a consistent comparison with other disks. The dust mass vs radius comparison between HBC 494 N and HBC 494 S, a sample of 14 resolved FUors and EXors (extracted from Hales et al., 2020) and Class 0/I systems (Tobin et al., 2020), can be seen in figure 2.8. Here, as previously stated, we notice that HBC 494 disks (black, hexagon symbols), as other eruptive systems (hexagon, square, and triangle symbols), present higher masses than young systems, which are not in the stage of episodic accretion. However, there is no obvious distinction between the disk sizes of individual systems, eruptive or not. A clear difference is seen when we compare the disks from multiple systems (hexagon symbols) and single systems. The latter present bigger sizes as they are not targets for tidal truncation, enhanced radial drift, and more aggressive photoevaporation — processes known to rule close-systems dynamics and evolution (see e.g., Kraus et al., 2012; Harris et al., 2012; Rosotti & Clarke, 2018; Zurlo et al., 2020a, 2021).

2.4.3 Binary formation and alignment

Different scenarios have been proposed to explain the formation of binary systems. The main one for close-separated systems is fragmentation, followed by dynamic interactions (for a review, see Offner et al., 2022).

The fragmentation process consists of partial gravitational collapse from self-gravitating objects. To be successful, many initial physical conditions are relevant as thermal pressure, density, turbulence, and magnetic fields. In addition, the fragmentation can be divided into two main classes: direct/turbulent (e.g., Boss & Bodenheimer, 1979; Bate & Burkert, 1997) and rotational (e.g., Larson, 1972; Bonnell, 1994; Bonnell & Bate, 1994a,b; Burkert et al., 1997).

The direct/turbulent fragmentation from a collapsing core is highly dependent on the initial density distribution. It can form wide-separated multiple YSO systems with uncorrelated angular momentum. Thus, the direct/turbulent fragmentation may lead to preferen-

tially misaligned multiple systems (Bate, 2000; Offner et al., 2016; Bate, 2018; Lee et al., 2019). The rotational fragmentation, instead, is caused by instabilities in rotating disks and leads to preferentially spin-aligned and coplanar systems (Offner et al., 2016; Bate, 2018). Moreover, later dynamical processes such as stellar flybys (Clarke & Pringle, 1993; Nealon et al., 2020; Cuello et al., 2023) and misaligned accretion from the environment (Dullemond et al., 2019; Kuffmeier et al., 2020, 2021) can also induce alignment or misalignment.

The HBC 494 disks have similar inclinations ($\Delta i = 7.5 \pm 4.1$ degrees) and similar PAs ($\Delta PA = 4.6 \pm 7.0$ degrees). The relative orientations of the disks suggest that the system is coplanar. Assuming they are quasi-coplanar, with the same PA, the unprojected separation would be $\sim 0.24''$ (99 au). Therefore, the HBC 494 disks may show a spin-alignment situation, more typical to observed close-separated systems (see, e.g., Tobin et al., 2016b, 2020). Thus, we tentatively suggest that HBC 494 was formed by rotational disk fragmentation rather than direct collapsing. However, more precise observation of the kinematics of the surrounding gas on a small scale (Vorobyov et al., 2021), complemented with orbital information coming from astrometrical measurements, is required to evaluate this hypothesis.

In this context, IRAS 04158+2805 is of interest as Ragusa et al. (2021) reported the detection of two circumstellar disks, similar to HBC 494 in terms of small to moderate misalignment, and an external circumbinary disk. However, in contrast to IRAS 04158+2805, no circumbinary disk was detected in HBC 494. This difference could be explained either by the absorption of the circumbinary disk emission due to cloud contamination, or because HBC 494 had enough time to sufficiently empty the circumbinary mass reservoir. Since most hydrodynamical models of star formation naturally produce young binaries with individual disks and a surrounding circumbinary disk (Bate, 2018, 2019; Kuruwita et al., 2020), it is likely that a circumbinary disk formed at some earlier evolutionary stage of HBC 494. If the circumbinary disk is actually there, but remains undetected, the supply of material could extend the disk lifetime of the circumstellar disks in HBC 494. Deeper multi-wavelength observations would provide more information, enabling us to solve this binary riddle.

2.5 Conclusions

In this work, we presented high-resolution 1.3 mm observations of HBC 494 with ALMA. The unprecedented angular resolution in this source ($0.027''$), reveals that HBC 494 is a binary that can be resolved into two disks, HBC 494 N and HBC 494 S. The disks have a projected separation of ~ 75 au. We derived sizes, orientations, inclinations, and dust masses for both components. Both objects appear to be in a quasi-coplanar configuration and with their sizes halted by dynamical evolution, besides preserving high masses, common to FUors and EXors than typical (not eruptive) Class 0/I disks. Comparing the two sources, we noticed that HBC 494 N is ~ 5 times brighter/more massive and ~ 2 times bigger than HBC 494 S.

The gas kinematics was analyzed at two different spatial scales: 8000 au and 150 au.

At large-scale, we have obtained similar results as those presented in [Ruíz-Rodríguez et al. \(2017\)](#), revealing the wide outflow arcs (traced by the ^{12}CO) and the infalling envelopes (^{13}CO and C^{18}O). At the small-scale, we detected depleted gas emission (cavities) for both disks (^{12}CO and ^{13}CO , moment 0). They were probably formed by slow outflows and jets coming from the disks along the line of sight or by optical depth effects and over-subtraction of the continuum emission. The dynamics of both disks in such scales were masked principally by cloud contamination.

Further observations with similar resolution but of optically thinner molecular lines may lead to the characterization of the dynamical interaction of the two components. For example, the identification of rotational signatures from the disks can be used to identify the dynamical masses of their central stars. With this information, we could also constrain truncation radii. Additionally, observations of small-scale gas structures, allied to astrometric measurements, can be used to constrain the possible formation scenarios.

We conclude that the HBC 494 system constitutes a test bed for eruptive binary-disk interactions and the connection between stellar multiplicity and accretion/luminosity processes (such as outbursts). Also, it provides a statistics enhancement about the rarely observed systems FUors and Exors.

2.6 Appendix

2.6.1 Effects of continuum over-subtraction

To evaluate the effects of continuum over-subtraction, we generated spatial profiles for each disk using ^{12}CO moment 0 maps at small scales before and after continuum subtraction. We created cuts that crossed the semi-major axis of each disk (see red lines in [Figure 2.9](#), top panels) for this purpose. [Figure 2.9](#), top-left panel displays moment 0 maps before continuum removal, while the top-right panel shows the same maps after this process. The comparison between these effects is better visualized in the bottom panels, where continuum emission (magenta diamonds/lines) has a similar shape as ^{12}CO before continuum subtraction (orange crosses/lines), but shifted in flux, for both disks. The spatial profile subtractions are displayed by black lines. However, they display higher fluxes when compared to the spatial profiles produced after continuum subtraction (blue-filled circles/lines). Additionally, the continuum was overestimated by foreground optical depth molecular lines that absorbed continuum emission and then propagated to the *uvcontsub* CASA task. The "holes" or cavities seen in the top-right panel could potentially be diminished by manually adding back some of the lost line signal, but this would only create a fake signal at the level of noise. Thus, optically thinner lines must be used to obtain the real signal of disks in moment 0 and 1 maps.

2.6.2 ^{12}CO , ^{13}CO and C^{18}O channel maps with contours and the effect of cloud contamination

This appendix presents the ^{12}CO , ^{13}CO , and C^{18}O channel maps with contour plots (see Figures 2.10 and 2.11). To visualize the signals and corresponding flux values using a color bar, we also provide versions of the same channel maps without contours (see Figures 2.4 and 2.13).

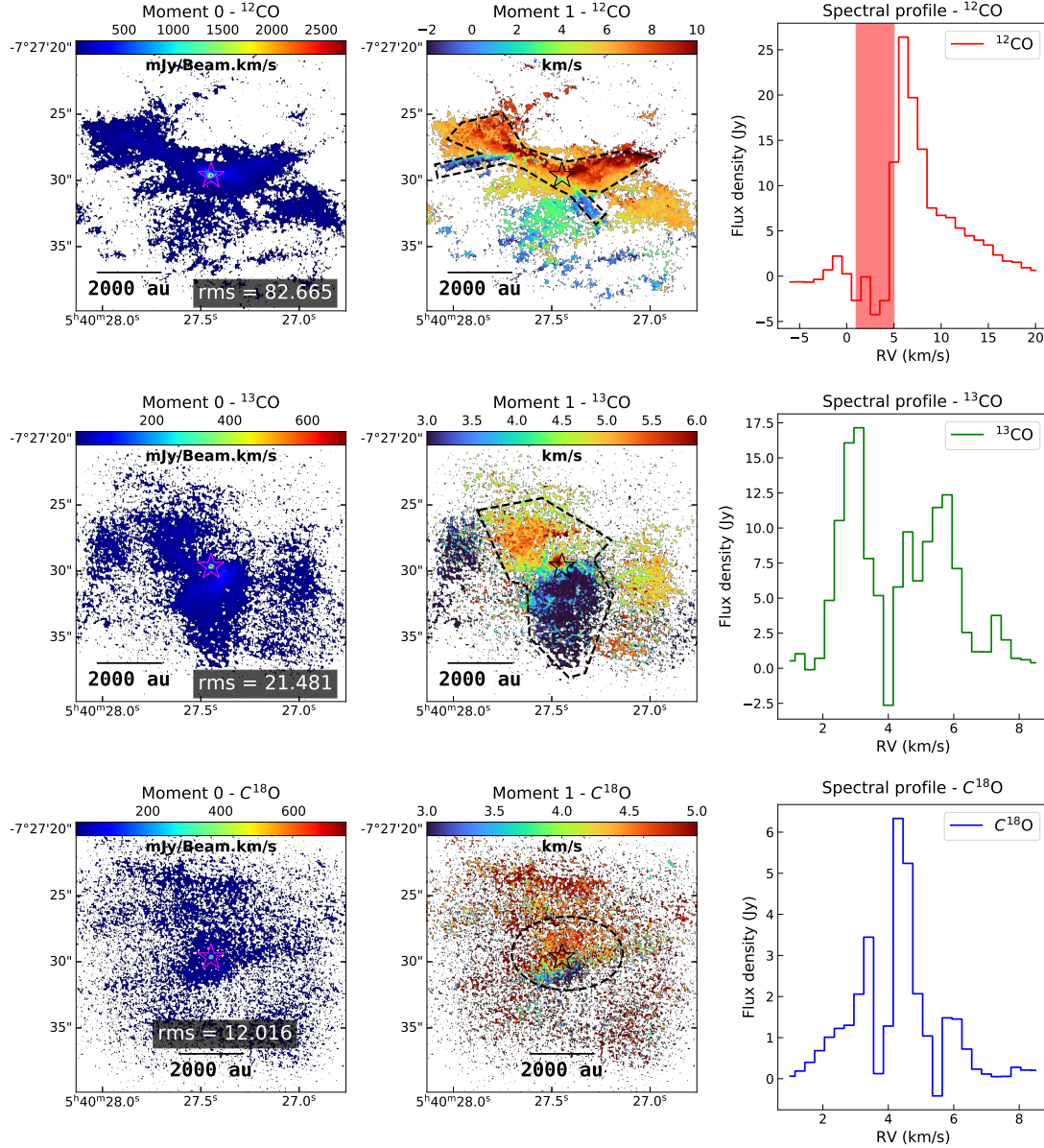
Figure 2.10 shows the 3-rms significant southern arcs (velocity channels from -6 km/s to 1 km/s) and northern arcs (velocity channels from 5 km/s to 18 km/s). However, cloud contamination affects channels between 2 km/s and 6 km/s. These channels were not used in the creation of large-scale moment maps. Channel 6 km/s shows the most evidence of cloud contamination, with contour plots showing innermost flux values near the disks (marked by the central orange star). It also shows some significant contours on both horizontal extremes, which can be tracers of the filtered signals using only the main array data. The data partially trace features that, due to their large extension, require a combination of the ALMA main and single dish arrays to recover extended flux emission.

In Figure 2.11, the ^{13}CO channel maps are heavily marked by 3-rms black contours, which show the significant gas signal on each channel. Specifically, channels from 2.20 km/s to 6.10 km/s indicate gas infalling clumps near where the disks are located, but also show random/scattered signals far from the disks due to cloud contamination.

The C^{18}O channel maps represented in Figure 2.12 are also heavily marked by 3-rms black contours. Channels from 2.80 km/s to 4.60 km/s indicate gas infalling clumps near where the disks are located, but also show random/scattered signals far from the disks due to cloud contamination. Other channels are affected by cloud contamination or lack a significant signal.

2.6.3 Extra channel maps

The ^{13}CO (large scale), C^{18}O (large scale), ^{12}CO (small scale and with continuum subtracted), ^{13}CO (small scale and with continuum subtracted), and C^{18}O (small scale and with continuum subtracted) channel maps are displayed in Figs. 2.13, 2.14, 2.15, 2.16, and 2.17, respectively.



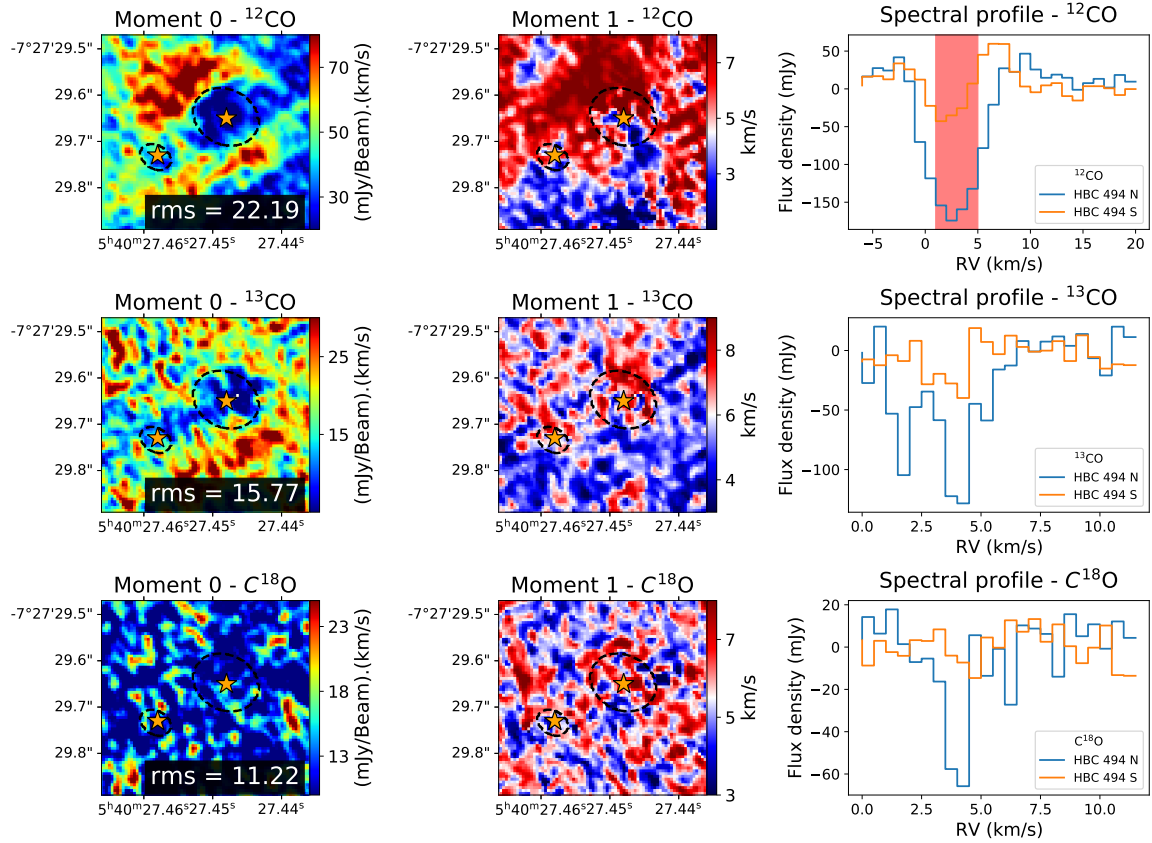


Figure 2.7: Small-scale moment maps for the analyzed CO isotopologues, after subtraction of the continuum, and their spectral profiles. The first column corresponds to moment 0 maps, and the middle one to moment 1 maps. The rms values at the bottom of each panel in the left column are in units (mJy/beam)(km/s). The molecular lines correspond to ^{12}CO (upper row), ^{13}CO (middle row) and C^{18}O (bottom row). The dashed black lines spatially correspond to the contour level equal to 100 times the continuum rms ($100 \times 34 \mu\text{Jy/beam}$), in the continuum combined image (Figure 2.2, right). The orange stars mark the peak flux positions of the continuum disks. The right column represents the spectral profiles measured from velocity maps taken within each disk. The red shaded area in ^{12}CO profile represents the channels we excluded before creating the moment maps lying in the same row (to avoid cloud contamination).

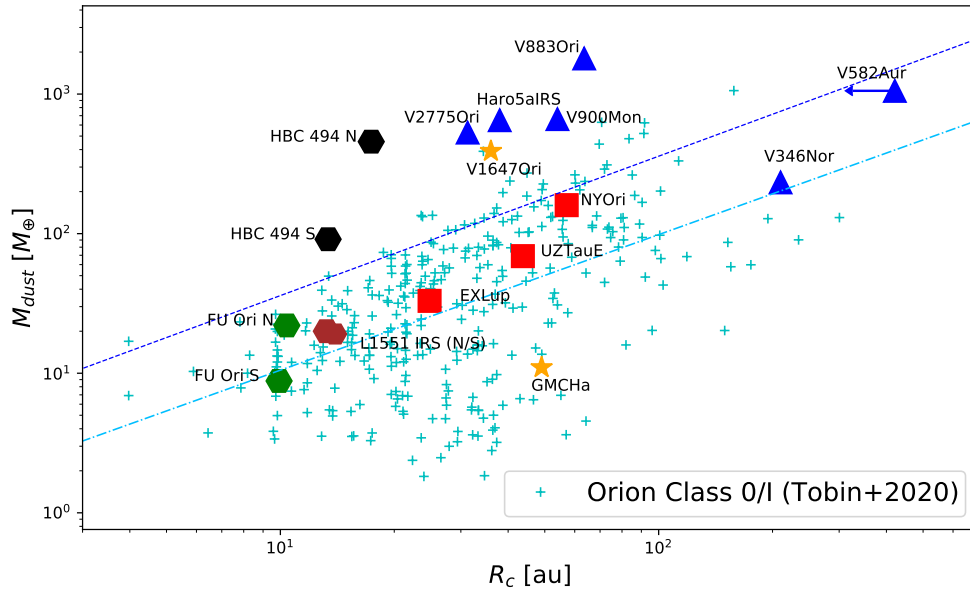


Figure 2.8: Dust disk masses as a function of characteristic radii (FWHM/2) for FUors (blue triangles), EXors (red squares), for double FUor and EXor classification (yellow stars), and Class 0/I objects (cyan crosses), as similarly presented in [Hales et al. \(2020\)](#). The horizontal arrow on V582 Aur denotes the disk radius in an upper limit. The hexagons represent eruptive/multiple systems, with matching colors for disks lying in the same system. The data for HBC 494 disks was generated in this work. The blue dashed line corresponds to the power-fit law to the FU/EXor data (Spearman correlation coefficient: 0.63), and the cyan dash-dotted line, to the Class 0/I data (Spearman correlation coefficient: 0.55). To generate this plot, we obtained data from [Kóspál et al. \(2017\)](#); [Hales et al. \(2018\)](#); [Cieza et al. \(2018\)](#); [Takami et al. \(2019\)](#); [Cruz-Sáenz de Miera et al. \(2019\)](#); [Pérez et al. \(2020\)](#); [Hales et al. \(2020\)](#).

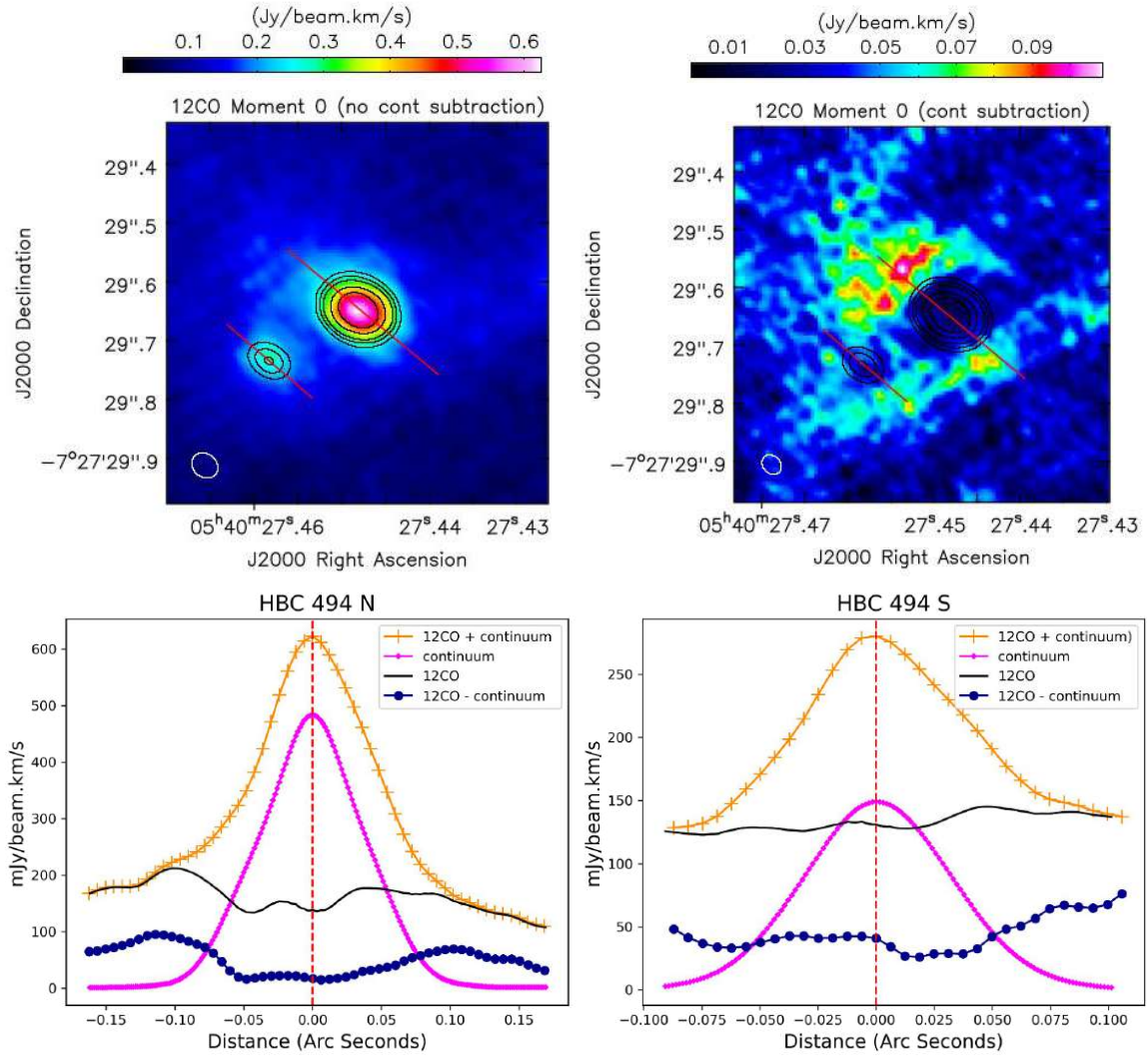


Figure 2.9: The top panels show the ^{12}CO moment 0 maps before (left) and after (right) continuum removal, along with their spatial profiles. The moment 0 contours represent values of 50, 75, 100, 150, and 200 times the rms (~ 0.06 mJy/beam.km/s). The red lines trace the axis used to create spatial profiles, which can be seen in the bottom panels. The bottom left panel shows the spatial profile of the HBC 494 N disk, while the bottom right panel shows that of the HBC 494 S disk. The vertical black dashed lines indicate the center of the disks. The orange crosses/lines represent spatial profiles before the continuum subtraction, created using the red line axis in the top panel, left. The magenta diamonds/lines represent the continuum spatial profile. The black lines represent the subtraction between the $^{12}\text{CO} + \text{continuum}$ and the continuum spatial profiles for each disk. The dark blue filled circles/lines represent spatial profiles after the continuum subtraction, created using the red line axis in the top panel, right.

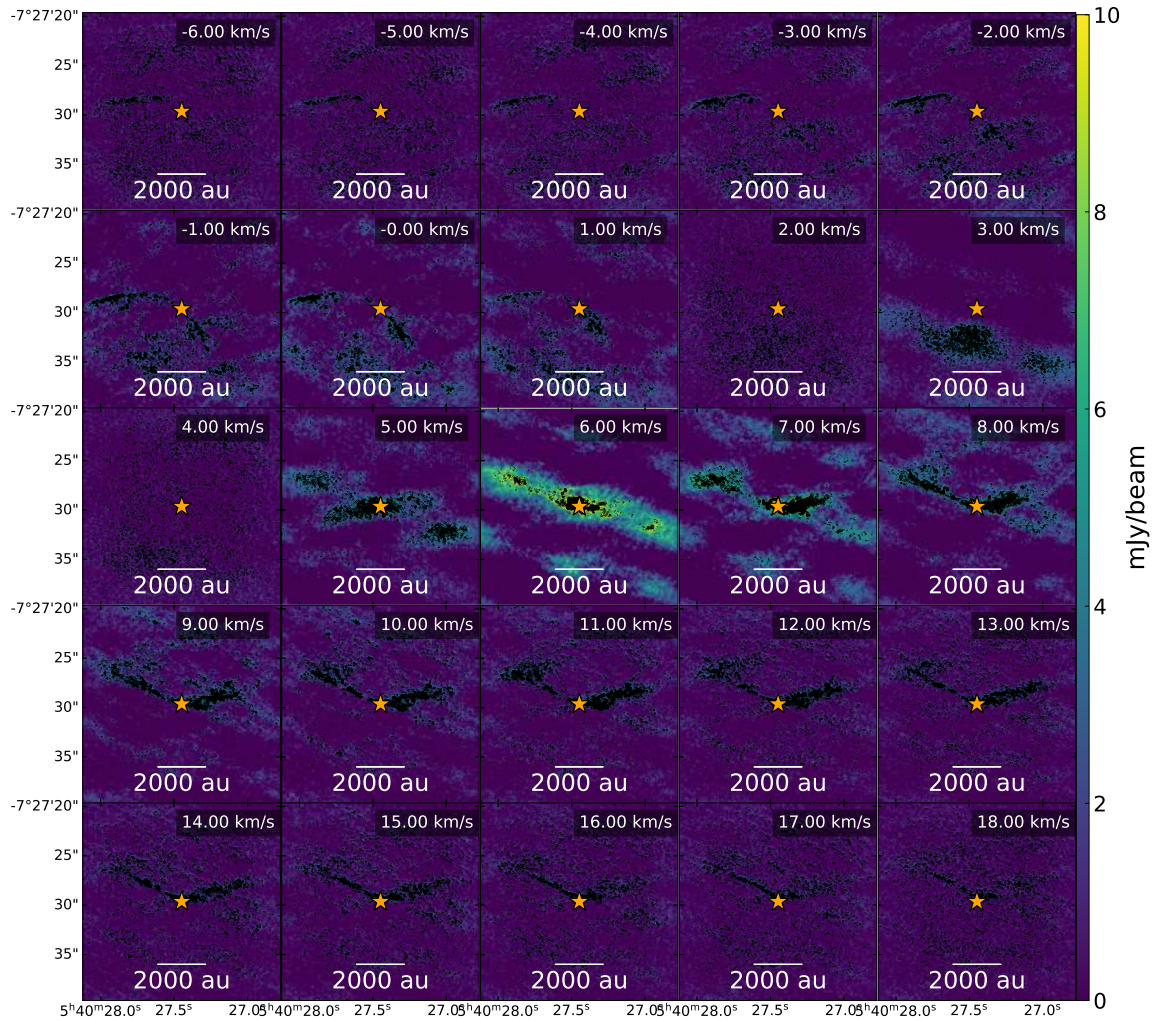


Figure 2.10: ^{12}CO channel maps of HBC 494 system with contours. The contours were displayed in black and they are equivalent to 3 times the rms of every channel. The rms values were calculated using all data in each channel, through the CASA task *imstat*. The peak flux values have reached up to 19 times the rms values. The star in the center marks the position of the continuum disk around HBC 494 N.

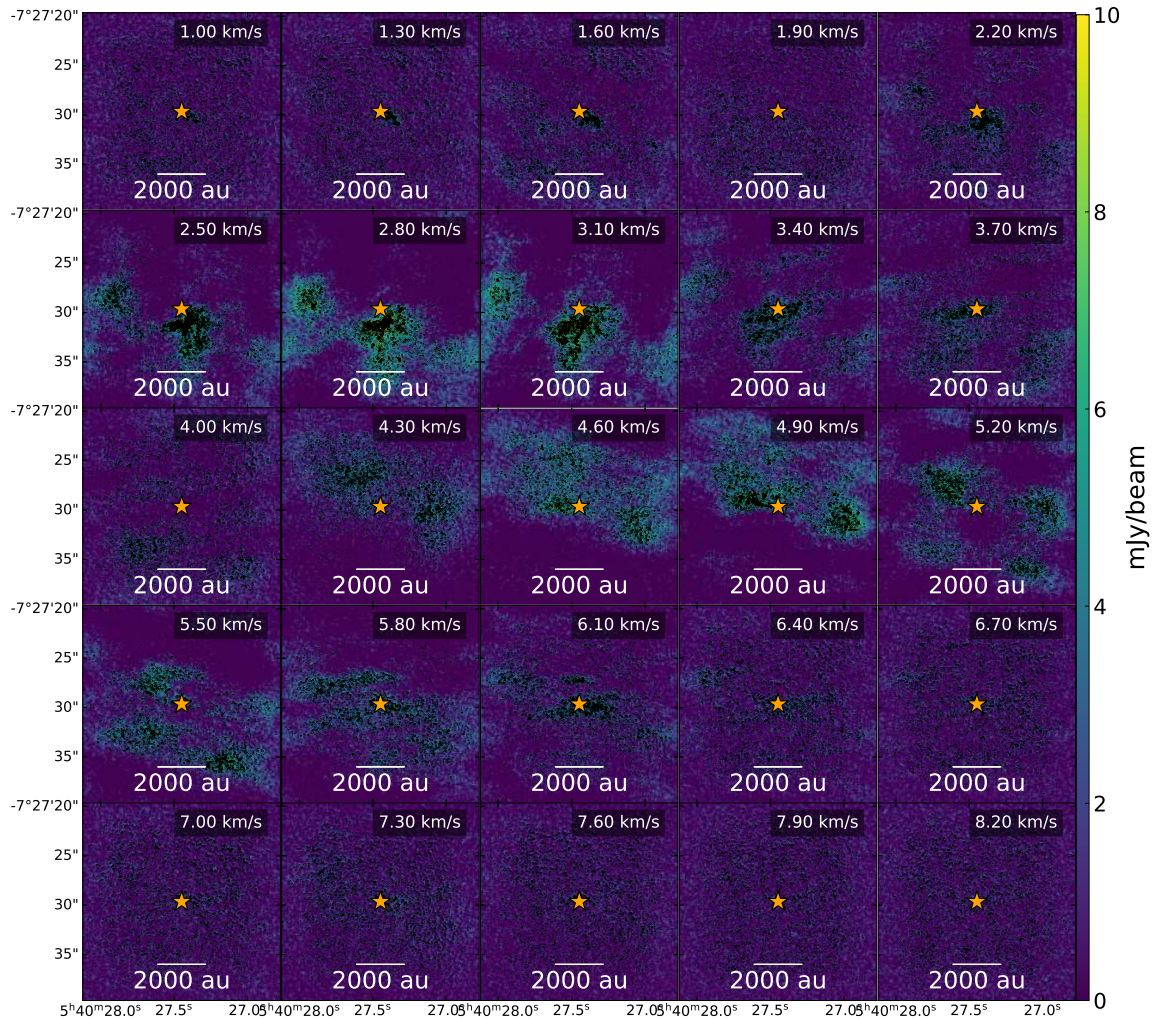


Figure 2.11: ^{13}CO channel maps of HBC 494 system with contours. The contours were displayed in black and they are equivalent to 3 times the rms of every channel. The rms values were calculated using all data in each channel, through the CASA task *imstat*. The peak flux values have reached up to 11 times the rms values. The star in the center marks the position of the continuum disk around HBC 494 N.

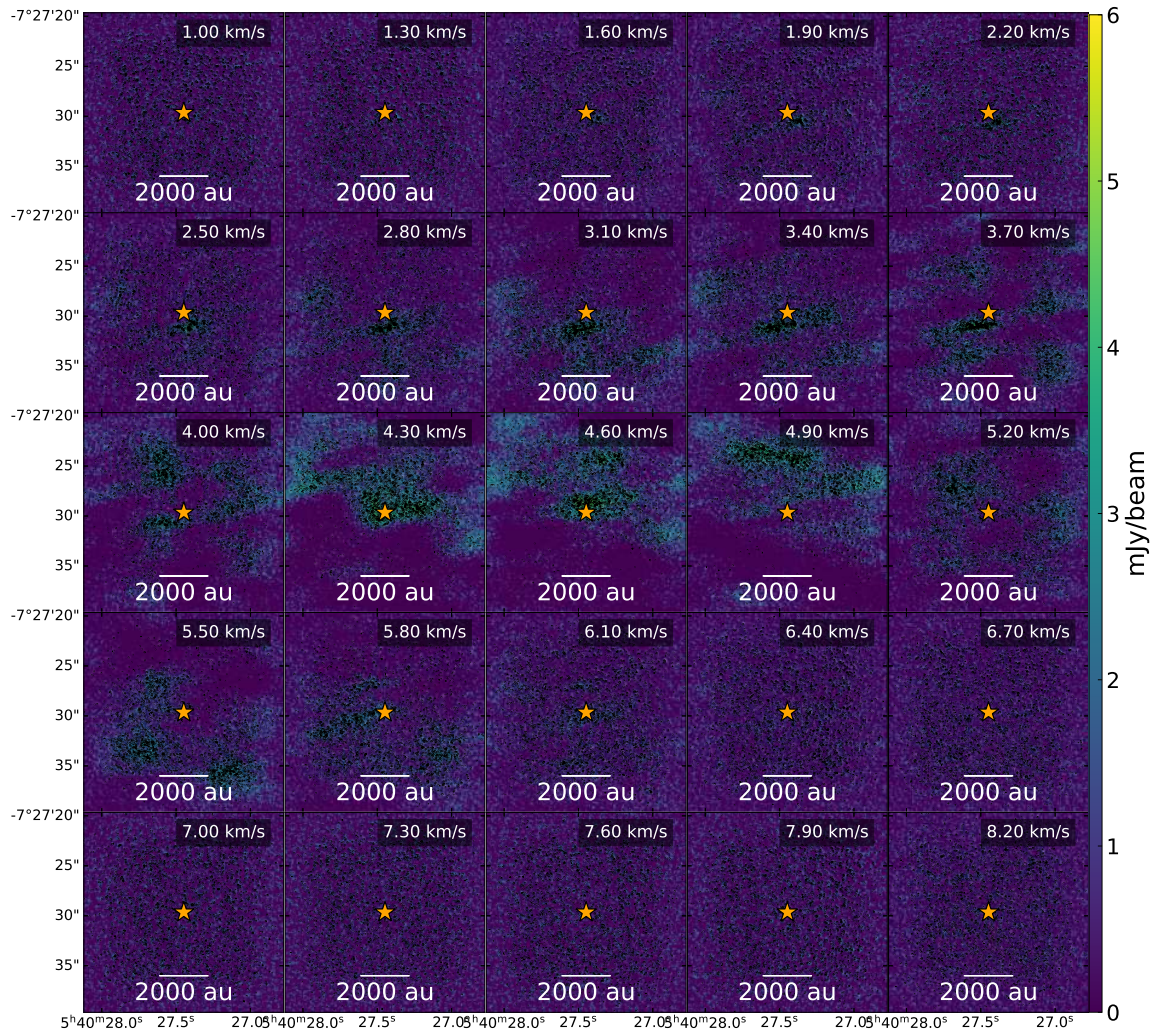


Figure 2.12: $C^{18}O$ channel maps of HBC 494 system with contours. The contours were displayed in black and they are equivalent to 3 times the rms of every channel. The rms values were calculated using all data in each channel, through the CASA task *imstat*. The peak flux values have reached up to 13 times the rms values. The star in the center marks the position of the continuum disk around HBC 494 N.

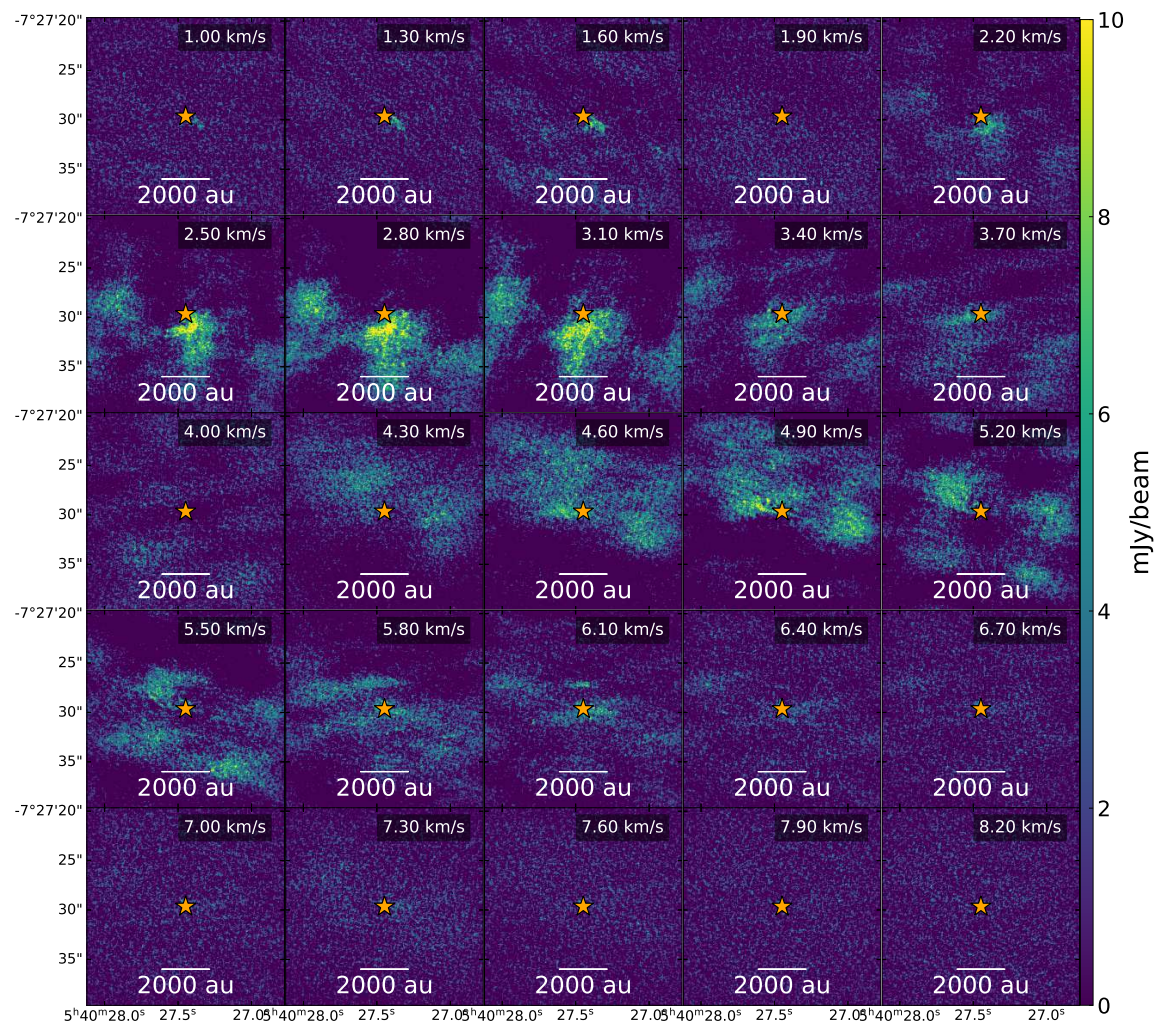


Figure 2.13: ^{13}CO channel maps of HBC 494 system. The star in the center marks the position of the continuum disk around HBC 494 N.

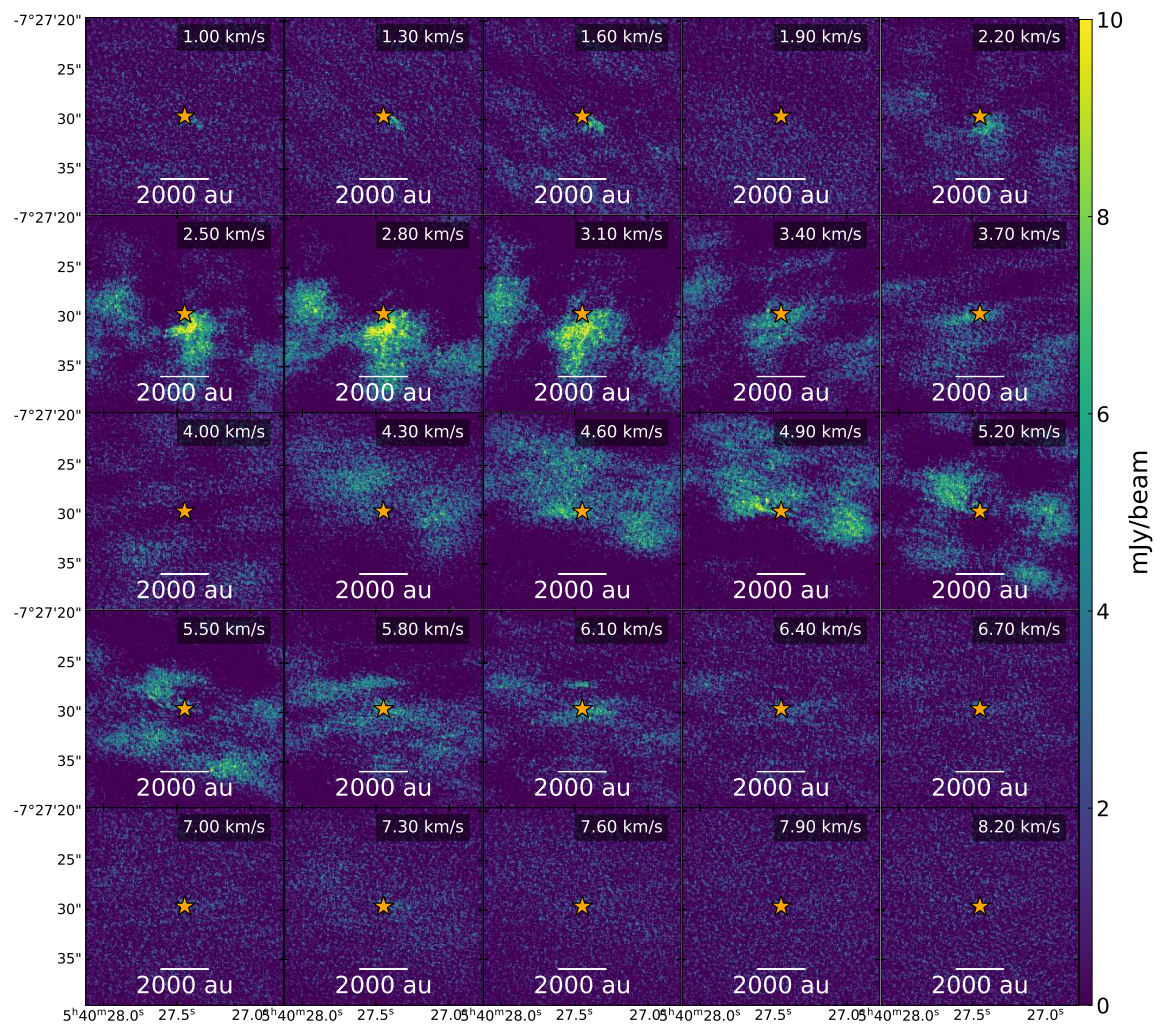


Figure 2.14: $C^{18}O$ channel maps of HBC 494 system.

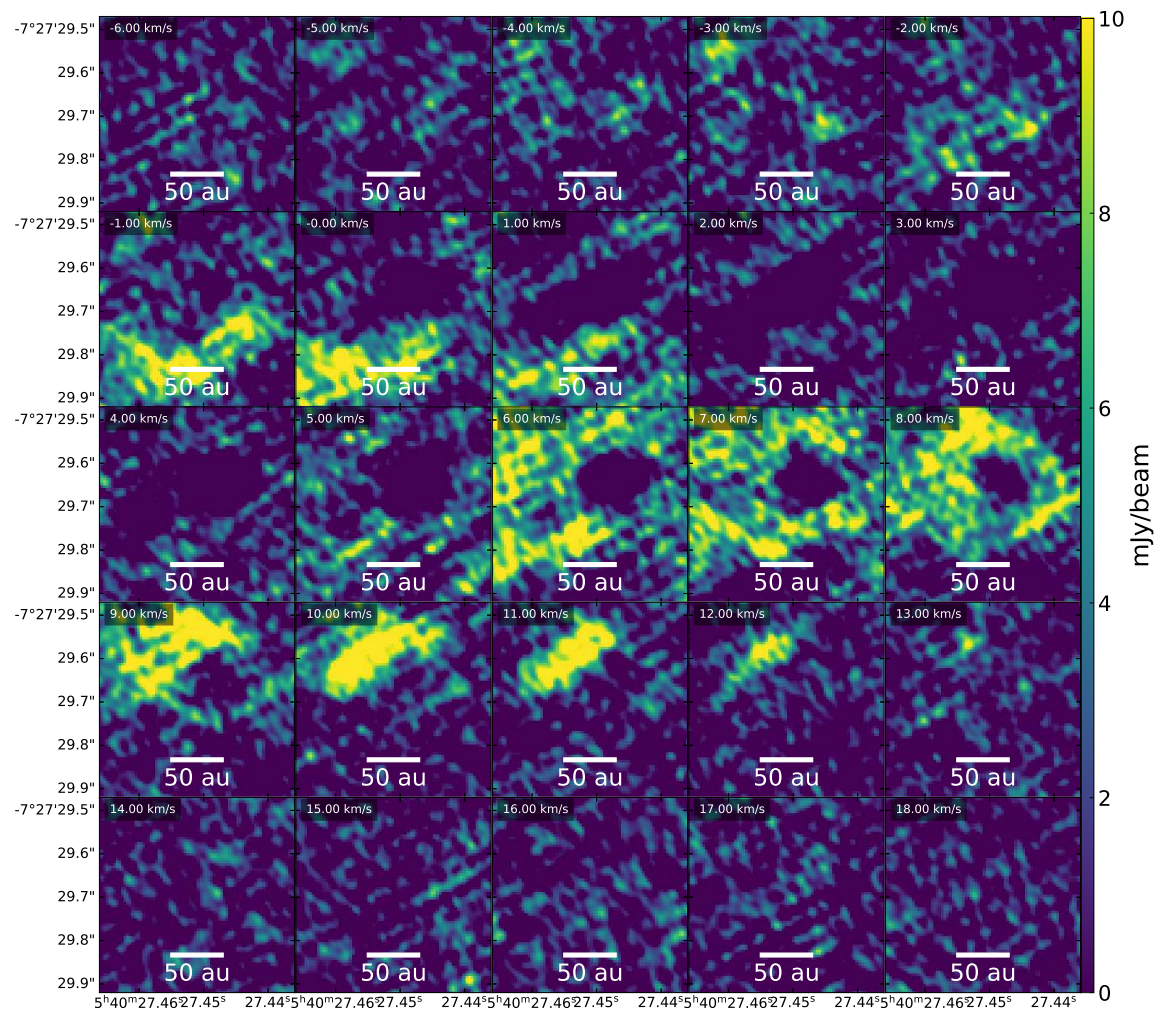


Figure 2.15: ^{12}CO channel maps of HBC 494 system, small-scale, after removing the continuum contribution.

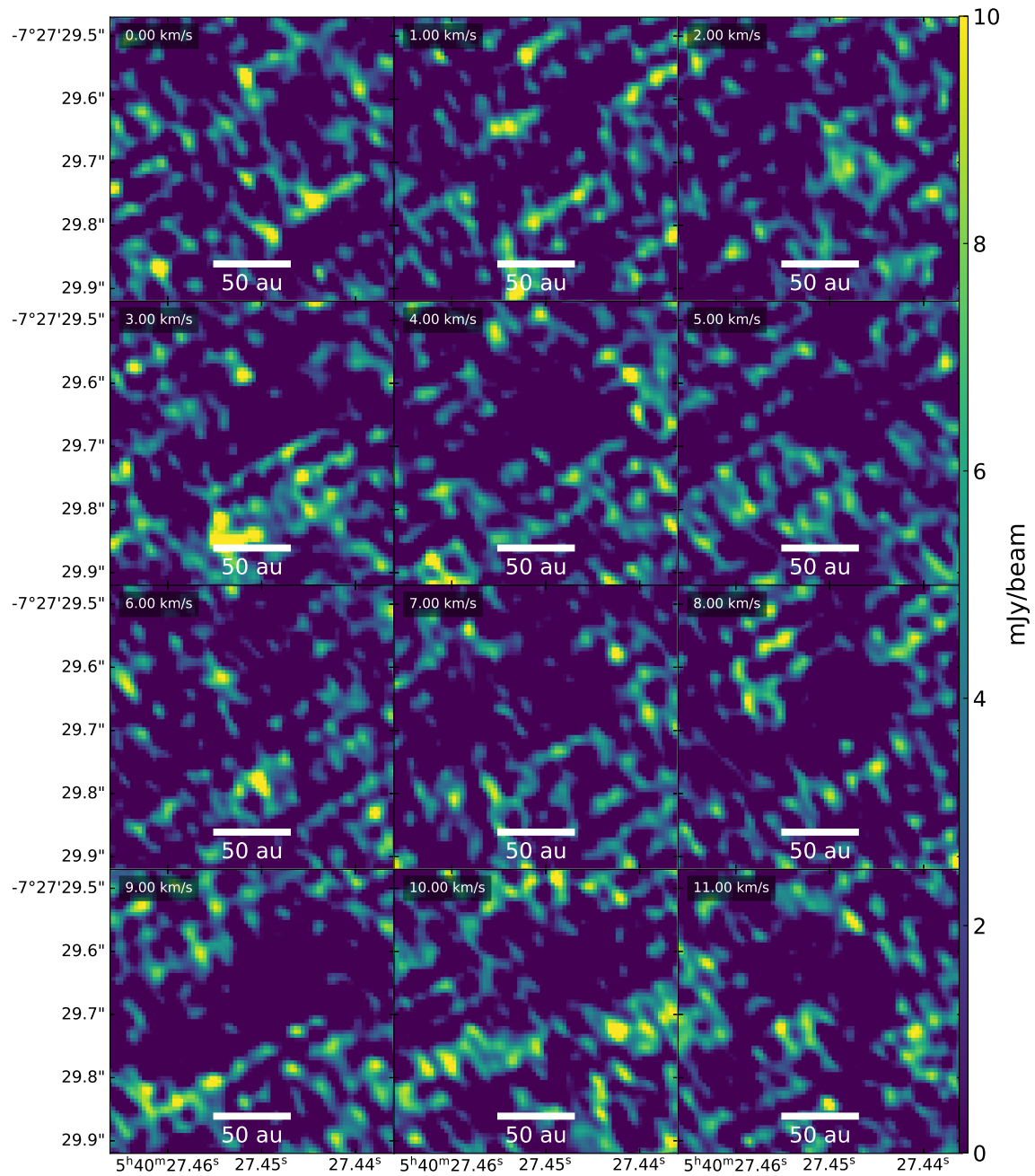


Figure 2.16: ^{13}CO channel maps of HBC 494 system, small-scale, after removing the continuum contribution.

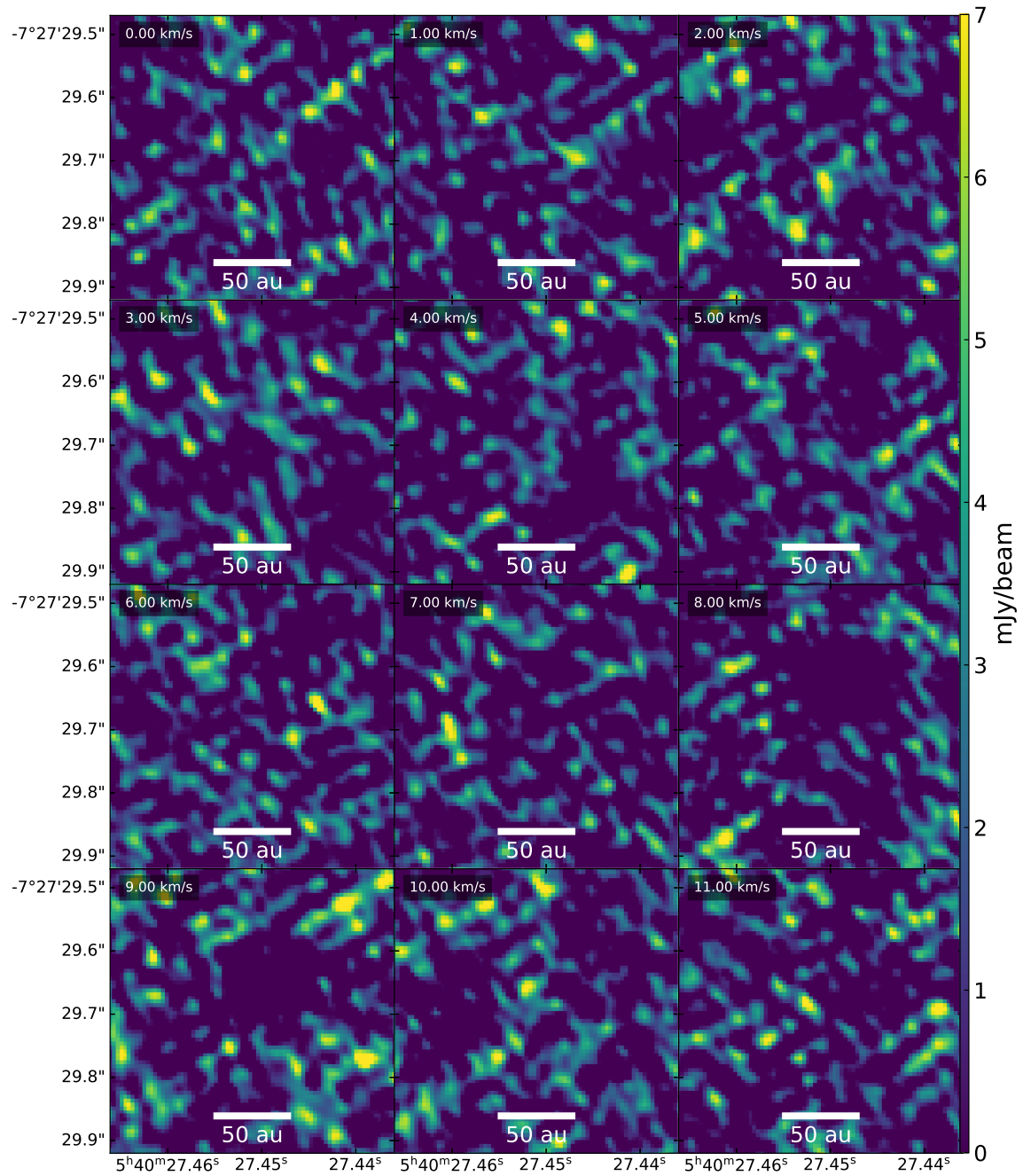


Figure 2.17: C^{18}O channel maps of HBC 494 system, small-scale, after removing the continuum contribution.

CHAPTER 3

ASTROMETRIC AND PHOTOMETRIC CHARACTERIZATION OF η TEL B COMBINING TWO DECADES OF OBSERVATIONS

*The content of this chapter was accepted for publication in the journal *Astronomy & Astrophysics (A&A)*, see *Nogueira et al. (2024)* - <https://ui.adsabs.harvard.edu/abs/2024arXiv240504723N/abstract>.*

3.1 Introduction

Since the first discovery of a planet around a main-sequence star (Mayor & Queloz, 1995), techniques and instruments for discovering and characterizing substellar objects have advanced exponentially. Today, more than 5500 exoplanets have been confirmed*, and more than 19,000 candidates of ultracool dwarfs (spectral type later than M7) are known (dal Ponte et al., 2023). However, little is known about where, when, and how substellar objects form. Thus, investigating newborn substellar objects in a stellar system is essential to address this knowledge gap, since they are expected to retain signatures of their formation pathway through the system architecture (e.g., Mayer et al., 2004; Pearce & Wyatt, 2014; Greaves et al., 2014; Davies, 2019; Bowler et al., 2020; Do Ó et al., 2023) and from their atmosphere (e.g., Marley et al., 2007a; Öberg et al., 2011; Dupuy et al., 2014; Baraffe et al., 2015; Crepp et al., 2018; Zhang et al., 2023; Petrus et al., 2024).

In particular, the high-contrast imaging technique (hereafter called HCI) is a capable tool to discover and characterize young giant planets and brown dwarfs. HCI is sensitive to recently formed objects that conserve some formation heat. Indeed, substellar objects have been discovered using HCI techniques in the past decade (e.g., 2MASSWJ 1207334-393254: Chauvin et al., 2004; β Pic b: Lagrange et al., 2010b; HD 95086 b: Rameau et al., 2013a; PDS 70 b: Keppler et al., 2018b; YSES 2b: Bohn et al., 2021). More recently, with the release of the Gaia catalogs and an update on astrometric precision, HCI has also been used to follow up on stars that showed anomalous accelerations (difference between their long-term HIPPARCOS-Gaia and short-term Gaia proper motion vectors), pointing towards the presence of companions in the system. One remarkable example is the discovery of AF

*Information extracted from the NASA Exoplanet archive database <https://exoplanetarchive.ipac.caltech.edu/> (Akeson et al., 2013).

Lep b through proper motion anomalies and HCI (Mesa et al., 2023; De Rosa et al., 2023; Franson et al., 2023).

Near-infrared substellar companions observed by High-Contrast Imaging (HCI) may offer valuable multiwavelength and multi-analysis data for the detection of circumplanetary disks (CPDs) or satellites in their surroundings. For instance, Pérez et al. (2019) analyzed ALMA band 6 observations featuring directly imaged companions, establishing upper limits on CPD detectabilities. Similarly, using SPHERE near-infrared (NIR) images, Lazzoni et al. (2020) set upper limits for satellite detections around substellar companions. Notably, Lazzoni et al. (2020) also identified a potential satellite candidate around DH Tau B, although confirmation of its nature is still pending. Subsequently, Lazzoni et al. (2022) provided a more robust analysis on the detectability of satellites through all standard exoplanet discovery techniques. Additionally, Ruffio et al. (2023) proposed to direct efforts towards detecting potential candidates through radial velocity monitoring, a method that can be implemented by monitoring companions with high-resolution spectroscopy. Another technique for searching for satellites is spectroastrometry, which consists of the fine measurement of any deviation from the position of the center of light (Agol et al., 2015). If an integral field spectrograph targets an unresolved planet-satellite system, it is expected that the center of the light shifts position depending on the wavelength. The movement of the centroid of the PSF would reveal if a satellite is present.

One system that comes to attention based on its age, being targetable from HCI and satellite analysis, and its astrometric follow-up is η Telescopii (hereafter called η Tel). η Tel is part of the β Pic moving group, with an estimated age of 18 Myr Miret-Roig et al. (2020) and a distance of 49.5 pc (Bailer-Jones et al., 2021). It is composed of an A0V, 2.09 M_{\odot} primary star (η Tel A; Houk & Cowley, 1975; Desidera et al., 2021a,b) and an M7-8, brown dwarf companion (η Tel B) at $\sim 4.2''$ separation and position angle of $\sim 169^{\circ}$ (Lowrance et al., 2000; Guenther et al., 2001, and references therein). η Tel A presents a likely warm debris belt at 4 au (unresolved, only inferred from the SED) and an edge-on cold debris belt at 24 au discovered via infrared excess (Backman & Paresce, 1993; Mannings & Barlow, 1998). The outer debris disk was later resolved with T-ReCS (Thermal-Region Camera Spectrograph) on Gemini South (Smith et al., 2009). Moreover, despite gas absorption towards η Tel debris disk was previously attributed to radiatively driven debris consistent with C/O solar ratio (Youngblood et al., 2021), more recent findings revealed that the origin of absorption lines is more likely of an interstellar cloud traversing the line of sight of η Tel A (Iglesias et al., 2023). η Tel B is a bright substellar companion with a contrast of 6.7 magnitudes in the VLT/NACO H band (Neuhäuser et al., 2011), or 11.85 in apparent magnitude. Its astrometrical points and orbital constraints were first compiled and analyzed in Neuhäuser et al. (2011), which used 11 years of imaging data (1998-2009). An additional NACO observation was presented in Rameau et al. (2013b), which broadened the time baseline to 2011.

In this paper, we present a characterization of the companion, including astrometrical and photometrical follow-up and orbital constraint analysis. We present three new epochs from the Spectro-Polarimetric High-contrast Exoplanet REsearch (SPHERE) instrument (Beuzit et al., 2019). With the addition of the new SPHERE data and a baseline of observa-

tions from 1998 to 2017, we present the most recent and complete orbital characterization of the system. Furthermore, we performed an analysis of the surroundings of η Tel B to constrain the possible presence of features such as satellites or circumplanetary disks.

The manuscript is structured in the following order. Observations and data reduction are described in Section 3.2. The photometric and astrometric measurements of the system of the new SPHERE observations are reported in Section 3.3.1. The orbital fitting analysis, taking into account the new data and the literature can be found in Section 3.3.2. The description of the study of the close vicinity of the substellar companion and the contrast curves around η Tel B are presented in Section 3.4.3. Final remarks and conclusions are presented in Section 3.5.

3.2 Observations and data reduction

3.2.1 Observations

We present new SPHERE/IRDIS coronagraphic data of the system around η Tel A. SPHERE is a VLT (Very Large Telescope) planet-finder instrument located at Paranal, Chile - UT3. It is an instrument dedicated to HCI. SPHERE is composed of four main scientific parts: the Common Path and Infrastructure (CPI), which includes an extreme adaptive optics system (SAXO, Fusco et al., 2006; Petit et al., 2014) and coronagraph systems; the Infrared Dual-band Imager and Spectrograph (IRDIS, Dohlen et al., 2008) with a pixel scale of 12.25 mas and field of view (FoV) of 11×12.5 arcsec; the integral field spectrograph (IFS, Claudi et al., 2008) with FoV of $1.73'' \times 1.73''$; and the Zurich Imaging Polarimeter (ZIMPOL, Schmid et al., 2018), the visible light imager and polarimeter of SPHERE. Both IRDIS and IFS belong to the NIR branch and can be used concomitantly if required during observations. Given the separation of η Tel B and its brightness in the near-infrared, IRDIS observations are the most suitable for the purpose of our paper.

The observations were performed with IRDIS on three different nights. Since the stellar companion is outside the field of view (FoV) of the integral field spectrograph (IFS) instrument, we do not report its data in this manuscript. The first observation (program 095.C-0298(A); PI Beuzit) was taken on 2015-05-05, generally under average conditions, with variable seeing ranging between 1 and 2 arcseconds (this epoch had photometric sky transparency). The second observation (program 097.C-0394(A); PI Milli) was taken under good conditions on 2016-06-15, and the seeing was mostly stable during the period of observation, varying between 1-1.4 arcseconds (this epoch had the sky transparency declared as thin). This program was performed as part of the SPHERE High-Angular Resolution Debris Disks Survey (SHARDDS; Dahlgvist et al., 2022), designed to image circumstellar disks around bright nearby stars (within 100 pc from the Earth). The third observation (program 198.C-0209(H); PI Beuzit) was taken on 2017-06-15, with a slightly higher value of the seeing and poorer conditions (“thin” sky transparency). An apodized Lyot coronagraph (N_ALC_YJH_S; inner working angle $\sim 0.15''$) was used on all three nights. A dual-band filter H2H3 was set ($\lambda = 1.593$ and $1.667 \mu\text{m}$ for H2 and H3, respectively; $\Delta\lambda = \sim 0.053 \mu\text{m}$ for both filters) on the first and third nights, while on the second night, a broadband filter

H ($\lambda = 1.625 \mu\text{m}$; $\Delta\lambda = 0.29 \mu\text{m}$) was used instead. A fourth IRDIS sequence was taken (2018-05-08; ID: 1100.C-0481(G); PI: Beuzit), but it was discarded from our analysis due to bad observing conditions. The observations and their specifications are summarized in Table 3.1.

3.2.2 Data reduction

The reduction of the three epochs was performed by the High Contrast Data Center pipeline[†] (hereafter called as HC DC; Delorme et al., 2017), which utilizes the Data Reduction and Handling software (v0.15.0; Pavlov et al., 2008) and routines presented in Galicher et al. (2018). The process includes standard pre-reduction steps such as background subtraction, flat-fielding, and bad pixel correction. The frames are recentered using the SPHERE waffle pattern, followed by corrections for the anamorphism of the instrument and astrometric calibration (pixel scale and True north correction), as described in Maire et al. (2016). The final products comprise a master cube that contains all frames, the position angle (PA) values of each frame, and an off-axis PSF reference cube. The off-axis PSF is an unsaturated image of the central star taken before and after the coronagraphic sequence for flux calibration.

We made use of the VIP code (Vortex Image Processing, Gomez Gonzalez et al., 2017; v.1.5.1) to reject the bad frames in each master cube, considering only frames with a Spearman correlation above 0.85 compared to the first frame taken under good conditions. After this step, we created post-processing images, employing the Angular Differential Imaging (ADI; Marois et al., 2006) and principal component analysis (PCA; Soummer et al., 2012b; Amara & Quanz, 2012b) with varied numbers of principal components. Since the PCA introduces deep over-subtraction due to the FoV rotation even for a few components, we favored the classical ADI images for our analysis. The result of this post-processing technique is presented in Fig. 3.1.

3.3 Methodology and results

3.3.1 Astrometry and photometry

The NEGFC technique

To precisely determine the position and flux of η Tel B, we employed the NEGative Fake Companion Technique (NEGFC), as described in studies such as Lagrange et al. (2010b) and Zurlo et al. (2014). This technique involves modeling the target source by introducing a negative model of the instrumental PSF into the pre-processed data. The procedure aims to minimize residuals in the final image, adjusting the flux and position of the model to align with the source's properties (astrometry and photometry). We implemented the NEGFC using the VIP package.

[†]Formerly known as SPHERE Data Center or SPHERE DC.

Table 3.1: List of the SPHERE/IRDIS η Telescopic observations used in this work.

Date (UT)	ESO ID - PI	IRDIS filter	DIT \times NDIT	Δ PA	Seeing ["]	Avg. coherence time [s]
2015-05-05	095.C-0298(A)- Beuzit	DB_H2H3	32 \times 8	46.83	Mostly 0.9-1.5 ^a	0.0011
2016-06-15	097.C-0394(A)- Milli	BB_H	8 \times 8	18.17	1-1.4	0.0024
2017-06-15	198.C-0209(H)- Beuzit	DB_H2H3	32 \times 12	2.04	1.5-2	0.0023
2018-05-08 ^b	1100.C-0481(G)- Beuzit	—	—	—	—	—

^aA subtle increase in seeing above 1.5 was registered between 08h40m-9h00m UTC at that night.^bDiscarded from the analysis for bad observing conditions.

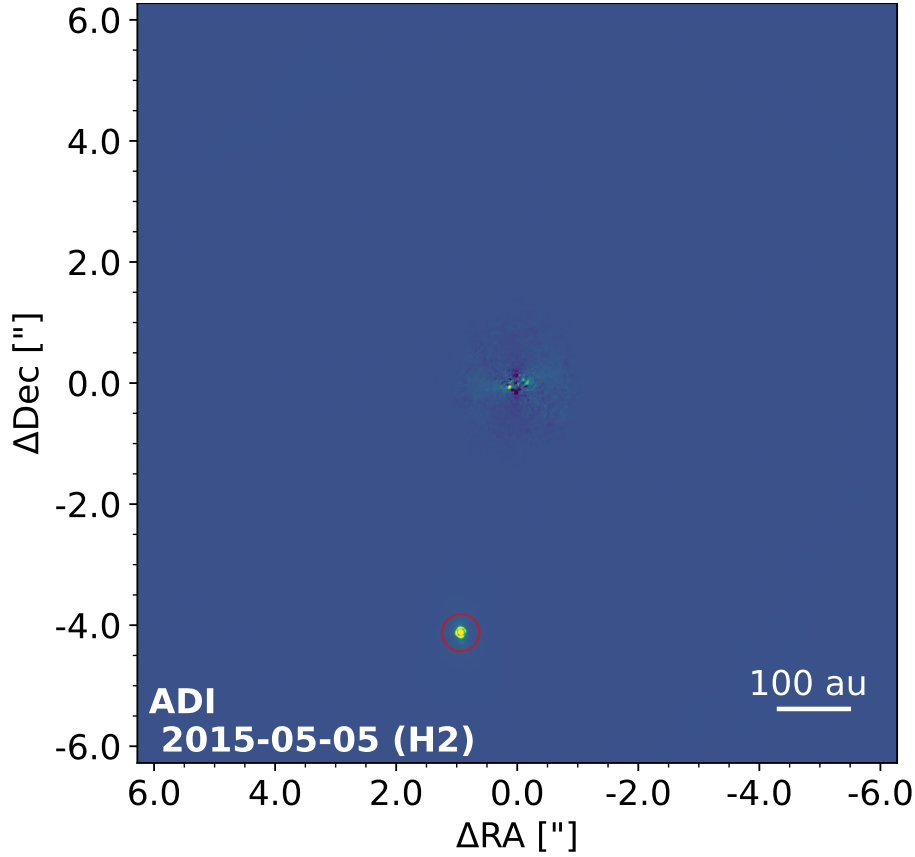


Figure 3.1: ADI-processed from IRDIS coronagraphic sequence (epoch: 2015-05-05; filter: H2) for the η Tel system. The red circle marks the position of η Tel B. The star is masked under the coronagraph at the center of the image. North is up, East is left.

For this purpose, we adapted the `single_framebyframe` routine proposed by [Lazzoni et al. \(2020\)](#). This routine provides estimates of separation, position angle, and photometry for the companion in each frame from the coronagraphic sequence. η Tel B's brightness (signal-to-noise ratio ≥ 100) and relative distance from the speckle-dominated region are sufficient for this approach to be applicable.

As a model PSF, we utilized the off-axis image of the central star captured before and after the coronagraphic sequence. For each set of coordinates, a negative flux was introduced, and the set of positions and fluxes yielding the lowest residual (standard deviation) in each frame was selected. Consequently, for each night and filter, the routine's results were represented by the median values of the parameters measured across all frames.

Measurement of the photometry

The contrast of the brown dwarf was calculated as the median of the NEGFC technique values on each frame of the coronagraphic sequence. Flux contrast uncertainties were derived from the standard deviation of the fluxes measured by the NEGFC technique. Fig.

3.2 sets flux measurements throughout the sequence using BB_H filter, showing how the values can vary. The contrast in flux and magnitude with respect to the central star for each filter is shown in Table 3.2. The results are consistent with the measurements presented in the literature for the companion.

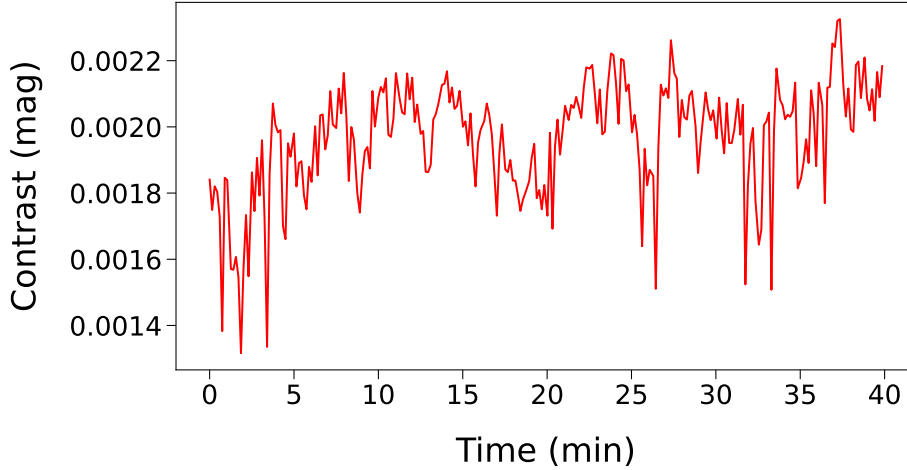


Figure 3.2: Contrast flux variations for the companion with respect to the star (filter: BB.H).

Table 3.2: IRDIS flux contrast in flux and magnitude with respect to the central star for η Tel B.

Epoch	Filter	Contrast [e-3]	Δ magnitude
2015-05-05	H2	1.52 ± 0.60	7.05 ± 0.45
2015-05-05	H3	1.92 ± 0.12	6.79 ± 0.07
2016-06-15	BB_H	2.00 ± 0.17	6.75 ± 0.09
2017-06-15	H2	1.53 ± 0.78	7.04 ± 0.61
2017-06-15	H3	1.92 ± 0.84	6.79 ± 0.51

After using the NEGFC technique, the signal of the companion was removed in each frame of the datacubes, creating therefore empty datacubes. Following, a 5-sigma contrast curve with respect to and around η Tel A was produced using the ADI processed data. The achieved contrast for epoch 2016-06-15 is shown in Fig. 3.3.

Measurement of the astrometric positions

To robustly determine the separation and position angle at each epoch, we applied multiple methods while concurrently estimating the disparities between these algorithms. Specifically, we employed:

- the NEGFC method detailed in Section 3.3.1;

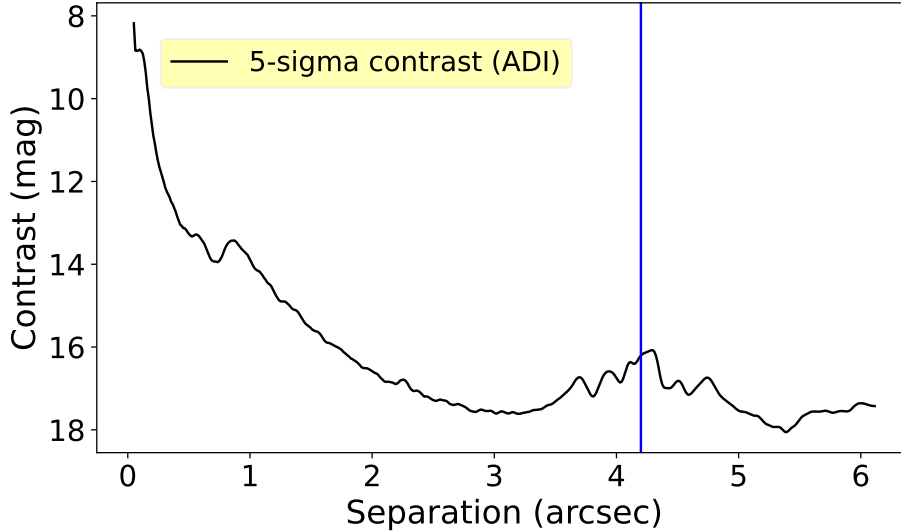


Figure 3.3: Contrast curve with respect to η Tel A, using the datacube corresponding to the 2016-06-15 (BB_H) observation. The vertical blue line corresponds to the position of the companion.

- a 2D-Gaussian fitting encompassing the companion. We optimized Gaussian statistics using two stochastic algorithms: Adam (Kingma & Ba, 2014) and the Levenberg–Marquardt algorithm (Moré, 2006);
- the peak intensity pixel location within a FWHM of the companion.

All the algorithms were applied to each frame of the coronagraphic (frame-by-frame) sequence as well as to their median-collapsed reduction. When using the frame-by-frame method, it is important to note that a sequence of positions is obtained and it is necessary to reduce them by using the median. Finally, the astrometric points for each night and filter were determined by calculating the median among the outputs of the algorithms. Similarly, the uncertainties of the astrometric fitting were calculated as the standard deviation across all results obtained from the various methods. We justify applying different methods as we observed that the final results of each method could differ by a maximum of 10 mas in separation and approximately 0.15 degrees in position angle. Therefore, we opted for implementing a median instead of an average to filter out values that may otherwise skew the results.

In addition to the uncertainties on the astrometric fitting of the companion, we have to consider other factors in the error budget, as previously stated by Wertz et al. (2017):

- Instrumental calibration, where the most relevant errors come from the orientation of the True North, pupil offset, plate-scale, and anamorphism;
- Determination of the position of the central star behind the coronagraph;

- Systematic error due to residual speckles;
- Statistical error due to planet position determination.

Therefore, considering R as the final expression for radial separation in arcseconds and Θ as the final expression for position angle in degrees, we applied the following approximated equations:

$$R = PS(R_* \pm R_{spec} \pm rR_{AF} \pm r) \text{ and} \quad (3.1)$$

$$\Theta = \Theta_* \pm \Theta_{spec} \pm \Theta_{AF}\theta \pm \Theta_{PO} \pm \Theta_{TN} \pm \theta, \quad (3.2)$$

where r is the radial distance and θ the position angle, R_* and Θ_* the radial and azimuthal values related to stellar centering; R_{spec} and Θ_{spec} the radial and azimuthal values related to speckle noise; R_{AF} and Θ_{AF} values related to the anamorphic factor expressed in percentage; TN related to the true north, PS to plate scale ("/pixel) and PO to the pupil offset. All distances are measured in pixels and all angles are measured in degrees.

Consequently, the Equations 3.1 and 3.2 can be used to propagate the errors:

$$\sigma_R^2 = PS^2[\sigma_{R_{spec}}^2 + \sigma_{R_*}^2 + r^2\sigma_{R_{AF}}^2 + (R_{AF} + 1)^2\sigma_r^2] + \frac{R^2}{PS^2}\sigma_{PS}^2 \quad (3.3)$$

and,

$$\sigma_\Theta^2 = \sigma_{\Theta_{spec}}^2 + \sigma_{\Theta_*}^2 + \theta^2\sigma_{\Theta_{AF}}^2 + \sigma_{PO}^2 + \sigma_{TN}^2 + (\Theta_{AF} + 1)^2\sigma_\theta^2. \quad (3.4)$$

The instrumental calibration uncertainties were determined through astrometric calibrations outlined in Maire et al. (2016), Maire et al. (2021), and the last version of the SPHERE manual, 18th release. Before July 2016, an issue with the synchronization between SPHERE and VLT internal clocks led to abnormal fluctuations in True North measurements. Consequently, for the initial two η Tel observations, the True North uncertainties were extracted from Table 3 of Maire et al. (2016). For the third observation, we adopted a fixed value of 0.04° , representing the stabilized uncertainty following calibrations and corrections.

The plate (pixel) scale uncertainties, were extracted from close-in-time coronagraphic observations, obtained with the SPHERE-SHINE GTO data, using the globular stellar cluster 47 Tuc as field reference (Table 7 of Maire et al. 2021). The pupil offset uncertainty, derived from commissioning and guaranteed time observations, is 0.11 degrees. Distortion is predominantly influenced by a $0.60\% \pm 0.02\%$ anamorphism between the horizontal and vertical axes of the detector. Since each frame has undergone correction by the HC DC, rescaling each image by 1.006 along the axis, the uncertainty of 0.02% (for both R_{AF} and Θ_{AF}) was incorporated into the error budget analysis.

The radial stellar centering uncertainty per dithering is 1.2 mas, derived from observations of bright stars during commissioning runs (Zurlo et al., 2014, 2016). This value was then adjusted by dividing it by the square root of the number of frames per observation.

Subsequently, the latter was translated into an uncertainty on position angle by division by the separation r of the companion.

Uncertainties arising from speckles may persist even after ADI post-processing and have an impact on photometric and astrometric measurements (Guyon et al., 2012; Wertz et al., 2017). To address this, we employed the `speckle_noise_uncertainty` function from VIP, injecting multiple simulated companions into companion-free cubes at the same radial distance and flux as the actual companion. The positions of these simulated companions were determined using Nelder-Mead optimization, and then the values of separation and position angle were measured. By comparing the offsets between the input values and the estimations by the code, a distribution of parameters was generated. A Gaussian function was then fitted to the distribution, and the uncertainties in R and Θ were estimated as the standard deviations of the fitting. In this instance, a total of 100 simulated companions, equally spaced azimuthally, were utilized. A similar methodology was employed by Maire et al. (2015); Wertz et al. (2017). In Fig. 3.4, three histograms illustrate the distribution of separation, position angle, and flux of the companion observed on 2015-05-05. The separation and position angle values for the epoch are shown in Table 3.3, and the detailed uncertainties used to calculate the error budget are compiled in Table 3.4.

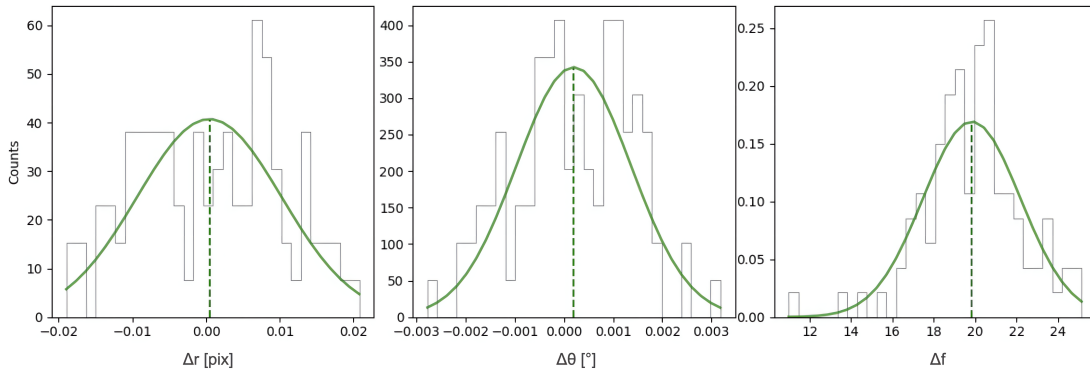


Figure 3.4: Speckle noise estimation for η Tel B in the data set of 2015-05-05. The histograms illustrate the offsets between the true position and flux of a fake companion and its position and flux obtained from the NEGFC technique. The dashed lines correspond to the 1D Gaussian fit from which we determined the speckle noise.

3.3.2 Orbital fitting analysis

The system around η Tel A was observed with the high-contrast imaging technique for the last two decades. The favorable contrast of the brown dwarf companion and the wide separation between the two objects make the system an ideal target for HCI. The astrometric follow-up of the brown dwarf companion counts 18 epochs of observation spanning almost 20 yr. For the orbit analysis, we included all the astrometrical points presented in the

Table 3.3: List of astrometric positions of η Tel B obtained from the IRDIS observations. The error budget is listed in Table 3.4.

Epoch	Filter ^a	Sep. (")	PA (°)
2015-05-05	H3	4.215±0.004	167.326±0.197
2016-06-15	BB_H	4.218±0.004	167.260±0.130
2017-06-15	H2	4.218±0.004	167.346±0.142

^aThe table only presents values related to the filters where the lowest uncertainties, retrieved from NEGFC, on each epoch, were achieved.

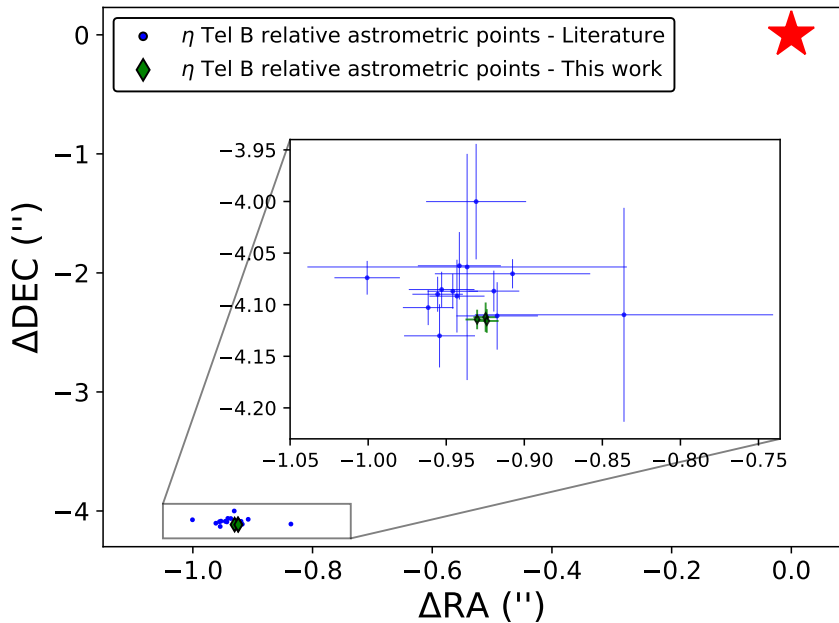


Figure 3.5: Relative astrometry for η Tel B. The red star marks the position of η Tel A. The blue-filled circles represent astrometric points extracted from the literature. The green-filled diamonds represent the astrometric points from this work. The astrometric point from epoch 2000.378 was not included due to its high uncertainties.

literature, as well as the ones obtained from the new analysis. The complete list is shown in Table 3.5 and their positions with respect to the central star are represented in Figure 3.5.

We employed the Orvara code (Orbits from Radial Velocity, Absolute, and/or Relative Astrometry; Brandt et al., 2021c) to perform the orbital fitting of the system. Orvara accepts input information on the acceleration of the central star from the Hipparcos vs Gaia early data-release 3 (EDR3; Bailer-Jones et al., 2021) catalogs.

The orbital elements and masses of both the host and the companion were computed by Orvara using a parallel tempered Markov Chain Monte Carlo (MCMC) ensemble sampler, ptemcee (Vousden et al., 2016), a variant of emcee (Foreman-Mackey et al., 2013). Parallel tempering enhances the exploration of complex parameter spaces by simultaneously running multiple chains at different temperatures, allowing for more efficient sampling and improved convergence compared to traditional MCMC methods. In a simulation, different temperatures refer to variations in the parameter that control the acceptance of proposed moves in the MCMC algorithm. Higher temperatures encourage more exploration by ac-

Table 3.4: Uncertainties used to calculate the error budget for the astrometry of the companion. The values correspond to errors associated with individual frames.

Epoch	σ_r (pixels)	$\sigma_{R_{spec}}$ (pixels)	σ_{R_*} (pixels)	$\sigma_{R_{AF}}$ (%)	σ_{PS} (mas/pixel)	σ_θ ($^\circ$)	$\sigma_{\Theta_{spec}}$ ($^\circ$)	σ_{Θ_*} ($^\circ$)	$\sigma_{\Theta_{AF}}$ (%)	σ_{PO} ($^\circ$)	σ_{TN} ($^\circ$)
2015-05-05	0.297	0.003	0.098	0.02	0.01	0.068	0.0005	0.016	0.02	0.11	0.145
2016-06-15	0.065	0.001	0.098	0.02	0.01	0.012	0.0001	0.016	0.02	0.11	0.060
2017-06-15	0.245	0.010	0.098	0.02	0.01	0.072	0.0015	0.016	0.02	0.11	0.040

The table only presents values related to the filters where the lowest uncertainties on each epoch were achieved: 2015-05-05 (H3); 2016-06-15 (BB-H), and 2017-06-15 (H2), thus referring to the filters also listed on Table 3.3.

Table 3.5: Astrometric positions of η Tel B from the literature and our analysis included in the Orvara analysis.

Date (yr)	Separation (")	PA ($^{\circ}$)	Ref.
1998.492	4.170 \pm 0.033	166.95 \pm 0.36	N11
2000.307	4.107 \pm 0.057	166.90 \pm 0.42	N11
2000.378	4.310 \pm 0.270	165.80 \pm 6.70	G01
2004.329	4.189 \pm 0.020	167.32 \pm 0.22	N11
2004.329	4.200 \pm 0.017	166.85 \pm 0.22	N11
2004.329	4.199 \pm 0.036	167.02 \pm 0.22	N11
2004.329	4.195 \pm 0.017	166.97 \pm 0.22	N11
2006.431	4.170 \pm 0.110	167.02 \pm 1.40	G08
2007.753	4.212 \pm 0.033	167.42 \pm 0.35	N11
2008.312	4.214 \pm 0.017	166.81 \pm 0.22	N11
2008.599	4.195 \pm 0.017	166.87 \pm 0.29	N11
2008.599	4.194 \pm 0.016	166.20 \pm 0.29	N11
2009.351	4.239 \pm 0.104	168.50 \pm 1.30	N11
2009.496	4.199 \pm 0.031	166.99 \pm 0.30	N11
2011.576	4.170 \pm 0.009	167.43 \pm 0.70	R13
2015.341	4.215 \pm 0.004	167.33 \pm 0.20	^a
2016.454	4.218 \pm 0.004	167.26 \pm 0.13	^a
2017.452	4.218 \pm 0.004	167.35 \pm 0.14	^a

N11: [Neuhäuser et al. \(2011\)](#); G01: [Guenther et al. \(2001\)](#); G08: [Geißler et al. \(2008\)](#); R13: [Rameau et al. \(2013b\)](#)

^a: This work.

cepting moves that might increase energy or objective function values, allowing the algorithm to escape local optima and explore a broader solution space. On the other hand, lower temperatures favor exploitation, focusing on refining solutions and improving the chance of finding the global optimum. Adjusting temperatures during the simulation influences the balance between exploration and exploitation, shaping the algorithm's behavior throughout the MCMC process. The MCMC simulation utilized 10 temperatures, 500 walkers, and 10^6 steps for each chain. The simulation outputs a point every 1000 steps.

Priors for the MCMC include distributions of the masses of celestial objects, parallax, and proper motion of the system. Additionally, the initial orbital elements distribution for the companions (semi-major axis: a ; eccentricity: e ; argument of the pericenter: ω ; inclination: i ; longitude of the ascending node: Ω ; and longitude at reference epoch: l) can also be incorporated. We used as priors the common proper motion extracted from [Kervella et al. \(2021, 2022\)](#), the parallax from Gaia DR3 ([Bailer-Jones et al., 2021](#)), the primary mass from [Desidera et al. \(2021a,b\)](#), and the companion (η Tel B) mass with loosened constraints on its uncertainties from [Lazzoni et al. \(2020\)](#). Given the low orbital coverage from relative astrometric points, we just set a mean initial value inspired by the semi-major axis proposed by ([Neuhäuser et al., 2011](#)), leaving other orbital elements to cover wider

values in the parameter space, as set by standard values from ORVARA. The specific priors and initial values set are detailed in Table 3.6. Further orbital constraints and results are analyzed and presented in section 3.4.1.

Table 3.6: Priors and initial and distribution of parameters for η Tel system astrometrical fitting^a.

Priors	η Tel A	η Tel B
Mass (M_{\odot})	2.09±0.03	0.045±0.014
Parallax (mas)	20.603±0.099	20.603±0.099
RA p.m. (mas/yr)	25.689±0.006	25.689±0.006
DEC p.m. (mas/yr)	-82.807±0.006	-82.807±0.006
Initial distribution ^b		
a (au)	—	220 ⁺³⁰⁰ ₋₂₂₀
$\sqrt{e} * \sin(\omega)$	—	0.4±0.3
$\sqrt{e} * \cos(\omega)$	—	0.4±0.3
i (radians)	—	1.57±1.57
Ω (radians)	—	3.2±2.2
l (radians)	—	0.8±0.5

^a Unphysical values such as negative values for masses or semi-major axis are automatically excluded from the code.

^b The initial distributions involve a lognormal distribution for the semi-major axis, while all other orbital values follow a normal distribution.

3.4 Discussion

3.4.1 Orbital fitting constraints

From the results of the MCMC simulation, we excluded the orbits that may cause instability in the system. In order to prevent disruption of the debris disk by the close-by passage of η Tel B, and considering that the masses of the star and companion are well-constrained by the MCMC simulations, we can delimit the possible orbits for η Tel B by inspecting the brown dwarf-disk interaction. Before applying any constraint, we obtained as values the mass of η Tel A ($m_* = 2.09M_{\odot}$) and mass of η Tel B ($m_{comp} = 48.10M_{Jup}$) from the original ORVARA simulation.

In this context, it is useful to introduce the concept of chaotic zone, a region in the proximity of the orbit of a planet or brown dwarf which is devoid of dust grains, since its gravitational influence sweeps out small dust particles. The chaotic zone depends on the ratio between the mass of the brown dwarf and the mass of the star, on the semi-major axis and eccentricity of the orbit. Given the outer disk's position, it is established that this zone cannot extend below 24 au. As η Tel B is positioned outside the disk, we employed the procedure outlined in Lazzoni et al. (2018) to compute the chaotic zone's extension for each

orbit during the pericenter passage. Specifically, we utilized equation 10 for cases where the eccentricity is less than a critical value (e_{crit}), or equation 12 for cases where it exceeds e_{crit} . Here, e_{crit} is determined as $0.21\mu^{3/7}$, equivalent to 0.022 (μ is the ratio between the mass of the companion and the mass of the star). In the end, we discarded 326674 orbits from an original number of 500000.

Furthermore, another constraint arises when determining that the pericenter of the brown dwarf (BD) cannot reach the disk. Consequently, considering the semi-major axis of the companion established by the MCMC simulations, ($a_{bd}^* = 178 \text{ au}$), we can use the following expression to discard highly eccentric orbits:

$$a_{bd}(1 - e_{max}) > 24 \text{ au} \quad (3.5)$$

where e_{max} is the maximum eccentricity allowed for the BD. Consequently, we obtained a maximum eccentricity of 0.865 and, therefore, we discarded an additional 139 orbits. Another constraint can be applied if we consider that the η Tel system has a wide comoving object, as mentioned previously in [Neuhäuser et al. \(2011\)](#). HD 181327 is an F5.5 V star, also a bona-fide member of the β Pic moving group, at a separation of ~ 7 arcmin (20066 au) ([Holmberg et al., 2009](#); [Neuhäuser et al., 2011](#); [Bailer-Jones et al., 2021](#)). The small proper motion difference in Gaia DR3, corresponding to a velocity difference on the plane of the sky of 370 m/s, is compatible with a bound object. The nominal RV difference derived in [Bailer-Jones et al., 2021](#); [Zúñiga-Fernández et al., 2021](#), is instead larger than the maximum expected one for a bound object (~ 400 m/s). However, it is well possible that the published RV errors are underestimated for a star with an extremely fast $v \sin i$ such as η Tel. There could also be contributions by additional objects, although both the Gaia RUWE (Gaia Renormalized Unit Weight Error) and the analysis of homogeneous RV time series do not indicate the presence of close companions ([Lagrange et al., 2009a](#); [Grandjean et al., 2020](#)). Therefore, we consider plausible, although not fully confirmed, that HD 181327 is bound to the η Tel system.

To ensure that HD 181327's presence in the system would not affect the long-term stability of η Tel B, we implemented equation 1 of ([Holman & Wiegert, 1999](#)). Therefore, we could exclude orbits where the critical semi-major axis is greater than the periastron of the brown dwarf. To proceed, we used the mass of the perturber as $1.3 M_{\odot}$ ([Desidera et al., 2021a,b](#)). Considering the eccentricities of the binaries as 0, a perturber with a similar mass would only impose constraints with a separation less than $13.25''$ (656 au) from η Tel A. Otherwise, for HD 181327 to act as a perturber at its separation from the η Tel system, the eccentricities between HD 181327 and η Tel should be greater than 0.947. Therefore, we choose not to exclude any orbit using the external perturber criteria.

Following, the results of the simulation after the cut-off are shown as the corner plot in [Fig. 3.10](#) and also summarized in [Table 3.7](#). The values obtained depict a pericenter of $2.9''$ (144 au) and an apocenter of $5.9''$ (292 au). Despite two decades of observations of η Tel B, the coverage only spans a fraction of the wide orbit of the companion, with a total

*The value of the semi-major axis of 178 au was the one retrieved before the exclusion of orbits. The final value is 218 au, as presented in [Table 3.7](#) and [Fig. 3.10](#).

Δ PA of approximately $\sim 2^\circ$. This accounts for less than 1% of the orbit, assuming a face-on and circular orbit. Consequently, constraining the semi-major axis and eccentricity proves challenging. Nevertheless, the MCMC effectively determines the inclination, yielding an orbit that is nearly edge-on and almost co-planar with the debris disk (Smith et al., 2009). Conversely, a variety of possible orbits can adequately fit the data, as illustrated in Fig. 3.6.

Table 3.7: Best orbital-fitting parameters for η Tel B calculated from the Orvara orbital characterization.

Mass (M_{jup})	48_{-15}^{+15}
a (au)	218_{-41}^{+180}
i (deg)	$81.9_{-3.5}^{+3.2}$
Ω (deg)	$174.6_{-7.1}^{+175}$
Mean longitude (deg)	184_{-74}^{+164}
Parallax (mas)	$20.60_{-0.10}^{+0.10}$
Period (yrs)	2201_{-592}^{+3224}
ω (deg)	159_{-99}^{+128}
e	$0.34_{-0.23}^{+0.26}$
a (mas)	4486_{-845}^{+3704}
Reference epoch T_0 (JD)	$2740996_{-107450}^{+488958}$
Mass ratio	$0.0219_{-0.0068}^{+0.0069}$

3.4.2 Possible formation scenarios

The coplanarity between η Tel B and the debris disk, as described in this work, and the relative spin-alignment between the star and the debris disk (Hurt & MacGregor, 2023), can offer insights into the formation scenario of the system. Stellar systems form through various mechanisms, typically categorized into three main types: 1) fragmentation of a core or filament, 2) fragmentation of a massive disk, or 3) capture and/or dynamical interactions (for a comprehensive review, including separation and formation time scales, see Offner et al., 2022). Given the separation of the star and the companion, scenarios involving massive disk fragmentation or capture and/or ejection of η Tel B appear more plausible.

Alternatively, core fragmentation, which occurs through direct/turbulent fragmentation (e.g., Boss & Bodenheimer, 1979; Bate & Burkert, 1997) or rotational fragmentation (e.g., Larson, 1972; Bonnell, 1994; Bonnell & Bate, 1994a,b; Burkert et al., 1997), followed by inward migration, is also a conceivable formation scenario. Binaries formed through direct fragmentation, with well-separated cores, may exhibit uncorrelated angular momenta between the objects (Offner et al., 2016; Bate, 2018; Lee et al., 2019; Bate, 2000). In contrast, stars and substellar objects formed through rotational fragmentation within the same plane tend to display preferentially spin-aligned and coplanar systems (Offner et al., 2016; Bate, 2018). In such a case, a rotational fragmentation followed by inward migration becomes more probable.

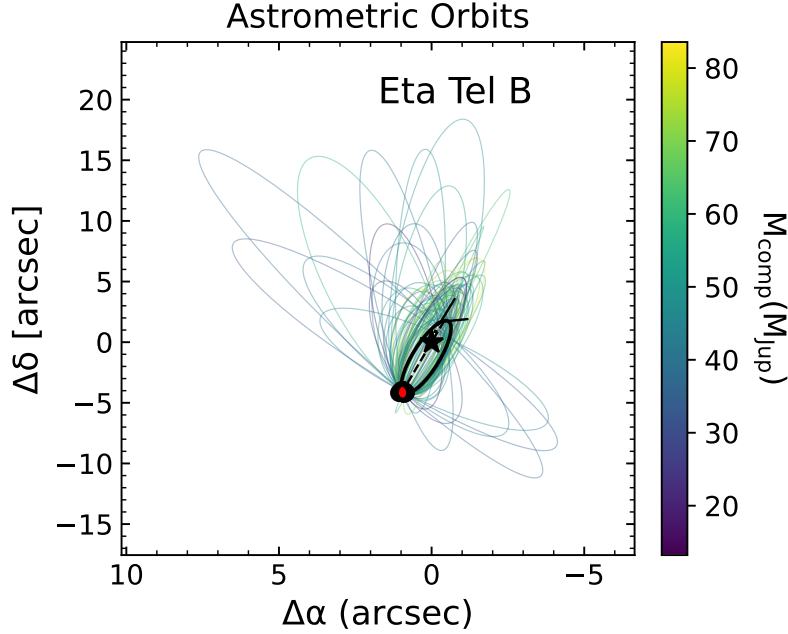


Figure 3.6: 87 randomly selected possible orbits calculated by the Orvara fitting, after excluding orbits based on constraints described in Section 4.1. The black star indicates the position of η Tel A. The best-fit orbit is shown in black.

Moreover, the eccentricity of the system plays a crucial role in inferring the formation scenario. If we consider the orbital fitting results where highly eccentric orbits are permitted, the preferred hypothesis for eccentricity enhancement would be recent dynamical interactions. If so, η Tel B did not reach near the debris disk of the star in the last few pericenter approximations. This scenario is highly improbable, given the short best-fitting orbital period in such cases (~ 1623 years). It is more likely that η Tel B has a low eccentric orbit, and the assumptions for excluding highly eccentric orbits may be the most suitable approach. Consequently, the system exhibits quasi-coplanarity and low eccentricity of the companion. Therefore, we tentatively suggest that the preferred formation scenarios for η Tel involve either the fragmentation of a massive disk with slow or no inwards migration or rotational fragmentation of a core with fast inwards migration. Long-term RV and astrometry monitoring of the star and the companion, along with multiwavelength observations of the system, could be useful to discard a capture or ejection scenario.

3.4.3 The close surroundings of η Tel B

In our Solar System, planets and small-sized bodies are often surrounded by satellites and dust rings or disk-like features (see e.g. [Alibert et al., 2005](#)). For instance, there are approximately 200 natural satellites in the Solar System, most of which orbit giant planets. This raises the possibility of similar objects existing around substellar companions, although

such discoveries have not yet been confirmed. Satellites or circumplanetary disks in these environments, if discovered, could provide valuable insights into their formation mechanisms. These mechanisms may include gravitational instability (Boss, 1997 and references therein), core-accretion (Pollack et al., 1996 and references therein), or capture and/or orbital crossing, which can lead to satellite companions with specific mass ratios and orbits. For instance, less massive exomoons are likely to form within a circumplanetary disk (CPD), as observed with the Galilean moons (see, e.g., Canup & Ward, 2002). Conversely, massive companion+satellite candidate systems likely form via orbital crossing+capture (Ochiai et al., 2014; Lazzoni et al., 2024). Furthermore, hydrodynamical simulations have shown that CPDs in the core-accretion scenario are eight times less massive and one order of magnitude hotter than those formed by gravitational instability (Szulágyi et al., 2017). Consequently, the characterization of exosatellites can be used to distinguish between these formation scenarios.

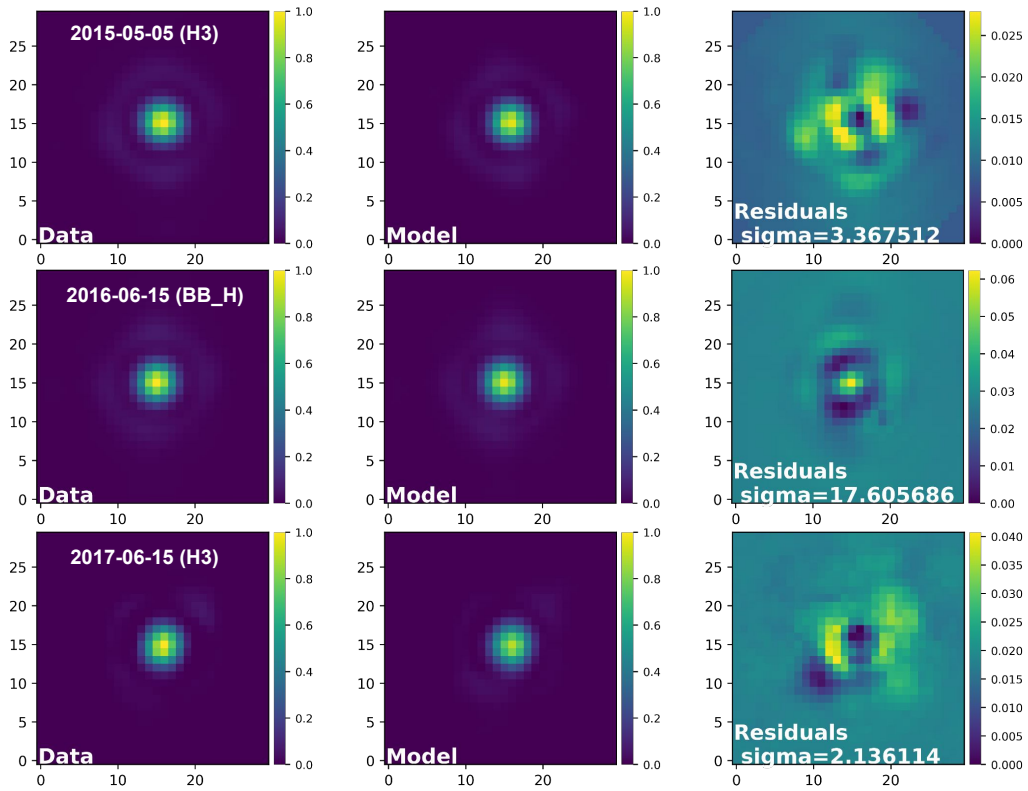


Figure 3.7: Analysis of the close surroundings of η Tel B to look for satellites and/or CPDs. In each row, the first panel shows the ADI image zoomed on η Tel B, the second panel shows the model, and the last one the residuals from the subtraction of the two. The three IRDIS epochs are shown. The residuals are expressed in counts. All the panels were normalized to the peak of the central PSF.

To analyze whether a satellite candidate or a CPD is present around the companion, we proceeded as follows: to compensate for the self-subtraction effect induced by post-processing, we forward-modeled the companion per frame based on the observations and

the PSF model. With the pre-processed data, the radial distance, position angle, and flux were obtained from the NEGFC approach (refer to Section 3.3.1). The off-axis PSF extracted before the sequence was positioned and flux-normalized with these parameters in an empty frame, creating what we refer to as “model”. Following, for each frame, the model was subtracted from the data, producing a residual image. The model and residual cubes were then collapsed using ADI or PCA+ADI. We compare the ADI post-processed data with the collapsed model and residual cubes per night in Fig. 3.7). The quality of the residuals is strongly related to the number of frames and quality of the night, showing a clearer result for the epoch 2016-06-15, where other epochs are more affected by systematics. Still, the residuals do not show any clear signal of a satellite or other nearby structure, imposing a threshold of detections at the contrast obtained with the NEGFC technique.

To generate contrast curves around η Tel B, we implemented a methodology similar to the one outlined in Lazzoni et al. (2020). The steps can be summarized as follows. Successive annuli, each centered on η Tel B and with a width equal to 1 FWHM, were chosen up to the Hill radius of the brown dwarf. The contrast at each radial position is computed as five times the standard deviation inside the annulus divided by the peak of the star (η Tel A).

For each annulus, we injected fake companions at various position angles, and their fluxes were determined after applying the NEGFC and PCA post-processing techniques. The ratio between the retrieved and injected flux provides the throughput value. A mean throughput is then calculated for each annulus and multiplied by the contrast at each separation. As a final step, we adjusted the contrast for small sample statistics, following the discussion presented in Mawet et al. (2014). A schematic representation of the steps used to calculate the contrast curves is illustrated in Fig. 3.8.

Finally, the contrasts were converted into mass constraints using the ATMO 2020 evolutionary models (Phillips et al., 2020). We utilized an estimated age for the system of 18 Myr (Miret-Roig et al., 2020) and a distance of 49.5 pc (Bailer-Jones et al., 2021). The best contrast curves for each data set are depicted in Fig. 3.9. We can discard the detection of satellites around the brown dwarf with masses between 3 and 1.6 M_{Jup} in the range of distances [10,33] au. Such massive objects, if present, would likely be the result of capture or trapping through tidal interactions (Lazzoni et al., 2024) or formation in situ via gravitational instability or direct collapsing. However, we cannot exclude the presence of closer-in and/or less massive objects which, for example, could have formed within a CPD via core accretion. Moreover, we can exclude the presence of an extended CPD from the shape and luminosity of the residuals around the companion.

3.5 Conclusions

In this paper, we present the most recent photometric and astrometric characterization of η Tel B, a brown dwarf situated at an approximate separation of $\sim 4.2''$ from its host star. The observations of this system were conducted using SPHERE/IRDIS H2H3 and BB_H filters, spanning three epochs across three consecutive years (2015-2017).

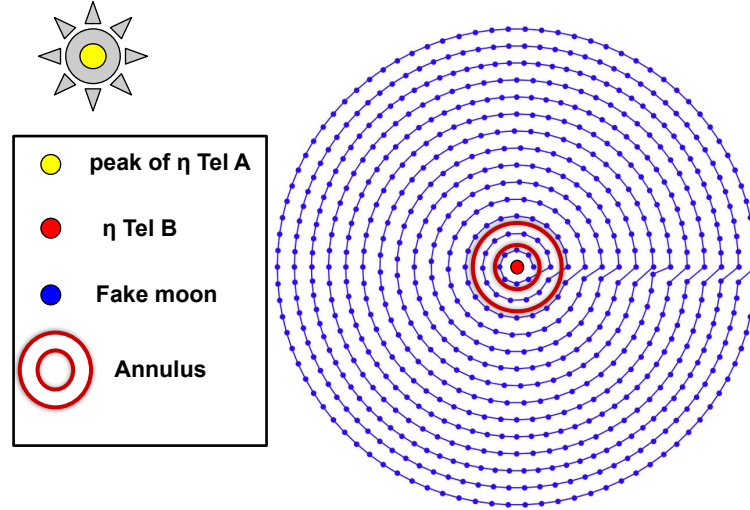


Figure 3.8: Schematic representation of the placement of putative fake satellites around η Tel B to calculate the contrast curves. In this illustration, just one annulus is represented.

To robustly establish astrometry and photometry for the sub-stellar companion, we employed the NEGFC customized routine presented in (Lazzoni et al., 2020). This approach was applied to each frame of the scientific datacube, as opposed to solely in the post-processed ADI image, as is conventionally practiced. Photometric results were derived by considering the median of each set of parameters per observation. Photometric errors were determined based on the standard deviation of the fluxes obtained per night. Astrometrical results (separation of 4.218 ± 0.004 arcsecs and position angle of 167.3 ± 0.2 degrees) were made taking into account not only the NEGFC approach but also incorporated an analysis using 2D Gaussian fitting and position of the peak intensity of the companion. This analysis was made for both the frame-by-frame approach and the median-collapsed ADI image. The final values represent the median of each approach. In addition, for the uncertainties, systematic and statistical uncertainties, akin to the methodology employed by Wertz et al. (2017), were employed. The separation reached depicts a 4-70 times improvement in precision in comparison with previous NACO observations described and observed by Neuhäuser et al. (2011), and ~ 2 times better precision than the L' NACO observations from Rameau et al. (2013b).

Furthermore, we conducted a comprehensive orbital characterization by compiling previous astrometric data, the new SPHERE data, and the Hipparcos-Gaia acceleration catalog, resulting in an orbital coverage spanning approximately 19 years. The findings indicate a well-characterized companion mass of $48 \pm 15 M_{\text{Jup}}$, with the best-fitting orbit demonstrating near-edge-on orientation ($i=81.9$ degrees) and low eccentricity ($e = 0.34$) when excluding orbits that can disrupt the debris disk around the star. However, it is essential to note that our observations did not encompass a significant portion of the entire orbit, leading to elevated uncertainties regarding the companion's orbital shape, period, eccentricity, and

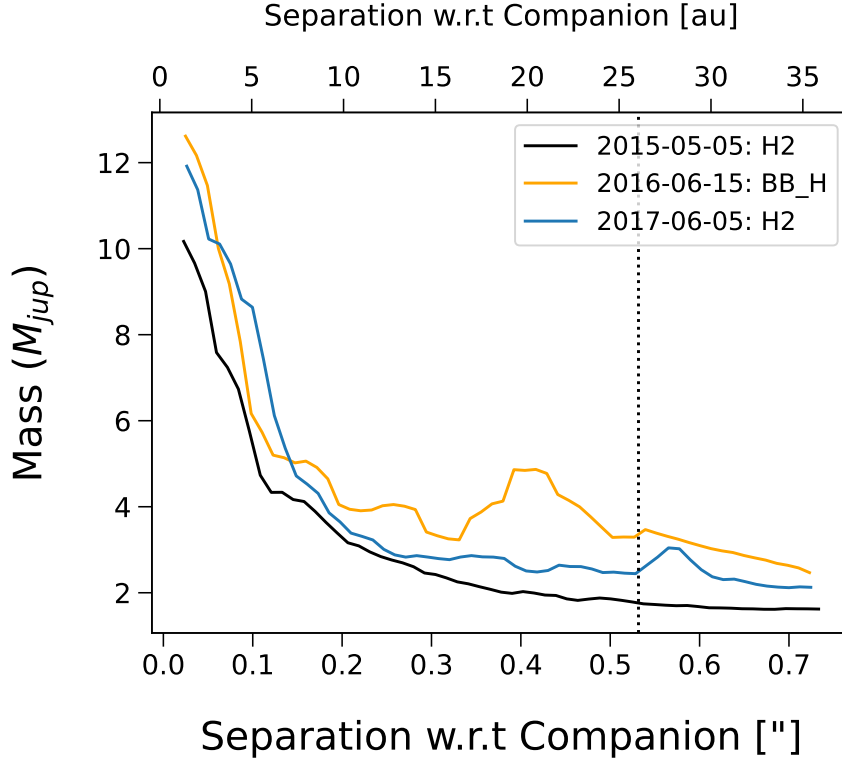


Figure 3.9: Contrast curves with respect to the star η Tel A, centered on the companion as depicted in Fig. 3.8. The three contrast curves, corresponding to different epochs, are showcased. The vertical dashed line indicates the Hill radius of η Tel B under the assumption of an orbit with an eccentricity of $e=0.34$

semi-major axis. We also highlight that due to the low orbital coverage, the orbital fitting presented represents a plausible family of orbits, and the orbital values listed in Table 3.7 must be taken as an example of a possible orbit. Further follow-ups will better constrain the orbit of the BD in the future. Also, based on the high $vsini$ of η Tel A, and the possible uncertainties on its measurements, we consider it plausible that HD 181327, at a separation of 20066 au, is bound to the system.

A brief discussion about possible formation scenarios has been conducted. The coplanarity between η Tel B and its debris disk, along with the relative spin alignment between the star and the debris disk, provides valuable insights into the system's formation. Stellar system formation scenarios were categorized into three main types: fragmentation of a core or filament, fragmentation of a massive disk, or dynamical interactions. Based on the separation of the star and companion, the likelihood of massive disk fragmentation or capture or ejection of η Tel B was highlighted as more plausible. Alternatively, the system's low eccentricity also allows for rotational fragmentation from a core scenario, if followed by fast inward migration. In summary, we tentatively propose the preferred formation involves either massive disk fragmentation with slow or no inward migration or rotational

fragmentation of a core with faster inward migration, whereas continuous monitoring and multiwavelength observations are crucial for refining these conclusions and further understanding the system's dynamics.

Lastly, a meticulous analysis of the companion's surroundings was undertaken by subtracting the companion's signal using instrument-response models. No clear signal of a substructure or satellite was seen. We conclude the systematics heavily affected the residuals. From the contrast curves generated in the regions surrounding the companion, we can discard satellites down to 3 and $1.6 M_{\text{Jup}}$ in the range of distances [10, 33] au, setting an upper limit on gravitational instability binary pairs or massive objects captured through tidal interactions at wider separations.

Future observations of the system with the next generation of high-contrast imagers mounted on space telescopes, likewise, JWST (James Webb Space Telescope) will further constrain the orbital analysis of the brown dwarf companion and allow for deeper contrast around the central star and the companion. This advancement will enable deeper contrast observations around both the central star and its companion. In the specific case of RV monitoring for detecting objects at closer separations, instruments like CRIRES+ (Cryogenic high-resolution InfraRed Echelle Spectrograph) or HiRISE (High Resolution Imaging Science Experiment), are suitable. Possible additional companions to the central star or the brown dwarf may be detected in the future.

3.6 Appendix

3.6.1 Cornerplot of the orbital fitting

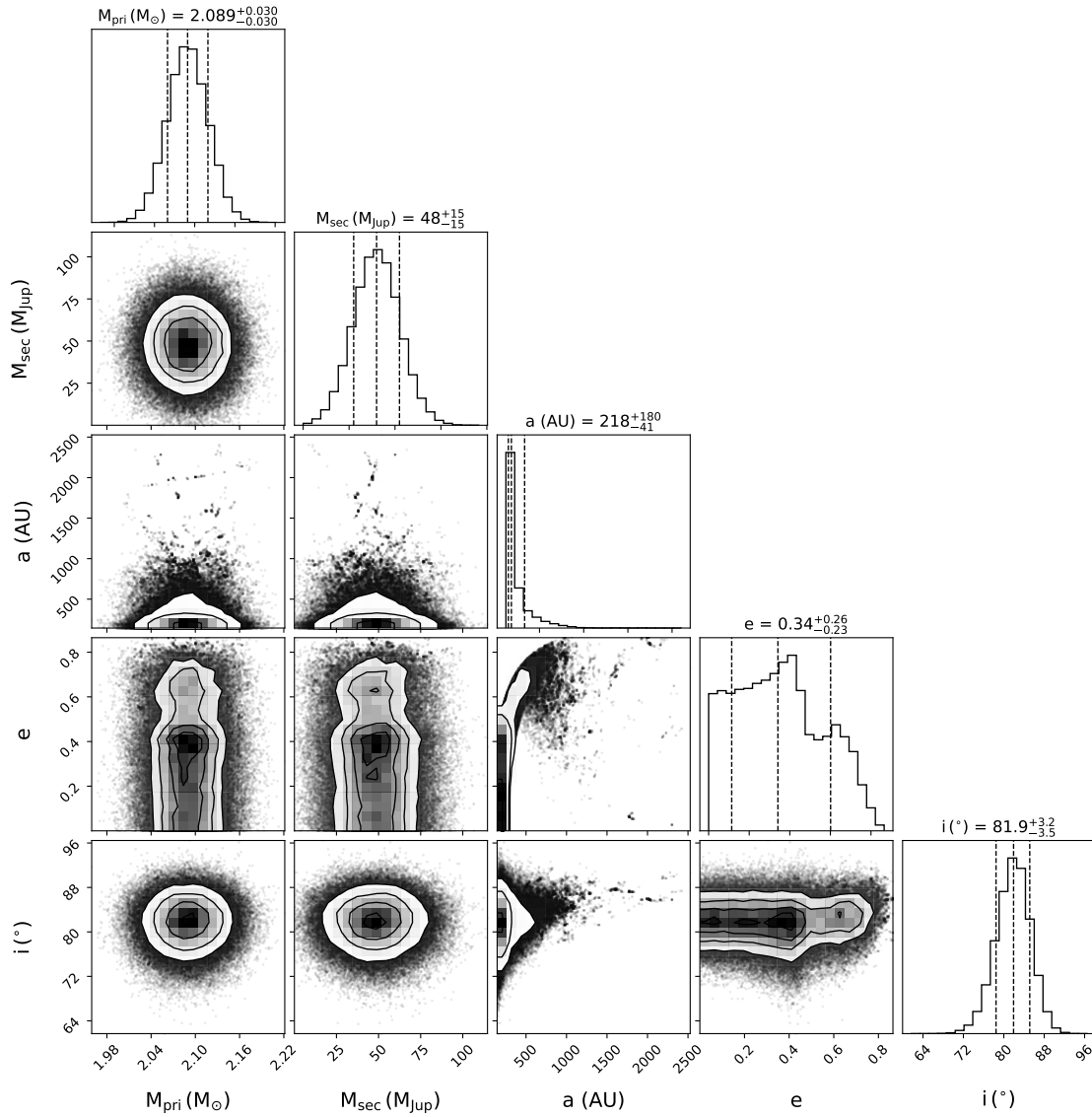


Figure 3.10: Corner plot showing the results of the orbital fitting performed by Orvara, after excluding orbits based on constraints described in section 3.4.1. The best-fit values are also reported in Table 3.7.

CHAPTER 4

FINAL REMARKS AND CONCLUSIONS

This thesis's main goal is to highlight the importance of observations regarding fundamental aspects of multiple (sub)stellar formation and evolution. The thesis comprises two comprehensive studies of distinct multiple systems: an eruptive binary system, HBC 494, and a more evolved binary system, η Telescopii. Each investigation employs different observational instruments operating at distinct wavelengths. I hope that new readers won't become entangled in the technical details presented in both papers in Chapter 2 and Chapter 3, as the fundamental concepts are (hopefully) elucidated in the comprehensive introduction (Chapter 1). The narrative presented in this thesis unfolds as follows.

In Chapter 2, we refer to the detailed study of HBC 494. HBC 494, as an eruptive YSO system in the Orion Molecular Cloud, was subjected to high-resolution ALMA observations. These observations resolved the system into two components separated by ~ 75 au, HBC 494 N and HBC 494 S, thus offering a comprehensive view of the morphology and dynamics of the system. The FUor-like characteristics of the northern component and EXor-like features in the southern component highlight the diversity within the system. Molecular line observations further revealed bipolar outflows and rotating, infalling envelopes, enriching our understanding of the dynamics in such eruptive binary systems.

Turning our attention to η Telescopii (Chapter 3), a binary system where the companion is a brown dwarf companion, high-contrast imaging campaigns spanning over two decades provided crucial data for orbital and photometric characterization. Detailed analysis of SPHERE/IRDIS coronagraphic observations allowed for precise measurements of the companion's astrometric positions, resulting in the smallest astrometric uncertainties for η Tel B to date. The orbital analysis unveiled a low eccentric orbit with a nearly edge-on inclination and a semi-major axis of 214 au. A rather new and promissory analysis using HCI observations was applied to search for satellites or other features around η Tel B, failing to detect but useful to provide deeper contrasts for upcoming analysis with different instruments and resolution power.

Together, these studies contribute valuable information to the broader field of multiple stellar formation. The episodic accretion phenomenon observed in HBC 494 showcases the mechanism of episodic accretion within binary systems, while the detailed characterization of η Telescopii's binary system enriches our understanding of binary dynamics and high-contrast imaging studies of substellar companions. These findings collectively emphasize the importance of investigating various stellar systems to unravel the intricate processes that govern their formation and evolution.

4.1 Specific questions/concepts addressed

In this work, we address, analyze, and provide insights on the following questions:

4.1.1 What is the correlation between stellar multiplicity and accretion processes, and why are binary eruptive systems so infrequently observed?

These questions remain unanswered, and due to the limited number of known multiple eruptive young stellar object (YSO) systems, expressing the occurrence and significance of these events proves challenging. However, two critical aspects warrant consideration. Firstly, binaries are notably prevalent in the Galaxy, as indicated by various citations. Secondly, certain studies propose that eruptive accretion, occurring on different scales, may be common among low-mass YSOs throughout their evolutionary stages (see, for example, [Cieza et al., 2018](#); [Hales et al., 2020](#)). Therefore, additional (sub)millimeter observations of eruptive binary systems are imperative to reveal the role of episodic accretion in the evolution of multiple systems.

To date, only a limited number of eruptive stars have been detected and spectroscopically characterized, with a small fraction of them being part of multiple systems. The findings presented in Chapter 2 suggest that the scarcity of observations may be linked to their resolution power. In the same chapter, attention is drawn to the lack of a precise answer regarding how multiple eruptive YSOs can influence the outbursting and accretion of individual components. The analysis reveals that the disks in multiple eruptive systems are more compact but also more massive than regular YSOs at the same stage/environment. However, the examination of HBC 494 gas on a scale appropriate to the continuum disks remains inconclusive about how the material can flow from one object to the other or remain unaltered by the other component. Therefore, a lingering question that remains and can be addressed with more observations of multiple eruptive YSO systems, using optically thinner tracers, is whether the enhancement of accretion in one disk can trigger effects on another disk, or if they both initiate the FUor/Exor stage simultaneously.

4.1.2 How robust astrometric analysis of a system contribute to its characterization

Despite the revealing nature of HCI observations in uncovering remarkable systems, the observed substellar companions, until now, have commonly shared a characteristic: a large semi-major axis of approximately 10 AU or more, leading to orbits with periods of years. Consequently, continuous HCI astrometric follow-up over the years is essential to refine our understanding of these systems and unravel their dynamics. One example of such an approach and successful results is given for η Tel system, in Chapter 3. The analysis of η Tel underscores its significance in achieving a comprehensive understanding of the system when integrated with extensive observations spanning nearly two decades.

However, it is crucial to acknowledge an important aspect. The orbital fitting for widely separated systems lacking thorough orbital coverage from HCI observations is highly sensitive to the precision of astrometric measurements. The initial “raw” results obtained for η Tel B were deemed physically implausible due to higher eccentricities obtained for the companion, which would cause instability and disruption in the closer-in debris disk. Fortunately, the η Tel system’s constraints allowed for a more refined assessment of possible orbits in this work. It’s worth noting that these priors may not be achievable for all HCI systems. Thus, the study underscores the significance of obtaining more precise astrometric measurements to derive more physically meaningful orbital results.

The importance of robust astrometric measurements for HCI companions becomes even more pronounced, particularly in the case of multiplanetary systems like HR 8799, β Pic, or even PDS 70 with its two protoplanets. The impact of dynamical analysis is not limited to orbital properties; it also extends to crucial aspects such as mass retrieval. In subsection 1.2.4, particularly in the discussion of remarkable systems observed via HCI, it becomes apparent that planetary masses, even when derived from various studies, exhibit considerable uncertainty. The spectrum of masses for each exoplanetary companion discussed in that section spans both dynamical masses and masses calculated from luminosity-age evolutionary models. The latter derivation also highlights the importance of robust photometric retrieval, as was done to η Tel B. In my analysis of the companion, however, I only assumed the mass derived from the orbit fitting.

4.1.3 How can one deduct the formation scenario for multiple systems?

I tentatively answer this question in the specific cases of HBC 494 (Chapter 2) and η Tel (Chapter 3) components. The only way to link formation scenarios from early YSO stages to mature systems is through simulations. While simulations play a pivotal role in this process, observations alone can also offer insights.

In environments with specific conditions, discerning a formation scenario becomes plausible. In the cases of HBC 494 and η Tel components, the proposed scenario suggests rotational disk fragmentation rather than direct collapsing. This conclusion is drawn from the orbital alignment—quasi-coplanarity of HBC 494 N and S inferred from similar inclinations and PAs between the components of the system, and quasi-coplanarity between η Tel B and the debris disk inferred from the inclinations. Therefore, observations of multiple systems in different stages may serve as a control test, establishing a connection between (sub)stellar formation and their subsequent evolution.

Alternative methods of detecting the formation scenario, such as observing regions of protoplanetary disks susceptible to gravitational instability (GI), can also provide useful insights. However, discovering the formation scenario without unveiling the gas/dust dynamics between YSOs (as in the case of HBC 494) or in more evolved systems with (nearly) depleted gas, such as in the case of η Tel, remains challenging.

4.1.4 Is it possible to search for satellites orbiting substellar companions via HCI?

The answer to this question is yes. The deep analysis done for η Tel B surroundings in Chapter 3 was heavily inspired by the notable satellite candidate unveiled through SPHERE observations around DH Tau B (Lazzoni et al., 2020), yet to be confirmed. Although we pushed to the limits of one of the best modern high-contrast imagers (SPHERE) till the moment, the non-detection of a satellite or structure surrounding η Tel B does not completely discard the possibility of an orbiting unresolved source. It just provides deeper contrasts showing limitations that HCI observations may overcome to possibly find objects surrounding η Tel B. I highlight that no blind detection will necessarily be proven successful, and η Tel B's surroundings can be indeed empty. But, as an HCI explorer/researcher, part of the journey is to sail through seas of the unknown.

To tackle the problem for η Tel and other systems but with the same instrument, better PSF models need to be created, which can be provided by different observing strategies and cadence of models' creation. Alternatively, the next generation of ground-based high-contrast imagers, boasting improved resolving power and enhanced Adaptive Optics (AO), or space-based high-contrast imagers like the James Webb Space Telescope, may provide noteworthy increase in sensitivity and/or resolution in the coming years and decades (see Currie et al., 2023 for an updated review of the next generation instruments dedicated to HCI). Indeed, the future of HCI is promising.

During the course of my PhD, I, as PI, got three successful observing proposals using SPHERE proposals to detect satellites/structures around 15 promising substellar companions, including η Tel. Using the star-hopping (a Reference-star differential imaging observing strategy; (Wahhaj et al., 2021), I plan to observe these substellar companions, obtaining a quasi-simultaneous model of the instrumental PSF. This approach involves alternating between our target and a reference star until the end of the sequence, minimizing turbulence and improving efficiency in retrieving features. Star-hopping enhances data quality by providing multiple PSFs compared to standard IRDIS observations. Additionally, the negative fake companion technique, also used in Chapter 3, will be applied in post-processing to create models of the companion from the reference star. Subsequently, these models will be subtracted from the data, and a following analysis of the residuals will be performed for further insights. This approach is thus, one example of how HCI can be performed and optimized for the search of companions' companions.

BIBLIOGRAPHY

- Ackerman, A. S. & Marley, M. S. (2001). Precipitating Condensation Clouds in Substellar Atmospheres. *Astrophysical Journal*, 556(2), 872–884.
- Adachi, I., Hayashi, C., & Nakazawa, K. (1976). The gas drag effect on the elliptical motion of a solid body in the primordial solar nebula. *Progress of Theoretical Physics*, 56, 1756–1771.
- Agol, E., Jansen, T., Lacy, B., Robinson, T. D., & Meadows, V. (2015). The Center of Light: Spectroastrometric Detection of Exomoons. *Astrophysical Journal*, 812(1), 5.
- Akeson, R. L., Chen, X., Ciardi, D., Crane, M., Good, J., Harbut, M., Jackson, E., Kane, S. R., Laity, A. C., Leifer, S., Lynn, M., McElroy, D. L., Papin, M., Plavchan, P., Ramírez, S. V., Rey, R., von Braun, K., Wittman, M., Abajian, M., Ali, B., Beichman, C., Beekley, A., Berriman, G. B., Berukoff, S., Bryden, G., Chan, B., Groom, S., Lau, C., Payne, A. N., Regelson, M., Saucedo, M., Schmitz, M., Stauffer, J., Wyatt, P., & Zhang, A. (2013). The NASA Exoplanet Archive: Data and Tools for Exoplanet Research. *Astronomical Society of the Pacific*, 125(930), 989.
- Alibert, Y., Mousis, O., & Benz, W. (2005). Modeling the Jovian subnebula. I. Thermodynamic conditions and migration of proto-satellites. *Astronomy and Astrophysics*, 439(3), 1205–1213.
- Allard, F., Hauschildt, P. H., Alexander, D. R., Tamanai, A., & Schweitzer, A. (2001). The Limiting Effects of Dust in Brown Dwarf Model Atmospheres. *Astrophysical Journal*, 556(1), 357–372.
- Amara, A. & Quanz, S. P. (2012a). PYNPOINT: an image processing package for finding exoplanets. *Monthly Notices of the RAS*, 427(2), 948–955.
- Amara, A. & Quanz, S. P. (2012b). PYNPOINT: an image processing package for finding exoplanets. *Monthly Notices of the RAS*, 427(2), 948–955.
- André, P., Arzoumanian, D., Könyves, V., Shimajiri, Y., & Palmeirim, P. (2019). The role of molecular filaments in the origin of the prestellar core mass function and stellar initial mass function. *Astronomy and Astrophysics*, 629, L4.

- Andrews, S. M., Huang, J., Pérez, L. M., Isella, A., Dullemond, C. P., Kurtovic, N. T., Guzmán, V. V., Carpenter, J. M., Wilner, D. J., Zhang, S., Zhu, Z., Birnstiel, T., Bai, X.-N., Benisty, M., Hughes, A. M., Öberg, K. I., & Ricci, L. (2018). The Disk Substructures at High Angular Resolution Project (DSHARP). I. Motivation, Sample, Calibration, and Overview. *Astrophysical Journal, Letters*, 869(2), L41.
- Andrews, S. M. & Williams, J. P. (2005). Circumstellar Dust Disks in Taurus-Auriga: The Submillimeter Perspective. *Astrophysical Journal*, 631, 1134–1160.
- Andrews, S. M. & Williams, J. P. (2007). A Submillimeter View of Circumstellar Dust Disks in ρ Ophiuchi. *Astrophysical Journal*, 671(2), 1800–1812.
- Arce, H. G. & Sargent, A. I. (2006). The Evolution of Outflow-Envelope Interactions in Low-Mass Protostars. *Astrophysical Journal*, 646(2), 1070–1085.
- Armitage, P. J., Livio, M., & Pringle, J. E. (2001). Episodic accretion in magnetically layered protoplanetary discs. *Monthly Notices of the RAS*, 324, 705–711.
- Audard, M., Ábrahám, P., Dunham, M. M., Green, J. D., Grosso, N., Hamaguchi, K., Kastner, J. H., Kóspál, Á., Lodato, G., Romanova, M. M., Skinner, S. L., Vorobyov, E. I., & Zhu, Z. (2014). Episodic Accretion in Young Stars. *Protostars and Planets VI*, (pp. 387–410).
- Avenhaus, H., Quanz, S. P., Garufi, A., Perez, S., Casassus, S., Pinte, C., Bertrang, G. H. M., Caceres, C., Benisty, M., & Dominik, C. (2018). Disks around T Tauri Stars with SPHERE (DARTTS-S). I. SPHERE/IRDIS Polarimetric Imaging of Eight Prominent T Tauri Disks. *Astrophysical Journal*, 863(1), 44.
- Backman, D. E. & Paresce, F. (1993). Main-Sequence Stars with Circumstellar Solid Material - the VEGA Phenomenon. In E. H. Levy & J. I. Lunine (Eds.), *Protostars and Planets III* (pp. 1253).
- Bae, J., Isella, A., Zhu, Z., Martin, R., Okuzumi, S., & Suriano, S. (2023). Structured Distributions of Gas and Solids in Protoplanetary Disks. In S. Inutsuka, Y. Aikawa, T. Muto, K. Tomida, & M. Tamura (Eds.), *Protostars and Planets VII*, volume 534 of *Astronomical Society of the Pacific Conference Series* (pp. 423).

- Bae, J., Zhu, Z., Baruteau, C., Benisty, M., Dullemond, C. P., Facchini, S., Isella, A., Keppler, M., Pérez, L. M., & Teague, R. (2019). An Ideal Testbed for Planet-Disk Interaction: Two Giant Protoplanets in Resonance Shaping the PDS 70 Protoplanetary Disk. *Astrophysical Journal, Letters*, 884(2), L41.
- Bailer-Jones, C. A. L., Rybizki, J., Fouesneau, M., Demleitner, M., & Andrae, R. (2021). Estimating Distances from Parallaxes. V. Geometric and Photogeometric Distances to 1.47 Billion Stars in Gaia Early Data Release 3. *Astronomical Journal*, 161(3), 147.
- Bailey, J. (2014). The Dawes Review 3: The Atmospheres of Extrasolar Planets and Brown Dwarfs. *Publications of the Astron. Soc. of Australia*, 31, e043.
- Banzatti, A., Pontoppidan, K. M., Bruderer, S., Muzerolle, J., & Meyer, M. R. (2015). Depletion of Molecular Gas by an Accretion Outburst in a Protoplanetary Disk. *Astrophysical Journal, Letters*, 798, L16.
- Baraffe, I., Homeier, D., Allard, F., & Chabrier, G. (2015). New evolutionary models for pre-main sequence and main sequence low-mass stars down to the hydrogen-burning limit. *Astronomy and Astrophysics*, 577, A42.
- Barman, T. S., Macintosh, B., Konopacky, Q. M., & Marois, C. (2011). Clouds and Chemistry in the Atmosphere of Extrasolar Planet HR8799b. *Astrophysical Journal*, 733(1), 65.
- Barrado Y Navascués, D. (2006). On the age of the TW Hydrae association and 2M1207334-393254. *Astronomy and Astrophysics*, 459(2), 511–518.
- Bate, M. R. (2000). Predicting the properties of binary stellar systems: the evolution of accreting protobinary systems. *Monthly Notices of the RAS*, 314(1), 33–53.
- Bate, M. R. (2018). On the diversity and statistical properties of protostellar discs. *Monthly Notices of the RAS*, 475(4), 5618–5658.
- Bate, M. R. (2019). The statistical properties of stars and their dependence on metallicity. *Monthly Notices of the RAS*, 484(2), 2341–2361.
- Bate, M. R. & Bonnell, I. A. (1997). Accretion during binary star formation - II. Gaseous accretion and disc formation. *Monthly Notices of the RAS*, 285(1), 33–48.

- Bate, M. R. & Burkert, A. (1997). Resolution requirements for smoothed particle hydrodynamics calculations with self-gravity. *Monthly Notices of the RAS*, 288(4), 1060–1072.
- Beckwith, S. V. W., Sargent, A. I., Chini, R. S., & Guesten, R. (1990). A Survey for Circumstellar Disks around Young Stellar Objects. *Astronomical Journal*, 99, 924.
- Bell, C. P. M., Mamajek, E. E., & Naylor, T. (2015). A self-consistent, absolute isochronal age scale for young moving groups in the solar neighbourhood. *Monthly Notices of the RAS*, 454(1), 593–614.
- Benisty, M., Bae, J., Facchini, S., Keppler, M., Teague, R., Isella, A., Kurtovic, N. T., Pérez, L. M., Sierra, A., Andrews, S. M., Carpenter, J., Czekala, I., Dominik, C., Henning, T., Menard, F., Pinilla, P., & Zurlo, A. (2021). A Circumplanetary Disk around PDS70c. *Astrophysical Journal, Letters*, 916(1), L2.
- Bergin, E. A. & Williams, J. P. (2017). The Determination of Protoplanetary Disk Masses. In M. Pessah & O. Gressel (Eds.), *Formation, Evolution, and Dynamics of Young Solar Systems*, volume 445 of *Astrophysics and Space Science Library* (pp. 1). (pp. 1).
- Beust, H., Augereau, J. C., Bonsor, A., Graham, J. R., Kalas, P., Lebreton, J., Lagrange, A. M., Ertel, S., Faramaz, V., & Thébault, P. (2014). An independent determination of Fomalhaut b’s orbit and the dynamical effects on the outer dust belt. *Astronomy and Astrophysics*, 561, A43.
- Beuzit, J. L., Vigan, A., Mouillet, D., Dohlen, K., Gratton, R., Boccaletti, A., Sauvage, J. F., Schmid, H. M., Langlois, M., Petit, C., Baruffolo, A., Feldt, M., Milli, J., Wahhaj, Z., Abe, L., Anselmi, U., Antichi, J., Barette, R., Baudrand, J., Baudoz, P., Bazzon, A., Bernardi, P., Blanchard, P., Brast, R., Bruno, P., Buey, T., Carbillet, M., Carle, M., Cascone, E., Chapron, F., Charton, J., Chauvin, G., Claudi, R., Costille, A., De Caprio, V., de Boer, J., Delboulbé, A., Desidera, S., Dominik, C., Downing, M., Dupuis, O., Fabron, C., Fantinel, D., Farisato, G., Feautrier, P., Fedrigo, E., Fusco, T., Gigan, P., Ginski, C., Girard, J., Giro, E., Gisler, D., Gluck, L., Gry, C., Henning, T., Hubin, N., Hugot, E., Incorvaia, S., Jaquet, M., Kasper, M., Lagadec, E., Lagrange, A. M., Le Coroller, H., Le Mignant, D., Le Ruyet, B., Lessio, G., Lizon, J. L., Llored, M., Lundin, L.,

Madec, F., Magnard, Y., Marteau, M., Martinez, P., Maurel, D., Ménard, F., Mesa, D., Möller-Nilsson, O., Moulin, T., Moutou, C., Origné, A., Parisot, J., Pavlov, A., Perret, D., Pragt, J., Puget, P., Rabou, P., Ramos, J., Reess, J. M., Rigal, F., Rochat, S., Roelfsema, R., Rousset, G., Roux, A., Saisse, M., Salasnich, B., Santambrogio, E., Scuderi, S., Segransan, D., Sevin, A., Siebenmorgen, R., Soenke, C., Stadler, E., Suarez, M., Tiphène, D., Turatto, M., Udry, S., Vakkili, F., Waters, L. B. F. M., Weber, L., Wildi, F., Zins, G., & Zurlo, A. (2019). SPHERE: the exoplanet imager for the Very Large Telescope. *Astronomy and Astrophysics*, 631, A155.

Bhowmik, T. (2020). *Resolved spectroscopy of debris disks with SPHERE/VLT*. PhD thesis, Observatoire de Paris, Laboratoire d'Etudes Spatiales et d'Instrumentation en Astrophysique.

Birnstiel, T., Dullemond, C. P., & Brauer, F. (2009). Dust retention in protoplanetary disks. *Astronomy and Astrophysics*, 503(1), L5–L8.

Blum, J. & Wurm, G. (2008). The growth mechanisms of macroscopic bodies in protoplanetary disks. *Annual Review of Astron and Astrophysics*, 46, 21–56.

Boccaletti, A., Lagage, P. O., Baudoz, P., Beichman, C., Bouchet, P., Cavarroc, C., Dubreuil, D., Glasse, A., Glauser, A. M., Hines, D. C., Lajoie, C. P., LEBRETON, J., Perrin, M. D., Pueyo, L., Reess, J. M., Rieke, G. H., Ronayette, S., Rouan, D., Soummer, R., & Wright, G. S. (2015). The Mid-Infrared Instrument for the James Webb Space Telescope, V: Predicted Performance of the MIRI Coronagraphs. *Astronomical Society of the Pacific*, 127(953), 633.

Bodenheimer, P. & Pollack, J. B. (1986). Calculations of the accretion and evolution of giant planets: The effects of solid cores. *Icarus*, 67(3), 391–408.

Boehler, Y., Weaver, E., Isella, A., Ricci, L., Grady, C., Carpenter, J., & Perez, L. (2017). A Close-up View of the Young Circumbinary Disk HD 142527. *Astrophysical Journal*, 840(1), 60.

Bohn, A. J., Ginski, C., Kenworthy, M. A., Mamajek, E. E., Pecaut, M. J., Mugrauer, M., Vogt, N., Adam, C., Meshkat, T., Reggiani, M., & Snik, F. (2021). Discovery of a directly imaged planet to the young solar analog YSES 2. *Astronomy and Astrophysics*, 648, A73.

- Bonnell, I. & Bastien, P. (1992). A binary origin for FU Orionis stars. *Astrophysical Journal, Letters*, 401, L31–L34.
- Bonnell, I. A. (1994). A New Binary Formation Mechanism. *Monthly Notices of the RAS*, 269, 837–848.
- Bonnell, I. A. & Bate, M. R. (1994a). Massive Circumbinary Discs and the Formation of Multiple Systems. *Monthly Notices of the RAS*, 269, L45–L48.
- Bonnell, I. A. & Bate, M. R. (1994b). The Formation of Close Binary Systems. *Monthly Notices of the RAS*, 271, 999–1004.
- Borchert, E. M. A., Price, D. J., Pinte, C., & Cuello, N. (2022a). On the rise times in FU Orionis events. *Monthly Notices of the RAS*, 510(1), L37–L41.
- Borchert, E. M. A., Price, D. J., Pinte, C., & Cuello, N. (2022b). Sustained FU Orionis-type outbursts from colliding discs in stellar flybys. *Monthly Notices of the RAS*, 517(3), 4436–4446.
- Borchert, E. M. A., Price, D. J., Pinte, C., & Cuello, N. (2022c). Sustained FU Orionis-type outbursts from colliding discs in stellar flybys. *Monthly Notices of the RAS*, 517(3), 4436–4446.
- Boss, A. P. (1997). Giant planet formation by gravitational instability. *Science*, 276, 1836–1839.
- Boss, A. P. & Bodenheimer, P. (1979). Fragmentation in a rotating protostar: a comparison of two three-dimensional computer codes. *Astrophysical Journal*, 234, 289–295.
- Boss, A. P., Butler, R. P., Hubbard, W. B., Ianna, P. A., Kürster, M., Lissauer, J. J., Mayor, M., Meech, K. J., Mignard, F., Penny, A. J., Quirrenbach, A., Tarter, J. C., & Vidal-Madjar, A. (2007). Working Group on Extrasolar Planets. *Transactions of the International Astronomical Union, Series A*, 26A, 183–186.
- Bowler, B. P., Blunt, S. C., & Nielsen, E. L. (2020). Population-level Eccentricity Distributions of Imaged Exoplanets and Brown Dwarf Companions: Dynamical Evidence for Distinct Formation Channels. *Astronomical Journal*, 159(2), 63.

- Brandt, G. M., Brandt, T. D., Dupuy, T. J., Li, Y., & Michalik, D. (2021a). Precise Dynamical Masses and Orbital Fits for β Pic b and β Pic c. *Astronomical Journal*, 161(4), 179.
- Brandt, G. M., Brandt, T. D., Dupuy, T. J., Michalik, D., & Marleau, G.-D. (2021b). The First Dynamical Mass Measurement in the HR 8799 System. *Astrophysical Journal, Letters*, 915(1), L16.
- Brandt, T. D. (2021). The Hipparcos-Gaia Catalog of Accelerations: Gaia EDR3 Edition. *Astrophysical Journal, Supplement*, 254(2), 42.
- Brandt, T. D., Dupuy, T. J., Li, Y., Brandt, G. M., Zeng, Y., Michalik, D., Bardalez Gagliuffi, D. C., & Raposo-Pulido, V. (2021c). orvara: An Efficient Code to Fit Orbits Using Radial Velocity, Absolute, and/or Relative Astrometry. *Astronomical Journal*, 162(5), 186.
- Brown-Sevilla, S. B., Maire, A. L., Mollière, P., Samland, M., Feldt, M., Brandner, W., Henning, T., Gratton, R., Janson, M., Stolker, T., Hagelberg, J., Zurlo, A., Cantalloube, F., Boccaletti, A., Bonnefoy, M., Chauvin, G., Desidera, S., D’Orazi, V., Lagrange, A. M., Langlois, M., Menard, F., Mesa, D., Meyer, M., Pavlov, A., Petit, C., Rochat, S., Rouan, D., Schmidt, T., Vigan, A., & Weber, L. (2023). Revisiting the atmosphere of the exoplanet 51 Eridani b with VLT/SPHERE. *Astronomy and Astrophysics*, 673, A98.
- Burkert, A., Bate, M. R., & Bodenheimer, P. (1997). Protostellar fragmentation in a power-law density distribution. *Monthly Notices of the RAS*, 289(3), 497–504.
- Burrows, A., Sudarsky, D., & Lunine, J. I. (2003). Beyond the T Dwarfs: Theoretical Spectra, Colors, and Detectability of the Coolest Brown Dwarfs. *Astrophysical Journal*, 596(1), 587–596.
- Canup, R. M. & Ward, W. R. (2002). Formation of the Galilean Satellites: Conditions of Accretion. *Astronomical Journal*, 124(6), 3404–3423.
- CASA Team, Bean, B., Bhatnagar, S., Castro, S., Donovan Meyer, J., Emonts, B., Garcia, E., Garwood, R., Golap, K., Gonzalez Villalba, J., Harris, P., Hayashi, Y., Hoskins, J., Hsieh, M., Jagannathan, P., Kawasaki, W., Keimpema, A., Kettanis, M., Lopez, J., Marvil, J., Masters, J., McNichols, A., Mehringer, D., Miel, R., Moellenbrock, G., Montesino, F., Nakazato, T., Ott, J., Petry, D., Pokorny,

- M., Raba, R., Rau, U., Schiebel, D., Schweighart, N., Sekhar, S., Shimada, K., Small, D., Steeb, J.-W., Sugimoto, K., Suoranta, V., Tsutsumi, T., van Bemmell, I. M., Verkouter, M., Wells, A., Xiong, W., Szomoru, A., Griffith, M., Glendenning, B., & Kern, J. (2022). CASA, the Common Astronomy Software Applications for Radio Astronomy. *Astronomical Society of the Pacific*, 134(1041), 114501.
- Chabrier, G. & Baraffe, I. (1997). Structure and evolution of low-mass stars. *Astronomy and Astrophysics*, 327, 1039–1053.
- Chambers, J. E. (2014). Giant planet formation with pebble accretion. *Icarus*, 233, 83–100.
- Chauvin, G., Lagrange, A. M., Dumas, C., Zuckerman, B., Mouillet, D., Song, I., Beuzit, J. L., & Lowrance, P. (2004). A giant planet candidate near a young brown dwarf. Direct VLT/NACO observations using IR wavefront sensing. *Astronomy and Astrophysics*, 425, L29–L32.
- Chauvin, G., Lagrange, A. M., Dumas, C., Zuckerman, B., Mouillet, D., Song, I., Beuzit, J. L., & Lowrance, P. (2005). Giant planet companion to 2MASSW J1207334-393254. *Astronomy and Astrophysics*, 438(2), L25–L28.
- Chiang, E., Kite, E., Kalas, P., Graham, J. R., & Clampin, M. (2009). Fomalhaut’s Debris Disk and Planet: Constraining the Mass of Fomalhaut b from disk Morphology. *Astrophysical Journal*, 693(1), 734–749.
- Chiang, E. & Youdin, A. N. (2010). Forming Planetesimals in Solar and Extrasolar Nebulae. *Annual Review of Earth and Planetary Sciences*, 38, 493–522.
- Chiang, E. I. & Goldreich, P. (1997). Spectral Energy Distributions of T Tauri Stars with Passive Circumstellar Disks. *Astrophysical Journal*, 490(1), 368–376.
- Chiang, H.-F., Reipurth, B., Walawender, J., Connelley, M. S., Pessev, P., Geballe, T. R., Best, W. M. J., & Paegert, M. (2015). The Brightening of Re50N: Accretion Event or Dust Clearing? *Astrophysical Journal*, 805(1), 54.
- Cieza, L. A., González-Ruilova, C., Hales, A. S., Pinilla, P., Ruíz-Rodríguez, D., Zurlo, A., Casassus, S., Pérez, S., Cánovas, H., Arce-Tord, C., Flock, M., Kurtovic, N., Marino, S., Nogueira, P. H., Perez, L., Price, D. J., Principe, D. A., & Williams,

- J. P. (2021). The Ophiuchus Disc Survey Employing ALMA (ODISEA) - III. The evolution of substructures in massive discs at 3-5 au resolution. *Monthly Notices of the RAS*, 501(2), 2934–2953.
- Cieza, L. A., Ruíz-Rodríguez, D., Perez, S., Casassus, S., Williams, J. P., Zurlo, A., Principe, D. A., Hales, A., Prieto, J. L., Tobin, J. J., Zhu, Z., & Marino, S. (2018). The ALMA early science view of FUor/EXor objects - V. Continuum disc masses and sizes. *Monthly Notices of the RAS*, 474(4), 4347–4357.
- Clarke, C. J. & Pringle, J. E. (1993). Accretion disc response to a stellar fly-by. *Monthly Notices of the RAS*, 261(1), 190–202.
- Claudi, R. U., Turatto, M., Gratton, R. G., Antichi, J., Bonavita, M., Bruno, P., Cascone, E., De Caprio, V., Desidera, S., Giro, E., Mesa, D., Scuderi, S., Dohlen, K., Beuzit, J. L., & Puget, P. (2008). SPHERE IFS: the spectro differential imager of the VLT for exoplanets search. In I. S. McLean & M. M. Casali (Eds.), *Ground-based and Airborne Instrumentation for Astronomy II*, volume 7014 of *Society of Photo-Optical Instrumentation Engineers (SPIE) Conference Series* (pp. 70143E).
- Cohen, M. & Kuhl, L. V. (1979). Observational studies of pre-main-sequence evolution. *Astrophysical Journal, Supplement*, 41, 743–843.
- Connelley, M. S. & Reipurth, B. (2018). A Near-infrared Spectroscopic Survey of FU Orionis Objects. *Astrophysical Journal*, 861(2), 145.
- Crepp, J. R., Principe, D. A., Wolff, S., Giorla Godfrey, P. A., Rice, E. L., Cieza, L., Pueyo, L., Bechter, E. B., & Gonzales, E. J. (2018). GPI Spectroscopy of the Mass, Age, and Metallicity Benchmark Brown Dwarf HD 4747 B. *Astrophysical Journal*, 853(2), 192.
- Cruz-Sáenz de Miera, F., Kóspál, Á., Abraham, P., Liu, H. B., & Takami, M. (2019). Resolved ALMA Continuum Image of the Circumbinary Ring and Circumstellar Disks in the L1551 IRS 5 System. *Astrophysical Journal, Letters*, 882(1), L4.
- Cuello, N., Dipierro, G., Mentiplay, D., Price, D. J., Pinte, C., Cuadra, J., Laibe, G., Ménard, F., Poblete, P. P., & Montesinos, M. (2019). Flybys in protoplanetary discs: I. Gas and dust dynamics. *Monthly Notices of the RAS*, 483(3), 4114–4139.

- Cuello, N., Louvet, F., Mentiplay, D., Pinte, C., Price, D. J., Winter, A. J., Nealon, R., Ménard, F., Lodato, G., Dipierro, G., Christiaens, V., Montesinos, M., Cuadra, J., Laibe, G., Cieza, L., Dong, R., & Alexander, R. (2020). Flybys in protoplanetary discs - II. Observational signatures. *Monthly Notices of the RAS*, 491(1), 504–514.
- Cuello, N., Ménard, F., & Price, D. J. (2023). Close encounters: How stellar flybys shape planet-forming discs. *European Physical Journal Plus*, 138(1), 11.
- Currie, T., Biller, B., Lagrange, A., Marois, C., Guyon, O., Nielsen, E. L., Bonnefoy, M., & De Rosa, R. J. (2023). Direct Imaging and Spectroscopy of Extrasolar Planets. In S. Inutsuka, Y. Aikawa, T. Muto, K. Tomida, & M. Tamura (Eds.), *Protostars and Planets VII*, volume 534 of *Astronomical Society of the Pacific Conference Series* (pp. 799).
- Currie, T., Burrows, A., Itoh, Y., Matsumura, S., Fukagawa, M., Apai, D., Madhusudhan, N., Hinz, P. M., Rodigas, T. J., Kasper, M., Pyo, T. S., & Ogino, S. (2011). A Combined Subaru/VLT/MMT 1-5 μm Study of Planets Orbiting HR 8799: Implications for Atmospheric Properties, Masses, and Formation. *Astrophysical Journal*, 729(2), 128.
- Currie, T., Cloutier, R., Brittain, S., Grady, C., Burrows, A., Muto, T., Kenyon, S. J., & Kuchner, M. J. (2015). Resolving the HD 100546 Protoplanetary System with the Gemini Planet Imager: Evidence for Multiple Forming, Accreting Planets. *Astrophysical Journal, Letters*, 814(2), L27.
- Currie, T., Cloutier, R., Debes, J. H., Kenyon, S. J., & Kaisler, D. (2013). A Deep Keck/NIRC2 Search for Thermal Emission from Planetary Companions Orbiting Fomalhaut. *Astrophysical Journal, Letters*, 777(1), L6.
- Currie, T., Fukagawa, M., Thalmann, C., Matsumura, S., & Plavchan, P. (2012). Direct Detection and Orbital Analysis of the Exoplanets HR 8799 bcd from Archival 2005 Keck/NIRC2 Data. *Astrophysical Journal, Letters*, 755(2), L34.
- Currie, T., Lawson, K., Schneider, G., Lyra, W., Wisniewski, J., Grady, C., Guyon, O., Tamura, M., Kotani, T., Kawahara, H., Brandt, T., Uyama, T., Muto, T., Dong, R., Kudo, T., Hashimoto, J., Fukagawa, M., Wagner, K., Lozi, J., Chilcote, J., Tobin, T., Groff, T., Ward-Duong, K., Januszewski, W., Norris, B., Tuthill, P.,

- van der Marel, N., Sitko, M., Deo, V., Vievard, S., Jovanovic, N., Martinache, F., & Skaf, N. (2022). Images of embedded Jovian planet formation at a wide separation around AB Aurigae. *Nature Astronomy*, 6, 751–759.
- Cushing, M. C., Kirkpatrick, J. D., Gelino, C. R., Griffith, R. L., Skrutskie, M. F., Mainzer, A., Marsh, K. A., Beichman, C. A., Burgasser, A. J., Prato, L. A., Simcoe, R. A., Marley, M. S., Saumon, D., Freedman, R. S., Eisenhardt, P. R., & Wright, E. L. (2011). The Discovery of Y Dwarfs using Data from the Wide-field Infrared Survey Explorer (WISE). *Astrophysical Journal*, 743(1), 50.
- Dahlqvist, C.-H. (2022). *Advanced Data Processing Techniques for Exoplanet Detection in High Contrast Images*. PhD thesis, University of Liège. Available at <https://orbi.uliege.be/handle/2268/293426>.
- Dahlqvist, C. H., Milli, J., Absil, O., Cantalloube, F., Matra, L., Choquet, E., del Burgo, C., Marshall, J. P., Wyatt, M., & Ertel, S. (2022). The SHARDDS survey: limits on planet occurrence rates based on point sources analysis via the Auto-RSM framework. *Astronomy and Astrophysics*, 666, A33.
- dal Ponte, M., Santiago, B., Carnero Rosell, A., De Paris, L., Pace, A. B., Bechtol, K., Abbott, T. M. C., Agüena, M., Allam, S., Alves, O., Bacon, D., Bertin, E., Bocquet, S., Brooks, D., Burke, D. L., Carrasco Kind, M., Carretero, J., Conselice, C., Costanzi, M., Desai, S., De Vicente, J., Doel, P., Everett, S., Ferrero, I., Flaugher, B., Frieman, J., García-Bellido, J., Gerdes, D. W., Gruendl, R. A., Gruen, D., Gutierrez, G., Hinton, S. R., Hollowood, D. L., James, D. J., Kuehn, K., Kuropatkin, N., Marshall, J. L., Mena-Fernández, J., Menanteau, F., Miquel, R., Ogando, R. L. C., Palmese, A., Paz-Chinchón, F., Pereira, M. E. S., Plazas Malagón, A. A., Pieres, A., Raveri, M., Rodriguez-Monroy, M., Sanchez, E., Scarpine, V., Schubnell, M., Sevilla-Noarbe, I., Smith, M., Soares-Santos, M., Suchyta, E., Swanson, M. E. C., Tarle, G., Thomas, D., To, C., Weaverdyck, N., & DES Collaboration (2023). Ultracool dwarfs candidates based on 6 yr of the Dark Energy Survey data. *Monthly Notices of the RAS*, 522(2), 1951–1967.
- Davies, C. L. (2019). Star-disc (mis-)alignment in Rho Oph and Upper Sco: insights from spatially resolved disc systems with K2 rotation periods. *Monthly Notices of the RAS*, 484(2), 1926–1935.

- De Rosa, R. J., Nielsen, E. L., Blunt, S. C., Graham, J. R., Konopacky, Q. M., Marois, C., Pueyo, L., Rameau, J., Ryan, D. M., Wang, J. J., Bailey, V., Chontos, A., Fabrycky, D. C., Follette, K. B., Macintosh, B., Marchis, F., Ammons, S. M., Arriaga, P., Chilcote, J. K., Cotten, T. H., Doyon, R., Duchêne, G., Esposito, T. M., Fitzgerald, M. P., Gerard, B., Goodsell, S. J., Greenbaum, A. Z., Hibon, P., Ingraham, P., Johnson-Groh, M., Kalas, P. G., Lafrenière, D., Maire, J., Metchev, S., Millar-Blanchaer, M. A., Morzinski, K. M., Oppenheimer, R., Patel, R. I., Patience, J. L., Perrin, M. D., Rajan, A., Rantakyö, F. T., Ruffio, J.-B., Schneider, A. C., Sivaramakrishnan, A., Song, I., Tran, D., Vasisht, G., Ward-Duong, K., & Wolff, S. G. (2015). Astrometric Confirmation and Preliminary Orbital Parameters of the Young Exoplanet 51 Eridani b with the Gemini Planet Imager. *Astrophysical Journal, Letters*, 814(1), L3.
- De Rosa, R. J., Nielsen, E. L., Wahhaj, Z., Ruffio, J.-B., Kalas, P. G., Peck, A. E., Hirsch, L. A., & Roberson, W. (2023). Direct imaging discovery of a super-Jovian around the young Sun-like star AF Leporis. *Astronomy and Astrophysics*, 672, A94.
- De Rosa, R. J., Nielsen, E. L., Wang, J. J., Ammons, S. M., Duchêne, G., Macintosh, B., Rameau, J., Bailey, V. P., Barman, T., Bulger, J., Chilcote, J., Cotten, T., Doyon, R., Esposito, T. M., Fitzgerald, M. P., Follette, K. B., Gerard, B. L., Goodsell, S. J., Graham, J. R., Greenbaum, A. Z., Hibon, P., Hom, J., Hung, L.-W., Ingraham, P., Kalas, P., Konopacky, Q., Larkin, J. E., Maire, J., Marchis, F., Marley, M. S., Marois, C., Metchev, S., Millar-Blanchaer, M. A., Oppenheimer, R., Palmer, D., Patience, J., Perrin, M., Poyneer, L., Pueyo, L., Rajan, A., Rantakyö, F. T., Ren, B., Ruffio, J.-B., Savransky, D., Schneider, A. C., Sivaramakrishnan, A., Song, I., Soummer, R., Tallis, M., Thomas, S., Wallace, J. K., Ward-Duong, K., Wiktorowicz, S., & Wolff, S. (2020). An Updated Visual Orbit of the Directly Imaged Exoplanet 51 Eridani b and Prospects for a Dynamical Mass Measurement with Gaia. *Astronomical Journal*, 159(1), 1.
- Delorme, P., Meunier, N., Albert, D., Lagadec, E., Le Coroller, H., Galicher, R., Mouillet, D., Boccaletti, A., Mesa, D., Meunier, J. C., Beuzit, J. L., Lagrange, A. M., Chauvin, G., Sapone, A., Langlois, M., Maire, A. L., Montargès, M., Gratton, R., Vigan, A., & Surace, C. (2017). The SPHERE Data Center: a reference for high contrast imaging processing. In C. Reylé, P. Di Matteo, F. Herpin, E.

Lagadec, A. Lançon, Z. Meliani, & F. Royer (Eds.), *SF2A-2017: Proceedings of the Annual meeting of the French Society of Astronomy and Astrophysics* (pp. 1-10).

Desidera, S., Chauvin, G., Bonavita, M., Messina, S., LeCoroller, H., Schmidt, T., Gratton, R., Lazzoni, C., Meyer, M., Schlieder, J., Cheetham, A., Hagelberg, J., Bonnefoy, M., Feldt, M., Lagrange, A. M., Langlois, M., Vigan, A., Tan, T. G., Hamsch, F. J., Millward, M., Alcalá, J., Benatti, S., Brandner, W., Carson, J., Covino, E., Delorme, P., D’Orazi, V., Janson, M., Rigliaco, E., Beuzit, J. L., Biller, B., Boccaletti, A., Dominik, C., Cantalloube, F., Fontanive, C., Galicher, R., Henning, T., Lagadec, E., Ligi, R., Maire, A. L., Menard, F., Mesa, D., Müller, A., Samland, M., Schmid, H. M., Sissa, E., Turatto, M., Udry, S., Zurlo, A., Asensio-Torres, R., Kopytova, T., Rickman, E., Abe, L., Antichi, J., Baruffolo, A., Baudoz, P., Baudrand, J., Blanchard, P., Bazzon, A., Buey, T., Carbillet, M., Carle, M., Charton, J., Cascone, E., Claudi, R., Costille, A., Deboulbé, A., De Caprio, V., Dohlen, K., Fantinel, D., Feautrier, P., Fusco, T., Gigan, P., Giro, E., Gisler, D., Gluck, L., Hubin, N., Hugot, E., Jaquet, M., Kasper, M., Madec, F., Magnard, Y., Martinez, P., Maurel, D., Le Mignant, D., Möller-Nilsson, O., Llored, M., Moulin, T., Origné, A., Pavlov, A., Perret, D., Petit, C., Pragt, J., Puget, P., Rabou, P., Ramos, J., Rigal, F., Rochat, S., Roelfsema, R., Rousset, G., Roux, A., Salasnich, B., Sauvage, J. F., Sevin, A., Soenke, C., Stadler, E., Suarez, M., Weber, L., & Wildi, F. (2021a). The SPHERE infrared survey for exoplanets (SHINE). I. Sample definition and target characterization. *Astronomy and Astrophysics*, 651, A70.

Desidera, S., Chauvin, G., Bonavita, M., Messina, S., Lecoroller, H., Schmidt, T., Gratton, R., Lazzoni, C., Meyer, M., Schlieder, J., Cheetham, A., Hagelberg, J., Bonnefoy, M., Feldt, M., Lagrange, A. M., Langlois, M., Vigan, A., Tan, T. G., Hamsch, F. J., Millward, M., Alcalá, J., Benatti, S., Brandner, W., Carson, J., Covino, E., Delorme, P., D’Orazi, V., Janson, M., Rigliaco, E., Beuzit, J. L., Biller, B., Boccaletti, A., Dominik, F., Cantalloube, C., Fontanive, C., Galicher, R., Henning, T., Lagadec, E., Ligi, R., Maire, A. L., Menard, F., Mesa, D., Mueller, A., Samland, M., Schmid, H. M., Sissa, E., Turatto, M., Udry, S., Zurlo, A., Asensio-Torres, R., Kopytova, T., Rickman, E., Abe, L., Antichi, J., Baruolo, A., Baudoz, P., Baudrand, J., Blanchard, P., Bazzon, A., Buey, T., Carbillet, M., Carle, M., Charton, J., Cascone, E., Claudi, R., Costille, A., De-

boulbe, A., de Caprio, V., Dohlen, K., Fantinel, D., Feautrier, P., Fusco, T., Gigan, P., Giro, E., Gisler, D., Gluck, L., Hubin, N., Hugot, E., Jaquet, M., Kasper, M., Madec, F., Magnard, Y., Martinez, P., Maurel, D., Le Mignant, D., Moeller-Nilsson, O., Llored, M., Moulin, T., Origne, A., Pavlov, A., Perret, D., Petit, C., Pragt, J., Puget, P., Rabou, P., Ramos, J., Rigal, F., Rochat, S., Roelfsema, R., Rousset, G., Roux, A., Salasnich, B., Sauvage, J. F., Sevin, A., Soenke, C., Stadler, E., Suarez, M., Weber, L., & Wildi, F. (2021b). VizieR Online Data Catalog: SHINE sample definition (Desidera+, 2021). *VizieR Online Data Catalog*, (pp. J/A+A/651/A70).

Do Ó, C. R., O’Neil, K. K., Konopacky, Q. M., Do, T., Martinez, G. D., Ruffio, J.-B., & Ghez, A. M. (2023). The Orbital Eccentricities of Directly Imaged Companions Using Observable-based Priors: Implications for Population-level Distributions. *Astronomical Journal*, 166(2), 48.

Dohlen, K., Langlois, M., Saisse, M., Hill, L., Origne, A., Jaquet, M., Fabron, C., Blanc, J.-C., Llored, M., Carle, M., Moutou, C., Vigan, A., Boccaletti, A., Carbillet, M., Mouillet, D., & Beuzit, J.-L. (2008). The infra-red dual imaging and spectrograph for SPHERE: design and performance. In I. S. McLean & M. M. Casali (Eds.), *Ground-based and Airborne Instrumentation for Astronomy II*, volume 7014 of *Society of Photo-Optical Instrumentation Engineers (SPIE) Conference Series* (pp. 70143L).

Dorval, J., Boily, C. M., Moraux, E., & Roos, O. (2017). Wide- and contact-binary formation in substructured young stellar clusters. *Monthly Notices of the RAS*, 465(2), 2198–2211.

Dullemond, C. P., Isella, A., Andrews, S. M., Skobleva, I., & Dzyurkevich, N. (2020). Midplane temperature and outer edge of the protoplanetary disk around HD 163296. *Astronomy and Astrophysics*, 633, A137.

Dullemond, C. P., Küffmeier, M., Goicovic, F., Fukagawa, M., Oehl, V., & Kramer, M. (2019). Cloudlet capture by transitional disk and FU Orionis stars. *Astronomy and Astrophysics*, 628, A20.

Dunham, M. M., Allen, L. E., Evans, Neal J., I., Broekhoven-Fiene, H., Cieza, L. A., Di Francesco, J., Gutermuth, R. A., Harvey, P. M., Hatchell, J., Heiderman, A., Huard, T. L., Johnstone, D., Kirk, J. M., Matthews, B. C., Miller, J. F.,

- Peterson, D. E., & Young, K. E. (2015). Young Stellar Objects in the Gould Belt. *Astrophysical Journal, Supplement*, 220(1), 11.
- Dunham, M. M., Stutz, A. M., Allen, L. E., Evans, N. J., I., Fischer, W. J., Megeath, S. T., Myers, P. C., Offner, S. S. R., Poteet, C. A., Tobin, J. J., & Vorobyov, E. I. (2014a). The Evolution of Protostars: Insights from Ten Years of Infrared Surveys with Spitzer and Herschel. In H. Beuther, R. S. Klessen, C. P. Dullemond, & T. Henning (Eds.), *Protostars and Planets VI* (pp. 195–218).
- Dunham, M. M. & Vorobyov, E. I. (2012). Resolving the Luminosity Problem in Low-mass Star Formation. *Astrophysical Journal*, 747(1), 52.
- Dunham, M. M., Vorobyov, E. I., & Arce, H. G. (2014b). On the reliability of protostellar disc mass measurements and the existence of fragmenting discs. *Monthly Notices of the RAS*, 444(1), 887–901.
- Dunhill, A. C., Cuadra, J., & Dougados, C. (2015). Precession and accretion in circumbinary discs: the case of HD 104237. *Monthly Notices of the RAS*, 448(4), 3545–3554.
- Dupuy, T. J., Brandt, G. M., & Brandt, T. D. (2022). Limits on the mass and initial entropy of 51 Eri b from Gaia EDR3 astrometry. *Monthly Notices of the RAS*, 509(3), 4411–4419.
- Dupuy, T. J., Liu, M. C., & Ireland, M. J. (2014). New Evidence for a Substellar Luminosity Problem: Dynamical Mass for the Brown Dwarf Binary Gl 417BC. *Astrophysical Journal*, 790(2), 133.
- Dutrey, A., Guilloteau, S., & Simon, M. (1994). Images of the GG Tauri rotating ring. *Astronomy and Astrophysics*, 286, 149–159.
- Epstein, P. S. (1924). On the Resistance Experienced by Spheres in their Motion through Gases. *Physical Review*, 23(6), 710–733.
- Evans, Neal J., I., Dunham, M. M., Jørgensen, J. K., Enoch, M. L., Merín, B., van Dishoeck, E. F., Alcalá, J. M., Myers, P. C., Stapelfeldt, K. R., Huard, T. L., Allen, L. E., Harvey, P. M., van Kempen, T., Blake, G. A., Koerner, D. W., Mundy, L. G., Padgett, D. L., & Sargent, A. I. (2009). The Spitzer c2d Legacy Results: Star-Formation Rates and Efficiencies; Evolution and Lifetimes. *Astrophysical Journal, Supplement*, 181(2), 321–350.

- Fabrycky, D. & Tremaine, S. (2007). Shrinking Binary and Planetary Orbits by Kozai Cycles with Tidal Friction. *Astrophysical Journal*, 669(2), 1298–1315.
- Feigelson, E. D., Lawson, W. A., Stark, M., Townsley, L., & Garmire, G. P. (2006). 51 Eridani and GJ 3305: A 10-15 Myr old Binary Star System at 30 Parsecs. *Astronomical Journal*, 131(3), 1730–1739.
- Fischer, W. J., Hillenbrand, L. A., Herczeg, G. J., Johnstone, D., Kospal, A., & Dunham, M. M. (2023). Accretion Variability as a Guide to Stellar Mass Assembly. In S. Inutsuka, Y. Aikawa, T. Muto, K. Tomida, & M. Tamura (Eds.), *Protostars and Planets VII*, volume 534 of *Astronomical Society of the Pacific Conference Series* (pp. 355).
- Fischer, W. J., Megeath, S. T., Furlan, E., Ali, B., Stutz, A. M., Tobin, J. J., Osorio, M., Stanke, T., Manoj, P., Poteet, C. A., Booker, J. J., Hartmann, L., Wilson, T. L., Myers, P. C., & Watson, D. M. (2017). The Herschel Orion Protostar Survey: Luminosity and Envelope Evolution. *Astrophysical Journal*, 840(2), 69.
- Follette, K. B. (2023). An Introduction to High Contrast Differential Imaging of Exoplanets and Disks. *Astronomical Society of the Pacific*, 135(1051), 093001.
- Foreman-Mackey, D., Hogg, D. W., Lang, D., & Goodman, J. (2013). emcee: The MCMC Hammer. *Astronomical Society of the Pacific*, 125(925), 306.
- Forgan, D. & Rice, K. (2013). Towards a population synthesis model of objects formed by self-gravitating disc fragmentation and tidal downsizing. *Monthly Notices of the RAS*, 432(4), 3168–3185.
- Frank, A., Ray, T. P., Cabrit, S., Hartigan, P., Arce, H. G., Bacciotti, F., Bally, J., Benisty, M., Eisloffel, J., Güdel, M., Lebedev, S., Nisini, B., & Raga, A. (2014). Jets and Outflows from Star to Cloud: Observations Confront Theory. In H. Beuther, R. S. Klessen, C. P. Dullemond, & T. Henning (Eds.), *Protostars and Planets VI* (pp. 451).
- Franson, K., Bowler, B. P., Zhou, Y., Pearce, T. D., Bardalez Gagliuffi, D. C., Biddle, L. I., Brandt, T. D., Crepp, J. R., Dupuy, T. J., Faherty, J., Jensen-Clem, R., Morgan, M., Sanghi, A., Theissen, C. A., Tran, Q. H., & Wolf, T. N. (2023). Astrometric Accelerations as Dynamical Beacons: A Giant Planet Imaged inside the Debris Disk of the Young Star AF Lep. *Astrophysical Journal, Letters*, 950(2), L19.

- Fusco, T., Rousset, G., Sauvage, J. F., Petit, C., Beuzit, J. L., Dohlen, K., Mouillet, D., Charton, J., Nicolle, M., Kasper, M., Baudoz, P., & Puget, P. (2006). High-order adaptive optics requirements for direct detection of extrasolar planets: Application to the SPHERE instrument. *Optics Express*, 14(17), 7515.
- Gaia Collaboration (2020). VizieR Online Data Catalog: Gaia EDR3 (Gaia Collaboration, 2020). VizieR On-line Data Catalog: I/350. Originally published in: 2020A&A...649A...1G; doi:10.5270/esa-1ug.
- Gaia Collaboration, Brown, A. G. A., Vallenari, A., Prusti, T., de Bruijne, J. H. J., Babusiaux, C., Bailer-Jones, C. A. L., Biermann, M., Evans, D. W., Eyer, L., Jansen, F., Jordi, C., Klioner, S. A., Lammers, U., Lindegren, L., Luri, X., Mignard, F., Panem, C., Pourbaix, D., Randich, S., Sartoretti, P., Siddiqui, H. I., Soubiran, C., van Leeuwen, F., Walton, N. A., Arenou, F., Bastian, U., Cropper, M., Drimmel, R., Katz, D., Lattanzi, M. G., Bakker, J., Cacciari, C., Castañeda, J., Chaoul, L., Cheek, N., De Angeli, F., Fabricius, C., Guerra, R., Holl, B., Masana, E., Messineo, R., Mowlavi, N., Nienartowicz, K., Panuzzo, P., Portell, J., Riello, M., Seabroke, G. M., Tanga, P., Thévenin, F., Gracia-Abril, G., Comoretto, G., Garcia-Reinaldos, M., Teyssier, D., Altmann, M., Andrae, R., Aurdard, M., Bellas-Velidis, I., Benson, K., Berthier, J., Blomme, R., Burgess, P., Busso, G., Carry, B., Cellino, A., Clementini, G., Clotet, M., Creevey, O., Davidson, M., De Ridder, J., Delchambre, L., Dell’Oro, A., Ducourant, C., Fernández-Hernández, J., Fouesneau, M., Frémat, Y., Galluccio, L., García-Torres, M., González-Núñez, J., González-Vidal, J. J., Gosset, E., Guy, L. P., Halbwegs, J. L., Hambly, N. C., Harrison, D. L., Hernández, J., Hestroffer, D., Hodgkin, S. T., Hutton, A., Jasiewicz, G., Jean-Antoine-Piccolo, A., Jordan, S., Korn, A. J., Krone-Martins, A., Lanzafame, A. C., Lebzelter, T., Löffler, W., Manteiga, M., Marrese, P. M., Martín-Fleitas, J. M., Moitinho, A., Mora, A., Muinonen, K., Osinde, J., Pancino, E., Pauwels, T., Petit, J. M., Recio-Blanco, A., Richards, P. J., Rimoldini, L., Robin, A. C., Sarro, L. M., Siopis, C., Smith, M., Sozzetti, A., Süveges, M., Torra, J., van Reeven, W., Abbas, U., Abreu Aramburu, A., Accart, S., Aerts, C., Altavilla, G., Álvarez, M. A., Alvarez, R., Alves, J., Anderson, R. I., Andrei, A. H., Anglada Varela, E., Antiche, E., Antoja, T., Arcay, B., Astraatmadja, T. L., Bach, N., Baker, S. G., Balaguer-Núñez, L., Balm, P., Barache, C., Barata, C., Barbato, D., Barblan, F., Barklem, P. S., Barrado, D., Barros, M., Barstow, M. A., Bartholomé Muñoz, S., Bassi-

ana, J. L., Becciani, U., Bellazzini, M., Berihuete, A., Bertone, S., Bianchi, L., Bienaymé, O., Blanco-Cuaresma, S., Boch, T., Boeche, C., Bombrun, A., Borrachero, R., Bossini, D., Bouquillon, S., Bourda, G., Bragaglia, A., Bramante, L., Breddels, M. A., Bressan, A., Brouillet, N., Brüsemeister, T., Brugaletta, E., Bucciarelli, B., Burlacu, A., Busonero, D., Butkevich, A. G., Buzzi, R., Caffau, E., Cancelliere, R., Cannizzaro, G., Cantat-Gaudin, T., Carballo, R., Carlucci, T., Carrasco, J. M., Casamiquela, L., Castellani, M., Castro-Ginard, A., Charlot, P., Chemin, L., Chiavassa, A., Cocozza, G., Costigan, G., Cowell, S., Crifo, F., Crosta, M., Crowley, C., Cuypers, J., Dafonte, C., Damerджи, Y., Dapergolas, A., David, P., David, M., de Laverny, P., De Luise, F., De March, R., de Martino, D., de Souza, R., de Torres, A., Debossher, J., del Pozo, E., Delbo, M., Delgado, A., Delgado, H. E., Di Matteo, P., Diakite, S., Diener, C., Distefano, E., Dolding, C., Drazinos, P., Durán, J., Edvardsson, B., Enke, H., Eriksson, K., Esquej, P., Eynard Bontemps, G., Fabre, C., Fabrizio, M., Faigler, S., Falcão, A. J., Farràs Casas, M., Federici, L., Fedorets, G., Fernique, P., Figueras, F., Filippi, F., Findeisen, K., Fonti, A., Fraile, E., Fraser, M., Frézouls, B., Gai, M., Galleti, S., Garabato, D., García-Sedano, F., Garofalo, A., Garralda, N., Gavel, A., Gavras, P., Gerssen, J., Geyer, R., Giacobbe, P., Gilmore, G., Girona, S., Giuffrida, G., Glass, F., Gomes, M., Granvik, M., Gueguen, A., Guerrier, A., Guiraud, J., Gutiérrez-Sánchez, R., Haigron, R., Hatzidimitriou, D., Hauser, M., Haywood, M., Heiter, U., Helmi, A., Heu, J., Hilger, T., Hobbs, D., Hofmann, W., Holland, G., Huckle, H. E., Hypki, A., Icardi, V., Janßen, K., Jevardat de Fombelle, G., Jonker, P. G., Juhász, Á. L., Julbe, F., Karampelas, A., Kewley, A., Klar, J., Kochoska, A., Kohley, R., Kolenberg, K., Kontizas, M., Kontizas, E., Kopusov, S. E., Kordopatis, G., Kostrzewa-Rutkowska, Z., Koubsky, P., Lambert, S., Lanza, A. F., Lasne, Y., Lavigne, J. B., Le Fustec, Y., Le Poncin-Lafitte, C., Lebreton, Y., Leccia, S., Leclerc, N., Lecoeur-Taïbi, I., Lenhardt, H., Leroux, F., Liao, S., Licata, E., Lindstrøm, H. E. P., Lister, T. A., Livanou, E., Lobel, A., López, M., Managau, S., Mann, R. G., Mantelet, G., Marchal, O., Marchant, J. M., Marconi, M., Marinoni, S., Marschalkó, G., Marshall, D. J., Martino, M., Marton, G., Mary, N., Massari, D., Matijević, G., Mazeh, T., McMillan, P. J., Messina, S., Michalik, D., Millar, N. R., Molina, D., Molinaro, R., Molnár, L., Montegriffo, P., Mor, R., Morbidelli, R., Morel, T., Morris, D., Mulone, A. F., Muraveva, T., Musella, I., Nelemans, G., Nicastro, L., Noval, L., O'Mullane, W., Ordénovic, C., Ordóñez-Blanco, D., Osborne, P., Pagani,

C., Pagano, I., Pailler, F., Palacin, H., Palaversa, L., Panahi, A., Pawlak, M., Piersimoni, A. M., Pineau, F. X., Plachy, E., Plum, G., Poggio, E., Poujoulet, E., Prša, A., Pulone, L., Racero, E., Ragaini, S., Rambaux, N., Ramos-Lerate, M., Regibo, S., Reylé, C., Riclet, F., Ripepi, V., Riva, A., Rivard, A., Rixon, G., Roegiers, T., Roelens, M., Romero-Gómez, M., Rowell, N., Royer, F., Ruiz-Dern, L., Sadowski, G., Sagristà Sellés, T., Sahlmann, J., Salgado, J., Salguero, E., Sanna, N., Santana-Ros, T., Sarasso, M., Saviotto, H., Schultheis, M., Sciacca, E., Segol, M., Segovia, J. C., Ségransan, D., Shih, I. C., Siltala, L., Silva, A. F., Smart, R. L., Smith, K. W., Solano, E., Solitro, F., Sordo, R., Soria Nieto, S., Souchay, J., Spagna, A., Spoto, F., Stampa, U., Steele, I. A., Steidelmüller, H., Stephenson, C. A., Stoev, H., Suess, F. F., Surdej, J., Szabados, L., Szegedielek, E., Tapiador, D., Taris, F., Tauran, G., Taylor, M. B., Teixeira, R., Terrett, D., Teyssandier, P., Thuillot, W., Titarenko, A., Torra Clotet, F., Turon, C., Ulla, A., Utrilla, E., Uzzi, S., Vaillant, M., Valentini, G., Valette, V., van Elteren, A., Van Hemelryck, E., van Leeuwen, M., Vaschetto, M., Vecchiato, A., Veljanoski, J., Viala, Y., Vicente, D., Vogt, S., von Essen, C., Voss, H., Votruba, V., Voutsinas, S., Walmsley, G., Weiler, M., Wertz, O., Wevers, T., Wyrzykowski, Ł., Yoldas, A., Žerjal, M., Ziaeeepour, H., Zorec, J., Zschocke, S., Zucker, S., Zurbach, C., & Zwitter, T. (2018). Gaia Data Release 2. Summary of the contents and survey properties. *Astronomy and Astrophysics*, 616, A1.

Gaia Collaboration, Brown, A. G. A., Vallenari, A., Prusti, T., de Bruijne, J. H. J., Babusiaux, C., Biermann, M., Creevey, O. L., Evans, D. W., Eyer, L., Hutton, A., Jansen, F., Jordi, C., Klioner, S. A., Lammers, U., Lindegren, L., Luri, X., Mignard, F., Panem, C., Pourbaix, D., Randich, S., Sartoretti, P., Soubiran, C., Walton, N. A., Arenou, F., Bailer-Jones, C. A. L., Bastian, U., Cropper, M., Drimmel, R., Katz, D., Lattanzi, M. G., van Leeuwen, F., Bakker, J., Cacciari, C., Castañeda, J., De Angeli, F., Ducourant, C., Fabricius, C., Fouesneau, M., Frémat, Y., Guerra, R., Guerrier, A., Guiraud, J., Jean-Antoine Piccolo, A., Masana, E., Messineo, R., Mowlavi, N., Nicolas, C., Nienartowicz, K., Pailler, F., Panuzzo, P., Riclet, F., Roux, W., Seabroke, G. M., Sordo, R., Tanga, P., Thévenin, F., Gracia-Abril, G., Portell, J., Teyssier, D., Altmann, M., Andrae, R., Bellas-Velidis, I., Benson, K., Berthier, J., Blomme, R., Brugaletta, E., Burgess, P. W., Busso, G., Carry, B., Cellino, A., Cheek, N., Clementini, G., Damerджи, Y., Davidson, M., Delchambre, L., Dell’Oro, A., Fernández-

Hernández, J., Galluccio, L., García-Lario, P., Garcia-Reinaldos, M., González-Núñez, J., Gosset, E., Haigrón, R., Halbwachs, J. L., Hambly, N. C., Harrison, D. L., Hatzidimitriou, D., Heiter, U., Hernández, J., Hestroffer, D., Hodgkin, S. T., Holl, B., Janßen, K., Jevardat de Fombelle, G., Jordan, S., Krone-Martins, A., Lanzafame, A. C., Löffler, W., Lorca, A., Manteiga, M., Marchal, O., Marse, P. M., Moitinho, A., Mora, A., Muinonen, K., Osborne, P., Pancino, E., Pauwels, T., Petit, J. M., Recio-Blanco, A., Richards, P. J., Riello, M., Rimoldini, L., Robin, A. C., Roegiers, T., Rybizki, J., Sarro, L. M., Siopis, C., Smith, M., Sozzetti, A., Ulla, A., Utrilla, E., van Leeuwen, M., van Reeve, W., Abbas, U., Abreu Aramburu, A., Accart, S., Aerts, C., Aguado, J. J., Ajaj, M., Altavilla, G., Álvarez, M. A., Álvarez Cid-Fuentes, J., Alves, J., Anderson, R. I., Anglada Varela, E., Antoja, T., Audard, M., Baines, D., Baker, S. G., Balaguer-Núñez, L., Balbinot, E., Balog, Z., Barache, C., Barbato, D., Barros, M., Barstow, M. A., Bartolomé, S., Bassilana, J. L., Bauchet, N., Baudesson-Stella, A., Becciani, U., Bellazzini, M., Bernet, M., Bertone, S., Bianchi, L., Blanco-Cuaresma, S., Boch, T., Bombrun, A., Bossini, D., Bouquillon, S., Braggaglia, A., Bramante, L., Breedt, E., Bressan, A., Brouillet, N., Bucciarelli, B., Burlacu, A., Busonero, D., Butkevich, A. G., Buzzi, R., Caffau, E., Cancelliere, R., Cánovas, H., Cantat-Gaudin, T., Carballo, R., Carlucci, T., Carnerero, M. I., Carrasco, J. M., Casamiquela, L., Castellani, M., Castro-Ginard, A., Castro Sampil, P., Chaoul, L., Charlot, P., Chemin, L., Chiavassa, A., Cioni, M. R. L., Comoretto, G., Cooper, W. J., Cornez, T., Cowell, S., Crifo, F., Crosta, M., Crowley, C., Dafonte, C., Dapergolas, A., David, M., David, P., de Laverny, P., De Luise, F., De March, R., De Ridder, J., de Souza, R., de Teodoro, P., de Torres, A., del Peloso, E. F., del Pozo, E., Delbo, M., Delgado, A., Delgado, H. E., Delisle, J. B., Di Matteo, P., Diakite, S., Diener, C., Distefano, E., Dolding, C., Eappachen, D., Edvardsson, B., Enke, H., Esquej, P., Fabre, C., Fabrizio, M., Faigler, S., Fedorets, G., Fernique, P., Fienga, A., Figueras, F., Fouron, C., Fragkoudi, F., Fraile, E., Franke, F., Gai, M., Garabato, D., Garcia-Gutierrez, A., García-Torres, M., Garofalo, A., Gavras, P., Gerlach, E., Geyer, R., Giacobbe, P., Gilmore, G., Girona, S., Giuffrida, G., Gomel, R., Gomez, A., Gonzalez-Santamaria, I., González-Vidal, J. J., Granvik, M., Gutiérrez-Sánchez, R., Guy, L. P., Hauser, M., Haywood, M., Helmi, A., Hidalgo, S. L., Hilger, T., Hładczuk, N., Hobbs, D., Holland, G., Huckle, H. E., Jasiewicz, G., Jonker, P. G., Juaristi Campillo, J., Julbe, F., Karbevaska, L., Kervella, P., Khanna, S., Ko-

choska, A., Kontizas, M., Kordopatis, G., Korn, A. J., Kostrzewa-Rutkowska, Z., Kruszyńska, K., Lambert, S., Lanza, A. F., Lasne, Y., Le Campion, J. F., Le Fustec, Y., Lebreton, Y., Lebzelter, T., Leccia, S., Leclerc, N., Lecoœur-Taibi, I., Liao, S., Licata, E., Lindstrøm, E. P., Lister, T. A., Livanou, E., Lobel, A., Madrero Pardo, P., Managau, S., Mann, R. G., Marchant, J. M., Marconi, M., Marcos Santos, M. M. S., Marinoni, S., Marocco, F., Marshall, D. J., Martin Polo, L., Martín-Fleitas, J. M., Masip, A., Massari, D., Mastrobuono-Battisti, A., Mazeh, T., McMillan, P. J., Messina, S., Michalik, D., Millar, N. R., Mints, A., Molina, D., Molinaro, R., Molnár, L., Montegriffo, P., Mor, R., Morbidelli, R., Morel, T., Morris, D., Mulone, A. F., Munoz, D., Muraveva, T., Murphy, C. P., Musella, I., Noval, L., Ordénovic, C., Orrù, G., Osinde, J., Pagani, C., Pagano, I., Palaversa, L., Palicio, P. A., Panahi, A., Pawlak, M., Peñalosa Esteller, X., Penttilä, A., Piersimoni, A. M., Pineau, F. X., Plachy, E., Plum, G., Poggio, E., Poretti, E., Poujoulet, E., Prša, A., Pulone, L., Racero, E., Ragaini, S., Rainer, M., Raiteri, C. M., Rambaux, N., Ramos, P., Ramos-Lerate, M., Re Fiorentin, P., Regibo, S., Reylé, C., Ripepi, V., Riva, A., Rixon, G., Robichon, N., Robin, C., Roelens, M., Rohrbasser, L., Romero-Gómez, M., Rowell, N., Royer, F., Rybicki, K. A., Sadowski, G., Sagristà Sellés, A., Sahlmann, J., Salgado, J., Salguero, E., Samaras, N., Sanchez Gimenez, V., Sanna, N., Santoveña, R., Sarasso, M., Schultheis, M., Sciacca, E., Segol, M., Segovia, J. C., Ségransan, D., Semeux, D., Shahaf, S., Siddiqui, H. I., Siebert, A., Siltala, L., Slezak, E., Smart, R. L., Solano, E., Solitro, F., Souami, D., Souchay, J., Spagna, A., Spoto, F., Steele, I. A., Steidelmüller, H., Stephenson, C. A., Süveges, M., Szabados, L., Szegedi-Elek, E., Taris, F., Tauran, G., Taylor, M. B., Teixeira, R., Thuillot, W., Tonello, N., Torra, F., Torra, J., Turon, C., Unger, N., Vaillant, M., van Dillen, E., Vanel, O., Vecchiato, A., Viala, Y., Vicente, D., Voutsinas, S., Weiler, M., Wevers, T., Wyrzykowski, Ł., Yoldas, A., Yvard, P., Zhao, H., Zorec, J., Zucker, S., Zurbach, C., & Zwitter, T. (2021). Gaia Early Data Release 3. Summary of the contents and survey properties. *Astronomy and Astrophysics*, 649, A1.

Gaia Collaboration, Prusti, T., de Bruijne, J. H. J., Brown, A. G. A., Vallenari, A., Babusiaux, C., Bailer-Jones, C. A. L., Bastian, U., Biermann, M., Evans, D. W., Eyer, L., Jansen, F., Jordi, C., Klioner, S. A., Lammers, U., Lindegren, L., Luri, X., Mignard, F., Milligan, D. J., Panem, C., Poinsignon, V., Pourbaix, D.,

Randich, S., Sarri, G., Sartoretti, P., Siddiqui, H. I., Soubiran, C., Valette, V., van Leeuwen, F., Walton, N. A., Aerts, C., Arenou, F., Cropper, M., Drimmel, R., Høg, E., Katz, D., Lattanzi, M. G., O'Mullane, W., Grebel, E. K., Holland, A. D., Huc, C., Passot, X., Bramante, L., Cacciari, C., Castañeda, J., Chaoul, L., Cheek, N., De Angeli, F., Fabricius, C., Guerra, R., Hernández, J., Jean-Antoine-Piccolo, A., Masana, E., Messineo, R., Mowlavi, N., Nienartowicz, K., Ordóñez-Blanco, D., Panuzzo, P., Portell, J., Richards, P. J., Riello, M., Seabroke, G. M., Tanga, P., Thévenin, F., Torra, J., Els, S. G., Gracia-Abril, G., Comoretto, G., Garcia-Reinaldos, M., Lock, T., Mercier, E., Altmann, M., Andrae, R., Astraatmadja, T. L., Bellas-Velidis, I., Benson, K., Berthier, J., Blomme, R., Busso, G., Carry, B., Cellino, A., Clementini, G., Cowell, S., Creevey, O., Cuypers, J., Davidson, M., De Ridder, J., de Torres, A., Delchambre, L., Dell'Oro, A., Ducourant, C., Frémat, Y., García-Torres, M., Gosset, E., Halbwegs, J. L., Hambly, N. C., Harrison, D. L., Hauser, M., Hestroffer, D., Hodgkin, S. T., Huckle, H. E., Hutton, A., Jasniewicz, G., Jordan, S., Kontizas, M., Korn, A. J., Lanzafame, A. C., Manteiga, M., Moitinho, A., Muinonen, K., Osinde, J., Pancino, E., Pauwels, T., Petit, J. M., Recio-Blanco, A., Robin, A. C., Sarro, L. M., Siopis, C., Smith, M., Smith, K. W., Sozzetti, A., Thuillot, W., van Reeve, W., Viala, Y., Abbas, U., Abreu Aramburu, A., Accart, S., Aguado, J. J., Allan, P. M., Allasia, W., Altavilla, G., Álvarez, M. A., Alves, J., Anderson, R. I., Andrei, A. H., Anglada Varela, E., Antiche, E., Antoja, T., Antón, S., Arcay, B., Atzei, A., Ayache, L., Bach, N., Baker, S. G., Balaguer-Núñez, L., Barache, C., Barata, C., Barbier, A., Barblan, F., Baroni, M., Barrado y Navascués, D., Barros, M., Barstow, M. A., Becciani, U., Bellazzini, M., Bellei, G., Bello García, A., Belokurov, V., Bendjoya, P., Berihuete, A., Bianchi, L., Bienaymé, O., Billebaud, F., Blagorodnova, N., Blanco-Cuaresma, S., Boch, T., Bombrun, A., Borrachero, R., Bouquillon, S., Bourda, G., Bouy, H., Bragaglia, A., Breddels, M. A., Brouillet, N., Brüsemeister, T., Bucciarelli, B., Budnik, F., Burgess, P., Burgon, R., Burlacu, A., Busonero, D., Buzzi, R., Caffau, E., Cambras, J., Campbell, H., Cancelliere, R., Cantat-Gaudin, T., Carlucci, T., Carrasco, J. M., Castellani, M., Charlot, P., Charnas, J., Charvet, P., Chassat, F., Chiavassa, A., Clotet, M., Cocozza, G., Collins, R. S., Collins, P., Costigan, G., Crifo, F., Cross, N. J. G., Crosta, M., Crowley, C., Dafonte, C., Damerджи, Y., Dapergolas, A., David, P., David, M., De Cat, P., de Felice, F., de Laverny, P., De Luise, F., De March, R., de Martino, D., de Souza, R., De-

bosscher, J., del Pozo, E., Delbo, M., Delgado, A., Delgado, H. E., di Marco, F., Di Matteo, P., Diakite, S., Distefano, E., Dolding, C., Dos Anjos, S., Drazinos, P., Durán, J., Dzigian, Y., Ecale, E., Edvardsson, B., Enke, H., Erdmann, M., Escolar, D., Espina, M., Evans, N. W., Eynard Bontemps, G., Fabre, C., Fabrizio, M., Faigler, S., Falcão, A. J., Farràs Casas, M., Faye, F., Federici, L., Fedorets, G., Fernández-Hernández, J., Fernique, P., Fienga, A., Figueras, F., Filippi, F., Findeisen, K., Fonti, A., Fouesneau, M., Fraile, E., Fraser, M., Fuchs, J., Furnell, R., Gai, M., Galleti, S., Galluccio, L., Garabato, D., García-Sedano, F., Garé, P., Garofalo, A., Garralda, N., Gavras, P., Gerssen, J., Geyer, R., Gilmore, G., Girona, S., Giuffrida, G., Gomes, M., González-Marcos, A., González-Núñez, J., González-Vidal, J. J., Granvik, M., Guerrier, A., Guillout, P., Guiraud, J., Gúrpide, A., Gutiérrez-Sánchez, R., Guy, L. P., Haignon, R., Hatzidimitriou, D., Haywood, M., Heiter, U., Helmi, A., Hobbs, D., Hofmann, W., Holl, B., Holland, G., Hunt, J. A. S., Hypki, A., Icardi, V., Irwin, M., Jevardat de Fombelle, G., Jofré, P., Jonker, P. G., Jorissen, A., Julbe, F., Karampelas, A., Kochoska, A., Kohley, R., Kolenberg, K., Kontizas, E., Kuposov, S. E., Kordopatis, G., Koubsky, P., Kowalczyk, A., Krone-Martins, A., Kudryashova, M., Kull, I., Bachchan, R. K., Lacoste-Seris, F., Lanza, A. F., Lavigne, J. B., Le Poncin-Lafitte, C., Lebreton, Y., Lebzelter, T., Leccia, S., Leclerc, N., Lecoeur-Taibi, I., Lemaitre, V., Lenhardt, H., Leroux, F., Liao, S., Licata, E., Lindstrøm, H. E. P., Lister, T. A., Livanou, E., Lobel, A., Löffler, W., López, M., Lopez-Lozano, A., Lorenz, D., Loureiro, T., MacDonald, I., Magalhães Fernandes, T., Managau, S., Mann, R. G., Mantelet, G., Marchal, O., Marchant, J. M., Marconi, M., Marie, J., Marinoni, S., Marrese, P. M., Marschalkó, G., Marshall, D. J., Martín-Fleitas, J. M., Martino, M., Mary, N., Matijevič, G., Mazeh, T., McMillan, P. J., Messina, S., Mestre, A., Michalik, D., Millar, N. R., Miranda, B. M. H., Molina, D., Molinaro, R., Molinaro, M., Molnár, L., Moniez, M., Montegriffo, P., Monteiro, D., Mor, R., Mora, A., Morbidelli, R., Morel, T., Morgenthaler, S., Morley, T., Morris, D., Mulone, A. F., Muraveva, T., Musella, I., Narbonne, J., Nelemans, G., Nicastro, L., Noval, L., Ordénovic, C., Ordieres-Meré, J., Osborne, P., Pagani, C., Pagano, I., Pailler, F., Palacin, H., Palaversa, L., Parsons, P., Paulsen, T., Pecoraro, M., Pedrosa, R., Pentikäinen, H., Pereira, J., Pichon, B., Piersimoni, A. M., Pineau, F. X., Plachy, E., Plum, G., Poujoulet, E., Prša, A., Pulone, L., Ragaini, S., Rago, S., Rambaux, N., Ramos-Lerate, M., Ranalli, P., Rauw, G., Read, A., Regibo, S., Renk, F., Reylé, C., Ribeiro,

R. A., Rimoldini, L., Ripepi, V., Riva, A., Rixon, G., Roelens, M., Romero-Gómez, M., Rowell, N., Royer, F., Rudolph, A., Ruiz-Dern, L., Sadowski, G., Sagristà Sellés, T., Sahlmann, J., Salgado, J., Salguero, E., Sarasso, M., Savietto, H., Schnorhk, A., Schultheis, M., Sciacca, E., Segol, M., Segovia, J. C., Segransan, D., Serpell, E., Shih, I. C., Smareglia, R., Smart, R. L., Smith, C., Solano, E., Solitro, F., Sordo, R., Soria Nieto, S., Souchay, J., Spagna, A., Spoto, F., Stampa, U., Steele, I. A., Steidelmüller, H., Stephenson, C. A., Stoev, H., Suess, F. F., Süveges, M., Surdej, J., Szabados, L., Szegedi-Elek, E., Tapiador, D., Taris, F., Tauran, G., Taylor, M. B., Teixeira, R., Terrett, D., Tingley, B., Trager, S. C., Turon, C., Ulla, A., Utrilla, E., Valentini, G., van Elteren, A., Van Hemelryck, E., van Leeuwen, M., Varadi, M., Vecchiato, A., Veljanoski, J., Via, T., Vicente, D., Vogt, S., Voss, H., Votruba, V., Voutsinas, S., Walmesley, G., Weiler, M., Weingrill, K., Werner, D., Wevers, T., Whitehead, G., Wyrzykowski, Ł., Yoldas, A., Žerjal, M., Zucker, S., Zurbach, C., Zwitter, T., Alecu, A., Allen, M., Allende Prieto, C., Amorim, A., Anglada-Escudé, G., Arsenijevic, V., Azaz, S., Balm, P., Beck, M., Bernstein, H. H., Bigot, L., Bijaoui, A., Blasco, C., Bonfigli, M., Bono, G., Boudreault, S., Bressan, A., Brown, S., Brunet, P. M., Bunclark, P., Buonanno, R., Butkevich, A. G., Carret, C., Carrion, C., Chemin, L., Chéreau, F., Corcione, L., Darmigny, E., de Boer, K. S., de Teodoro, P., de Zeeuw, P. T., Delle Luche, C., Domingues, C. D., Dubath, P., Fodor, F., Frézouls, B., Fries, A., Fustes, D., Fyfe, D., Gallardo, E., Gallegos, J., Gardiol, D., Gebran, M., Gomboc, A., Gómez, A., Grux, E., Gueguen, A., Heyrovsky, A., Hoar, J., Iannicola, G., Isasi Parache, Y., Janotto, A. M., Joliet, E., Jonckheere, A., Keil, R., Kim, D. W., Klagyivik, P., Klar, J., Knude, J., Kochukhov, O., Kolka, I., Kos, J., Kutka, A., Lainey, V., LeBouquin, D., Liu, C., Loreggia, D., Makarov, V. V., Marseille, M. G., Martayan, C., Martinez-Rubi, O., Massart, B., Meynadier, F., Mignot, S., Munari, U., Nguyen, A. T., Nordlander, T., Ocvirk, P., O’Flaherty, K. S., Olias Sanz, A., Ortiz, P., Osorio, J., Oszkiewicz, D., Ouzounis, A., Palmer, M., Park, P., Pasquato, E., Peltzer, C., Peralta, J., Péturaud, F., Pieniluoma, T., Pigozzi, E., Poels, J., Prat, G., Prod’homme, T., Raison, F., Rebordao, J. M., Risquez, D., Rocca-Volmerange, B., Rosen, S., Ruiz-Fuertes, M. I., Russo, F., Sembay, S., Serraller Vizcaino, I., Short, A., Siebert, A., Silva, H., Sinachopoulos, D., Slezak, E., Soffel, M., Sosnowska, D., Straižys, V., ter Linden, M., Terrell, D., Theil, S., Tiede, C., Troisi, L., Tsalmantza, P., Tur, D., Vaccari, M., Vachier, F., Valles, P., Van Hamme, W.,

Veltz, L., Virtanen, J., Wallut, J. M., Wichmann, R., Wilkinson, M. I., Ziaee-pour, H., & Zschocke, S. (2016). The Gaia mission. *Astronomy and Astrophysics*, 595, A1.

Gaia Collaboration, Vallenari, A., Brown, A. G. A., Prusti, T., de Bruijne, J. H. J., Arenou, F., Babusiaux, C., Biermann, M., Creevey, O. L., Ducourant, C., Evans, D. W., Eyer, L., Guerra, R., Hutton, A., Jordi, C., Klioner, S. A., Lammers, U. L., Lindegren, L., Luri, X., Mignard, F., Panem, C., Pourbaix, D., Randich, S., Sartoretti, P., Soubiran, C., Tanga, P., Walton, N. A., Bailer-Jones, C. A. L., Bastian, U., Drimmel, R., Jansen, F., Katz, D., Lattanzi, M. G., van Leeuwen, F., Bakker, J., Cacciari, C., Castañeda, J., De Angeli, F., Fabricius, C., Fouesneau, M., Frémat, Y., Galluccio, L., Guerrier, A., Heiter, U., Masana, E., Messineo, R., Mowlavi, N., Nicolas, C., Nienartowicz, K., Pailler, F., Panuzzo, P., Riclet, F., Roux, W., Seabroke, G. M., Sordo, R., Thévenin, F., Gracia-Abril, G., Portell, J., Teyssier, D., Altmann, M., Andrae, R., Audard, M., Bellas-Velidis, I., Benson, K., Berthier, J., Blomme, R., Burgess, P. W., Busonero, D., Busso, G., Cánovas, H., Carry, B., Cellino, A., Cheek, N., Clementini, G., Damerджи, Y., Davidson, M., de Teodoro, P., Nuñez Campos, M., Delchambre, L., Dell'Oro, A., Esquej, P., Fernández-Hernández, J., Fraile, E., Garabato, D., García-Lario, P., Gosset, E., Haigron, R., Halbwegs, J. L., Hambly, N. C., Harrison, D. L., Hernández, J., Hestroffer, D., Hodgkin, S. T., Holl, B., Janßen, K., Jevardat de Fombelle, G., Jordan, S., Krone-Martins, A., Lanzafame, A. C., Löffler, W., Marchal, O., Marrese, P. M., Moitinho, A., Muinonen, K., Osborne, P., Pancino, E., Pauwels, T., Recio-Blanco, A., Reylé, C., Riello, M., Rimoldini, L., Roegiers, T., Rybizki, J., Sarro, L. M., Siopis, C., Smith, M., Sozzetti, A., Utrilla, E., van Leeuwen, M., Abbas, U., Abraham, P., Abreu Aramburu, A., Aerts, C., Aguado, J. J., Ajaj, M., Aldea-Montero, F., Altavilla, G., Álvarez, M. A., Alves, J., Anders, F., Anderson, R. I., Anglada Varela, E., Antoja, T., Baines, D., Baker, S. G., Balaguer-Núñez, L., Balbinot, E., Balog, Z., Barache, C., Barbato, D., Barros, M., Barstow, M. A., Bartolomé, S., Bassilana, J. L., Bauchet, N., Becciani, U., Bellazzini, M., Berihuete, A., Bernet, M., Bertone, S., Bianchi, L., Binnenfeld, A., Blanco-Cuaresma, S., Blazere, A., Boch, T., Bombrun, A., Bossini, D., Bouquillon, S., Bragaglia, A., Bramante, L., Breedt, E., Bressan, A., Brouillet, N., Brugaletta, E., Bucciarelli, B., Burlacu, A., Butkevich, A. G., Buzzi, R., Caffau, E., Cancelliere, R., Cantat-Gaudin, T., Carballo,

R., Carlucci, T., Carnerero, M. I., Carrasco, J. M., Casamiquela, L., Castellani, M., Castro-Ginard, A., Chaoul, L., Charlot, P., Chemin, L., Chiaramida, V., Chiavassa, A., Chornay, N., Comoretto, G., Contursi, G., Cooper, W. J., Cornez, T., Cowell, S., Crifo, F., Cropper, M., Crosta, M., Crowley, C., Daffonte, C., Dapergolas, A., David, M., David, P., de Laverny, P., De Luise, F., De March, R., De Ridder, J., de Souza, R., de Torres, A., del Peloso, E. F., del Pozo, E., Delbo, M., Delgado, A., Delisle, J. B., Demouchy, C., Dharmawardena, T. E., Di Matteo, P., Diakite, S., Diener, C., Distefano, E., Dolding, C., Edvardsson, B., Enke, H., Fabre, C., Fabrizio, M., Faigler, S., Fedorets, G., Fernique, P., Fienga, A., Figueras, F., Fournier, Y., Fouron, C., Fragkoudi, F., Gai, M., Garcia-Gutierrez, A., Garcia-Reinaldos, M., García-Torres, M., Garofalo, A., Gavel, A., Gavras, P., Gerlach, E., Geyer, R., Giacobbe, P., Gilmore, G., Girona, S., Giuffrida, G., Gomel, R., Gomez, A., González-Núñez, J., González-Santamaría, I., González-Vidal, J. J., Granvik, M., Guillout, P., Guiraud, J., Gutiérrez-Sánchez, R., Guy, L. P., Hatzidimitriou, D., Hauser, M., Haywood, M., Helmer, A., Helmi, A., Sarmiento, M. H., Hidalgo, S. L., Hilger, T., Hładczuk, N., Hobbs, D., Holland, G., Huckle, H. E., Jardine, K., Jasniewicz, G., Jean-Antoine Piccolo, A., Jiménez-Arranz, Ó., Jorissen, A., Juaristi Campillo, J., Julbe, F., Karbevská, L., Kervella, P., Khanna, S., Kontizas, M., Kordopatis, G., Korn, A. J., Kóspál, Á., Kostrzewa-Rutkowska, Z., Kruszyńska, K., Kun, M., Laizeau, P., Lambert, S., Lanza, A. F., Lasne, Y., Le Campion, J. F., Lebreton, Y., Lebzelter, T., Leccia, S., Leclerc, N., Lecoeur-Taïbi, I., Liao, S., Licata, E. L., Lindstrøm, H. E. P., Lister, T. A., Livanou, E., Lobel, A., Lorca, A., Loup, C., Madrero Pardo, P., Magdaleno Romeo, A., Managau, S., Mann, R. G., Manteiga, M., Marchant, J. M., Marconi, M., Marcos, J., Marcos Santos, M. M. S., Marín Pina, D., Marinoni, S., Marocco, F., Marshall, D. J., Martin Polo, L., Martín-Fleitas, J. M., Marton, G., Mary, N., Masip, A., Massari, D., Mastrobuono-Battisti, A., Mazeh, T., McMillan, P. J., Messina, S., Michalik, D., Millar, N. R., Mints, A., Molina, D., Molinaro, R., Molnár, L., Monari, G., Monguió, M., Montegriffo, P., Montero, A., Mor, R., Mora, A., Morbidelli, R., Morel, T., Morris, D., Muraveva, T., Murphy, C. P., Musella, I., Nagy, Z., Noval, L., Ocaña, F., Ogden, A., Ordenovic, C., Osinde, J. O., Pagani, C., Pagano, I., Palaversa, L., Palicio, P. A., Pallas-Quintela, L., Panahi, A., Payne-Wardenaar, S., Peñalosa Esteller, X., Penttilä, A., Pichon, B., Piersimoni, A. M., Pineau, F. X., Plachy, E., Plum, G., Poggio, E., Prša, A., Pulone, L., Racero, E., Ra-

gaini, S., Rainer, M., Raiteri, C. M., Rambaux, N., Ramos, P., Ramos-Lerate, M., Re Fiorentin, P., Regibo, S., Richards, P. J., Rios Diaz, C., Ripepi, V., Riva, A., Rix, H. W., Rixon, G., Robichon, N., Robin, A. C., Robin, C., Roelens, M., Rogues, H. R. O., Rohrbasser, L., Romero-Gómez, M., Rowell, N., Royer, F., Ruz Mieres, D., Rybicki, K. A., Sadowski, G., Sáez Núñez, A., Sagristà Sellés, A., Sahlmann, J., Salguero, E., Samaras, N., Sanchez Gimenez, V., Sanna, N., Santoveña, R., Sarasso, M., Schultheis, M., Sciacca, E., Segol, M., Segovia, J. C., Ségransan, D., Semeux, D., Shahaf, S., Siddiqui, H. I., Siebert, A., Siltala, L., Silvelo, A., Slezak, E., Slezak, I., Smart, R. L., Snaith, O. N., Solano, E., Solitro, F., Souami, D., Souchay, J., Spagna, A., Spina, L., Spoto, F., Steele, I. A., Steidelmüller, H., Stephenson, C. A., Süveges, M., Surdej, J., Szabados, L., Szegedi-Elek, E., Taris, F., Taylor, M. B., Teixeira, R., Tolomei, L., Tonello, N., Torra, F., Torra, J., Torralba Elipe, G., Trabucchi, M., Tsounis, A. T., Turon, C., Ulla, A., Unger, N., Vaillant, M. V., van Dillen, E., van Reeven, W., Vanel, O., Vecchiato, A., Viala, Y., Vicente, D., Voutsinas, S., Weiler, M., Wevers, T., Wyrzykowski, Ł., Yoldas, A., Yvard, P., Zhao, H., Zorec, J., Zucker, S., & Zwitter, T. (2023). Gaia Data Release 3. Summary of the content and survey properties. *Astronomy and Astrophysics*, 674, A1.

Galicher, R., Boccaletti, A., Mesa, D., Delorme, P., Gratton, R., Langlois, M., Lagrange, A. M., Maire, A. L., Le Coroller, H., Chauvin, G., Biller, B., Cantalloube, F., Janson, M., Lagadec, E., Meunier, N., Vigan, A., Hagelberg, J., Bonnefoy, M., Zurlo, A., Rocha, S., Maurel, D., Jaquet, M., Buey, T., & Weber, L. (2018). Astrometric and photometric accuracies in high contrast imaging: The SPHERE speckle calibration tool (SpeCal). *Astronomy and Astrophysics*, 615, A92.

Gaspar, A. & Rieke, G. (2020). New HST data and modeling reveal a massive planetesimal collision around Fomalhaut. *Proceedings of the National Academy of Science*, 117(18), 9712–9722.

Geißler, K., Chauvin, G., & Sterzik, M. F. (2008). Mid-infrared imaging of brown dwarfs in binary systems. *Astronomy and Astrophysics*, 480(1), 193–198.

Geller, A. M. & Leigh, N. W. C. (2015). Interrupted Stellar Encounters in Star Clusters. *Astrophysical Journal, Letters*, 808(1), L25.

Giannini, T., Giunta, A., Gangi, M., Carini, R., Lorenzetti, D., Antonucci, S., Caratti o Garatti, A., Cassarà, L., Nisini, B., Rossi, A., Testa, V., & Vitali, F. (2022).

EXORCISM: A Spectroscopic Survey of Young Eruptive Variables (EXor and Candidates). *Astrophysical Journal*, 929(2), 129.

Golimowski, D. A., Ardila, D. R., Krist, J. E., Clampin, M., Ford, H. C., Illingworth, G. D., Bartko, F., Benítez, N., Blakeslee, J. P., Bouwens, R. J., Bradley, L. D., Broadhurst, T. J., Brown, R. A., Burrows, C. J., Cheng, E. S., Cross, N. J. G., Demarco, R., Feldman, P. D., Franx, M., Goto, T., Gronwall, C., Hartig, G. F., Holden, B. P., Homeier, N. L., Infante, L., Jee, M. J., Kimble, R. A., Lesser, M. P., Martel, A. R., Mei, S., Menanteau, F., Meurer, G. R., Miley, G. K., Motta, V., Postman, M., Rosati, P., Sirianni, M., Sparks, W. B., Tran, H. D., Tsvetanov, Z. I., White, R. L., Zheng, W., & Zirm, A. W. (2006). Hubble Space Telescope ACS Multiband Coronagraphic Imaging of the Debris Disk around β Pictoris. *Astronomical Journal*, 131(6), 3109–3130.

Gomez Gonzalez, C. A., Absil, O., & Van Droogenbroeck, M. (2018). Supervised detection of exoplanets in high-contrast imaging sequences. *Astronomy and Astrophysics*, 613, A71.

Gomez Gonzalez, C. A., Wertz, O., Absil, O., Christiaens, V., Defrère, D., Mawet, D., Milli, J., Absil, P.-A., Van Droogenbroeck, M., Cantalloube, F., Hinz, P. M., Skemer, A. J., Karlsson, M., & Surdej, J. (2017). VIP: Vortex Image Processing Package for High-contrast Direct Imaging. *Astronomical Journal*, 154(1), 7.

Grandjean, A., Lagrange, A. M., Keppler, M., Meunier, N., Mignon, L., Borgniet, S., Chauvin, G., Desidera, S., Galland, F., Messina, S., Sterzik, M., Pantoja, B., Rodet, L., & Zicher, N. (2020). A HARPS RV search for planets around young nearby stars. *Astronomy and Astrophysics*, 633, A44.

Gray, R. O., Corbally, C. J., Garrison, R. F., McFadden, M. T., Bubar, E. J., McGahee, C. E., O'Donoghue, A. A., & Knox, E. R. (2006). Contributions to the Nearby Stars (NStars) Project: Spectroscopy of Stars Earlier than M0 within 40 pc-The Southern Sample. *Astronomical Journal*, 132(1), 161–170.

Greaves, J. S., Kennedy, G. M., Thureau, N., Eiroa, C., Marshall, J. P., Maldonado, J., Matthews, B. C., Olofsson, G., Barlow, M. J., Moro-Martín, A., Sibthorpe, B., Absil, O., Ardila, D. R., Booth, M., Broekhoven-Fiene, H., Brown, D. J. A., Collier Cameron, A., del Burgo, C., Di Francesco, J., Eisloffel, J., Duchêne, G., Ertel, S., Holland, W. S., Horner, J., Kalas, P., Kavelaars, J. J., Lestrade,

- J. F., Vican, L., Wilner, D. J., Wolf, S., & Wyatt, M. C. (2014). Alignment in star-debris disc systems seen by Herschel. *Monthly Notices of the RAS*, 438(1), L31–L35.
- Greene, T. P., Wilking, B. A., Andre, P., Young, E. T., & Lada, C. J. (1994). Further Mid-Infrared Study of the rho Ophiuchi Cloud Young Stellar Population: Luminosities and Masses of Pre–Main-Sequence Stars. *Astrophysical Journal*, 434, 614.
- Guenther, E. W., Neuhäuser, R., Huélamo, N., Brandner, W., & Alves, J. (2001). Infrared spectrum and proper motion of the brown dwarf companion of HR 7329 in Tucanae. *Astronomy and Astrophysics*, 365, 514–518.
- Gundlach, B., Kiliyas, S., Beitz, E., & Blum, J. (2011). Micrometer-sized ice particles for planetary-science experiments - I. Preparation, critical rolling friction force, and specific surface energy. *Icarus*, 214(2), 717–723.
- Guszejnov, D. & Hopkins, P. F. (2015). Mapping the core mass function to the initial mass function. *Monthly Notices of the RAS*, 450(4), 4137–4149.
- Guszejnov, D., Hopkins, P. F., & Krumholz, M. R. (2017). Protostellar feedback in turbulent fragmentation: consequences for stellar clustering and multiplicity. *Monthly Notices of the RAS*, 468(4), 4093–4106.
- Guyon, O., Bendek, E. A., Eisner, J. A., Angel, R., Woolf, N. J., Milster, T. D., Ammons, S. M., Shao, M., Shaklan, S., Levine, M., Nemati, B., Pitman, J., Woodruff, R. A., & Belikov, R. (2012). High-precision Astrometry with a Diffractive Pupil Telescope. *Astrophysical Journal, Supplement*, 200(2), 11.
- Guyon, O., Pluzhnik, E. A., Kuchner, M. J., Collins, B., & Ridgway, S. T. (2006). Theoretical Limits on Extrasolar Terrestrial Planet Detection with Coronagraphs. *Astrophysical Journal, Supplement*, 167(1), 81–99.
- Gómez González, C. (2017). *Advanced data processing for high-contrast imaging - Pushing exoplanet direct detection limits with machine learning*. PhD thesis, University of Liège. Available at <https://orbi.uliege.be/handle/2268/214337>.

- Haffert, S. Y., Bohn, A. J., de Boer, J., Snellen, I. A. G., Brinchmann, J., Girard, J. H., Keller, C. U., & Bacon, R. (2019). Two accreting protoplanets around the young star PDS 70. *Nature Astronomy*, 3, 749–754.
- Hales, A. S., Pérez, S., Gonzalez-Ruilova, C., Cieza, L. A., Williams, J. P., Sheehan, P. D., López, C., Casassus, S., Principe, D. A., & Zurlo, A. (2020). ALMA Observations of Young Eruptive Stars: Continuum Disk Sizes and Molecular Outflows. *Astrophysical Journal*, 900(1), 7.
- Hales, A. S., Pérez, S., Saito, M., Pinte, C., Knee, L. B. G., de Gregorio-Monsalvo, I., Dent, B., López, C., Plunkett, A., Cortés, P., Corder, S., & Cieza, L. (2018). The Circumstellar Disk and Asymmetric Outflow of the EX Lup Outburst System. *Astrophysical Journal*, 859(2), 111.
- Hamers, A. S. & Samsing, J. (2020). Binary-binary scattering in the secular limit. *Monthly Notices of the RAS*, 494(1), 850–867.
- Harris, R. J., Andrews, S. M., Wilner, D. J., & Kraus, A. L. (2012). A Resolved Census of Millimeter Emission from Taurus Multiple Star Systems. *Astrophysical Journal*, 751(2), 115.
- Harsono, D., Alexander, R. D., & Levin, Y. (2011). Global gravitational instabilities in discs with infall. *Monthly Notices of the RAS*, 413(1), 423–433.
- Hartmann, L., Calvet, N., Gullbring, E., & D’Alessio, P. (1998). Accretion and the Evolution of T Tauri Disks. *Astrophysical Journal*, 495(1), 385–400.
- Hartmann, L. & Kenyon, S. J. (1996). The FU Orionis Phenomenon. *Annual Review of Astron and Astrophysics*, 34, 207–240.
- Heim, L.-O., Blum, J., Preuss, M., & Butt, H.-J. (1999). Adhesion and Friction Forces between Spherical Micrometer-Sized Particles. *Physical Review Letters*, 83(16), 3328–3331.
- Herbig, G. H. (1966). On the interpretation of FU Orionis. *Vistas in Astronomy*, 8, 109–125.
- Herbig, G. H. (2007). EX Lupi: History and Spectroscopy. *Astronomical Journal*, 133(6), 2679–2683.

- Hinz, P. M., Rodigas, T. J., Kenworthy, M. A., Sivanandam, S., Heinze, A. N., Mamajek, E. E., & Meyer, M. R. (2010). Thermal Infrared MMTAO Observations of the HR 8799 Planetary System. *Astrophysical Journal*, 716(1), 417–426.
- Holman, M. J. & Wiegert, P. A. (1999). Long-Term Stability of Planets in Binary Systems. *Astronomical Journal*, 117(1), 621–628.
- Holmberg, J., Nordström, B., & Andersen, J. (2009). The Geneva-Copenhagen survey of the solar neighbourhood. III. Improved distances, ages, and kinematics. *Astronomy and Astrophysics*, 501(3), 941–947.
- Hou Yip, K., Nikolaou, N., Coronica, P., Tsiaras, A., Edwards, B., Changeat, Q., Morvan, M., Biller, B., Hinkley, S., Salmond, J., Archer, M., Sumption, P., Choquet, E., Soummer, R., Pueyo, L., & Waldmann, I. P. (2019). Pushing the Limits of Exoplanet Discovery via Direct Imaging with Deep Learning. *arXiv e-prints*, (pp. arXiv:1904.06155).
- Houk, N. & Cowley, A. P. (1975). *University of Michigan Catalogue of two-dimensional spectral types for the HD stars. Volume I. Declinations -90_ to -53_f0*. University of Michigan.
- Hurt, S. A. & MacGregor, M. A. (2023). Evidence for Misalignment between Debris Disks and Their Host Stars. *Astrophysical Journal*, 954(1), 10.
- Hyodo, R., Ida, S., & Charnoz, S. (2019). Formation of rocky and icy planetesimals inside and outside the snow line: effects of diffusion, sublimation, and back-reaction. *Astronomy and Astrophysics*, 629, A90.
- Ida, S. & Guillot, T. (2016). Formation of dust-rich planetesimals from sublimated pebbles inside of the snow line. *Astronomy and Astrophysics*, 596, L3.
- Iglesias, D. P., Panić, O., & Rebollido, I. (2023). Gas absorption towards the η Tel debris disc: winds or clouds? *Monthly Notices of the RAS*, 526(2), 2500–2505.
- Inutsuka, S.-I. & Miyama, S. M. (1992). Self-similar Solutions and the Stability of Collapsing Isothermal Filaments. *Astrophysical Journal*, 388, 392.
- Inutsuka, S.-i. & Miyama, S. M. (1997). A Production Mechanism for Clusters of Dense Cores. *Astrophysical Journal*, 480(2), 681–693.

- Isella, A., Benisty, M., Teague, R., Bae, J., Keppler, M., Facchini, S., & Pérez, L. (2019). Detection of Continuum Submillimeter Emission Associated with Candidate Protoplanets. *Astrophysical Journal, Letters*, 879(2), L25.
- Janson, M., Quanz, S. P., Carson, J. C., Thalmann, C., Lafrenière, D., & Amara, A. (2015). High-contrast imaging with Spitzer: deep observations of Vega, Fomalhaut, and ϵ Eridani. *Astronomy and Astrophysics*, 574, A120.
- Johansen, A., Blum, J., Tanaka, H., Ormel, C., Bizzarro, M., & Rickman, H. (2014). The Multifaceted Planetesimal Formation Process. In H. Beuther, R. S. Klessen, C. P. Dullemond, & T. Henning (Eds.), *Protostars and Planets VI* (pp. 547–570).
- Johansen, A. & Lambrechts, M. (2017). Forming Planets via Pebble Accretion. *Annual Review of Earth and Planetary Sciences*, 45(1), 359–387.
- Jurdana-Šepić, R., Munari, U., Antonucci, S., Giannini, T., & Lorenzetti, D. (2018). Towards a better classification of unclear eruptive variables: the cases of V2492 Cyg, V350 Cep, and ASASSN-15qi. *Astronomy and Astrophysics*, 614, A9.
- Kalas, P., Graham, J. R., Chiang, E., Fitzgerald, M. P., Clampin, M., Kite, E. S., Stapelfeldt, K., Marois, C., & Krist, J. (2008). Optical Images of an Exosolar Planet 25 Light-Years from Earth. *Science*, 322(5906), 1345.
- Kant, I. (1755). *Allgemeine Naturgeschichte und Theorie des Himmels*. Germany.
- Kasper, M., Apai, D., Janson, M., & Brandner, W. (2007). A novel L-band imaging search for giant planets in the Tucana and β Pictoris moving groups. *Astronomy and Astrophysics*, 472(1), 321–327.
- Kenyon, S. J. & Hartmann, L. (1987). Spectral Energy Distributions of T Tauri Stars: Disk Flaring and Limits on Accretion. *Astrophysical Journal*, 323, 714.
- Kenyon, S. J., Hartmann, L. W., Strom, K. M., & Strom, S. E. (1990). An IRAS Survey of the Taurus-Auriga Molecular Cloud. *Astronomical Journal*, 99, 869.
- Keppler, M., Benisty, M., Müller, A., Henning, T., van Boekel, R., Cantalloube, F., Ginski, C., van Holstein, R. G., Maire, A. L., Pohl, A., Samland, M., Avenhaus, H., Baudino, J. L., Boccaletti, A., de Boer, J., Bonnefoy, M., Chauvin, G., Desidera,

S., Langlois, M., Lazzoni, C., Marleau, G. D., Mordasini, C., Pawellek, N., Stolker, T., Vigan, A., Zurlo, A., Birnstiel, T., Brandner, W., Feldt, M., Flock, M., Girard, J., Gratton, R., Hagelberg, J., Isella, A., Janson, M., Juhasz, A., Kemmer, J., Kral, Q., Lagrange, A. M., Launhardt, R., Matter, A., Ménard, F., Milli, J., Mollière, P., Olofsson, J., Pérez, L., Pinilla, P., Pinte, C., Quanz, S. P., Schmidt, T., Udry, S., Wahhaj, Z., Williams, J. P., Buenzli, E., Cudel, M., Dominik, C., Galicher, R., Kasper, M., Lannier, J., Mesa, D., Mouillet, D., Peretti, S., Perrot, C., Salter, G., Sissa, E., Wildi, F., Abe, L., Antichi, J., Augereau, J. C., Baruffolo, A., Baudoz, P., Bazzon, A., Beuzit, J. L., Blanchard, P., Brems, S. S., Buey, T., De Caprio, V., Carbillet, M., Carle, M., Cascone, E., Cheetham, A., Claudi, R., Costille, A., Delboulbé, A., Dohlen, K., Fantinel, D., Feautrier, P., Fusco, T., Giro, E., Gluck, L., Gry, C., Hubin, N., Hugot, E., Jaquet, M., Le Mignant, D., Llored, M., Madec, F., Magnard, Y., Martinez, P., Maurel, D., Meyer, M., Möller-Nilsson, O., Moulin, T., Mugnier, L., Origné, A., Pavlov, A., Perret, D., Petit, C., Pragt, J., Puget, P., Rabou, P., Ramos, J., Rigal, F., Rochat, S., Roelfsema, R., Rousset, G., Roux, A., Salasnich, B., Sauvage, J. F., Sevin, A., Soenke, C., Stadler, E., Suarez, M., Turatto, M., & Weber, L. (2018a). Discovery of a planetary-mass companion within the gap of the transition disk around PDS 70. *Astronomy and Astrophysics*, 617, A44.

Keppler, M., Benisty, M., Müller, A., Henning, T., van Boekel, R., Cantalloube, F., Ginski, C., van Holstein, R. G., Maire, A. L., Pohl, A., Samland, M., Avenhaus, H., Baudino, J. L., Boccaletti, A., de Boer, J., Bonnefoy, M., Chauvin, G., Desidera, S., Langlois, M., Lazzoni, C., Marleau, G. D., Mordasini, C., Pawellek, N., Stolker, T., Vigan, A., Zurlo, A., Birnstiel, T., Brandner, W., Feldt, M., Flock, M., Girard, J., Gratton, R., Hagelberg, J., Isella, A., Janson, M., Juhasz, A., Kemmer, J., Kral, Q., Lagrange, A. M., Launhardt, R., Matter, A., Ménard, F., Milli, J., Mollière, P., Olofsson, J., Pérez, L., Pinilla, P., Pinte, C., Quanz, S. P., Schmidt, T., Udry, S., Wahhaj, Z., Williams, J. P., Buenzli, E., Cudel, M., Dominik, C., Galicher, R., Kasper, M., Lannier, J., Mesa, D., Mouillet, D., Peretti, S., Perrot, C., Salter, G., Sissa, E., Wildi, F., Abe, L., Antichi, J., Augereau, J. C., Baruffolo, A., Baudoz, P., Bazzon, A., Beuzit, J. L., Blanchard, P., Brems, S. S., Buey, T., De Caprio, V., Carbillet, M., Carle, M., Cascone, E., Cheetham, A., Claudi, R., Costille, A., Delboulbé, A., Dohlen, K., Fantinel, D., Feautrier, P., Fusco, T., Giro, E., Gluck, L., Gry, C., Hubin, N., Hugot, E.,

- Jaquet, M., Le Mignant, D., Llored, M., Madec, F., Magnard, Y., Martinez, P., Maurel, D., Meyer, M., Möller-Nilsson, O., Moulin, T., Mugnier, L., Origné, A., Pavlov, A., Perret, D., Petit, C., Pragt, J., Puget, P., Rabou, P., Ramos, J., Rigal, F., Rochat, S., Roelfsema, R., Rousset, G., Roux, A., Salasnich, B., Sauvage, J. F., Sevin, A., Soenke, C., Stadler, E., Suarez, M., Turatto, M., & Weber, L. (2018b). Discovery of a planetary-mass companion within the gap of the transition disk around PDS 70. *Astronomy and Astrophysics*, 617, A44.
- Kervella, P., Arenou, F., & Thevenin, F. (2021). VizieR Online Data Catalog: Stellar and substellar companions from Gaia EDR3 (Kervella+, 2022). *VizieR Online Data Catalog*, (pp. J/A+A/657/A7).
- Kervella, P., Arenou, F., & Thévenin, F. (2022). Stellar and substellar companions from Gaia EDR3. Proper-motion anomaly and resolved common proper-motion pairs. *Astronomy and Astrophysics*, 657, A7.
- Kiefer, F., Hébrard, G., Sahlmann, J., Sousa, S. G., Forveille, T., Santos, N., Mayor, M., Deleuil, M., Wilson, P. A., Dalal, S., Díaz, R. F., Henry, G. W., Hagelberg, J., Hobson, M. J., Demangeon, O., Bourrier, V., Delfosse, X., Arnold, L., Astudillo-Defru, N., Beuzit, J. L., Boisse, I., Bonfils, X., Borgniet, S., Bouchy, F., Courcol, B., Ehrenreich, D., Hara, N., Lagrange, A. M., Lovis, C., Montagnier, G., Moutou, C., Pepe, F., Perrier, C., Rey, J., Santerne, A., Ségransan, D., Udry, S., & Vidal-Madjar, A. (2019). Detection and characterisation of 54 massive companions with the SOPHIE spectrograph. Seven new brown dwarfs and constraints on the brown dwarf desert. *Astronomy and Astrophysics*, 631, A125.
- Kiefer, S., Bohn, A. J., Quanz, S. P., Kenworthy, M., & Stolker, T. (2021). Spectral and angular differential imaging with SPHERE/IFS. Assessing the performance of various PCA-based approaches to PSF subtraction. *Astronomy and Astrophysics*, 652, A33.
- Kim, C.-G. & Ostriker, E. C. (2018). Numerical Simulations of Multiphase Winds and Fountains from Star-forming Galactic Disks. I. Solar Neighborhood TIGRESS Model. *Astrophysical Journal*, 853(2), 173.
- Kingma, D. P. & Ba, J. (2014). Adam: A method for stochastic optimization. *arXiv preprint arXiv:1412.6980*.

- Kirkpatrick, J. D., Reid, I. N., Liebert, J., Cutri, R. M., Nelson, B., Beichman, C. A., Dahn, C. C., Monet, D. G., Gizis, J. E., & Skrutskie, M. F. (1999). Dwarfs Cooler than “M”: The Definition of Spectral Type “L” Using Discoveries from the 2 Micron All-Sky Survey (2MASS). *Astrophysical Journal*, 519(2), 802–833.
- Konopacky, Q. M., Barman, T. S., Macintosh, B. A., & Marois, C. (2013). Detection of Carbon Monoxide and Water Absorption Lines in an Exoplanet Atmosphere. *Science*, 339(6126), 1398–1401.
- Kóspál, Á., Ábrahám, P., Csengeri, T., Fehér, O., Hogerheijde, M. R., Brinch, C., Dunham, M. M., Vorobyov, E. I., Salter, D. M., & Henning, T. (2017). Mass Transport from the Envelope to the Disk of V346 Nor: A Case Study for the Luminosity Problem in an FUor-type Young Eruptive Star. *Astrophysical Journal*, 843(1), 45.
- Kozai, Y. (1962). Secular perturbations of asteroids with high inclination and eccentricity. *Astronomical Journal*, 67, 591–598.
- Kratter, K. & Lodato, G. (2016). Gravitational Instabilities in Circumstellar Disks. *Annual Review of Astron and Astrophysics*, 54, 271–311.
- Kratter, K. M. & Matzner, C. D. (2006). Fragmentation of massive protostellar discs. *Monthly Notices of the RAS*, 373(4), 1563–1576.
- Kratter, K. M., Matzner, C. D., Krumholz, M. R., & Klein, R. I. (2010a). On the Role of Disks in the Formation of Stellar Systems: A Numerical Parameter Study of Rapid Accretion. *Astrophysical Journal*, 708(2), 1585–1597.
- Kratter, K. M., Murray-Clay, R. A., & Youdin, A. N. (2010b). The Runts of the Litter: Why Planets Formed Through Gravitational Instability Can Only Be Failed Binary Stars. *Astrophysical Journal*, 710(2), 1375–1386.
- Kraus, A. L., Ireland, M. J., Hillenbrand, L. A., & Martinache, F. (2012). The Role of Multiplicity in Disk Evolution and Planet Formation. *Astrophysical Journal*, 745(1), 19.
- Kraus, A. L., Ireland, M. J., Martinache, F., & Hillenbrand, L. A. (2011). Mapping the Shores of the Brown Dwarf Desert. II. Multiple Star Formation in Taurus-Auriga. *Astrophysical Journal*, 731(1), 8.

- Kraus, A. L., Ireland, M. J., Martinache, F., & Lloyd, J. P. (2008). Mapping the Shores of the Brown Dwarf Desert. I. Upper Scorpius. *Astrophysical Journal*, 679(1), 762–782.
- Kuffmeier, M., Dullemond, C. P., Reissl, S., & Goicovic, F. G. (2021). Misaligned disks induced by infall. *Astronomy and Astrophysics*, 656, A161.
- Kuffmeier, M., Frimann, S., Jensen, S. S., & Haugbølle, T. (2018). Episodic accretion: the interplay of infall and disc instabilities. *Monthly Notices of the RAS*, 475(2), 2642–2658.
- Kuffmeier, M., Goicovic, F. G., & Dullemond, C. P. (2020). Late encounter events as source of disks and spiral structures. Forming second generation disks. *Astronomy and Astrophysics*, 633, A3.
- Kuruwita, R. L., Federrath, C., & Haugbølle, T. (2020). The dependence of episodic accretion on eccentricity during the formation of binary stars. *Astronomy and Astrophysics*, 641, A59.
- Kusaka, T., Nakano, T., & Hayashi, C. (1970). Growth of Solid Particles in the Primordial Solar Nebula. *Progress of Theoretical Physics*, 44(6), 1580–1595.
- Lada, C. J. (1987). Star formation: from OB associations to protostars. In M. Peimbert & J. Jugaku (Eds.), *Star Forming Regions*, volume 115 (pp. 1–11).
- Lafrenière, D., Marois, C., Doyon, R., & Barman, T. (2009). HST/NICMOS Detection of HR 8799 b in 1998. *Astrophysical Journal, Letters*, 694(2), L148–L152.
- Lafrenière, D., Marois, C., Doyon, R., Nadeau, D., & Artigau, É. (2007). A New Algorithm for Point-Spread Function Subtraction in High-Contrast Imaging: A Demonstration with Angular Differential Imaging. *Astrophysical Journal*, 660(1), 770–780.
- Lagrange, A. M., Bonnefoy, M., Chauvin, G., Apai, D., Ehrenreich, D., Boccaletti, A., Gratadour, D., Rouan, D., Mouillet, D., Lacour, S., & Kasper, M. (2010a). A Giant Planet Imaged in the Disk of the Young Star β Pictoris. *Science*, 329(5987), 57.

- Lagrange, A. M., Bonnefoy, M., Chauvin, G., Apai, D., Ehrenreich, D., Boccaletti, A., Gratadour, D., Rouan, D., Mouillet, D., Lacour, S., & Kasper, M. (2010b). A Giant Planet Imaged in the Disk of the Young Star β Pictoris. *Science*, 329(5987), 57.
- Lagrange, A. M., Desort, M., Galland, F., Udry, S., & Mayor, M. (2009a). Extrasolar planets and brown dwarfs around A-F type stars. VI. High precision RV survey of early type dwarfs with HARPS. *Astronomy and Astrophysics*, 495(1), 335–352.
- Lagrange, A. M., Gratadour, D., Chauvin, G., Fusco, T., Ehrenreich, D., Mouillet, D., Rousset, G., Rouan, D., Allard, F., Gendron, É., Charton, J., Mugnier, L., Rabou, P., Montri, J., & Lacombe, F. (2009b). A probable giant planet imaged in the β Pictoris disk. VLT/NaCo deep L'-band imaging. *Astronomy and Astrophysics*, 493(2), L21–L25.
- Lagrange, A. M., Meunier, N., Rubini, P., Keppler, M., Galland, F., Chapellier, E., Michel, E., Balona, L., Beust, H., Guillot, T., Grandjean, A., Borgniet, S., Mékarnia, D., Wilson, P. A., Kiefer, F., Bonnefoy, M., Lillo-Box, J., Pantoja, B., Jones, M., Iglesias, D. P., Rodet, L., Diaz, M., Zapata, A., Abe, L., & Schmider, F.-X. (2019). Evidence for an additional planet in the β Pictoris system. *Nature Astronomy*, 3, 1135–1142.
- Lai, D. & Muñoz, D. J. (2022). Circumbinary Accretion: From Binary Stars to Massive Binary Black Holes. *arXiv e-prints*, (pp. arXiv:2211.00028).
- Laplace, P.-S. (1796). *Exposition du système du monde*. Imprimerie Cercle-Social, Paris.
- Larson, R. B. (1972). The Collapse of a Rotating Cloud. *Monthly Notices of the RAS*, 156, 437.
- Lau, Y. Y. & Bertin, G. (1978). Discrete spiral modes, spiral waves, and the local dispersion relationship. *Astrophysical Journal*, 226, 508–520.
- Lawler, S. M., Greenstreet, S., & Gladman, B. (2015). Fomalhaut b as a Dust Cloud: Frequent Collisions within the Fomalhaut Disk. *Astrophysical Journal, Letters*, 802(2), L20.

- Lazzoni, C., Desidera, S., Gratton, R., Zurlo, A., Mesa, D., & Ray, S. (2022). Detectability of satellites around directly imaged exoplanets and brown dwarfs. *Monthly Notices of the RAS*, 516(1), 391–409.
- Lazzoni, C., Desidera, S., Marzari, F., Boccaletti, A., Langlois, M., Mesa, D., Gratton, R., Kral, Q., Pawellek, N., Olofsson, J., Bonnefoy, M., Chauvin, G., Lagrange, A. M., Vigan, A., Sissa, E., Antichi, J., Avenhaus, H., Baruffolo, A., Baudino, J. L., Bazzon, A., Beuzit, J. L., Biller, B., Bonavita, M., Brandner, W., Bruno, P., Buenzli, E., Cantalloube, F., Cascone, E., Cheetham, A., Claudi, R. U., Cudel, M., Daemgen, S., De Caprio, V., Delorme, P., Fantinel, D., Farisato, G., Feldt, M., Galicher, R., Ginski, C., Girard, J., Giro, E., Janson, M., Hagelberg, J., Henning, T., Incorvaia, S., Kasper, M., Kopytova, T., LeCoroller, H., Lessio, L., Ligi, R., Maire, A. L., Ménard, F., Meyer, M., Milli, J., Mouillet, D., Peretti, S., Perrot, C., Rouan, D., Samland, M., Salasnich, B., Salter, G., Schmidt, T., Scuderi, S., Sezestre, E., Turatto, M., Udry, S., Wildi, F., & Zurlo, A. (2018). Dynamical models to explain observations with SPHERE in planetary systems with double debris belts. *Astronomy and Astrophysics*, 611, A43.
- Lazzoni, C., Rice, K., Zurlo, A., Hinkley, S., & Desidera, S. (2024). Binary planet formation through tides. *Monthly Notices of the RAS*, 527(2), 3837–3846.
- Lazzoni, C., Zurlo, A., Desidera, S., Mesa, D., Fontanive, C., Bonavita, M., Ertel, S., Rice, K., Vigan, A., Boccaletti, A., Bonnefoy, M., Chauvin, G., Delorme, P., Gratton, R., Houllé, M., Maire, A. L., Meyer, M., Rickman, E., Spalding, E. A., Asensio-Torres, R., Langlois, M., Müller, A., Baudino, J. L., Beuzit, J. L., Biller, B., Brandner, W., Buenzli, E., Cantalloube, F., Cheetham, A., Cudel, M., Feldt, M., Galicher, R., Janson, M., Hagelberg, J., Henning, T., Kasper, M., Keppler, M., Lagrange, A. M., Lannier, J., LeCoroller, H., Mouillet, D., Peretti, S., Perrot, C., Salter, G., Samland, M., Schmidt, T., Sissa, E., & Wildi, F. (2020). The search for disks or planetary objects around directly imaged companions: a candidate around DH Tauri B. *Astronomy and Astrophysics*, 641, A131.
- Lee, A. T., Offner, S. S. R., Kratter, K. M., Smullen, R. A., & Li, P. S. (2019). The Formation and Evolution of Wide-orbit Stellar Multiples In Magnetized Clouds. *Astrophysical Journal*, 887(2), 232.
- Lee, A. T. & Stahler, S. W. (2011). Dynamical friction in a gas: the subsonic case. *Monthly Notices of the RAS*, 416(4), 3177–3186.

- Lee, J., Song, I., & Murphy, S. J. (2022). Low-mass members of nearby young stellar moving groups from Gaia EDR3. *Monthly Notices of the RAS*, 511(4), 6179–6192.
- Lidov, M. L. (1962). The evolution of orbits of artificial satellites of planets under the action of gravitational perturbations of external bodies. *Planetary Space Science*, 9(10), 719–759.
- Lin, Z.-Y. D., Li, Z.-Y., Yang, H., Looney, L., Lee, C.-F., Stephens, I., & Lai, S.-P. (2020). Probing the temperature structure of optically thick discs using polarized emission of aligned grains. *Monthly Notices of the RAS*, 493(4), 4868–4883.
- Liu, M. C., Magnier, E. A., Deacon, N. R., Allers, K. N., Dupuy, T. J., Kotson, M. C., Aller, K. M., Burgett, W. S., Chambers, K. C., Draper, P. W., Hodapp, K. W., Jedicke, R., Kaiser, N., Kudritzki, R. P., Metcalfe, N., Morgan, J. S., Price, P. A., Tonry, J. L., & Wainscoat, R. J. (2013). The Extremely Red, Young L Dwarf PSO J318.5338-22.8603: A Free-floating Planetary-mass Analog to Directly Imaged Young Gas-giant Planets. *Astrophysical Journal, Letters*, 777(2), L20.
- Lodato, G. & Clarke, C. J. (2004). Massive planets in FU Orionis discs: implications for thermal instability models. *Monthly Notices of the RAS*, 353, 841–852.
- Lowrance, P. J., Schneider, G., Kirkpatrick, J. D., Becklin, E. E., Weinberger, A. J., Zuckerman, B., Plait, P., Malmuth, E. M., Heap, S. R., Schultz, A., Smith, B. A., Terrielle, R. J., & Hines, D. C. (2000). A Candidate Substellar Companion to HR 7329. *Astrophysical Journal*, 541(1), 390–395.
- Luhman, K. L., Tremblin, P., Birkmann, S. M., Manjavacas, E., Valenti, J., Alves de Oliveira, C., Beck, T. L., Giardino, G., Lützendorf, N., Rauscher, B. J., & Sirianni, M. (2023). JWST/NIRSpec Observations of the Planetary Mass Companion TWA 27B. *Astrophysical Journal, Letters*, 949(2), L36.
- Lynden-Bell, D. & Pringle, J. E. (1974). The evolution of viscous discs and the origin of the nebular variables. *Monthly Notices of the RAS*, 168, 603–637.
- Macintosh, B., Graham, J. R., Barman, T., De Rosa, R. J., Konopacky, Q., Marley, M. S., Marois, C., Nielsen, E. L., Pueyo, L., Rajan, A., Rameau, J., Saumon, D., Wang, J. J., Patience, J., Ammons, M., Arriaga, P., Artigau, E., Beckwith, S., Brewster, J., Bruzzone, S., Bulger, J., Burningham, B., Burrows, A. S., Chen, C., Chiang,

E., Chilcote, J. K., Dawson, R. I., Dong, R., Doyon, R., Draper, Z. H., Duchêne, G., Esposito, T. M., Fabrycky, D., Fitzgerald, M. P., Follette, K. B., Fortney, J. J., Gerard, B., Goodsell, S., Greenbaum, A. Z., Hibon, P., Hinkley, S., Cotten, T. H., Hung, L. W., Ingraham, P., Johnson-Groh, M., Kalas, P., Lafreniere, D., Larkin, J. E., Lee, J., Line, M., Long, D., Maire, J., Marchis, F., Matthews, B. C., Max, C. E., Metchev, S., Millar-Blanchaer, M. A., Mittal, T., Morley, C. V., Morzinski, K. M., Murray-Clay, R., Oppenheimer, R., Palmer, D. W., Patel, R., Perrin, M. D., Poyneer, L. A., Rafikov, R. R., Rantakyro, F. T., Rice, E. L., Rojo, P., Rudy, A. R., Ruffio, J. B., Ruiz, M. T., Sadakuni, N., Saddlemyer, L., Salama, M., Savransky, D., Schneider, A. C., Sivaramakrishnan, A., Song, I., Soummer, R., Thomas, S., Vasisht, G., Wallace, J. K., Ward-Duong, K., Wiktorowicz, S. J., Wolff, S. G., & Zuckerman, B. (2015). Discovery and spectroscopy of the young jovian planet 51 Eri b with the Gemini Planet Imager. *Science*, 350(6256), 64–67.

Macintosh, B. A., Graham, J. R., Palmer, D. W., Doyon, R., Dunn, J., Gavel, D. T., Larkin, J., Oppenheimer, B., Saddlemyer, L., Sivaramakrishnan, A., Wallace, J. K., Bauman, B., Erickson, D. A., Marois, C., Poyneer, L. A., & Soummer, R. (2008). The Gemini Planet Imager: from science to design to construction. In N. Hubin, C. E. Max, & P. L. Wizinowich (Eds.), *Adaptive Optics Systems*, volume 7015 of *Society of Photo-Optical Instrumentation Engineers (SPIE) Conference Series* (pp. 701518).

Macías Quevedo, E. (2016). *From circumstellar disks to planetary systems: observation and modeling of protoplanetary disks*. PhD thesis, Universidad de Granada; CSIC - Instituto de Astrofísica de Andalucía (IAA). Available at <http://hdl.handle.net/10261/149498>.

Madec, P. Y. (2012). Overview of deformable mirror technologies for adaptive optics and astronomy. In B. L. Ellerbroek, E. Marchetti, & J.-P. Véran (Eds.), *Adaptive Optics Systems III*, volume 8447 of *Society of Photo-Optical Instrumentation Engineers (SPIE) Conference Series* (pp. 844705).

Maire, A.-L., Langlois, M., Delorme, P., Chauvin, G., Gratton, R., Vigan, A., Girard, J. H., Wahhaj, Z., Pott, J.-U., Burtscher, L., Boccaletti, A., Carlotti, A., Henning, T., Kenworthy, M. A., Kervella, P., Rickman, E. L., & Schmidt, T. O. B. (2021).

Lessons learned from SPHERE for the astrometric strategy of the next generation of exoplanet imaging instruments. *Journal of Astronomical Telescopes, Instruments, and Systems*, 7, 035004.

- Maire, A.-L., Langlois, M., Dohlen, K., Lagrange, A.-M., Gratton, R., Chauvin, G., Desidera, S., Girard, J. H., Milli, J., Vigan, A., Zins, G., Delorme, P., Beuzit, J.-L., Claudi, R. U., Feldt, M., Mouillet, D., Puget, P., Turatto, M., & Wildi, F. (2016). SPHERE IRDIS and IFS astrometric strategy and calibration. In C. J. Evans, L. Simard, & H. Takami (Eds.), *Ground-based and Airborne Instrumentation for Astronomy VI*, volume 9908 of *Society of Photo-Optical Instrumentation Engineers (SPIE) Conference Series* (pp. 990834).
- Maire, A. L., Skemer, A. J., Hinz, P. M., Desidera, S., Esposito, S., Gratton, R., Marzari, F., Skrutskie, M. F., Biller, B. A., Defrère, D., Bailey, V. P., Leisenring, J. M., Apai, D., Bonnefoy, M., Brandner, W., Buenzli, E., Claudi, R. U., Close, L. M., Crepp, J. R., De Rosa, R. J., Eisner, J. A., Fortney, J. J., Henning, T., Hofmann, K. H., Kopytova, T. G., Males, J. R., Mesa, D., Morzinski, K. M., Oza, A., Patience, J., Pinna, E., Rajan, A., Schertl, D., Schlieder, J. E., Su, K. Y. L., Vaz, A., Ward-Duong, K., Weigelt, G., & Woodward, C. E. (2015). The LEECH Exoplanet Imaging Survey. Further constraints on the planet architecture of the HR 8799 system. *Astronomy and Astrophysics*, 576, A133.
- Mamajek, E. E. (2012). On the Age and Binarity of Fomalhaut. *Astrophysical Journal Letters*, 754(2), L20.
- Mannings, V. & Barlow, M. J. (1998). Candidate Main-Sequence Stars with Debris Disks: A New Sample of Vega-like Sources. *Astrophysical Journal*, 497(1), 330–341.
- Marengo, M., Stapelfeldt, K., Werner, M. W., Hora, J. L., Fazio, G. G., Schuster, M. T., Carson, J. C., & Megeath, S. T. (2009). Spitzer/Infrared Array Camera Limits to Planetary Companions of Fomalhaut and epsilon Eridani. *Astrophysical Journal*, 700(2), 1647–1657.
- Marley, M. S., Fortney, J., Seager, S., & Barman, T. (2007a). Atmospheres of Extrasolar Giant Planets. In B. Reipurth, D. Jewitt, & K. Keil (Eds.), *Protostars and Planets V* (pp. 733).
- Marley, M. S., Fortney, J. J., Hubickyj, O., Bodenheimer, P., & Lissauer, J. J. (2007b). On the Luminosity of Young Jupiters. *Astrophysical Journal*, 655(1), 541–549.

- Marois, C., Correia, C., Galicher, R., Ingraham, P., Macintosh, B., Currie, T., & De Rosa, R. (2014). GPI PSF subtraction with TLOCI: the next evolution in exoplanet/disk high-contrast imaging. In E. Marchetti, L. M. Close, & J.-P. Vran (Eds.), *Adaptive Optics Systems IV*, volume 9148 of *Society of Photo-Optical Instrumentation Engineers (SPIE) Conference Series* (pp. 91480U).
- Marois, C., Lafrenière, D., Doyon, R., Macintosh, B., & Nadeau, D. (2006). Angular Differential Imaging: A Powerful High-Contrast Imaging Technique. *Astrophysical Journal*, 641(1), 556–564.
- Marois, C., Macintosh, B., Barman, T., Zuckerman, B., Song, I., Patience, J., Lafrenière, D., & Doyon, R. (2008). Direct Imaging of Multiple Planets Orbiting the Star HR 8799. *Science*, 322(5906), 1348.
- Marois, C., Zuckerman, B., Konopacky, Q. M., Macintosh, B., & Barman, T. (2010). Images of a fourth planet orbiting HR 8799. *Nature*, 468(7327), 1080–1083.
- Mathieu, R. D., Stassun, K., Basri, G., Jensen, E. L. N., Johns-Krull, C. M., Valenti, J. A., & Hartmann, L. W. (1997). The Classical T Tauri Spectroscopic Binary DQ Tau.I.Orbital Elements and Light Curves. *Astronomical Journal*, 113, 1841.
- Maureira, M. J., Pineda, J. E., Segura-Cox, D. M., Caselli, P., Testi, L., Lodato, G., Loinard, L., & Hernández-Gómez, A. (2020). Orbital and Mass Constraints of the Young Binary System IRAS 16293-2422 A. *Astrophysical Journal*, 897(1), 59.
- Mawet, D., Milli, J., Wahhaj, Z., Pelat, D., Absil, O., Delacroix, C., Boccaletti, A., Kasper, M., Kenworthy, M., Marois, C., Mennesson, B., & Pueyo, L. (2014). Fundamental Limitations of High Contrast Imaging Set by Small Sample Statistics. *Astrophysical Journal*, 792(2), 97.
- Mayer, L., Quinn, T., Wadsley, J., & Stadel, J. (2004). The Evolution of Gravitationally Unstable Protoplanetary Disks: Fragmentation and Possible Giant Planet Formation. *Astrophysical Journal*, 609(2), 1045–1064.
- Mayor, M. & Queloz, D. (1995). A Jupiter-mass companion to a solar-type star. *Nature*, 378(6555), 355–359.

- McMullin, J. P., Waters, B., Schiebel, D., Young, W., & Golap, K. (2007). CASA Architecture and Applications. In R. A. Shaw, F. Hill, & D. J. Bell (Eds.), *Astronomical Data Analysis Software and Systems XVI*, volume 376 of *Astronomical Society of the Pacific Conference Series* (pp. 127).
- Mendoza V., E. E. (1966). Infrared Photometry of T Tauri Stars and Related Objects. *Astrophysical Journal*, 143, 1010.
- Menten, K. M., Reid, M. J., Forbrich, J., & Brunthaler, A. (2007). The distance to the Orion Nebula. *Astronomy and Astrophysics*, 474(2), 515–520.
- Mesa, D., Gratton, R., Kervella, P., Bonavita, M., Desidera, S., D’Orazi, V., Marino, S., Zurlo, A., & Rigliaco, E. (2023). AF Lep b: The lowest-mass planet detected by coupling astrometric and direct imaging data. *Astronomy and Astrophysics*, 672, A93.
- Metchev, S. A., Heinze, A., Apai, D., Flateau, D., Radigan, J., Burgasser, A., Marley, M. S., Artigau, É., Plavchan, P., & Goldman, B. (2015). Weather on Other Worlds. II. Survey Results: Spots are Ubiquitous on L and T Dwarfs. *Astrophysical Journal*, 799(2), 154.
- Miotello, A., Facchini, S., van Dishoeck, E. F., & Bruderer, S. (2018). Probing the protoplanetary disk gas surface density distribution with ^{13}CO emission. *Astronomy and Astrophysics*, 619, A113.
- Miotello, A., Kamp, I., Birnstiel, T., Cleeves, L. C., & Kataoka, A. (2023). Setting the Stage for Planet Formation: Measurements and Implications of the Fundamental Disk Properties. In S. Inutsuka, Y. Aikawa, T. Muto, K. Tomida, & M. Tamura (Eds.), *Protostars and Planets VII*, volume 534 of *Astronomical Society of the Pacific Conference Series* (pp. 501).
- Miret-Roig, N., Galli, P. A. B., Brandner, W., Bouy, H., Barrado, D., Olivares, J., Antoja, T., Romero-Gómez, M., Figueras, F., & Lillo-Box, J. (2020). Dynamical trace-back age of the β Pictoris moving group. *Astronomy and Astrophysics*, 642, A179.
- Mohanty, S., Jayawardhana, R., Huélamo, N., & Mamajek, E. (2007). The Planetary Mass Companion 2MASS 1207-3932B: Temperature, Mass, and Evidence for an Edge-on Disk. *Astrophysical Journal*, 657(2), 1064–1091.

- Montet, B. T., Bowler, B. P., Shkolnik, E. L., Deck, K. M., Wang, J., Horch, E. P., Liu, M. C., Hillenbrand, L. A., Kraus, A. L., & Charbonneau, D. (2015). Dynamical Masses of Young M Dwarfs: Masses and Orbital Parameters of GJ 3305 AB, the Wide Binary Companion to the Imaged Exoplanet Host 51 Eri. *Astrophysical Journal, Letters*, 813(1), L11.
- Moré, J. J. (2006). The levenberg-marquardt algorithm: implementation and theory. In *Numerical analysis: proceedings of the biennial Conference held at Dundee, June 28–July 1, 1977* (pp. 105–116): Springer.
- Müller, A., Keppler, M., Henning, T., Samland, M., Chauvin, G., Beust, H., Maire, A. L., Molaverdikhani, K., van Boekel, R., Benisty, M., Boccaletti, A., Bonnefoy, M., Cantalloube, F., Charnay, B., Baudino, J. L., Gennaro, M., Long, Z. C., Cheetham, A., Desidera, S., Feldt, M., Fusco, T., Girard, J., Gratton, R., Hagelberg, J., Janson, M., Lagrange, A. M., Langlois, M., Lazzoni, C., Ligi, R., Ménard, F., Mesa, D., Meyer, M., Mollière, P., Mordasini, C., Moulin, T., Pavlov, A., Pawellek, N., Quanz, S. P., Ramos, J., Rouan, D., Sissa, E., Stadler, E., Vigan, A., Wahhaj, Z., Weber, L., & Zurlo, A. (2018). Orbital and atmospheric characterization of the planet within the gap of the PDS 70 transition disk. *Astronomy and Astrophysics*, 617, L2.
- Müller, S. & Helled, R. (2021). Synthetic evolution tracks of giant planets. *Monthly Notices of the RAS*, 507(2), 2094–2102.
- Nealon, R., Cuello, N., & Alexander, R. (2020). Flyby-induced misalignments in planet-hosting discs. *Monthly Notices of the RAS*, 491(3), 4108–4115.
- Neuhäuser, R., Ginski, C., Schmidt, T. O. B., & Mugrauer, M. (2011). Further deep imaging of HR 7329 A (η Tel A) and its brown dwarf companion B. *Monthly Notices of the RAS*, 416(2), 1430–1435.
- Nielsen, E. L., De Rosa, R. J., Macintosh, B., Wang, J. J., Ruffio, J.-B., Chiang, E., Marley, M. S., Saumon, D., Savransky, D., Ammons, S. M., Bailey, V. P., Barman, T., Blain, C., Bulger, J., Burrows, A., Chilcote, J., Cotten, T., Czekala, I., Doyon, R., Duchêne, G., Esposito, T. M., Fabrycky, D., Fitzgerald, M. P., Follette, K. B., Fortney, J. J., Gerard, B. L., Goodsell, S. J., Graham, J. R., Greenbaum, A. Z., Hibon, P., Hinkley, S., Hirsch, L. A., Hom, J., Hung, L.-W., Dawson, R. I., Ingraham, P., Kalas, P., Konopacky, Q., Larkin, J. E., Lee, E. J.,

- Lin, J. W., Maire, J., Marchis, F., Marois, C., Metchev, S., Millar-Blanchaer, M. A., Morzinski, K. M., Oppenheimer, R., Palmer, D., Patience, J., Perrin, M., Poyneer, L., Pueyo, L., Rafikov, R. R., Rajan, A., Rameau, J., Rantakyrö, F. T., Ren, B., Schneider, A. C., Sivaramakrishnan, A., Song, I., Soummer, R., Tallis, M., Thomas, S., Ward-Duong, K., & Wolff, S. (2019). The Gemini Planet Imager Exoplanet Survey: Giant Planet and Brown Dwarf Demographics from 10 to 100 au. *Astronomical Journal*, 158(1), 13.
- Nogueira, P. H., Lazzoni, C., Zurlo, A., Bhowmik, T., Donoso-Oliva, C., Desidera, S., Milli, J., Pérez, S., Delorme, P., Fernandez, A., Langlois, M., Petrus, S., Cabrera-Vives, G., & Chauvin, G. (2024). Astrometric and photometric characterization of η Tel B combining two decades of observations. *arXiv e-prints*, (pp. arXiv:2405.04723).
- Nogueira, P. H., Zurlo, A., Pérez, S., González-Ruilova, C., Cieza, L. A., Hales, A., Bhowmik, T., Ruíz-Rodríguez, D. A., Principe, D. A., Herczeg, G. J., Williams, J. P., Cuadra, J., Montesinos, M., Cuello, N., Chavan, P., Casassus, S., Zhu, Z., & Goicovic, F. G. (2023). Resolving the binary components of the outbursting protostar HBC 494 with ALMA. *Monthly Notices of the RAS*, 523(4), 4970–4991.
- Nowak, M., Lacour, S., Lagrange, A. M., Rubini, P., Wang, J., Stolker, T., Abuter, R., Amorim, A., Asensio-Torres, R., Bauböck, M., Benisty, M., Berger, J. P., Beust, H., Blunt, S., Boccaletti, A., Bonnefoy, M., Bonnet, H., Brandner, W., Cantalloube, F., Charnay, B., Choquet, E., Christiaens, V., Clénet, Y., Coudé Du Foresto, V., Cridland, A., de Zeeuw, P. T., Dembet, R., Dexter, J., Drescher, A., Duvert, G., Eckart, A., Eisenhauer, F., Gao, F., Garcia, P., Garcia Lopez, R., Gardner, T., Gendron, E., Genzel, R., Gillessen, S., Girard, J., Grandjean, A., Haubois, X., Heißel, G., Henning, T., Hinkley, S., Hippler, S., Horrobin, M., Houllé, M., Hubert, Z., Jiménez-Rosales, A., Jocu, L., Kammerer, J., Kervella, P., Keppler, M., Kreidberg, L., Kulikauskas, M., Lapeyrère, V., Le Bouquin, J. B., Léna, P., Mérand, A., Maire, A. L., Mollière, P., Monnier, J. D., Moutlet, D., Müller, A., Nasedkin, E., Ott, T., Otten, G., Paumard, T., Paladini, C., Perraut, K., Perrin, G., Pueyo, L., Pfuhl, O., Rameau, J., Rodet, L., Rodríguez-Coira, G., Rousset, G., Scheithauer, S., Shangguan, J., Stadler, J., Straub, O., Straubmeier, C., Sturm, E., Tacconi, L. J., van Dishoeck, E. F., Vigan, A., Vin-

- cent, F., von Fellenberg, S. D., Ward-Duong, K., Widmann, F., Wieprecht, E., Wiezorrek, E., Woillez, J., & GRAVITY Collaboration (2020). Direct confirmation of the radial-velocity planet β Pictoris c. *Astronomy and Astrophysics*, 642, L2.
- Öberg, K. I., Murray-Clay, R., & Bergin, E. A. (2011). The Effects of Snowlines on C/O in Planetary Atmospheres. *Astrophysical Journal, Letters*, 743(1), L16.
- Ochi, Y., Sugimoto, K., & Hanawa, T. (2005). Evolution of a Protobinary: Accretion Rates of the Primary and Secondary. *Astrophysical Journal*, 623(2), 922–939.
- Ochiai, H., Nagasawa, M., & Ida, S. (2014). Extrasolar Binary Planets. I. Formation by Tidal Capture during Planet-Planet Scattering. *Astrophysical Journal*, 790(2), 92.
- Offner, S. S. R., Dunham, M. M., Lee, K. I., Arce, H. G., & Fielding, D. B. (2016). The Turbulent Origin of Outflow and Spin Misalignment in Multiple Star Systems. *Astrophysical Journal, Letters*, 827(1), L11.
- Offner, S. S. R. & McKee, C. F. (2011). The Protostellar Luminosity Function. *Astrophysical Journal*, 736(1), 53.
- Offner, S. S. R., Moe, M., Kratter, K. M., Sadavoy, S. I., Jensen, E. L. N., & Tobin, J. J. (2022). The Origin and Evolution of Multiple Star Systems. *arXiv e-prints*, (pp. arXiv:2203.10066).
- Ollivier, M., Roques, F., Casoli, F., Encrenaz, T., & Selsis, F. (2009). *Planetary Systems*. Springer Berlin, Heidelberg.
- Ossenkopf, V. & Henning, T. (1994). Dust opacities for protostellar cores. *Astronomy and Astrophysics*, 291, 943–959.
- Padoan, P., Haugbølle, T., Nordlund, Å., & Frimann, S. (2017). Supernova Driving. IV. The Star-formation Rate of Molecular Clouds. *Astrophysical Journal*, 840(1), 48.
- Patel, R. I., Metchev, S. A., & Heinze, A. (2014). A Sensitive Identification of Warm Debris Disks in the Solar Neighborhood through Precise Calibration of Saturated WISE Photometry. *Astrophysical Journal, Supplement*, 212(1), 10.

- Pavlov, A., Möller-Nilsson, O., Feldt, M., Henning, T., Beuzit, J.-L., & Mouillet, D. (2008). SPHERE data reduction and handling system: overview, project status, and development. In A. Bridger & N. M. Radziwill (Eds.), *Advanced Software and Control for Astronomy II*, volume 7019 of *Society of Photo-Optical Instrumentation Engineers (SPIE) Conference Series* (pp. 701939).
- Pawellek, N., Wyatt, M., Matrà, L., Kennedy, G., & Yelverton, B. (2021). A ~ 75 per cent occurrence rate of debris discs around F stars in the β Pic moving group. *Monthly Notices of the RAS*, 502(4), 5390–5416.
- Pearce, T. D. & Wyatt, M. C. (2014). Dynamical evolution of an eccentric planet and a less massive debris disc. *Monthly Notices of the RAS*, 443(3), 2541–2560.
- Pecaut, M. J. & Mamajek, E. E. (2016). The star formation history and accretion-disc fraction among the K-type members of the Scorpius-Centaurus OB association. *Monthly Notices of the RAS*, 461(1), 794–815.
- Pedrotti, F. L., Pedrotti, L. M., & Pedrotti, L. S. (2017). *Introduction to Optics*. Cambridge University Press.
- Pérez, S., Hales, A., Liu, H. B., Zhu, Z., Casassus, S., Williams, J., Zurlo, A., Cuello, N., Cieza, L., & Principe, D. (2020). Resolving the FU Orionis System with ALMA: Interacting Twin Disks? *Astrophysical Journal*, 889(1), 59.
- Pérez, S., Marino, S., Casassus, S., Baruteau, C., Zurlo, A., Flores, C., & Chauvin, G. (2019). Upper limits on protolunar disc masses using ALMA observations of directly imaged exoplanets. *Monthly Notices of the RAS*, 488(1), 1005–1011.
- Perryman, M. (2011). *The Exoplanet Handbook*. Cambridge University Press.
- Perryman, M. (2014). *The Exoplanet Handbook*. Cambridge University Press.
- Petit, C., Sauvage, J. F., Fusco, T., Sevin, A., Suarez, M., Costille, A., Vigan, A., Soenke, C., Perret, D., Rochat, S., Barufolo, A., Salasnich, B., Beuzit, J. L., Dohlen, K., Mouillet, D., Puget, P., Wildi, F., Kasper, M., Conan, J. M., Kulcsár, C., & Raynaud, H. F. (2014). SPHERE eXtreme AO control scheme: final performance assessment and on sky validation of the first auto-tuned LQG based operational system. In E. Marchetti, L. M. Close, & J.-P. Vran (Eds.), *Adaptive Optics Systems IV*, volume 9148 of *Society of Photo-Optical Instrumentation Engineers (SPIE) Conference Series* (pp. 91480O).

- Petrus, S., Whiteford, N., Patapis, P., Biller, B. A., Skemer, A., Hinkley, S., Suárez, G., Palma-Bifani, P., Morley, C. V., Tremblin, P., Charnay, B., Vos, J. M., Wang, J. J., Stone, J. M., Bonnefoy, M., Chauvin, G., Miles, B. E., Carter, A. L., Lueber, A., Helling, C., Sutcliffe, B. J., Janson, M., Gonzales, E. C., Hoch, K. K. W., Absil, O., Balmer, W. O., Boccaletti, A., Bonavita, M., Booth, M., Bowler, B. P., Briesemeister, Z. W., Bryan, M. L., Calissendorff, P., Cantalloube, F., Chen, C. H., Choquet, E., Christiaens, V., Cugno, G., Currie, T., Danielski, C., De Furio, M., Dupuy, T. J., Factor, S. M., Faherty, J. K., Fitzgerald, M. P., Fortney, J. J., Franson, K., Girard, J. H., Grady, C. A., Henning, T., Hines, D. C., Hood, C. E., Howe, A. R., Kalas, P., Kammerer, J., Kennedy, G. M., Kenworthy, M. A., Kervella, P., Kim, M., Kitzmann, D., Kraus, A. L., Kuzuhara, M., Lagage, P.-O., Lagrange, A.-M., Lawson, K., Lazzoni, C., Leisenring, J. M., Lew, B. W. P., Liu, M. C., Liu, P., Llop-Sayson, J., Lloyd, J. P., Macintosh, B., Mâlin, M., Manjavacas, E., Marino, S., Marley, M. S., Marois, C., Martinez, R. A., Matthews, E. C., Matthews, B. C., Mawet, D., Mazoyer, J., McElwain, M. W., Metchev, S., Meyer, M. R., Millar-Blanchaer, M. A., Mollière, P., Moran, S. E., Mukherjee, S., Pantin, E., Perrin, M. D., Pueyo, L., Quanz, S. P., Quirrenbach, A., Ray, S., Rebollido, I., Adams Redai, J., Ren, B. B., Rickman, E., Sallum, S., Samland, M., Sargent, B., Schlieder, J. E., Stapelfeldt, K. R., Tamura, M., Tan, X., Theissen, C. A., Uyama, T., Vasist, M., Vigan, A., Wagner, K., Ward-Duong, K., Wolff, S. G., Worthen, K., Wyatt, M. C., Ygouf, M., Zurlo, A., Zhang, X., Zhang, K., Zhang, Z., & Zhou, Y. (2024). The JWST Early Release Science Program for Direct Observations of Exoplanetary Systems. V. Do Self-consistent Atmospheric Models Represent JWST Spectra? A Showcase with VHS 1256–1257 b. *Astrophysical Journal, Letters*, 966(1), L11.
- Phillips, M. W., Tremblin, P., Baraffe, I., Chabrier, G., Allard, N. F., Spiegelman, F., Goyal, J. M., Drummond, B., & Hébrard, E. (2020). A new set of atmosphere and evolution models for cool T-Y brown dwarfs and giant exoplanets. *Astronomy and Astrophysics*, 637, A38.
- Pineda, J. E., Arzoumanian, D., Andre, P., Friesen, R. K., Zavagno, A., Clarke, S. D., Inoue, T., Chen, C., Lee, Y., Soler, J. D., & Kuffmeier, M. (2023). From Bubbles and Filaments to Cores and Disks: Gas Gathering and Growth of Structure Leading to the Formation of Stellar Systems. In S. Inutsuka, Y. Aikawa, T.

- Muto, K. Tomida, & M. Tamura (Eds.), *Protostars and Planets VII*, volume 534 of *Astronomical Society of the Pacific Conference Series* (pp. 233).
- Piso, A.-M. A. & Youdin, A. N. (2014). On the Minimum Core Mass for Giant Planet Formation at Wide Separations. *Astrophysical Journal*, 786(1), 21.
- Pollack, J. B., Hollenbach, D., Beckwith, S., Simonelli, D. P., Roush, T., & Fong, W. (1994). Composition and Radiative Properties of Grains in Molecular Clouds and Accretion Disks. *Astrophysical Journal*, 421, 615.
- Pollack, J. B., Hubickyj, O., Bodenheimer, P., Lissauer, J. J., Podolak, M., & Greenzweig, Y. (1996). Formation of the Giant Planets by Concurrent Accretion of Solids and Gas. *Icarus*, 124(1), 62–85.
- Por, E. H. (2020). Phase-apodized-pupil Lyot Coronagraphs for Arbitrary Telescope Pupils. *Astrophysical Journal*, 888(2), 127.
- Por, E. H., Soummer, R., Noss, J., & St. Laurent, K. (2020). Exploiting symmetries and progressive refinement for apodized pupil Lyot coronagraph design. In M. Lystrup & M. D. Perrin (Eds.), *Space Telescopes and Instrumentation 2020: Optical, Infrared, and Millimeter Wave*, volume 11443 of *Society of Photo-Optical Instrumentation Engineers (SPIE) Conference Series* (pp. 114433P).
- Postel, A., Audard, M., Vorobyov, E., Dionatos, O., Rab, C., & Güdel, M. (2019). Infrared and sub-mm observations of outbursting young stars with Herschel and Spitzer. *Astronomy and Astrophysics*, 631, A30.
- Pueyo, L., Crepp, J. R., Vasisht, G., Brenner, D., Oppenheimer, B. R., Zimmerman, N., Hinkley, S., Parry, I., Beichman, C., Hillenbrand, L., Roberts, L. C., Dekany, R., Shao, M., Burruss, R., Bouchez, A., Roberts, J., & Soummer, R. (2012a). Application of a Damped Locally Optimized Combination of Images Method to the Spectral Characterization of Faint Companions Using an Integral Field Spectrograph. *Astrophysical Journal, Supplement*, 199(1), 6.
- Pueyo, L., Hillenbrand, L., Vasisht, G., Oppenheimer, B. R., Monnier, J. D., Hinkley, S., Crepp, J., Roberts, Lewis C., J., Brenner, D., Zimmerman, N., Parry, I., Beichman, C., Dekany, R., Shao, M., Burruss, R., Cady, E., Roberts, J., & Soummer,

- R. (2012b). Constraining Mass Ratio and Extinction in the FU Orionis Binary System with Infrared Integral Field Spectroscopy. *Astrophysical Journal*, 757(1), 57.
- Qi, C., Ho, P. T. P., Wilner, D. J., Takakuwa, S., Hirano, N., Ohashi, N., Bourke, T. L., Zhang, Q., Blake, G. A., Hogerheijde, M., Saito, M., Choi, M., & Yang, J. (2004). Imaging the Disk around TW Hydrae with the Submillimeter Array. *Astrophysical Journal, Letters*, 616(1), L11–L14.
- Quirrenbach, A., Trifonov, T., Lee, M. H., & Reffert, S. (2019). Precise radial velocities of giant stars. XI. Two brown dwarfs in 6:1 mean motion resonance around the K giant star ν Ophiuchi. *Astronomy and Astrophysics*, 624, A18.
- Racine, R., Walker, G. A. H., Nadeau, D., Doyon, R., & Marois, C. (1999). Speckle Noise and the Detection of Faint Companions. *Astronomical Society of the Pacific*, 111(759), 587–594.
- Radigan, J. (2014). An Independent Analysis of the Brown Dwarf Atmosphere Monitoring (BAM) Data: Large-amplitude Variability is Rare Outside the L/T Transition. *Astrophysical Journal*, 797(2), 120.
- Radigan, J., Lafrenière, D., Jayawardhana, R., & Artigau, E. (2014). Strong Brightness Variations Signal Cloudy-to-clear Transition of Brown Dwarfs. *Astrophysical Journal*, 793(2), 75.
- Ragusa, E., Fasano, D., Toci, C., Duchêne, G., Cuello, N., Villenave, M., van der Plas, G., Lodato, G., Ménard, F., Price, D. J., Pinte, C., Stapelfeldt, K., & Wolff, S. (2021). Circumbinary and circumstellar discs around the eccentric binary IRAS 04158+2805 - a testbed for binary-disc interaction. *Monthly Notices of the RAS*, 507(1), 1157–1174.
- Rameau, J., Chauvin, G., Lagrange, A. M., Boccaletti, A., Quanz, S. P., Bonnefoy, M., Girard, J. H., Delorme, P., Desidera, S., Klahr, H., Mordasini, C., Dumas, C., & Bonavita, M. (2013a). Discovery of a Probable 4-5 Jupiter-mass Exoplanet to HD 95086 by Direct Imaging. *Astrophysical Journal, Letters*, 772(2), L15.
- Rameau, J., Chauvin, G., Lagrange, A. M., Klahr, H., Bonnefoy, M., Mordasini, C., Bonavita, M., Desidera, S., Dumas, C., & Girard, J. H. (2013b). A survey of

young, nearby, and dusty stars conducted to understand the formation of wide-orbit giant planets. VLT/NaCo adaptive optics thermal and angular differential imaging. *Astronomy and Astrophysics*, 553, A60.

- Rathjen, T.-E., Naab, T., Girichidis, P., Walch, S., Wünsch, R., Dinnbier, F., Seifried, D., Klessen, R. S., & Glover, S. C. O. (2021). SILCC VI - Multiphase ISM structure, stellar clustering, and outflows with supernovae, stellar winds, ionizing radiation, and cosmic rays. *Monthly Notices of the RAS*, 504(1), 1039–1061.
- Reggiani, M., Meyer, M. R., Chauvin, G., Vigan, A., Quanz, S. P., Biller, B., Bonavita, M., Desidera, S., Delorme, P., Hagelberg, J., Maire, A. L., Boccaletti, A., Beuzit, J. L., Buenzli, E., Carson, J., Covino, E., Feldt, M., Girard, J., Gratton, R., Henning, T., Kasper, M., Lagrange, A. M., Mesa, D., Messina, S., Montagnier, G., Mordasini, C., Mouillet, D., Schlieder, J. E., Segransan, D., Thalmann, C., & Zurlo, A. (2016). The VLT/NaCo large program to probe the occurrence of exoplanets and brown dwarfs at wide orbits . III. The frequency of brown dwarfs and giant planets as companions to solar-type stars. *Astronomy and Astrophysics*, 586, A147.
- Reipurth, B. (1985). Small nebulae and Herbig-Haro objects. II. The Orion region. *Astronomy and Astrophysics, Supplement*, 61, 319–330.
- Reipurth, B. & Aspin, C. (2004). The FU Orionis Binary System and the Formation of Close Binaries. *Astrophysical Journal, Letters*, 608(1), L65–L68.
- Reipurth, B. & Bally, J. (1986). First light from a young star? *Nature*, 320(6060), 336–338.
- Riaud, P., Mawet, D., Absil, O., Boccaletti, A., Baudoz, P., Herwats, E., & Surdej, J. (2006). Coronagraphic imaging of three weak-line T Tauri stars: evidence of planetary formation around PDS 70. *Astronomy and Astrophysics*, 458(1), 317–325.
- Rigaut, F. (2015). Astronomical Adaptive Optics. *Astronomical Society of the Pacific*, 127(958), 1197.
- Riviere-Marichalar, P., Barrado, D., Montesinos, B., Duchêne, G., Bouy, H., Pinte, C., Menard, F., Donaldson, J., Eiroa, C., Krivov, A. V., Kamp, I., Mendigutía, I., Dent, W. R. F., & Lillo-Box, J. (2014). Gas and dust in the beta Pictoris moving

group as seen by the Herschel Space Observatory. *Astronomy and Astrophysics*, 565, A68.

- Robitaille, T. P., Whitney, B. A., Indebetouw, R., Wood, K., & Denzmore, P. (2006). Interpreting Spectral Energy Distributions from Young Stellar Objects. I. A Grid of 200,000 YSO Model SEDs. *Astrophysical Journal, Supplement*, 167(2), 256–285.
- Rosotti, G. P. & Clarke, C. J. (2018). The evolution of photoevaporating viscous discs in binaries. *Monthly Notices of the RAS*, 473(4), 5630–5640.
- Ruane, G., Ngo, H., Mawet, D., Absil, O., Choquet, É., Cook, T., Gomez Gonzalez, C., Huby, E., Matthews, K., Meshkat, T., Reggiani, M., Serabyn, E., Wallack, N., & Xuan, W. J. (2019). Reference Star Differential Imaging of Close-in Companions and Circumstellar Disks with the NIRC2 Vortex Coronagraph at the W. M. Keck Observatory. *Astronomical Journal*, 157(3), 118.
- Ruffio, J.-B., Horstman, K., Mawet, D., Rosenthal, L. J., Batygin, K., Wang, J. J., Millar-Blanchaer, M., Wang, J., Fulton, B. J., Konopacky, Q. M., Agrawal, S., Hirsch, L. A., Howard, A. W., Blunt, S., Nielsen, E., Baker, A., Bartos, R., Bond, C. Z., Calvin, B., Cetre, S., Delorme, J.-R., Doppmann, G., Echeverri, D., Finnerty, L., Fitzgerald, M. P., Jovanovic, N., López, R., Martin, E. C., Morris, E., Pezzato, J., Ruane, G., Sappey, B., Schofield, T., Skemer, A., Venenciano, T., Wallace, J. K., Wallack, N. L., Wizinowich, P., & Xuan, J. W. (2023). Detecting Exomoons from Radial Velocity Measurements of Self-luminous Planets: Application to Observations of HR 7672 B and Future Prospects. *Astronomical Journal*, 165(3), 113.
- Ruíz-Rodríguez, D., Cieza, L. A., Williams, J. P., Tobin, J. J., Hales, A., Zhu, Z., Mužić, K., Principe, D., Canovas, H., Zurlo, A., Casassus, S., Perez, S., & Prieto, J. L. (2017). The ALMA early science view of FUor/EXor objects - II. The very wide outflow driven by HBC 494. *Monthly Notices of the RAS*, 466(3), 3519–3532.
- Ruíz-Rodríguez, D. A., Williams, J. P., Kastner, J. H., Cieza, L., Leemker, M., & Principe, D. A. (2022). A chemical map of the outbursting V883 Ori system: vertical and radial structures. *Monthly Notices of the RAS*, 515(2), 2646–2671.
- Sahlmann, J., Ségransan, D., Queloz, D., & Udry, S. (2011). A possible dividing line between massive planets and brown-dwarf companions. In A. Sozzetti, M. G.

Lattanzi, & A. P. Boss (Eds.), *The Astrophysics of Planetary Systems: Formation, Structure, and Dynamical Evolution*, volume 276 (pp. 117–120).

Saito, E. & Sirono, S.-i. (2011). Planetesimal Formation by Sublimation. *Astrophysical Journal*, 728(1), 20.

Samland, M., Mollière, P., Bonnefoy, M., Maire, A. L., Cantalloube, F., Cheetham, A. C., Mesa, D., Gratton, R., Biller, B. A., Wahhaj, Z., Bouwman, J., Brandner, W., Melnick, D., Carson, J., Janson, M., Henning, T., Homeier, D., Mordasini, C., Langlois, M., Quanz, S. P., van Boekel, R., Zurlo, A., Schlieder, J. E., Avenhaus, H., Beuzit, J. L., Boccaletti, A., Bonavita, M., Chauvin, G., Claudi, R., Cudel, M., Desidera, S., Feldt, M., Fusco, T., Galicher, R., Kopytova, T. G., Lagrange, A. M., Le Coroller, H., Martinez, P., Moeller-Nilsson, O., Mouillet, D., Mugnier, L. M., Perrot, C., Sevin, A., Sissa, E., Vigan, A., & Weber, L. (2017). Spectral and atmospheric characterization of 51 Eridani b using VLT/SPHERE. *Astronomy and Astrophysics*, 603, A57.

Sauvage, J.-F., Fusco, T., Petit, C., Costille, A., Mouillet, D., Beuzit, J.-L., Dohlen, K., Kasper, M., Suarez, M., Soenke, C., Baruffolo, A., Salasnich, B., Rochat, S., Fedrigo, E., Baudoz, P., Hugot, E., Sevin, A., Perret, D., Wildi, F., Downing, M., Feautrier, P., Puget, P., Vigan, A., O’Neal, J., Girard, J., Mawet, D., Schmid, H. M., & Roelfsema, R. (2016). SAXO: the extreme adaptive optics system of SPHERE (I) system overview and global laboratory performance. *Journal of Astronomical Telescopes, Instruments, and Systems*, 2, 025003.

Schmid, H. M., Bazzon, A., Roelfsema, R., Mouillet, D., Milli, J., Menard, F., Gisler, D., Hunziker, S., Pragt, J., Dominik, C., Boccaletti, A., Ginski, C., Abe, L., Antonucci, S., Avenhaus, H., Baruffolo, A., Baudoz, P., Beuzit, J. L., Carbillet, M., Chauvin, G., Claudi, R., Costille, A., Daban, J. B., de Haan, M., Desidera, S., Dohlen, K., Downing, M., Elswijk, E., Engler, N., Feldt, M., Fusco, T., Girard, J. H., Gratton, R., Hanenburg, H., Henning, T., Hubin, N., Joos, F., Kasper, M., Keller, C. U., Langlois, M., Lagadec, E., Martinez, P., Mulder, E., Pavlov, A., Podio, L., Puget, P., Quanz, S. P., Rigal, F., Salasnich, B., Sauvage, J. F., Schuil, M., Siebenmorgen, R., Sissa, E., Snik, F., Suarez, M., Thalmann, C., Turatto, M., Udry, S., van Duin, A., van Holstein, R. G., Vigan, A., & Wildi, F. (2018). SPHERE/ZIMPOL high resolution polarimetric imager. I.

System overview, PSF parameters, coronagraphy, and polarimetry. *Astronomy and Astrophysics*, 619, A9.

Schneider, G., Weinberger, A. J., Becklin, E. E., Debes, J. H., & Smith, B. A. (2009). STIS Imaging of the HR 4796A Circumstellar Debris Ring. *Astronomical Journal*, 137(1), 53–61.

Sepulveda, A. G. & Bowler, B. P. (2022). Dynamical Mass of the Exoplanet Host Star HR 8799. *Astronomical Journal*, 163(2), 52.

Smith, R., Churcher, L. J., Wyatt, M. C., Moerchen, M. M., & Telesco, C. M. (2009). Resolved debris disc emission around η Telescopii: a young solar system or ongoing planet formation? *Astronomy and Astrophysics*, 493(1), 299–308.

Soummer, R., Ferrari, A., Aime, C., & Jolissaint, L. (2007). Speckle Noise and Dynamic Range in Coronagraphic Images. *Astrophysical Journal*, 669(1), 642–656.

Soummer, R., Hagan, J. B., Pueyo, L., Thormann, A., Rajan, A., & Marois, C. (2011). Orbital Motion of HR 8799 b, c, d Using Hubble Space Telescope Data from 1998: Constraints on Inclination, Eccentricity, and Stability. *Astrophysical Journal*, 741(1), 55.

Soummer, R., Pueyo, L., & Larkin, J. (2012a). Detection and Characterization of Exoplanets and Disks Using Projections on Karhunen-Loève Eigenimages. *Astrophysical Journal, Letters*, 755(2), L28.

Soummer, R., Pueyo, L., & Larkin, J. (2012b). Detection and Characterization of Exoplanets and Disks Using Projections on Karhunen-Loève Eigenimages. *Astrophysical Journal, Letters*, 755(2), L28.

Sparks, W. B. & Ford, H. C. (2002). Imaging Spectroscopy for Extrasolar Planet Detection. *Astrophysical Journal*, 578(1), 543–564.

Spiegel, D. S., Burrows, A., & Milsom, J. A. (2011). The Deuterium-burning Mass Limit for Brown Dwarfs and Giant Planets. *Astrophysical Journal*, 727(1), 57.

Stahler, S. W. (2010). The orbital decay of embedded binary stars. *Monthly Notices of the RAS*, 402(3), 1758–1766.

- Stamatellos, D. & Whitworth, A. P. (2009). The role of thermodynamics in disc fragmentation. *Monthly Notices of the RAS*, 400(3), 1563–1573.
- Stewart, G. R. & Wetherill, G. W. (1988). Evolution of planetesimal velocities. *Icarus*, 74(3), 542–553.
- Stolker, T., Marleau, G. D., Cugno, G., Mollière, P., Quanz, S. P., Todorov, K. O., & Kühn, J. (2020). MIRACLES: atmospheric characterization of directly imaged planets and substellar companions at 4-5 μm . II. Constraints on the mass and radius of the enshrouded planet PDS 70 b. *Astronomy and Astrophysics*, 644, A13.
- Strom, K. M., Strom, S. E., Edwards, S., Cabrit, S., & Skrutskie, M. F. (1989). Circumstellar Material Associated with Solar-Type Pre-Main-Sequence Stars: A Possible Constraint on the Timescale for Planet Building. *Astronomical Journal*, 97, 1451.
- Sudol, J. J. & Haghighipour, N. (2012). High-mass, Four-planet Configurations for HR 8799: Constraining the Orbital Inclination and Age of the System. *Astrophysical Journal*, 755(1), 38.
- Szulágyi, J., Mayer, L., & Quinn, T. (2017). Circumplanetary discs around young giant planets: a comparison between core-accretion and disc instability. *Monthly Notices of the RAS*, 464(3), 3158–3168.
- Takami, M., Chen, T.-S., Liu, H. B., Hirano, N., Kóspál, Á., Ábrahám, P., Vorobyov, E. I., Cruz-Sáenz de Miera, F., Csengeri, T., Green, J., Hogerheijde, M., Hsieh, T.-H., Karr, J. L., Dong, R., Trejo, A., & Chen, L. (2019). An ALMA Study of the FU Ori-type Object V900 Mon: Implications for the Progenitor. *Astrophysical Journal*, 884(2), 146.
- Testi, L., Birnstiel, T., Ricci, L., Andrews, S., Blum, J., Carpenter, J., Dominik, C., Isella, A., Natta, A., Williams, J. P., & Wilner, D. J. (2014). Dust Evolution in Protoplanetary Disks. In H. Beuther, R. S. Klessen, C. P. Dullemond, & T. Henning (Eds.), *Protostars and Planets VI* (pp. 339).
- Thatte, N., Abuter, R., Tecza, M., Nielsen, E. L., Clarke, F. J., & Close, L. M. (2007). Very high contrast integral field spectroscopy of AB Doradus C: 9-mag contrast at 0.2arcsec without a coronagraph using spectral deconvolution†. *Monthly Notices of the RAS*, 378(4), 1229–1236.

- Tobin, J. J., Kratter, K. M., Persson, M. V., Looney, L. W., Dunham, M. M., Segura-Cox, D., Li, Z.-Y., Chandler, C. J., Sadavoy, S. I., Harris, R. J., Melis, C., & Pérez, L. M. (2016a). A triple protostar system formed via fragmentation of a gravitationally unstable disk. *Nature*, 538(7626), 483–486.
- Tobin, J. J., Looney, L. W., Li, Z.-Y., Chandler, C. J., Dunham, M. M., Segura-Cox, D., Sadavoy, S. I., Melis, C., Harris, R. J., Kratter, K., & Perez, L. (2016b). The VLA Nascent Disk and Multiplicity Survey of Perseus Protostars (VANDAM). II. Multiplicity of Protostars in the Perseus Molecular Cloud. *Astrophysical Journal*, 818(1), 73.
- Tobin, J. J., Offner, S. S. R., Kratter, K. M., Megeath, S. T., Sheehan, P. D., Looney, L. W., Diaz-Rodriguez, A. K., Osorio, M., Anglada, G., Sadavoy, S. I., Furlan, E., Segura-Cox, D., Karnath, N., van't Hoff, M. L. R., van Dishoeck, E. F., Li, Z.-Y., Sharma, R., Stutz, A. M., & Tychoniec, Ł. (2022). The VLA/ALMA Nascent Disk And Multiplicity (VANDAM) Survey of Orion Protostars. V. A Characterization of Protostellar Multiplicity. *Astrophysical Journal*, 925(1), 39.
- Tobin, J. J., Sheehan, P. D., Megeath, S. T., Díaz-Rodríguez, A. K., Offner, S. S. R., Murillo, N. M., van 't Hoff, M. L. R., van Dishoeck, E. F., Osorio, M., Anglada, G., Furlan, E., Stutz, A. M., Reynolds, N., Karnath, N., Fischer, W. J., Persson, M., Looney, L. W., Li, Z.-Y., Stephens, I., Chandler, C. J., Cox, E., Dunham, M. M., Tychoniec, Ł., Kama, M., Kratter, K., Kounkel, M., Mazur, B., Maud, L., Patel, L., Perez, L., Sadavoy, S. I., Segura-Cox, D., Sharma, R., Stephenson, B., Watson, D. M., & Wyrowski, F. (2020). The VLA/ALMA Nascent Disk and Multiplicity (VANDAM) Survey of Orion Protostars. II. A Statistical Characterization of Class 0 and Class I Protostellar Disks. *Astrophysical Journal*, 890(2), 130.
- Toci, C., Rosotti, G., Lodato, G., Testi, L., & Trapman, L. (2021). On the secular evolution of the ratio between gas and dust radii in protoplanetary discs. *Monthly Notices of the RAS*, 507(1), 818–833.
- Todorov, K., Luhman, K. L., & McLeod, K. K. (2010). Discovery of a Planetary-mass Companion to a Brown Dwarf in Taurus. *Astrophysical Journal, Letters*, 714(1), L84–L88.

- Tomisaka, K. (2014). Magnetohydrostatic Equilibrium Structure and Mass of Filamentary Isothermal Cloud Threaded by Lateral Magnetic Field. *Astrophysical Journal*, 785(1), 24.
- Toomre, A. (1964). On the gravitational stability of a disk of stars. *Astrophysical Journal*, 139, 1217–1238.
- Tu, Y., Li, Z.-Y., & Lam, K. H. (2022). Grain growth during protostellar disc formation. *Monthly Notices of the RAS*, 515(4), 4780–4796.
- van der Marel, N. (2023). Transition disks: the observational revolution from SEDs to imaging. *European Physical Journal Plus*, 138(3), 225.
- van Leeuwen, F. (2007). Validation of the new Hipparcos reduction. *Astronomy and Astrophysics*, 474(2), 653–664.
- Vigan, A., Bonnefoy, M., Ginski, C., Beust, H., Galicher, R., Janson, M., Baudino, J. L., Buenzli, E., Hagelberg, J., D’Orazi, V., Desidera, S., Maire, A. L., Gratton, R., Sauvage, J. F., Chauvin, G., Thalmann, C., Malo, L., Salter, G., Zurlo, A., Antichi, J., Baruffolo, A., Baudoz, P., Blanchard, P., Boccaletti, A., Beuzit, J. L., Carle, M., Claudi, R., Costille, A., Delboulbé, A., Dohlen, K., Dominik, C., Feldt, M., Fusco, T., Gluck, L., Girard, J., Giro, E., Gry, C., Henning, T., Hubin, N., Hugot, E., Jaquet, M., Kasper, M., Lagrange, A. M., Langlois, M., Le Mignant, D., Llored, M., Madec, F., Martinez, P., Mawet, D., Mesa, D., Milli, J., Mouillet, D., Moulin, T., Moutou, C., Origné, A., Pavlov, A., Perret, D., Petit, C., Pragt, J., Puget, P., Rabou, P., Rochat, S., Roelfsema, R., Salasnich, B., Schmid, H. M., Sevin, A., Siebenmorgen, R., Smette, A., Stadler, E., Suarez, M., Turatto, M., Udry, S., Vakili, F., Wahhaj, Z., Weber, L., & Wildi, F. (2016). First light of the VLT planet finder SPHERE. I. Detection and characterization of the substellar companion GJ 758 B. *Astronomy and Astrophysics*, 587, A55.
- Villenave, M., Ménard, F., Dent, W. R. F., Duchêne, G., Stapelfeldt, K. R., Benisty, M., Boehler, Y., van der Plas, G., Pinte, C., Telkamp, Z., Wolff, S., Flores, C., Lesur, G., Louvet, F., Riols, A., Dougados, C., Williams, H., & Padgett, D. (2020). Observations of edge-on protoplanetary disks with ALMA. I. Results from continuum data. *Astronomy and Astrophysics*, 642, A164.
- Vorobyov, E. I. & Basu, S. (2005). The Origin of Episodic Accretion Bursts in the Early Stages of Star Formation. *Astrophysical Journal, Letters*, 633, L137–L140.

- Vorobyov, E. I. & Basu, S. (2015). Variable Protostellar Accretion with Episodic Bursts. *Astrophysical Journal*, 805(2), 115.
- Vorobyov, E. I., Elbakyan, V. G., Liu, H. B., & Takami, M. (2021). Distinguishing between different mechanisms of FU-Orionis-type luminosity outbursts. *Astronomy and Astrophysics*, 647, A44.
- Vousden, W. D., Farr, W. M., & Mandel, I. (2016). Dynamic temperature selection for parallel tempering in Markov chain Monte Carlo simulations. *Monthly Notices of the RAS*, 455(2), 1919–1937.
- Wagner, K., Follete, K. B., Close, L. M., Apai, D., Gibbs, A., Keppler, M., Müller, A., Henning, T., Kasper, M., Wu, Y.-L., Long, J., Males, J., Morzinski, K., & McClure, M. (2018). Magellan Adaptive Optics Imaging of PDS 70: Measuring the Mass Accretion Rate of a Young Giant Planet within a Gapped Disk. *Astrophysical Journal, Letters*, 863(1), L8.
- Wahhaj, Z., Milli, J., Romero, C., Cieza, L., Zurlo, A., Vigan, A., Peña, E., Valdes, G., Cantalloube, F., Girard, J., & Pantoja, B. (2021). A search for a fifth planet around HR 8799 using the star-hopping RDI technique at VLT/SPHERE. *Astronomy and Astrophysics*, 648, A26.
- Wang, J. J., Ginzburg, S., Ren, B., Wallack, N., Gao, P., Mawet, D., Bond, C. Z., Cetre, S., Wizinowich, P., De Rosa, R. J., Ruane, G., Liu, M. C., Absil, O., Alvarez, C., Baranec, C., Choquet, É., Chun, M., Defrère, D., Delorme, J.-R., Duchêne, G., Forsberg, P., Ghez, A., Guyon, O., Hall, D. N. B., Huby, E., Jolivet, A., Jensen-Clem, R., Jovanovic, N., Karlsson, M., Lilley, S., Matthews, K., Ménard, F., Meshkat, T., Millar-Blanchaer, M., Ngo, H., Orban de Xivry, G., Pinte, C., Ragland, S., Serabyn, E., Catalán, E. V., Wang, J., Wetherell, E., Williams, J. P., Ygouf, M., & Zuckerman, B. (2020). Keck/NIRC2 L'-band Imaging of Jovian-mass Accreting Protoplanets around PDS 70. *Astronomical Journal*, 159(6), 263.
- Wang, J. J., Graham, J. R., Dawson, R., Fabrycky, D., De Rosa, R. J., Pueyo, L., Konopacky, Q., Macintosh, B., Marois, C., Chiang, E., Ammons, S. M., Arriaga, P., Bailey, V. P., Barman, T., Bulger, J., Chilcote, J., Cotten, T., Doyon, R., Duchêne, G., Esposito, T. M., Fitzgerald, M. P., Follette, K. B., Gerard, B. L., Goodsell, S. J., Greenbaum, A. Z., Hibon, P., Hung, L.-W., Ingraham,

- P., Kalas, P., Larkin, J. E., Maire, J., Marchis, F., Marley, M. S., Metchev, S., Millar-Blanchaer, M. A., Nielsen, E. L., Oppenheimer, R., Palmer, D., Patience, J., Perrin, M., Poyneer, L., Rajan, A., Rameau, J., Rantakyrö, F. T., Ruffio, J.-B., Savransky, D., Schneider, A. C., Sivaramakrishnan, A., Song, I., Soummer, R., Thomas, S., Wallace, J. K., Ward-Duong, K., Wiktorowicz, S., & Wolff, S. (2018). Dynamical Constraints on the HR 8799 Planets with GPI. *Astronomical Journal*, 156(5), 192.
- Wang, J. J., Vigan, A., Lacour, S., Nowak, M., Stolker, T., De Rosa, R. J., Ginzburg, S., Gao, P., Abuter, R., Amorim, A., Asensio-Torres, R., Bauböck, M., Benisty, M., Berger, J. P., Beust, H., Beuzit, J. L., Blunt, S., Boccaletti, A., Bohn, A., Bonnefoy, M., Bonnet, H., Brandner, W., Cantalloube, F., Caselli, P., Charnay, B., Chauvin, G., Choquet, E., Christiaens, V., Clénet, Y., Coudé Du Foresto, V., Cridland, A., de Zeeuw, P. T., Dembet, R., Dexter, J., Drescher, A., Duvert, G., Eckart, A., Eisenhauer, F., Facchini, S., Gao, F., Garcia, P., Garcia Lopez, R., Gardner, T., Gendron, E., Genzel, R., Gillessen, S., Girard, J., Haubois, X., Heißel, G., Henning, T., Hinkley, S., Hippler, S., Horrobin, M., Houllé, M., Hubert, Z., Jiménez-Rosales, A., Jocu, L., Kammerer, J., Keppler, M., Kervella, P., Meyer, M., Kreidberg, L., Lagrange, A. M., Lapeyrère, V., Le Bouquin, J. B., Léna, P., Lutz, D., Maire, A. L., Ménard, F., Mérand, A., Mollière, P., Monnier, J. D., Mouillet, D., Müller, A., Nasedkin, E., Ott, T., Otten, G. P. P. L., Paladini, C., Paumard, T., Perraut, K., Perrin, G., Pfuhl, O., Pueyo, L., Rameau, J., Rodet, L., Rodríguez-Coira, G., Rousset, G., Scheithauer, S., Shangguan, J., Shimizu, T., Stadler, J., Straub, O., Straubmeier, C., Sturm, E., Tacconi, L. J., van Dishoeck, E. F., Vincent, F., von Fellenberg, S. D., Ward-Duong, K., Widmann, F., Wieprecht, E., Wierzorrek, E., Woillez, J., & Gravity Collaboration (2021). Constraining the Nature of the PDS 70 Protoplanets with VLT/GRAVITY. *Astronomical Journal*, 161(3), 148.
- Weaver, E., Isella, A., & Boehler, Y. (2018). Empirical Temperature Measurement in Protoplanetary Disks. *Astrophysical Journal*, 853(2), 113.
- Weidenschilling, S. J. (1977). Aerodynamics of solid bodies in the solar nebula. *Monthly Notices of the RAS*, 180, 57–70.
- Wertz, O., Absil, O., Gómez González, C. A., Milli, J., Girard, J. H., Mawet, D., & Pueyo, L. (2017). VLT/SPHERE robust astrometry of the HR8799 planets at

- milliarcsecond-level accuracy. Orbital architecture analysis with PyAstrOFit. *Astronomy and Astrophysics*, 598, A83.
- Wetherill, G. W. & Stewart, G. R. (1989). Accumulation of a swarm of small planetesimals. *Icarus*, 77(2), 330–357.
- Williams, J. P. & Cieza, L. A. (2011). Protoplanetary Disks and Their Evolution. *Annual Review of Astron and Astrophysics*, 49(1), 67–117.
- Williams, J. P. & McPartland, C. (2016). Measuring Protoplanetary Disk Gas Surface Density Profiles with ALMA. *Astrophysical Journal*, 830(1), 32.
- Wilson, P. A., Rajan, A., & Patience, J. (2014). The brown dwarf atmosphere monitoring (BAM) project. I. The largest near-IR monitoring survey of L and T dwarfs. *Astronomy and Astrophysics*, 566, A111.
- Ygouf, M., Beichman, C. A., Llop-Sayson, J., Bryden, G., Leisenring, J. M., Gáspár, A., Krist, J. E., Rieke, M. J., Rieke, G. H., Wolff, S. G., Roellig, T. L., Su, K., Hainline, K. N., Hodapp, K. W., Greene, T. P., Meyer, M. R., Kelly, D. M., Misselt, K., Stansberry, J., Boyer, M., Johnstone, D., Horner, S., & Greenbaum, A. Z. (2024). Searching for Planets Orbiting Fomalhaut with JWST/NIRCam. *Astronomical Journal*, 167(1), 26.
- Young, M. D. & Clarke, C. J. (2015). Binary accretion rates: dependence on temperature and mass ratio. *Monthly Notices of the RAS*, 452(3), 3085–3091.
- Youngblood, A., Roberge, A., MacGregor, M. A., Brandeker, A., Weinberger, A. J., Pérez, S., Grady, C., & Welsh, B. (2021). A Radiatively Driven Wind from the η Tel Debris Disk. *Astronomical Journal*, 162(6), 235.
- Zhang, K., Blake, G. A., & Bergin, E. A. (2015). Evidence of Fast Pebble Growth Near Condensation Fronts in the HL Tau Protoplanetary Disk. *Astrophysical Journal Letters*, 806(1), L7.
- Zhang, Z., Mollière, P., Hawkins, K., Manea, C., Fortney, J. J., Morley, C. V., Skemer, A., Marley, M. S., Bowler, B. P., Carter, A. L., Franson, K., Maas, Z. G., & Sneden, C. (2023). ELemental abundances of Planets and brown dwarfs Imaged around Stars (ELPIS). I. Potential Metal Enrichment of the Exoplanet AF Lep b and a Novel Retrieval Approach for Cloudy Self-luminous Atmospheres. *Astronomical Journal*, 166(5), 198.

- Zhu, Z., Hartmann, L., Gammie, C., & McKinney, J. C. (2009). Two-dimensional Simulations of FU Orionis Disk Outbursts. *Astrophysical Journal*, 701, 620–634.
- Zhu, Z., Hartmann, L., Nelson, R. P., & Gammie, C. F. (2012). Challenges in Forming Planets by Gravitational Instability: Disk Irradiation and Clump Migration, Accretion, and Tidal Destruction. *Astrophysical Journal*, 746, 110.
- Zsom, A., Ormel, C. W., Güttler, C., Blum, J., & Dullemond, C. P. (2010). The outcome of protoplanetary dust growth: pebbles, boulders, or planetesimals? II. Introducing the bouncing barrier. *Astronomy and Astrophysics*, 513, A57.
- Zúñiga-Fernández, S., Bayo, A., Elliott, P., Zamora, C., Corvalán, G., Haubois, X., Corral-Santana, J. M., Olofsson, J., Huélamo, N., Sterzik, M. F., Torres, C. A. O., Quast, G. R., & Melo, C. H. F. (2021). Search for associations containing young stars (SACY). VIII. An updated census of spectroscopic binary systems exhibiting hints of non-universal multiplicity among their associations. *Astronomy and Astrophysics*, 645, A30.
- Zuckerman, B., Rhee, J. H., Song, I., & Bessell, M. S. (2011). The Tucana/Horologium, Columba, AB Doradus, and Argus Associations: New Members and Dusty Debris Disks. *Astrophysical Journal*, 732(2), 61.
- Zuckerman, B., Song, I., Bessell, M. S., & Webb, R. A. (2001). The β Pictoris Moving Group. *Astrophysical Journal, Letters*, 562(1), L87–L90.
- Zurlo, A., Cieza, L. A., Ansdell, M., Christiaens, V., Pérez, S., Lovell, J., Mesa, D., Williams, J. P., Gonzalez-Ruilova, C., Carraro, R., Ruíz-Rodríguez, D., & Wyatt, M. (2021). The effect of stellar multiplicity on protoplanetary discs: a near-infrared survey of the Lupus star-forming region. *Monthly Notices of the RAS*, 501(2), 2305–2315.
- Zurlo, A., Cieza, L. A., Pérez, S., Christiaens, V., Williams, J. P., Guidi, G., Cánovas, H., Casassus, S., Hales, A., Principe, D. A., Ruíz-Rodríguez, D., & Fernandez-Figueroa, A. (2020a). The Ophiuchus Disc Survey Employing ALMA (ODISEA) - II. The effect of stellar multiplicity on disc properties. *Monthly Notices of the RAS*, 496(4), 5089–5100.
- Zurlo, A., Cugno, G., Montesinos, M., Perez, S., Canovas, H., Casassus, S., Christiaens, V., Cieza, L., & Huelamo, N. (2020b). The widest H α survey of accreting

protoplanets around nearby transition disks. *Astronomy and Astrophysics*, 633, A119.

Zurlo, A., Vigan, A., Galicher, R., Maire, A. L., Mesa, D., Gratton, R., Chauvin, G., Kasper, M., Moutou, C., Bonnefoy, M., Desidera, S., Abe, L., Apai, D., Baruffolo, A., Baudoz, P., Baudrand, J., Beuzit, J. L., Blancard, P., Boccaletti, A., Cantalloube, F., Carle, M., Cascone, E., Charton, J., Claudi, R. U., Costille, A., de Caprio, V., Dohlen, K., Dominik, C., Fantinel, D., Feautrier, P., Feldt, M., Fusco, T., Gigan, P., Girard, J. H., Gisler, D., Gluck, L., Gry, C., Henning, T., Hugot, E., Janson, M., Jaquet, M., Lagrange, A. M., Langlois, M., Llored, M., Madec, F., Magnard, Y., Martinez, P., Maurel, D., Mawet, D., Meyer, M. R., Milli, J., Moeller-Nilsson, O., Mouillet, D., Origné, A., Pavlov, A., Petit, C., Puget, P., Quanz, S. P., Rabou, P., Ramos, J., Rousset, G., Roux, A., Salasnich, B., Salter, G., Sauvage, J. F., Schmid, H. M., Soenke, C., Stadler, E., Suarez, M., Turatto, M., Udry, S., Vakili, F., Wahhaj, Z., Wildi, F., & Antichi, J. (2016). First light of the VLT planet finder SPHERE. III. New spectrophotometry and astrometry of the HR 8799 exoplanetary system. *Astronomy and Astrophysics*, 587, A57.

Zurlo, A., Vigan, A., Mesa, D., Gratton, R., Moutou, C., Langlois, M., Claudi, R. U., Pueyo, L., Boccaletti, A., Baruffolo, A., Beuzit, J. L., Costille, A., Desidera, S., Dohlen, K., Feldt, M., Fusco, T., Henning, T., Kasper, M., Martinez, P., Moeller-Nilsson, O., Mouillet, D., Pavlov, A., Puget, P., Sauvage, J. F., Turatto, M., Udry, S., Vakili, F., Waters, R., & Wildi, R. F. (2014). Performance of the VLT Planet Finder SPHERE. I. Photometry and astrometry precision with IRDIS and IFS in laboratory. *Astronomy and Astrophysics*, 572, A85.